

**SURGICAL MANAGEMENT OF ISCHEMIC MITRAL  
REGURGITATION: AN IN-VITRO INVESTIGATION**

A Dissertation  
Presented to  
The Academic Faculty

by

Jean-Pierre M. Rabbah

In Partial Fulfillment  
of the Requirements for the Degree  
Doctor in Philosophy in the  
School of Biomedical Engineering

Georgia Institute of Technology  
May 2014

**COPYRIGHT 2014 BY JEAN-PIERRE M. RABBAH**

**SURGICAL MANAGEMENT OF ISCHEMIC MITRAL  
REGURGITATION: AN IN-VITRO INVESTIGATION**

Approved by:

Dr. Ajit P. Yoganathan, Advisor  
Department of Biomedical Engineering  
*Georgia Institute of Technology*

Dr. Robert E. Guldberg  
School of Mechanical Engineering  
*Georgia Institute of Technology*

Dr. Rudolph "Rudy" Gleason  
Department of Biomedical Engineering  
*Georgia Institute of Technology*

Dr. W. Robert Taylor  
School of Medicine  
*Emory University*

Dr. Joseph H. Gorman, III  
School of Medicine  
*University of Pennsylvania*

Date Approved: January 7, 2014

For my ever growing family.

# TABLE OF CONTENTS

	Page
LIST OF TABLES	x
LIST OF FIGURES	xiii
LIST OF ABBREVIATIONS	xxv
SUMMARY	xxvi
<u>CHAPTER</u>	
1 INTRODUCTION	1
2 BACKGROUND	5
2.1 The Mitral Valve	5
2.1.1 The Mitral Annulus	7
2.1.2 The Mitral Leaflets	8
2.1.3 The Mitral Chordae	11
2.1.4 The Papillary Muscles	13
2.2 Mitral Valve Mechanics	14
2.2.1 Mitral Valve Annular Mechanics	14
2.2.1.1 Quantification of Cyclic Mitral Annular Areal Reduction	14
2.2.1.2 Quantification of Mitral Annular Saddle and Flattening with Disease	15
2.2.2 Leaflet Mechanics	17
2.2.2.1 Mechanical Properties	17
2.2.2.2 Adaptive Remodeling Due to Mechanical Stimuli	26
2.2.3 Chordae Mechanics	27
2.2.3.1 Mechanical Properties of Chordae Tendineae	28

2.2.3.2	Experimental Measurement of Chordal Forces: Physiological Conditions	29
2.2.3.3	Experimental Measurement of Chordal Forces: Pathological Conditions	32
2.2.3.4	Experimental Measurement of Chordal Forces: Mitral Valve Repair	34
2.2.4	Papillary Muscle Mechanics	35
2.2.4.1	Experimental Measurement of Papillary Muscle Force	35
2.3	Mitral Valve Insufficiency	37
2.4	Surgical Repair for Mitral Valve Insufficiency	44
2.5	Quantification of Mitral Regurgitation	51
2.6	Computational Mitral Valve Models	57
3	OBJECTIVE AND SPECIFIC AIMS	61
4	MATERIALS	66
4.1	Pulsatile Left Heart Simulator	66
4.2	Echocardiography	74
4.3	High Speed Imaging	75
4.4	Chordal Force Transducers	75
4.5	Modified Left Heart Simulator	77
4.6	Particle Image Velocimetry	81
4.7	Micro-computed Tomography	85
4.8	Instrument Calibration	86
4.8.1	Flow Probe Calibration	86
4.8.2	Pressure Calibration	87
4.8.3	Viscosity Calibration	88
4.8.4	Papillary Muscle and Chordal Force Transducer Calibration	88

5	EXPERIMENTAL METHODS AND PROTOCOLS	90
5.1	Common Experimental Techniques	90
5.1.1	Mitral Valve Excision	90
5.1.2	Mitral Valve Preparation	92
5.1.3	Establishing a Control	94
5.2	Specific Aim 1 – Accurate Quantification of Mitral Regurgitation	95
5.2.1	Experimental Protocol	97
5.2.2	Data Analysis	99
5.3	Specific Aim 2 – Evaluating the Efficacy of Surgical Repair for Ischemic Mitral Regurgitation	106
5.3.1	Basal Papillary Muscle Relocation	106
5.3.1.1	Experimental Protocol	106
5.3.1.2	Data Analysis	109
5.3.2	Anterior Leaflet Augmentation	112
5.3.2.1	Experimental Protocol	112
5.3.2.2	Data Analysis	115
5.4	Specific Aim 3 – Developing an Experimental Database to Advance Mitral Valve Surgical Planning Tools	116
5.4.1	Experimental Protocol	116
5.4.1.1	Hemodynamic Boundary Conditions	116
5.4.1.2	Clinical Imaging and Biomechanical Evaluation	117
5.4.1.3	Micro-computed Tomography	117
5.4.1.3.1	Paraformaldehyde Pressure Fixation	119
5.4.1.3.2	Phosphotungstic Acid Contrast Enhancement	119

5.4.1.4	Stereoscopic Particle Image Velocimetry	119
5.4.1.5	Geometric Boundary Conditions	122
5.4.2	Data Analysis	123
5.4.2.1	Geometric Reconstruction from Micro-computed Tomography	123
5.4.2.2	Geometric Reconstruction from Echocardiography	124
5.4.2.3	Velocity Field Reconstruction	124
6	<b>SPECIFIC AIM 1: IN-VITRO VALIDATION OF THE PHILIPS 3D FIELD OPTIMIZATION METHOD</b>	128
6.1	Introduction	128
6.2	Results	130
6.2.1	Mitral Regurgitation Model	130
6.2.2	2D Proximal Isovelocity Surface Area Analysis	132
6.2.3	Philips 3D Field Optimization Method	138
6.2.3.1	Iteration 1: Fixed Radii of Velocity Integration	139
6.2.3.2	Iteration 2: Adaptive Adjustment of Radii for Velocity Integration	144
6.2.3.3	Iteration 3: Adaptive Adjustment of Regurgitant Orifice Z-height	148
6.2.4	3D Integrative Proximal Isovelocity Surface Area	152
6.3	Discussion	156
6.4	Conclusions	166
7	<b>SPECIFIC AIM 2: SURGICAL MANAGEMENT OF ISCHEMIC MITRAL REGURGITATION</b>	168
7.1	Introduction	168
7.2	Anterior Leaflet Augmentation	171
7.2.1	Results	171

7.2.1.1 Ischemic Mitral Regurgitation	172
7.2.1.2 Undersized Annuloplasty Versus Anterior Leaflet Augmentation with True-Sized Annuloplasty	176
7.2.2 Discussion	181
7.2.3 Conclusions	187
7.3 Basal Papillary Muscle Relocation	188
7.3.1 Results	189
7.3.1.1 Disease Progression and Ring Annuloplasty	189
7.3.1.2 Basal Papillary Muscle Relocation	191
7.3.2 Discussion	200
7.3.2.1 Efficacy of Basal Papillary Muscle Repair	200
7.3.2.2 Effect of Annular Anchor Location	201
7.3.2.3 Clinical Parameters to Inform Papillary Muscle Relocation Distance	204
7.3.2.4 Effect of Papillary Muscle Selection	205
7.3.3 Conclusions	206
8 SPECIFIC AIM 3: NOVEL LEFT HEART SIMULATOR FOR THE DEVELOPMENT AND VALIDATION OF COMPUTATIONAL MITRAL VALVE MODELS	207
8.1 Introduction	207
8.2 Results	208
8.2.1 Hemodynamic Boundary Conditions	208
8.2.2 Geometric Characterization	211
8.2.3 Micro-Computed Tomography	213
8.2.4 Stereoscopic Particle Image Velocimetry	219
8.2.5 Valve Biomechanics	228



8.3 Discussion	234
8.4 Conclusions	243
9 CLINICAL SIGNIFICANCE, LIMITATIONS, AND FUTURE WORK	245
9.1 Clinical Significance	245
9.2 Limitations	254
9.3 Future Studies	256
9.3.1 Specific Aim 1	256
9.3.2 Specific Aim 2	258
9.3.3 Specific Aim 3	260
10 CONCLUSIONS	262
APPENDIX A: PROTOCOLS	264
APPENDIX B: EXPERIMENTAL DATA	268
APPENDIX C: MATLAB CODES	285
APPENDIX D: COMPUTER AIDED DESIGN	294
REFERENCES	302

## LIST OF TABLES

		Page
Table 1-1	Modulus of elasticity for posterior and anterior leaflets.	19
Table 1-2	Measured significant differences in leaflets' stiffness between normal and pathological valves.	20
Table 1-3	Anterior and posterior leaflet strain and strain rates from in-vivo and in-vitro data.	22
Table 1-4	Significantly measured difference in leaflet strain from normal to pathological and repaired conditions.	23
Table 1-5	Mechanical properties of various chordal groups, reproduced from [1].	29
Table 1-6	Experimental measurements of physiological chordal forces. Types of chordae are: AA anterolateral PM to anterior leaflet; AP – anterolateral PM to posterior leaflet; PA – posteromedial PM to anterior leaflet; PP – posteromedial PM to posterior leaflet; CCT – commissural chordae tendinae.	30
Table 1-7	Changes in chordal force due to pathological and surgical repair conditions as compared to normal physiology.	33
Table 1-8	Papillary muscle force measurements [2]. $P \cdot A$ is the product of transvalvular pressure (P) and leaflet surface area (A).	36
Table 2-1	Changes in mitral annular dimensions associated with ischemic mitral regurgitation [3].	42
Table 4-1	Annular dimensions used for each experimental configuration.	70
Table 4-2	Timing and effect of air solenoid valves.	73
Table 5-1	Time difference between image pairs for various segments of the cardiac cycle.	121
Table 6-1	Mitral regurgitation was binned into mild, moderate and severe based on clinical guidelines.	132
Table 6-2	Reported errors for the 2D PISA method grouped by orifice type and regurgitant severity.	136
Table 6-3	Misdiagnosis incidence by regurgitant grade was reported for the 2D PISA method.	137

Table 6-4	Reported errors for the 3D FOM grouped by orifice type and regurgitant severity.	142
Table 6-5	Misdiagnosis incidence by regurgitant grade was reported for the 3D FOM.	143
Table 6-6	Reanalysis of round orifice outliers.	145
Table 6-7	Misdiagnosis incidence by regurgitant grade was reported for the 3D FOM adaptive radii algorithm.	147
Table 6-8	Misdiagnosis incidence by regurgitant grade was reported for the 3D FOM adaptive z-height algorithm.	151
Table 6-9	Reported errors for the Integrative 3D PISA method grouped by orifice type and regurgitant severity.	154
Table 6-10	Misdiagnosis incidence by regurgitant grade was reported for the 3D Integrative 3D PISA method.	155
Table 6-11	Discrete temporal sampling by the ultrasound system may affect regurgitant quantification by up to 20 mL per beat. These values were extracted from representative hemodynamic waveforms.	163
Table 7-1	Mitral regurgitation grade of N = 15 experiments for the ischemic mitral regurgitation model.	172
Table 7-2	Coaptation length was significantly decreased from Control to IMR.	174
Table 7-3	Chordal forces for all four instrumented chordae in the control and Ischemic Mitral Regurgitation group.	176
Table 7-4	Dimensions of the small and large anterior leaflet patch inserts.	177
Table 7-5	Coaptation length was significantly increased by all three repairs compared to the IMR condition. * Denotes significance ( $p < 0.05$ ) between large patch and both RMA and small patch.	177
Table 7-6	Chordal forces for all four instrumented for the surgical repair conditions. * denotes significance ( $p < 0.05$ ) as compared to IMR. † indicates significance between groups.	179
Table 7-7	Coaptation length and tenting area for disease progression and mitral annuloplasty repair.	190

Table 7-8:	Coaptation length and tenting area for all four repairs at the 4mm and 6 mm increments. 2mm repair increment now shown as this level of repair did not improve leaflet closure.	192
Table 7-9:	Coaptation length is inversely proportional to papillary muscle distance whereas tenting area is linearly proportional to papillary muscle distance.	196
Table 7-10:	Relationships between leaflet parameters and papillary muscle distance are tabulated. Coefficients are comparable between repair groups.	198
Table 7-11:	Tenting area at the off-center coaptation lines.	199
Table 7-12:	Residual papillary muscle displacement after each incremental basal repair.	204
Table 8-1:	Currently available data for computational validation. Repository population is ongoing.	236
Table 8-1:	Comprehensive experimental benchmark data are generated through multiple complementary experimental techniques.	244
Table B-1:	Summary of Average PISA data for all analysis techniques.	274
Table B-2:	Mitral regurgitation for all anterior leaflet augmentation conditions.	276
Table B-3:	Coaptation length for all anterior leaflet augmentation conditions.	276
Table B-4:	Anterior strut chordal force data for all anterior leaflet augmentation conditions from the posteromedial PM.	277
Table B-5:	Posterior strut chordal force for all anterior leaflet augmentation conditions from the posteromedial PM.	277
Table B-6:	Anterior strut chordal force data for all anterior leaflet augmentation conditions from the anterolateral PM.	278
Table B-7:	Posterior strut chordal force data for all anterior leaflet augmentation conditions from the anterolateral PM.	278
Table B-8:	Leaflet coaptation length and tenting area data for all papillary muscle relocation experimental conditions	279

## LIST OF FIGURES

	Page	
Figure 2-1	The ventricular side of a porcine mitral valve is displayed, highlighting the mitral leaflets, chordae tendinae, and papillary muscles. The valve was excised from an explanted heart and cut in half at the P2 scallop of the posterior leaflet.	6
Figure 2-2	Forces acting on the mitral apparatus. Overall mitral force balance requires the structural interplay between each of the individual components. This is most commonly disrupted in functional mitral valve disease where left atrial and ventricular dilation lead to restricted leaflet closure and mitral regurgitation.	7
Figure 2-3	Atrial view of the mitral leaflets during systole shows the anterior leaflet extends to cover two-thirds of the mitral orifice. The posterior leaflet is comprised of three scallops P1, P2, and P3, which are opposed by similarly named regions of the anterior leaflet. AC: Anterior commissure. PC: Posterior commissure.	9
Figure 2-4	Histological cross-section of the mitral leaflets. Histological cross-sections of the mitral leaflets reveal an organized layered structure. In addition to elastin, collagen (main load bearing element) and proteoglycans, the mitral leaflets are known to contain smooth muscle cells, nonmyelinated nerve fibers, and vasculature at their base. (Images adapted with permission from Grande Allen et al. [130]).	11
Figure 2-5	Non-linear stress strain curve of the mitral leaflets shows directionally dependent response and minimal hysteresis. There is minimal stress developed in the “toe” region due to uncimping of the collagen fibers. A non-linear transition region (recruitment and alignment of collagen fibers) is followed by a linear, high tensile modulus regime (locking of collagen fibers). (image adapted with permission from Grashow et al [4]).	18
Figure 2-6	(Top Panel) Superficial grids marked on mitral leaflets include tissue marker dye ( <i>in vitro</i> ), sonomicrometry crystals (image courtesy of Dr. Gorman), and radio-opaque markers (image adapted with permission from Rausch et al. [5]). (Bottom Panel) Leaflet strains calculated over the cardiac cycle show large and rapid anisotropic stretch. (Images adapted with permission from Sacks et al. [6].)	21

Figure 2-7	<i>In vivo</i> areal, circumferential, and radial strains are shown at maximum left ventricular pressure. The strain is anisotropic, and largest in the radial direction due to the preferential alignment of collagen fibers. The largest stretch is observed at the free edge, which helps create redundant coaptation. (Image adapted with permission from Rausch et al. [7].)	24
Figure 2-8	Miniature C-arm force transducers selectively record chordal forces throughout the cardiac cycle (Image adapted with permission from Nielsen et al. [8]).	30
Figure 2-9	Papillary muscle force transducers: Force transducers sutured between severed papillary muscles record forces throughout the cardiac cycle (Image adapted with permission from Askov et al. [9].)	37
Figure 2-10	(Left) Patient survival is significantly decreased with the presence of mitral regurgitation following myocardial ischemia. (Right) This relationship is proportional to regurgitation severity. [10]	39
Figure 2-11	Mitral annular dilation and flattening result from ischemic remodeling of the surrounding myocardium [11].	40
Figure 2-12	Following myocardial ischemia, papillary muscle displacement away from the mitral annular plane results in restricted leaflet closure and mitral regurgitation [12].	41
Figure 2-13	Mitral annular dilation and posteromedial papillary muscle displacement was significantly different between animals that did and did not develop chronic ischemic mitral regurgitation after myocardial infarction [13].	43
Figure 2-14	Isolated and combined effects of annular dilation and papillary muscle displacement on mitral valvular function [14].	44
Figure 2-15	Ring annuloplasty aims to surgically restore physiological size and shape of the native mitral annulus (image adapted from Carpentier's Reconstructive Valve Surgery).	45
Figure 2-16	3 year follow up of patients treated with mitral annuloplasty for functional mitral regurgitation reveals high rates of recurrence as early as 3 years. [15]	46
Figure 2-17	Recurrent mitral regurgitation following ring annuloplasty of ischemic valve disease has been observed in a wide range of studies [12].	47

Figure 2-18	Adjunctive leaflet augmentation results in larger anterior leaflet surface area to promote valve competency while displacing chordal insertion points [16].	49
Figure 2-19	In the Kron procedure, the posteromedial papillary muscle is surgically relocated to the adjacent mitral annulus to relieve subvalvular tethering caused by a severely dilated left ventricle [17].	50
Figure 2-20	The 2D PISA method is explained in this schematic from the echocardiographer.org.	54
Figure 2-21	The observed velocity vectors along the ultrasound scan lines have lower magnitudes than the true velocity field because of the cosine angle correction [18].	56
Figure 2-22	The observed velocity vectors along the ultrasound scan lines have lower magnitudes than the true velocity field because of the cosine angle correction [18].	57
Figure 2-23	Patient specific anatomical mitral valve models derived from CT (left) and three-dimensional echocardiography (right) imaging will ultimately be used for predictive surgical planning. CT imaging is better capable of capturing the detailed chordal structure. (Images adapted with permission from Wang et al. [19] and Mansi et al. [20].)	58
Figure 4-1	Schematic representation of the pulsatile left heart simulator.	67
Figure 4-2	Adjustable mitral annular plate.	69
Figure 4-3	The Left Heart.	71
Figure 4-4	Mechanical papillary muscle positioning rods.	72
Figure 4-5	Representative hemodynamic waveforms, ensemble average over 15 cardiac cycles, from the left heart simulator.	73
Figure 4-6	Chordal force transducer sutured onto posterior leaflet secondary chordae.	76
Figure 4-7	The new modular left heart simulator.	78
Figure 4-8	Simplified papillary muscle positioning system.	81
Figure 4-9	Schematic representation of the stereo-photography and laser plane configurations.	83

Figure 4-10	Schematic representation of calibration target.	84
Figure 4-11	Representative flow probe calibration.	87
Figure 4-12	Representative pressure calibration.	88
Figure 5-1	Mitral valve sizing is performed with a C-E Physio annuloplasty ring sizer measured to the anterior leaflet. (Image adapted from Carpentier's Reconstructive Valve Surgery)	91
Figure 5-2	Excised mitral valve apparatus.	92
Figure 5-3	Interrupted knots strategically placed to position the mitral annulus. Right: Continuous Ford interlocking stitch secures the native mitral annulus to the silicon annulus.	93
Figure 5-4	Mitral valve mounted onto annulus plate.	94
Figure 5-5	An en-face view of the normal mitral valve closure. Inlay: Apical-basal long axis view of normal mitral valve closure. (Images adapted from Carpentier's Reconstructive Valve Surgery.)	96
Figure 5-6	Left: "Round" regurgitant mitral orifice. Right: "Slit" regurgitant mitral orifice".	98
Figure 5-7	2D apical-basal long axis echocardiography shows a large regurgitant jet and proximal isovelocity surface area.	99
Figure 5-8	A representative mitral flow waveform shows. Mitral regurgitation is calculated by integrating over the late systolic portion of the flow curve.	100
Figure 5-9	PISA radius and $V_{alias}$ are determined.	101
Figure 5-10	$V_{max}$ and VTI are measured from continuous wave (CW) echocardiography.	102
Figure 5-11	Representative long (left) and short (right) axis slices of the regurgitant jet. The short axis slice was used to position the long-axis slices, from which the PISA shell was manually segmented.	103
Figure 5-12	Points along the PISA for a given aliasing velocity were manually selected. A surface mesh was fit to the resulting point cloud using Geomagic Studio. Total surface of the mesh was computed to provide the effective regurgitant area.	104



Figure 5-13	Screen capture of the QFlow preferences. “Flow” and “Flow + Z” analysis were performed with and without “Enable Adjust Orifice and Flow Band” options.	105
Figure 5-14	Annular landmarks depict targets for traction suture. Highlighted in red is the pathologically displaced posteromedial papillary muscle.	108
Figure 5-15	Basal papillary muscle relocation was performed in 2 mm increments to either the trigone (blue vector) or the commissure (red vector). Pathological papillary muscle displacement was performed in the apical (black dashed vector), lateral (purple dashed vector), and the posterior (green dashed vector) directions.	109
Figure 5-16	Three lines of coaptation are shown: A1-P1, A2-P2, and A3-P3.	110
Figure 5-17	Coaptation height and tenting area are depicted.	111
Figure 5-18	Annular sizes and pm positions for repair protocol. Repairs were randomized to either small or large patch treatments	113
Figure 5-19	Atrial (left) and ventricular (right) views of an anterior leaflet augmented with a pericardial patch. Two chordal force transducers can be seen attached to the anterior strut chordae.	115
Figure 5-20	Representative paired images acquired during peak systole.	120
Figure 5-21	Representative mitral flow curve depicting time points sampled for particle image velocimetry.	121
Figure 5-22	Surface mesh of the left heart simulator.	122
Figure 5-23	Micro-CT segmentation protocol is outlined.	124
Figure 5-24	Mask creation for PIV data processing was performed in the following steps: a mask was created (A) and applied (B) to the image in Camera 1; mask from Camera 1 was overlaid (C) and applied (D) to image from Camera 2; an additional mask was created for Camera 2 (E), and velocity vectors were calculated for remaining flow field (F).	126
Figure 5-25	Particle image velocimetry processing flow chart.	127
Figure 6-1	Representative images of round (Left) and slit (Right) regurgitant orifices. Inlays show corresponding C-plane echocardiography or proximal isovelocity surface area observed 1-3 mm sub-annularly.	131

Figure 6-2	Scatter plot of mitral regurgitation shows a range of volumes from 10 to 70 mL.	132
Figure 6-3	Mitral regurgitation volume quantified through 2D PISA underestimated true mitral regurgitation. Dashed line represents 1:1.	134
Figure 6-4	Mitral regurgitation volume quantified through 2D PISA underestimated true mitral regurgitation. Dashed lines show mean $\pm 2$ standard deviations.	134
Figure 6-5	Data were grouped for round and slit orifice. 2D PISA was accurate for the round data, but systematically underestimated regurgitant volume for the slit orifice data.	135
Figure 6-6	Histogram distribution of percent errors were grouped for round and slit orifice data.	138
Figure 6-7	Mitral regurgitation volume quantified through 3D FOM underestimated true mitral regurgitation. Dashed line represents 1:1.	139
Figure 6-8	Mitral regurgitation volume quantified through 3D FO underestimated true mitral regurgitation. Dashed lines show mean $\pm 2$ standard deviations	140
Figure 6-9	Data were grouped for round and slit orifice. 3D FOM was accurate for the round data, but systematically underestimated regurgitant volume for the slit orifice data.	141
Figure 6-10	Histogram distribution of percent errors were grouped for round and slit orifice data.	143
Figure 6-11	The top panels show the radius is adaptive between frames of the cardiac cycle. In the bottom panel, the radius is predefined and constrained. (Green dot is the origin of the flow convergence. The two curved bands are the minimum and maximum radius over which the velocities are integrated).	144
Figure 6-12	Mitral regurgitation volume quantified through adaptive radii 3D FOM slightly overestimates the data. Dashed line represents 1:1.	146
Figure 6-13	Histogram distribution of percent errors between measured and truth regurgitant volumes for slit orifices.	147
Figure 6-14	Mitral regurgitation volume quantified through adaptive z-height 3D FOM slightly overestimates the data. Dashed line represents 1:1.	149

Figure 6-15	Histogram distribution of percent errors between measured and truth regurgitant volumes for slit orifices.	151
Figure 6-16	Mitral regurgitation volume quantified through the integrative 3D PISA method correlates closely to the truth data. Dashed line represents 1:1.	152
Figure 6-17	Mitral regurgitation volume quantified through the integrative 3D PISA method has a minimal measurement bias. Dashed lines show mean $\pm 2$ standard deviations.	153
Figure 6-18	Data were grouped for round and slit orifice. The Integrative 3D PISA method was comparably accurate for the round and slit orifice data.	154
Figure 6-19	Histogram distribution of percent errors between measured and truth regurgitant volumes for slit orifices.	155
Figure 6-20	There is an uncertainty associated with identifying the origin of flow convergence and the subsequent radial measurement to the velocity isosurface.	157
Figure 6-21	(Left) Near to the mitral orifice, highly turbulent and chaotic flow defines the decorrelation zone. (Right) In the decorrelation zone, the velocity profile no longer follows the expected relationship ( $V \propto 1/R^2$ ).	159
Figure 6-22	Erroneous migration of the apical-basal position of the mitral orifice is seen between two frames in the cardiac cycle.	161
Figure 7-1	Restrictive mitral annuloplasty is performed by systematically downsizing the mitral annulus by two sizes using a rigid ring. As a result, mitral coaptation is dominated by the anterior leaflet; the posterior leaflet is chordalized.	170
Figure 7-2	Large asymmetric regurgitant jet. White arrow indicates flow direction.	173
Figure 7-3	Minimal coaptation is observed at the A2-P2 coaptation line. Anterior and posterior leaflets are tethered apically into the ventricle. A notable kink in each leaflet is observed due to chordal tethering.	174
Figure 7-4	Chordal forces were increased from the healthy to the IMR conditions. * denotes significance between conditions at $p < 0.05$ .	175

Figure 7-5	% improvement in coaptation length of each repair as compared to IMR. * denotes significance between repairs. † Indicate significance as compared to IMR condition.	178
Figure 7-6	% improvements in chordal forces for all repairs as compared to IMR. †denotes significance ( $p < 0.05$ ) as compared to IMR. * indicates significance between groups.	181
Figure 7-7	Schematic representation of the effects Ischemic Mitral Regurgitation (IMR), Restrictive Mitral Annuloplasty (RMA), and Anterior Leaflet Augmentation (ALA) has on chordal tethering. PMPM: posteromedial papillary muscle.	184
Figure 7-8	Figure 7-8 Echocardiography shows that the anterior strut chordae have been translocated apically with the insertion of an anterior leaflet patch. This moved the chordae into the coaptation zone and away from the belly of the leaflet.	184
Figure 7-9	Coaptation length and tenting area are shown for the disease progression and mitral annuloplasty conditions. * denotes significance to control ( $p < 0.05$ ). † indicates significance between conditions ( $p < 0.05$ ).	191
Figure 7-10	Coaptation length and tenting area for all four repairs at the 4mm and 6 mm increments. * denotes significance from Control, while † denotes significance from Chronic MI with MA. 2mm repair increment now shown as this level of repair did not improve leaflet closure.	193
Figure 7-11	Normalized coaptation length has an inverse relationship with papillary muscle distance. Tenting area is linearly proportional to papillary muscle distance. Papillary muscle distance is measured from the tip of the papillary muscle to the mitral annular plane. Scatter points show consistent trends between experiments.	195
Figure 7-12	The relationship between normalized coaptation length and papillary muscle distance is shown for a representative basal papillary muscle repair. Tenting area is linearly proportional to papillary muscle distance. Papillary muscle distance is measured from the tip of the papillary muscle to the mitral annular plane. Scatter points show consistent trends between experiments.	197
Figure 7-13	Tenting area at the off-center coaptation lines.	199
Figure 7-14	Papillary muscles and annular landmarks are shown.	202
Figure 7-15	Physio annuloplasty ring demarked with difference in trigone and commissure dimensions.	203

Figure 8-1	Representative pressure waveforms in the Atrium, Ventricle, and Aorta.	210
Figure 8-2	Representative mitral flow has low cycle to cycle variability as denoted by $\pm 1$ standard deviation.	210
Figure 8-3	Representative aortic outflow and bladder pump inlet flow.	211
Figure 8-4	Segmented mitral valve leaflets reconstructed from full volume echocardiography.	212
Figure 8-5	Full volume echocardiography images acquired through new acoustic imaging windows capture subvalvular apparatus.	213
Figure 8-6	Mitral valve apparatus as reconstructed from micro-computed tomography imaging.	215
Figure 8-7	Comparison of mitral valve anatomy obtained through micro-computed tomography imaging (off-white) and full volume echocardiography (cyan).	217
Figure 8-8	Comparison of open mitral leaflets reconstructed from echocardiography (left) and micro-computed tomography (right).	217
Figure 8-9	Comparable image slices from Siemens Inveon and Scanco micro-computed tomography systems. Data from the Siemens system has lower signal to noise and a larger field of viewing. A simple band-pass threshold is sufficient (applied in images as green) for the Siemens data.	218
Figure 8-10	Comparison of PIV optical access from orthogonal and angled camera configurations. Dotted red line highlights increased field of view, which captures flow through and proximal to the mitral valve.	220
Figure 8-11	Flow field during early systole is mostly quiescent. Mitral annular plane is to the right in the image. Inlay shows the point on the cardiac demarked on the mitral flow curve.	221
Figure 8-12	Flow field during early diastole shows the onset of left ventricular filling through the mitral valve. Mitral annular plane is to the right in the image. Inlay shows the point on the cardiac demarked on the mitral flow curve.	221
Figure 8-13	Flow field during peak diastole shows a strong, anteriorly oriented central filling jet through the mitral valve. Mitral annular plane is to the right in the image. Inlay shows the point on the cardiac demarked on the mitral flow curve.	223

Figure 8-14	Flow field during end systole shows mostly quiescent flow with low velocity flow reversal, which helps drive the valve closed. Mitral annular plane is to the right in the image. Inlay shows the point on the cardiac demarked on the mitral flow curve. .	224
Figure 8-15	Contour plot of out of plane velocity during peak diastole confirms flow through mitral valve is mostly two-dimensional. Mitral annular plane is to the right in the image. Inlay shows the point on the cardiac demarked on the mitral flow curve. .	225
Figure 8-16	Out of plane vorticity is strongest at edges of central filling jet during peak diastole. Mitral annular plane is to the right in the image. Inlay shows the point on the cardiac demarked on the mitral flow curve.	225
Figure 8-17	Flow in the left atrium during diastole shows a strong pulmonary venous return jet. Velocity vectors are directed towards the mitral orifice. Mitral annular plane is to the left in the image.	227
Figure 8-18	Flow in the left atrium during early systole shows a low velocity retrograde jet; as this valve was competent, this was the closing volume. Mitral annular plane is to the left in the image.	228
Figure 8-19	Surface markers on the anterior (green circles) and posterior (blue circles) leaflets were digitized from dual camera photogrammetry in a reference and systolic configuration.	230
Figure 8-20	Anterior and posterior areal, circumferential and radial strain.	231
Figure 8-21	Anterior and posterior areal strain.	232
Figure 8-22	Anterior and posterior circumferential strain.	232
Figure 8-23	Anterior and posterior radial strain.	233
Figure 8-24	Forces at each papillary muscle can be resolved in the tensile and bending directions throughout the cardiac cycle. Force profiles follow the transmitral waveform. The largest force component is in the tensile direction.	234
Figure 8-25	Mitral valve anatomy reconstructed from micro-computed tomography imaging (Left) and full volume echocardiography (Right). Notice the idealized chordal structure in the echo generated model. [21]	237
Figure 8-26	Simulated mitral valve closure is compared for models generated from micro-computed tomography and echocardiography imaging. [21]	238

Figure 8-27	Proposed flow chart to iteratively tune mitral valve anatomy.	239
Figure 8-28	Radio opaque glass beads are used to register microstructure fiber orientation to micro-computed tomography reconstructed mitral leaflet geometry.	241
Figure 8-29	Highly resolved mesh of the anatomically accurate mitral valve model generated from micro-computed tomography.	242
Figure 9-1	Patient specific treatment planning is a multi-factorial process that combines clinical diagnosis, understanding treatment options and efficacy, and utilizing novel computational methods for predicative virtual modeling.	245
Figure 9-2	Three separate mitral valves are reconstructed from micro-computed tomography (Top: posterior view; Bottom: anterior commissure view). There are noted differences in leaflet lengths, scallop indentations, chordal branching, and papillary muscle tips.	250
Figure 9-3	Patient specific treatment planning is a multi-factorial process that combines clinical diagnosis, understanding treatment options and efficacy, and utilizing novel computational methods for predictive surgical planning.	252
Figure 9-4	Patient specific predictive surgical planning flow chart.	253
Figure 9-5	Hemi-elliptical isovelocity contour in two perpendicular planes.	258
Figure B-1	PISA B, Orifices 1 and 2.	268
Figure B-2	PISA B, Orifices 3 and 4	269
Figure B-3	PISA C, Orifices 1 and 2.	269
Figure B-4	PISA C, Orifices 3 and 4.	269
Figure B-5	PISA E, Orifices 1 and 2.	270
Figure B-6	PISA E, Orifices 3 and 4.	270
Figure B-7	PISA A, Orifice 2, Flow 1 and Orifice 3, Flow 2.	270
Figure B-8	PISA A, Orifice 4, Flow 1 and Flow 2.	271
Figure B-9	PISA B, Orifice 4, Flow 2 and Flow 3.	271
Figure B-10	PISA C, Orifice 1, Flow 1 and Flow 2.	271
Figure B-11	PISA C, Orifice 1, Flow 3 and Orifice 2, Flow 1.	271

Figure B-12	PISA C, Orifice 2, Flow 2 and Flow 3.	272
Figure B-13	PISA C, Orifice 3, Flow 1 and Flow 2.	272
Figure B-14	PISA C, Orifice 3, Flow 3 and Orifice 4, Flow 1.	272
Figure B-15	PISA C, Orifice 4, Flow 2 and Flow 3.	272
Figure B-16	PISA E, Orifice 1, Flow 1 and Flow 2.	273
Figure B-17	PISA E, Orifice 1, Flow 3 and Orifice 2, Flow 2.	273
Figure B-18	PISA E, Orifice 2, Flow 3 and Flow 5.	273
Figure B-19	PISA E, Orifice 3, Flow 1 and Flow 2.	273
Figure B-20	PISA E, Orifice 3, Flow 3 and Orifice 4, Flow 1.	274
Figure B-21	PISA E, Orifice 4, Flow 2 and Flow 3.	274
Figure B-22	Normal Papillary Muscle Position: Low Flow.	281
Figure B-23	Normal Papillary Muscle Position: High Flow.	281
Figure B-24	Anterolateral Papillary Muscle Displaced Anteriorly, Posterior, Apically: Low Flow.	282
Figure B-25	Anterolateral Papillary Muscle Displaced Anteriorly, Posterior, Apically: High Flow.	282
Figure B-26	Symmetric Anterior, Posterior, and Apical PM Displacement: Low Flow.	283
Figure B-27	Symmetric Anterior, Posterior, and Apical PM Displacement: High Flow.	283
Figure B-28	Posteromedial Papillary Muscle Displaced Anteriorly, Posterior, Apically: Low Flow.	284
Figure B-29	Posteromedial Papillary Muscle Displaced Anteriorly, Posterior, Apically: High Flow.	284



## LIST OF ABBREVIATIONS

CT	Chordae Tendinae
FOM	Field Optimization Method
IMR	Ischemic Mitral Regurgitation
MV	Mitral Valve
LA	Left Atrium
LV	Left Ventricle
MA	Mitral Annuloplasty
MI	Myocardial Infarction
MR	Mitral Regurgitation
PISA	Proximal Isovelocity Surface Area
PM	Papillary Muscle
RMA	Restrictive Mitral Annuloplasty
VTI	Velocity Time Integral

## SUMMARY

Owing to its complex structure and dynamic loading, surgical repair of the heart's mitral valve poses a significant clinical burden. Specifically, repair of ischemic mitral regurgitation, which is caused by the geometric disruption of the mitral apparatus in the setting of ventricular dysfunction, results in poor long-term patient survival. Clinical data have shown that the preferred surgical treatment, restrictive mitral annuloplasty, may result in 15-30% early (< 6 months) recurrence of mitral regurgitation; this may exceed 70% after five years. Studies have suggested that isolated annuloplasty may not be a comprehensive repair suitable for all patients because ischemic pathology is multifactorial and results in variable ventricular and valvular geometric distortions. Therefore, in this thesis, a new surgical planning paradigm was developed through three specific aims. In specific aim 1, in collaboration with Philips Healthcare, a novel tool to more accurately and quantitatively assess mitral valve insufficiency was developed and rigorously validated using the Georgia Tech Left Heart Simulator. This tool was found to be more efficacious and robust than the current clinical standard. Ultimately, this improved diagnostics may better inform surgical indication, specifically, to identify patients that may not benefit from simple ring annuloplasty. In specific aim 2, targeted adjunctive surgical repair for such patients were investigated. Anterior leaflet augmentation and basal papillary muscle relocation were observed to restore mitral valve function while reducing the leaflet-subvalvular tethering associated with ischemic left ventricular remodeling. These efficacious repairs were found to be robust to variability in surgical implementation, which may encourage more widespread clinical adaptation. Finally, in specific aim 3, an integrative experimental framework was developed to

promote pre-operative patient specific evaluation of mitral valve surgical repair using novel computational methods. The experimental framework combined high-resolution state of the art imaging with clinical imaging to provide the most realistic anatomical reconstructions possible. For the first time, ventricular flow fields through and proximal to a native mitral valve were acquired using stereoscopic particle image velocimetry. These data were combined with measurements of leaflet dynamics and subvalvular forces to create a comprehensive database for the rigorous validation of mitral valve finite element and fluid-structure interaction models. Collectively, these studies comprise a surgical planning paradigm that may better inform repair of mitral valve insufficiency.

# CHAPTER 1

## INTRODUCTION

The heart's mitral valve is the left atrioventricular valve, which maintains unidirectional oxygenated blood flow from the left atrium into the left ventricle. Owing to its complex structure and dynamic mechanical loading, mitral valve dysfunction is a complex and morbid condition with increasing clinical prevalence that challenges cardiac surgeons and cardiologists alike. If left untreated, mitral valve insufficiency is associated with high rates of patient mortality and with adverse patient prognosis [10,22,23]; these relationships are further strained with increasing regurgitation severity [10].

Although surgical repair of the heart's mitral valve is the preferred mode of treatment for valvular insufficiency [24], reported repair rates are as low as 40% of total mitral operations [25]. Complex surgical repairs are often eschewed in favor of mitral replacement, despite several studies which report the superiority of surgical repair [26-29]. The reasons behind the underutilization of surgical repair are multifactorial, but may be attributed to two principle causes: (i) accurately identifying valve dysfunction and disease severity, and (ii) surgeon experience and understanding of targeted repair therapy [30,31]. Understanding valve dysfunction and accurately quantifying mitral regurgitation are necessary for surgical indication and to best inform cardiologist referral. Moreover, the median number of mitral valve operations among cardiac surgeons is five per year [25]; this alarming statistic highlights the relative surgical inexperience in most low volume centers.

Aside from referring all mitral valve patients to high volume specialized centers, cardiologists and cardiac surgeons need new tools to inform their decision making process. To this end, in this thesis, a new treatment planning paradigm is being developed on the strength of recent advances in medical imaging technology, targeted etiology specific repairs, and computational mitral valve repair models. This integrative multi-factorial approach to mitral valve disease treatment seeks to improve diagnostic tools, provide a mechanistic understanding of post-repair valvular function, and validate novel predictive computational mitral valve models, which may make patient-specific surgical planning possible.

In this thesis, in collaboration with Philips Healthcare, a novel mitral regurgitation quantitative assessment tool will be systematically validated using the well-established pulsatile Georgia Tech Left Heart Simulator [32-39] over a range of clinically relevant regurgitant fractions. The efficacy and robustness of this tool will be compared against the current clinically preferred method, 2D Proximal Isovelocity Surface Area. The validation of this tool offers the promise of simple and accurate quantification of mitral regurgitation, which can replace the current limited qualitative grading scheme. This will remove uncertainty associated with surgical indication, which is dependent on mitral regurgitation severity, observations of valvular lesions, and left ventricular dysfunction.

Following clinical diagnosis, informed clinical referral may promote appropriately targeted surgical therapy based on patient specific valvular dysfunction. This should improve long-term repair durability as it has long been purported that recurrent mitral regurgitation is a consequence of patient valvular dysfunction to surgical repair mismatch; this is most often observed in the treatment of ischemic mitral

regurgitation [40-48]. While typically effective, the preferred surgical repair, mitral annuloplasty, has been shown to result in recurrent or persistent mitral regurgitation, have low rates of reverse left ventricular remodeling, and exhibit poor survival [13-17]. Several studies have sought to identify preoperative characteristics which are predictive of simple annuloplasty failure, including mitral regurgitation grade [49] and jet characteristics [46]. These and similar studies [48,50-52] [53] have identified excessive leaflet restriction through tethered chordae and pathologically displaced papillary muscles as the key contributor to repair failure.

Consequently, new adjunctive surgical strategies have been attempted to compensate for severe leaflet-chordal tethering [17,54-58]. Of note, anterior leaflet augmentation [57,58] and basal papillary muscle relocation (Kron Procedure) [17,56] have been recently demonstrated to restore leaflet coaptation and mobility, while potentially relieving subvalvular tethering. In this thesis, a mechanistic understanding of these complex surgical repairs is sought to: (i) identify their functional efficacy as compared to the preferred surgical option, (ii) understand their impact on leaflet-subvalvular tethering, and (iii) understand the impact of surgical variability on resultant valvular function and mechanics. Ultimately, this knowledge will add to the toolbox at the surgeon's disposal, allowing them to tailor repairs based on informed diagnosis and an intimate understanding of the mechanistic effects of applied repairs.

The definitive step in the new surgical planning paradigm is to expand the mechanistic understanding of mitral valve function and repair through the use of novel computational mitral valve modeling platforms. These computational models provide a unique and non-invasive analysis of mitral valve function and biomechanics for direct

surgical applications, such as ring annuloplasty [59-62], edge-to-edge [20,63] and neochordea [64,65] implantation, and stress analysis [66,67]. Currently however, these models vary considerably in their execution owing to differences in anatomical construction (mainly simplifications to leaflet and chordal geometry), material laws, boundary conditions, and preferred numerical solvers methods. These limitations affect the clinical accuracy and applicability of such computational simulations. Therefore, in this thesis, an experimental framework was developed for the direct one-to-one validations of computational methods against comprehensive, time-resolved experimental data with multiple measured endpoints and well defined boundary conditions.

Collectively, the work in this thesis will seek to improve mitral valve repair incidence and efficacy. This will be accomplished through developing the tools to: (i) improve diagnosis, (ii) demonstrate the efficacy of novel targeted repairs, and (iii) help realize the potential of patient-specific predictive computational modeling.

## CHAPTER 2

### BACKGROUND

#### 2.1 The Mitral Valve

The human heart is comprised of four unidirectional valves that control the direction of flow through its four distinct chambers and out through the pulmonary and systemic circulatory systems. Of these valves, the left atrioventricular valve, or the mitral valve, is a complex structure that ensures unidirectional flow of oxygenated blood from the pulmonary veins to the left ventricle. During the diastolic phase of the cardiac cycle, following isovolumic relaxation, the mitral valve opens to allow filling of the left ventricle. After the onset of systole, following ventricular contraction, the mitral valve closes, and the blood is directed to the outflow tract, through the aortic valve. The morphological construction of this atrioventricular valve consists of four components, which include the annulus, leaflets, chordae tendinae, and papillary muscles (Figure 2-1).



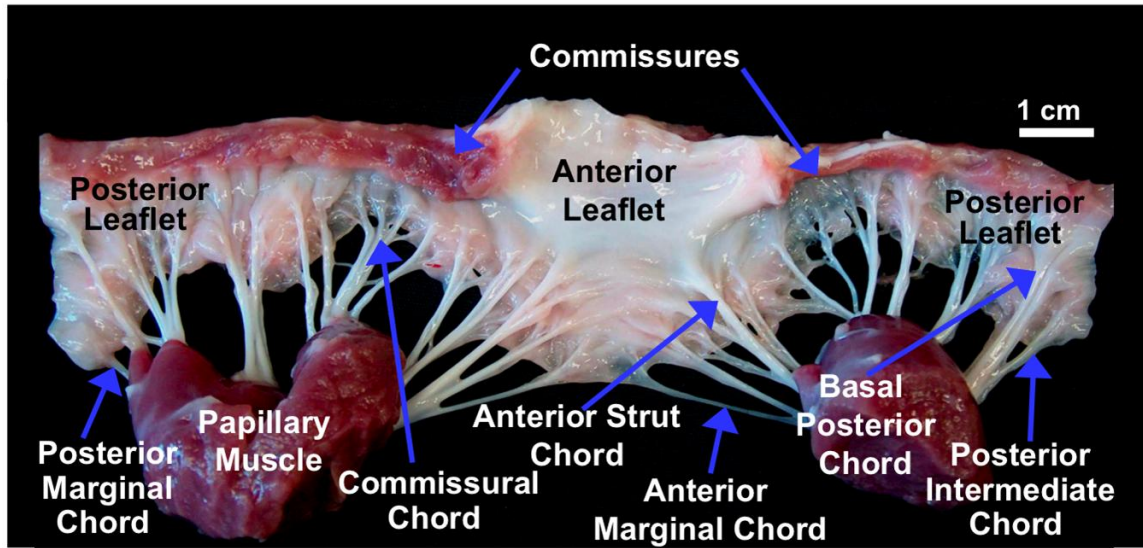


**Figure 2-1 The mitral valve.** The ventricular side of a porcine mitral valve is displayed, highlighting the mitral leaflets, chordae tendinae, and papillary muscles. The valve was excised from an explanted heart and cut in half at the P2 scallop of the posterior leaflet.

Overall, the normal function of the mitral valve is dictated by the structural interplay of the individual components synergistically opposing the left ventricular pressure forces. These includes: mitral annular contraction and bending, apical-basal motion and membrane deformation of the leaflets, restraining tensile chordal forces, and the tension generated by the contracting papillary muscles (Figure 2-2).

Further, the structure-function relationships within the mitral valve are closely associated with the dynamics of left atrium and ventricle. Therefore, pathophysiological conditions affecting left atrial and ventricular musculature can in turn impact mitral valve functionality. This is most readily observed in functional mitral valve disease where deleterious remodeling of the left ventricle, most often due to myocardial infarction, leads to impaired leaflet motion and subsequent mitral regurgitation. This manifests as

decreased annular contraction, restricted systolic leaflet motion, and larger restraining forces transmitted through the papillary muscles and chordae tendineae (Figure 2-2).

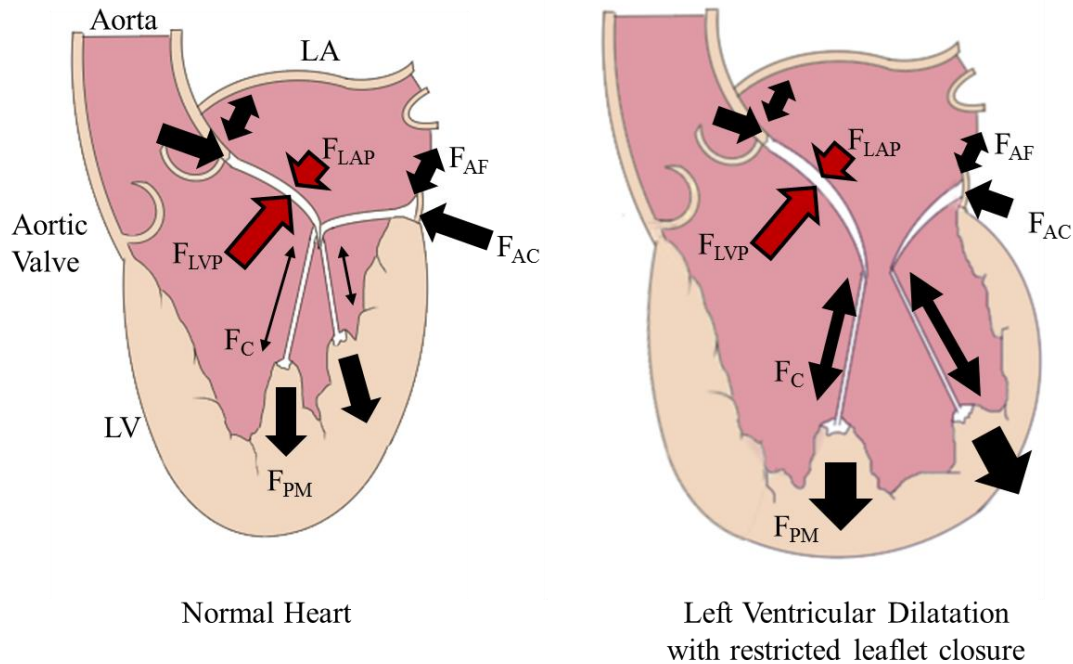


**Figure 2-2 Forces acting on the mitral apparatus. Overall mitral force balance requires the structural interplay between each of the individual components. This is most commonly disrupted in functional mitral valve disease where left atrial and ventricular dilation lead to restricted leaflet closure and mitral regurgitation.**

### 2.1.1 The Mitral Annulus

The mitral annulus is the anatomical junction between the left atrium and the left ventricle and serves as the insertion site for the mitral leaflets. It is a discontinuous band of connective tissue existing within the atrioventricular junction of the left heart. Due to its unique location, the geometry of the mitral annulus changes throughout the cardiac cycle from contraction of adjacent myocardial fibers and expansion of the aortic root.

The anterior annulus is delimited by two structurally supportive fibrous trigones and is continuous with the left and non-coronary aortic leaflets through the intra-valvular curtain. For these reasons, the area of the mitral annulus is asymmetrically reduced and conforms to the shape of a three-dimensional saddle during systole – low points correspond to the antero-lateral and postero-medial commissures. During diastole, the annulus assumes a flattened profile with its largest annular area for maximal filling.

### **2.1.2 The Mitral Leaflets**

The function of the mitral valve in controlling flow between the left atrium and left ventricle is ultimately conveyed through the combined motion of the anterior (or aortic) and posterior (or mural) leaflets. The two mitral leaflets have relative asymmetry in size and shape but with nearly similar surface area. The mitral leaflets originate from one continuous piece of tissue, with the free edge showing two distinct indentations called commissures. The commissures serve dual purposes of dividing continuous tissue into two leaflets for maximal opening during diastole and allowing for proper coaptation (closure) during systole. The base of the leaflets attaches to the mitral annulus; chordae tendinae through papillary muscles support the free edges.

The posterior leaflet is quadrangular in shape, inserts into two-thirds of the mitral annulus circumference, with a typical width and height of 55 mm 13 mm respectively. The posterior leaflet is connected to the muscular base of the left ventricle and its surface shows two indentations known as scallops that are supported by numerous chordae tendinae. These indentations divide the posterior leaflet into three regions known as lateral (P1, smallest in size), central (P2, largest in size) and medial (P3) scallops. The anterior leaflet is semi-circular in shape, inserts into approximately one-third of the mitral

annulus circumference, and has a typical width of 32 mm and height of 23 mm. The regions of the anterior leaflet geometrically opposing the posterior leaflet scallops are denoted as A1, A2 and A3 (Figure 2-3).

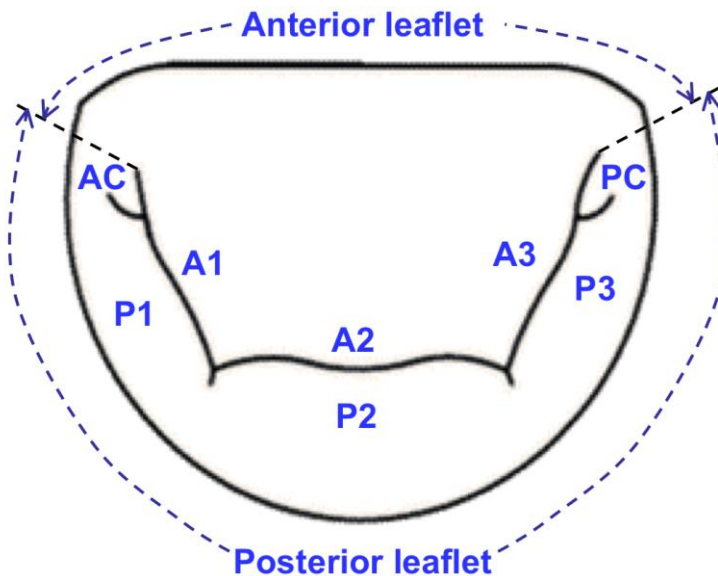


**Figure 2-3 Schematic of Mitral Leaflets.** Atrial view of the mitral leaflets during systole shows the anterior leaflet extends to cover two-thirds of the mitral orifice. The posterior leaflet is comprised of three scallops P1, P2, and P3, which are opposed by similarly named regions of the anterior leaflet. AC: Anterior commissure. PC: Posterior commissure.

The total surface area of both mitral valve leaflets is approximately twice of the valvular orifice [68]. This geometric relationship provides redundancy during closure and prevents retrograde flow from the ventricle to atrium [69]. Geometrically, either leaflet is divided into the base (closest to annulus), belly (central) and free edge (distal to the annulus) regions. Due to numerous chordal insertions, the free edge of the leaflets is thicker, has an irregular texture, and is identified as the rough zone. Conversely, the clear

zone lies between the line of coaptation and the mitral annulus, has minimal chordae attachment, is thin, regular in texture, and is translucent.

The structure of the mitral leaflets primarily consists of fibrous tissue comprising three types of collagen (type I, III and V), along with smooth muscle cells and nonmyelinated nerve fibers. The anterior leaflet base is vascularized from branches of the coronary arteries. Histology of the mitral leaflets has shown a discrete and layered microstructure (Figure 2-4). From the atrium down to the ventricle are the atrialis, spongiosa, fibrosa, and ventricularis, with either side covered with endothelial cells [70,71]. The fibrosa is the thickest layer comprised of dense organized collagen fibers, which provide the majority of load-bearing support to the leaflet. The collagen fibers align preferentially along the circumferential direction. The atrialis contains a layer of loose connective tissue made up of collagen and elastin fibers, which are supported by a proteoglycan and glycosaminoglycan gel in the spongiosa. This aids in lubrication and distribution of compressive loads, while the thin ventricularis is rich in elastic fibers [72]. This layered arrangement is thought to decrease the resistance of leaflets to bending, and decrease the overall bending stresses on the leaflet. [62,73] Taken together, the adaptive microstructure predicates durable functionality in a harsh and dynamic mechanical environment.

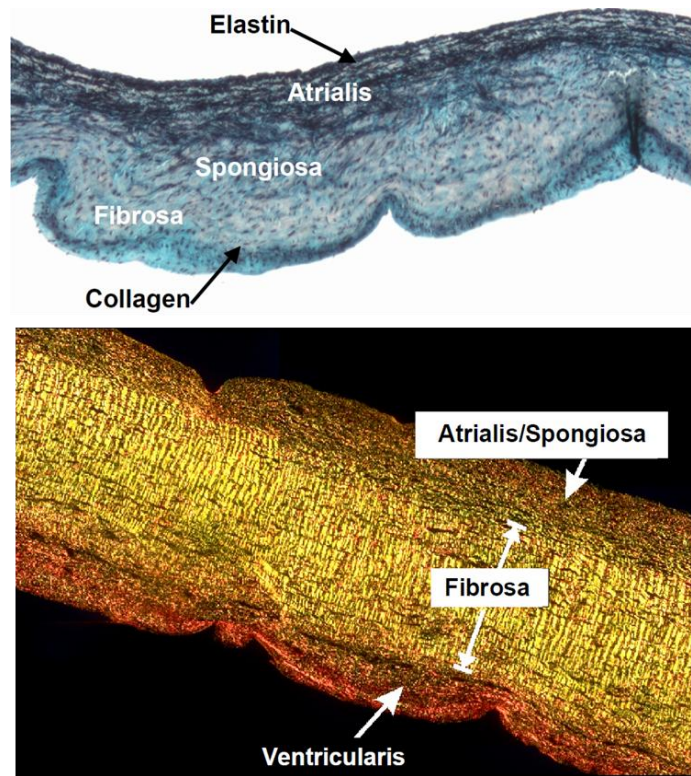


**Figure 2-4 Histological cross-section of the mitral leaflets. Histological cross-sections of the mitral leaflets reveal an organized layered structure. In addition to elastin, collagen (main load bearing element) and proteoglycans, the mitral leaflets are known to contain smooth muscle cells, nonmyelinated nerve fibers, and vasculature at their base. (Images adapted with permission from Grande Allen et al. [130]).**

### 2.1.3 The Mitral Chordae

The leaflets are attached to the LV via the subvalvular apparatus that functions as a suspension system, facilitating leaflet opening during diastole and preventing the upward displacement of the leaflets into the LA during ventricular systole. This subvalvular apparatus consists of the papillary muscles (PMs) and chordae tendineae (CT). The CT extend from the mitral leaflets to the PMs and display wide variation in branching as well as PM attachment.

In general, three types can be recognized:

- *primary* (marginal) chordae that are attached uniformly via bifurcations or trifurcations to the free edge of the leaflets,
- *secondary* (intermediary) chordae that are inserted in layers to the rough zones of the anterior leaflet,
- and *tertiary* (basal) chordae that extend either from the PMs or directly from the LV free wall and attach to the base of the posterior leaflet or directly to the MA [74,75].

It must be noted that two thickened secondary chordae, known as the *strut chordae*, attach to the belly region of the anterior leaflet, and highly branched fan-like chordae attach to the commissures. Anatomically, marginal chordae are typically thinner than basal chordae, while strut chordae are the thickest in human valves [1,74]. In porcine valves, which closely mimic human valves in anatomy and function, posterior leaflet chordae are thinner than the corresponding anterior leaflet chordae [76]. Average length and thickness properties obtained from autopsied human mitral valves can be found in [74].

The chordae tendineae are made of two major components – an outer elastin sheath with scattered collagen and an inner core of collagen with traces of elastin [77]. These are enclosed by layers of endothelial cells on a basal lamina [70]. Scanning electron microscopy has revealed the collagen fibers in the chordae's central core exhibit a wavy undulated pattern that contributes to the extensibility of chordae [78,79]. During PM contraction, the crimped collagen fibrils straighten, thus reducing the peak strain developed in the chord. Additionally, the high crosslinking of collagen within the chordae

prevent creep during valve closure. Transmission electron micrographs have additionally shown the density of collagen fibrils decrease with increases in chordal size between chordal types.

#### **2.1.4 The Papillary Muscles**

The primary role of the PMs is to stabilize MV function by adjustment of tension during the cardiac cycle, and their functionality is intimately associated with the ventricular free wall to which they are attached. Two groups of PMs are attached to the LV free wall and are typically identified based on their relative position below the two MV leaflet commissures, *anterolateral* and *posteromedial*.

Morphological variability exists amongst the PM groups, with some notable arrangements including:

- single ‘bulky’ PM with a single head (*type I*) attached to multiple CT
- single ‘bulky’ PM with multiple heads (*type II*) attached to multiple CT
- narrow PM with few CT (*type III*)
- arch-shaped PM with multiple CT (*type IV*)
- PM attached to the LV free wall with multiple CT

Detailed anatomic descriptions of the MV anatomy can be found elsewhere [68,74,80-82].

The anterolateral PM is vascularized by multiple branches of the anterior descending coronary artery and the circumflex vessels, while the posteromedial PM is supplied from either the circumflex artery or branches of the right coronary artery. These differences in vascularization of the papillary muscles explain why the posteromedial PM is more prone to necrosis and dysfunction than the anterolateral PM.



The PMs actively contract during ventricular systole, yet, despite the complex dynamics of the left heart, the PM tips have been demonstrated to maintain a near constant distance with the annulus. Additionally, it is hypothesized that the PMs act as shock absorbers, by maintaining a consistent mitral valve geometry through the entire cardiac cycle [83]. Sonomicrometry studies in healthy sheep and transesophageal echocardiography (TEE) studies in humans have demonstrated that the PMs elongate by 2-5 mm during diastole, compared to their systolic length [84,85]. Mechanistically, the net force experienced by a particular PM is the vectorial resultant of the forces experienced by the chordae inserting into that PM as well as the force imparted by the relaxing/contracting PM. This force is expected to be transmitted to the LV wall, ensuring proper valvular-ventricular force continuity.

## **2.2 Mitral Valve Mechanics**

### **2.2.1 Mitral Annular Mechanics**

#### **2.2.1.1 Quantification of Cyclic Mitral Annular Areal Reduction**

The mitral annulus is a pliant fibro-muscular structure and shows dynamic variation in shape throughout the cardiac cycle. The cyclic areal reduction of the mitral annulus plays a significant role in valve competence and mechanics. Numerous studies have been conducted to visualize the motion and quantify annular velocities in normal [86,87] and pathological conditions [88-90] using echocardiography, Doppler Tissue Imaging and Cardiac Magnetic Resonance Imaging techniques.

During ventricular diastole, the annulus is more circular whereas at peak systole the annulus takes on a kidney-shaped orifice. In healthy humans, the mitral annulus can reduce its area and circumference by  $26 \pm 3 \%$  and  $13 \pm 3 \%$  from diastole to mid-systole respectively [86]. The cyclic reduction of mitral annular area has been demonstrated to be preserved in sheep. In healthy ovine models, the mitral annular area and circumference reduce by approximately 15% and 9% respectively [91,92]. Further, Rausch et al. demonstrated a significant difference between the percent reduction in the septal-lateral (12%) and transverse (5.5%) annular diameters [91].

Diseases of both the mitral valve and left ventricular complex have been demonstrated to impair the cyclic mitral annular contraction. In 149 patients, left ventricular dysfunction correlated to significant depressed mitral annular contraction [93]. Similar significant decreases have been determined in patients with dilated cardiomyopathy and ischemic mitral regurgitation [94]. These trends have been shown to be conserved in ovine chronic ischemic mitral regurgitation models [95]. Compared to healthy ovine subjects, ischemic mitral regurgitation animals exhibit significant decreases in the reduction of the mitral annular area.

#### 2.2.1.2 Quantification of Mitral Annular Saddle and Flattening with Disease

The three-dimensional mitral annular geometry has historically been described as a hyperbolic paraboloid or saddle shaped. First observed by Levine, the non-planar geometry of the mitral annulus has been demonstrated in both healthy human and mammalian species [96-99]. The mechanisms by which the annulus conforms to the saddle geometry has been described and proposed by two mechanisms. In the first, unequal apical-basal translation of the mitral annulus during left ventricular contraction

(due to aortic root tethering) causes annular folding across the inter-commissural axis [100]. In the second, expansion of the aortic root during systolic left ventricular contraction displaces the anterior annulus laterally, which folds the anterior and lateral portions of the mitral annulus across the intercommissural axis [101,102].

The saddled shape of the mitral annulus has been investigated in both experimental and computational studies and demonstrated to change by as much as 30% throughout the cardiac cycle [66,95,96]. The annular saddle is typically quantified in one of two manners - as either an annular height or annular height to commissural width ratio (AHCWR). In healthy humans, the annular height has been observed to range from 0.6 mm to 1.4 cm with an AHCWR approaching 20 to 25% [95,96]. In ovine models, the AHCWR has been reported to range from 12 to 15% [40,97]. With functional mitral regurgitation due to left ventricular ischemia, the annular saddle has been shown to flatten with only subtle changes throughout the cardiac cycle. In humans, the AHCWR has been shown to significantly decrease to 12-15 %, whereas in a chronic ischemic mitral regurgitation ovine model, the AHCWR hovers between 11% and 12 %. Beyond its quantification, the non-planarity of the mitral annulus is believed to confer several mechanistic benefits.

The saddle shape of the mitral annulus has been demonstrated in numerical studies to reduce stress in the mitral leaflets [66]. In the same study, echocardiographic mitral valve images acquired in humans, sheep, and baboons, as well as sonomicrometry array localization in sheep, demonstrated that the annular saddle lay within the stress-optimized range found in the computational studies. Based on these findings, the authors suggested the non-planarity of the mitral annulus conferred a mechanical advantage to the

leaflets by adding curvature and reducing stress. Reductions in leaflet strain with a saddle annulus have been additionally confirmed through carefully controlled *in vitro* studies [103,104]. The saddle annulus has been additionally shown to reduce chordal tethering by altering coaptation and leading to an optimally balanced valvular configuration [105].

## **2.2.2 Leaflet Mechanics**

### 2.2.2.1 Mechanical Properties

Ex vivo uniaxial and biaxial testing (Table 1: control; Table 2: disease) have shown the mitral leaflets exhibit classical soft tissue biomechanical responses to stretch, which is mainly a result of the mechanical response of the load-bearing collagen fibers [106-114]. Initially, there is very little resistance to applied load in the “toe” region of the stress-strain curve (Figure 2-5). This is observed as a long region of relatively low tensile modulus and is due to the uncrimping of the collagen fibers. This is followed by a non-linear transition region where collagen fibers are recruited and aligned, effectively increasing the leaflet’s stiffness. The transition is succeeded by a final linear region of relatively large tensile modulus where the collagen fibers have reached their maximum distension and recruitment is saturated. Additionally, this mechanical response is strain rate independent, and has minimal hysteresis [4,115]. Post-transitional modulus is on average, two orders of magnitude greater than the pre-transition modulus. Inverse finite element analysis of *in vivo* valvular function calculated a substantially larger post translational modulus [111-113]. The discrepancy between *in vivo* and *ex vivo* data may be attributed to the hypothesized active contraction of the mitral leaflets *in vivo*, which can transiently modulate stiffness throughout the cardiac cycle [111,112,116]. The variability of the data is mainly due to the experimental errors associated with uniaxial

and biaxial testing, the inherent variability in leaflet structure and composition, relative age of the sample [114], and interspecies differences (ovine, porcine, and human).

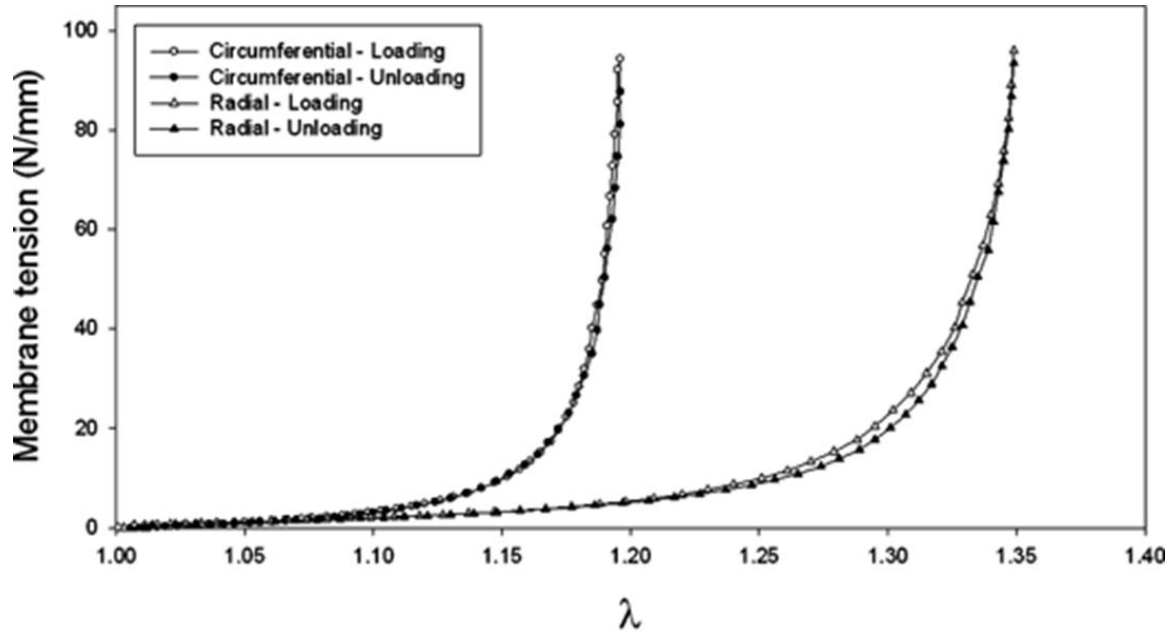


**Figure 2-5 Leaflet Stress-Strain Curve** Non-linear stress strain curve of the mitral leaflets shows directionally dependent response and minimal hysteresis. There is minimal stress developed in the “toe” region due to uncimping of the collagen fibers. A non-linear transition region (recruitment and alignment of collagen fibers) is followed by a linear, high tensile modulus regime (locking of collagen fibers). (image adapted with permission from Grashow et al [4]).

**Table 1-1 Modulus of elasticity for posterior and anterior leaflets.**

Study	Model	Leaflet	Transition Regime	Modulus (N/mm <sup>2</sup> )	Comments
Kunzelman (1992) [106]	Uniaxial, porcine (N = 99)	Anterior Radial	Pre Post	0.021 ± 0.002 2.0 ± 0.7	Uniaxial testing was performed with two loading cycles: 5 mm/min and 10 mm/min. Data for 5 mm/min tabulated. Data are mean ± SEM
		Anterior Circ. Belly	Pre Post	0.044 ± 0.004 7.4 ± 1.0	
		Anterior Circ. Marginal	Pre Post	0.055 ± 0.005 5.0 ± 0.5	
		Posterior Radial	Pre Post	0.027 ± 0.003 1.9 ± 0.2	
		Posterior Circ.	Pre Post	0.040 ± 0.005 2.1 ± 0.2	
May-Newman (1995) [107]	Biaxial, Porcine (N =15-28)	Anterior Radial	Pre Post	0.061 ± 0.044 2.4 ± 1.5	Uniaxial and biaxial testing of anterior and posterior mitral leaflets.
		Anterior Circ.	Pre Post	0.089 ± 0.092 9.0 ± 8.8	
		Posterior Radial	Pre Post	0.043 ± 0.024 1.9 ± 1.3	
		Posterior Circ.	Pre Post	0.094 ± 0.052 3.4 ± 2.1	
Chen (2004) [108]	Biaxial, porcine (N = 6)	Anterior	Pre Post	0.02 – 0.05 0.26 – 1.01	Biaxial testing of leaflet-strut chordae transition zone. Range reflects proximity to chordal insertion.
Grande-Allen (2005) [117]	Uniaxial, human (N = 21)	Anterior Radial	Post	2.29 ± 0.83	Control leaflets harvested from autopsy of patients who died of non-cardiovascular related deaths. (Study also investigated effects of dilated cardiomyopathy.)
		Anterior Circ.		3.55 ± 2.05	
		Posterior Circ.		3.39 ± 1.66	
Liao (2007) [110]	Biaxial, porcine (N = 5)	Anterior	Post	3.58 ± 1.23	
Krishnamurthy (2009) [113]	Inverse FEA, Ovine (N =10)	Anterior Radial Base	Post	48 ± 16 – 68 ± 19	Material properties were tuned using an orthotropic linear elastic FEM to match <i>in vivo</i> leaflet displacement during isovolumic relaxation and contraction. (Study also investigated effects of active contraction.)
		Anterior Radial Belly		34 ± 10 – 54 ± 13	
		Anterior Radial Free Edge		42 ± 14 – 59 ± 17	
		Anterior Circ. Base		17 ± 4 – 26 ± 6	
		Anterior Circ. Belly		12 ± 3 – 19 ± 5	
		Anterior Circ. Free Edge		15 ± 4 – 23 ± 5	

**Table 1-2 Measured significant differences in leaflets' stiffness between normal and pathological valves.**

Study	Model	Significant Measured Differences	Comments
Grande-Allen (2005) [117]	Uniaxial, human (N = 23)	<ul style="list-style-type: none"> <li>• Anterior leaflet radial /circumferential tensile modulus/stiffness increased from control</li> <li>• The posterior leaflet remained unaffected</li> </ul>	Leaflets were harvested from transplant patients who presented with ischemic and dilated cardiomyopathy.
Imanaka (2006) [109]	Piezo-electric vibration, Human (N = 11)	<ul style="list-style-type: none"> <li>• Rheumatic leaflets stiffer than control/degenerative at base/belly/free edge</li> <li>• Degenerative leaflets stiffer at free edge, yet more compliant elsewhere.</li> </ul>	Leaflets harvested from patients presenting with Rheumatic (stenosis) and degenerative (regurgitation) valve disease.
Krishnamurthy (2009) [113]	Inverse FEA, Ovine (N =10)	<ul style="list-style-type: none"> <li>• Blocking active contraction of leaflets reduced basal/belly leaflet stiffness during isovolumic contraction.</li> </ul>	Regional effects of active stiffness were investigated by blocking contraction of the leaflets.
Stephens (2010) [114]	Uniaxial, Porcine (N = 5-8)	<ul style="list-style-type: none"> <li>• With increasing age, radial/circumferential pre-/post-transitional stiffness increased.</li> </ul>	Testing was performed on 6 week, 6 month, and year old porcine leaflet tissue.

Complementary studies have been used to characterize dynamic leaflet deformation during physiologic valvular function (Table 3: control; Table 4: disease). In short, in vitro studies have utilized dual camera stereo-photogrammetry to track the deformation of a superficial grid (graphite or tissue dye markers) on the mitral leaflets in mitral valve simulators (Figure 2-6) [103,104,108,118-120]. Similarly, in vivo techniques have utilized a localized array of piezoelectric sonomicrometry crystals or

video-fluoroscopy of radiopaque tantalum markers to measure dynamic leaflet deformation. [6,7,121,122]. Using finite element analysis, Euler-Almansi strain is subsequently calculated throughout the cardiac cycle. These studies found that the mitral leaflets experience rapid, and large anisotropic, or directionally dependent, stretch during closure, followed by minimal further deformation while the valve is closed (Figure 2-6). Both mitral leaflets were stiffer and less extensible in the circumferential direction than the radial direction. The observed anisotropy is a result of the preferential alignment of the underlying collagen fibers.

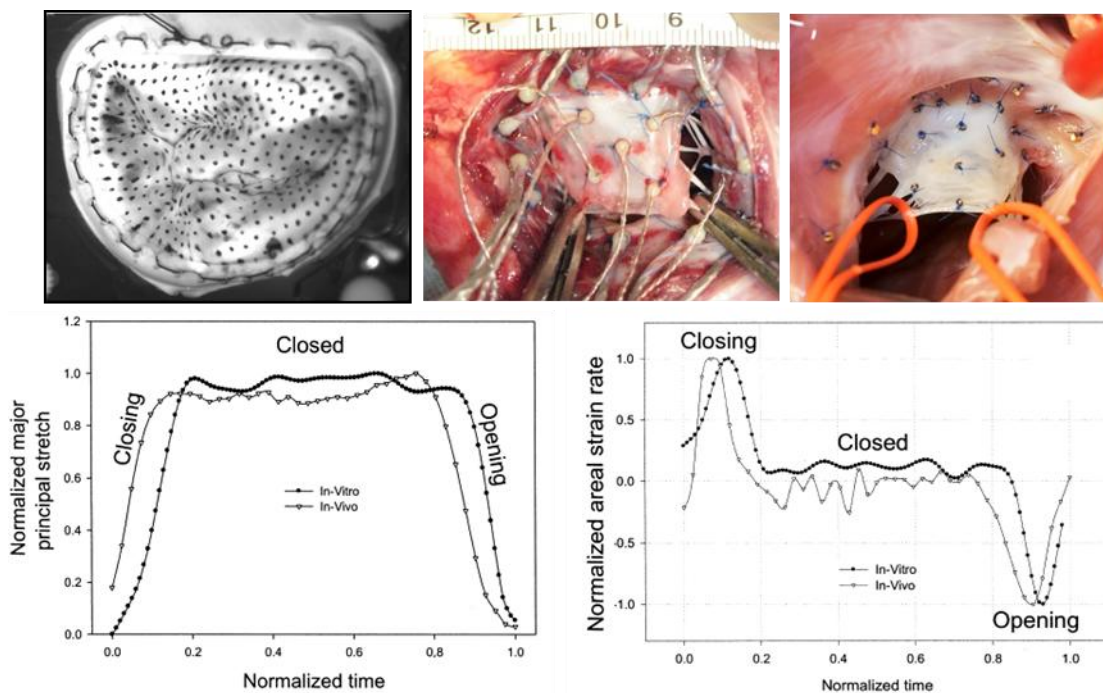


**Figure 2-6 (Top Panel) Superficial grids marked on mitral leaflets include tissue marker dye (*in vitro*), sonomicrometry crystals (image courtesy of Dr. Gorman), and radio-opaque markers (image adapted with permission from Rausch et al. [5]). (Bottom Panel) Leaflet strains calculated over the cardiac cycle show large and rapid anisotropic stretch. (Images adapted with permission from Sacks et al. [6].)**



**Table 1-3 Anterior and Posterior leaflet strain and strain rates from *in vivo* and *in vitro* data.**

Study	Model	Direction	Strain (%)	Strain Rate (% s <sup>-1</sup> )	Comments
<b>Anterior Leaflet</b>					
Sacks (2002) [118]	<i>in vitro</i> , porcine	Major Minor Areal	30 ± 8 11 ± 3 47 ± 10	750 – 900 300 – 400 1000 – 1300	16 graphite markers in 4 x 4 array
He (2003) [119]	<i>in vitro</i> , porcine (N = 11)	Major Minor Areal	30 ± 18 8 ± 6 42 ± 20	~ 750 ~ 300 973 ± 517	16 graphite markers in 4 x 4 array (Study also investigated effects of taut and slack PM positions.)
Chen (2004) [108]	Ex planted porcine heart (N = 6)	Radial Circ.	-1 ± 2 to 14 ± 2 2 ± 2 to 4 ± 2 (From annulus towards coaptation)		30 – 50 leaflet surface markers, statically pressurized heart (120 mmHg)
Sacks (2006) [6]	<i>in vivo</i> Ovine (N = 9)	Radial Circ. Areal	16 ± 3 3 ± 0.4 15 ± 0.8	314 ± 43 143 ± 13 --	9 sonomicrometry crystals in a 3 x 3 array (Range of pressures) Data presented for 90 mmHg
Jimenez (2007) [103]	<i>in vitro</i> Porcine (N = 8)	Major Minor Areal	22 ± 7 11 ± 5 36 ± 14	383 ± 195 192 ± 150 --	5 x 8 tissue dye (Study also investigated effects of saddle height.)
Bothe (2010) [121]	<i>in vivo</i> Ovine (N = 59)	Radial Circ. Areal	7 ± 5 to 9 ± 5 5 ± 4 to 7 ± 3 --		16 radiopaque markers equally distributed (Study also investigated effects of annuloplasty rings.)
Rausch (2012) [7]	<i>in vivo</i> Ovine (N = 57)	Radial Circ. Areal	8 ± 4 5 ± 3 13 ± 5	332 ± 150 112 ± 59 432 ± 174	23 radiopaque markers equally distributed
Amini (2012) [122]	<i>in vivo</i> Ovine (N = 10)	Radial Circ. Areal	31 ± 3 10 ± 1 --	-- -- --	4 sonomicrometry crystals in a 2 x 2 grid Data presented for 150 mmHg LVP (Study also investigated effects of annuloplasty.)
<b>Posterior Leaflet</b>					
He (2005) [120]	<i>in vitro</i> Porcine (N = 18)	Major Minor Areal	23 ± 14 3 ± 10 30 ± 17	273 ± 156 27 ± 83 313 ± 171	16 graphite markers in a 4 x 4 array (Study also investigated effects of taut and slack PM positions.)
Padala (2009) [104]	<i>in vitro</i> Porcine (N = 8)	Radial Circ. Areal	29 ± 8 10 ± 8 38 ± 9	-- -- --	16 tissue dye markers in a 4 x 4 array (Study also investigated effect of saddle height.)

**Table 1-4 Significantly measured difference in leaflet strain from normal to pathological and repaired conditions.**

Study	Model	Significant Measured Differences	Comments
<b>Anterior Leaflet</b>			
He (2003) [119]	<i>in vitro</i> , porcine (N = 11)	<ul style="list-style-type: none"> <li>No significant differences observed between altered conditions and control.</li> </ul>	Investigated the effect of taut (3-5 mm apical) and slack (5 mm basal) PM position.
Sacks (2006) [6]	<i>in vivo</i> Ovine (N = 9)	<ul style="list-style-type: none"> <li>Little effect of elevated pressure on leaflet strain.</li> <li>Only peak circumferential strain decreased from 90 to 200 mmHg.</li> </ul>	Left ventricular pressure was systematically elevated from 90 mmHg to 200 mmHg.
Jimenez (2007) [103]	<i>in vitro</i> Porcine (N = 8)	<ul style="list-style-type: none"> <li>Major/areal strains decreased from a flat (0%) annulus to a physiologic annulus (20%) height.</li> <li>Radial strain unaffected.</li> </ul>	Systematically decreased saddle height from 30% to 20% (physiologic) to 0%.
Bothe (2010) [121]	<i>in vivo</i> Ovine (N = 59)	<ul style="list-style-type: none"> <li>Circumferential strain increased from control with the RSAR, Physio, and ETlogix.</li> <li>Radial strain increased with the RSAR.</li> <li>Cosgrove did not significantly affect strain.</li> </ul>	Similar experiments were performed with 5 annuloplasty rings: Cosgrove, RSAR, Physio, Etlogix, and Geoform.
Amini (2012) [122]	<i>in vivo</i> Ovine (N = 10)	<ul style="list-style-type: none"> <li>Physio increased radial strain</li> <li>Circumferential strain reduced.</li> </ul>	Implanted a flat annuloplasty ring (Physio).
<b>Posterior Leaflet</b>			
He (2005) [120]	<i>in vitro</i> Porcine (N = 18)	<ul style="list-style-type: none"> <li>No significant differences observed between altered conditions and control.</li> </ul>	Investigated the effect of taut (3-5 mm apical) and slack (5 mm basal) PM position.
Padala (2009) [104]	<i>in vitro</i> Porcine (N = 8)	<ul style="list-style-type: none"> <li>Radial/circumferential/areal strain decreased between flat and 20% saddle height.</li> </ul>	Systematically decreased saddle height from 20% (physiologic) to 0%.

Further heterogeneity was observed within each leaflet as the base (near the annulus) and belly region of the leaflets were less extensible and stiffer than the corresponding free edge (Figure 2-7) [7,108,109]. Finally, the posterior leaflet, which has a higher density of chordal insertions (1.5-1.8 posterior to anterior chords) to provide mechanical support [107], is more extensible and less stiff compared to the anterior leaflet. These findings are consistent with the mechanical behavior that has been extensively characterized using uniaxial and biaxial testing. Collectively, these characteristics allow for optimal mitral valve closure. With increasing left ventricular pressure, the leaflets may undergo considerable deformation to promote coaptation. Following closure, a tight seal is maintained because of the organized microstructure, large post-translational stiffness, and minimal creep [115], which provide the strength to withstand the large pressure gradient.

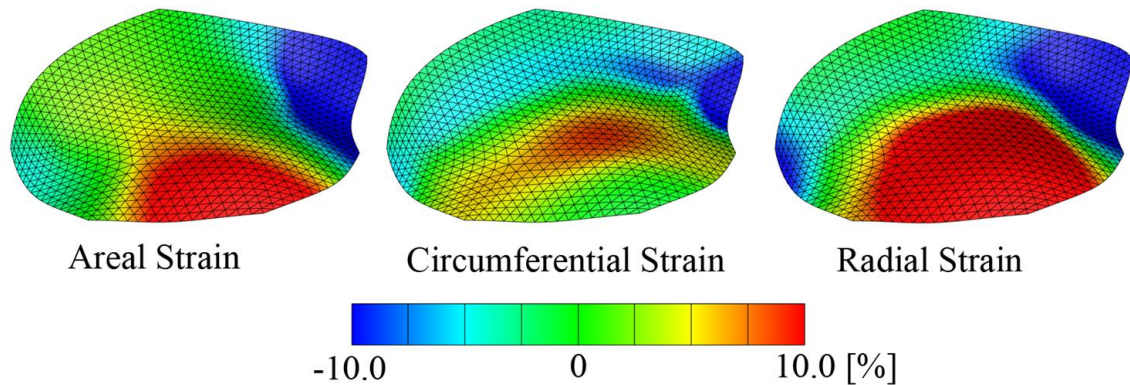


**Figure 2-7** *In vivo* areal, circumferential, and radial strain are shown at maximum left ventricular pressure. The strain is anisotropic, and largest in the radial direction due to the preferential alignment of collagen fibers. The largest stretch is observed at the free edge, which helps create redundant coaptation. (Image adapted with permission from Rausch et al. [7].)

Recently, the selection of a referential configuration of the mitral leaflets for corresponding strain and stretch measurements has been challenged, which is typically selected as the time frame of minimum left ventricular pressure. Rausch et al. showed strain magnitude is insensitive to choice of diastolic reference frame [7]. Perhaps more importantly, however, Amini et al. showed the mitral leaflets contract up to 29% from in-vivo to ex-vivo excision, in what is perceived to be the stress-free state. This indicates the leaflets experience some amount of “pre-strain” in-vivo. [122]. Consequently, the strain magnitude calculated was affected by the selection of the reference configuration, from minimum in-vivo pressure, to excised heart, to excised valve. This also confounds where on the non-linear stress-strain curve the mitral leaflets may reside during experimental and computational experiments. However, a more laborious study is still needed due to the small sample size ( $n = 5$ ) and the elementary marker grid used ( $2 \times 2$ ).

Using a left heart simulator with control over annular geometry, complementary studies showed both anterior and posterior leaflet strain is significantly reduced with increasing mitral annular saddle [103,104]. These results are consistent with numerical analysis of the mitral leaflets [123]. As a result, many annuloplasty ring devices now feature a prescribed saddle height in the hopes of improving long-term repair durability. Conversely, animal studies report increased strain following annuloplasty ring implantation [121]. However, this is likely to be a result of the rigid ring implantation, which ablates the natural dynamic motion of the healthy animal annulus. For the in-vitro studies, the comparisons were made between similarly sized and akinetic annuli.

### 2.2.2.2 Adaptive Remodeling Due to Mechanical Stimuli

Altered mechanical stimuli have been hypothesized to elicit changes in leaflet microstructural composition, which in turn affects mechanical properties and valvular function [124]. More specifically, secondary valve pathologies, due to left atrial or left ventricular dysfunction disrupt the mechanical environment through mitral annular dilation and papillary muscle displacement with concomitant mitral regurgitation.

These changes were first observed in retrospective analysis of explanted patient hearts. Grande-Allen et al observed that leaflets from patients with dilated and ischemic cardiomyopathy were stiffer, less extensible, and less viscous compared to normal controls [117]. These changes appeared to represent a fibrotic remodeling, as there was an associated increase in collagen, glycanoaminoglycans, and cell count, with a decrease in water content. [62,72]. Such changes were shown to lead to reduced coaptation and increased valve stresses, which hints at a troubling feedback. Chaput et al. showed that leaflet area can increase up to 35% with inferior wall motion abnormality or dilated cardiomyopathy [125,126]. This growth was proportional to corresponding annular enlargement, such that the ratio of leaflet to annular area remained relatively constant.

To isolate the mechanistic causes of these observed changes, animal models have been pursued. Timek et al showed both mitral leaflets remodel in an ovine model of cardiomyopathy [127]. In particular, they found regions closer to the free edge of both leaflets underwent significant lengthening, which is consistent with knowledge that this region experiences the largest deformation. Stephens et al showed this lengthening is associated with greater cell density, delineation between organized layers, greater collagen and elastic fiber turnover, and an increase in myofibroblasts [128]. Again,

remodeling was heterogeneous as the belly to the free edge experienced the most pronounced changes. In a follow up study, the same group showed isolated mitral regurgitation was sufficient to induce active matrix turnover, represented by a reduction in type I collagen and an elevation in type III collagen (lower tensile strength), matrix metalloproteinase, and elastin fiber turnover [129]. In a model of isolated papillary muscle displacement, leaflet tethering induced significant increase in leaflet area and thickness [130]. Associated cell activation is believed to progress through a developmental pathway, which supports a hypothesis of an actively adapting mitral valve. Understanding the mechanisms of adaptive leaflet remodeling may create new potentials for therapeutic repairs to augment leaflet area in response to post-myocardial infarction LV dilation [5].

### **2.2.3 Chordae Mechanics**

Considered in isolation, the chordae tendineae of the mitral valve experience counteracting tensile loads from the apically contracting PMs and basally directed pressure forces acting on the valve leaflets (coapting force). Additionally, the passive elongation and active contraction of the left ventricle influences the magnitude of tension experienced by a chord. The chordae experience maximum tension during systole when the pressure load acting on the leaflets is transmitted to the chordae, and this tension is relieved during ventricular diastole. Since chordal structure, size and insertions are uniquely complex, many *in vitro* and *in vivo* investigations have focused on identifying the role and function of the various chordae [33].

From a mechanistic standpoint, the intermediary/strut chordae carry a majority of the systolic load acting on the valve leaflets, and maintain proper left ventricular function

and geometry [131]. Basal chordae provide a constant connection between the annulus and papillary muscles, while marginal chordae maintain leaflet flexibility, governing proper valve closure. Further, the anterior basal chordae play a role in balancing the elastic recoil of the ascending aorta, and transection of these chordae can reduce the aortomitral angle and potentially result in post-repair systolic anterior motion (SAM) [132].

#### 2.2.3.1 Mechanical properties of chordae tendineae

Uniaxial testing studies of chordae tendineae have demonstrated non-linear viscoelastic behavior with a discrete transition in the tensile elastic modulus [133-136]. Initially, the inner collagen core straightens upon application of tension, after which it 'locks'. At this point, the outer elastin fibers begin to stretch and withstand the effects of constant strain and prevent the plastic deformation of collagen fibers. However, the gross mechanical properties of the chordae are primarily determined by the collagen core, since removal of the outer elastin sheath does not change their non-linear stress response [134]. The thinner marginal chordae have the greatest average fibril density, and are the stiffest of all chordal groups [1]. Although the marginal chordae have the least extensibility among chordae, they also have the smallest failure tensions [76]. The thicker strut chordae have smaller tensile modulus and greater extensibility, primarily due to the extensively crimped collagen, which can elongate upon the application of tensile forces [77]. Table 5 provides a summary of mechanical properties of various chordal groups.

**Table 1-5 Mechanical properties of various chordal groups, reproduced from [1].**

<b>Chordal Type</b>	<b>Marginal</b>	<b>Basal</b>	<b>Strut</b>	<b>p-value</b>
Extensibility (% strain)	4.3 ± 1.6	8.5 ± 2.0	17.5 ± 3.3	p<0.001
Tensile Modulus (MPa)	84.4 ± 21.2	86.1 ± 20.9	64.2 ± 13.5	p=0.002
Average cross-sectional area (mm <sup>2</sup> )	0.38 ± 0.18	0.71 ± 0.25	2.05 ± 0.40	p<0.001

### 2.2.3.2 Experimental measurement of chordal forces: Physiological conditions

Various *in vivo* and *in vitro* studies measuring chordal forces under pulsatile physiological conditions have been listed in Table 6. Due to inherent procedural difficulty, *in vivo* studies have been unable to measure the chordal forces across all types of chordae, due to which an entire force balance cannot be constructed from *in vivo* data alone. Most of these studies utilized a C-shaped strain gauge based transducer, first described by Salisbury et al and refined by Nielsen et al [8,137]. Briefly, strain gauges mounted on a C-shaped brass ring measure the tensile forces in the chordae as a change in voltage (Figure 2-8). By implanting the C-ring transducer on various chordae, the loads carried by them can be measured at every time point in the cardiac cycle. This transducer has been successfully implanted in multiple *in vitro* and *in vivo* studies [137-146]. Another recent strain gauge based transducer has been designed with the intent of instrumenting smaller chordae, however this transducer has not been tested in a dynamic mitral valve system [147].





**Figure 2-8** Miniature C-arm force transducers selectively record chordal forces throughout the cardiac cycle (Image adapted with permission from Nielsen et al. [8]).

**Table 1-6** Experimental measurements of physiological chordal forces. Types of chordae are: AA – anterolateral PM to anterior leaflet; AP – anterolateral PM to posterior leaflet; PA – posteromedial PM to anterior leaflet; PP – posteromedial PM to posterior leaflet; CCT – commissural chordae tendinae.

Study	Model Used	Peak Forces (N) Mean ± Std. Error (where available)			Comments
			Flat	Saddle	
Salisbury (1963)[137]	<i>in vivo</i> , mongrel dogs (N=15)	0.75			Increasing SV=> Increased CT; Increased systemic pressure => Increased CT
Lomholt (2002)[138]	<i>in vivo</i> , porcine MVs (N=23)	0.66 (Strut) 0.14 (Marginal)			LVP alone determines CT. Did not group chordae based on origin
Nielsen (2002) [141]	<i>in vitro</i> , porcine MVs, (N=5)	AA, Marginal PA, Marginal AP, Marginal PP, Marginal	0.46 ± 0.08 0.45 ± 0.06 0.44 ± 0.05 0.50 ± 0.07		Only marginal chordae were instrumented in this study.
Nielsen (2003) [142]	<i>in vivo</i> , sheep MVs (N=8)	0.81 ± 0.10 (PA, strut) 0.52 ± 0.08 (AA, strut)			Acute study only, no chronic data available. PA tension is significantly higher than AA tension (p<0.01)
Jimenez (2003)[105]	<i>in vitro</i> , human MVs (N=6)	AA/PA, Marginal AA/PA, Strut AP/PP, Marginal AP/PP, Strut AP/PP, Basal CCT	0.31±0.07 1.22±0.21 0.03±0.02 0.25±0.06 0.19±0.04 0.17±0.08	0.35±0.07 0.95±0.14 0.06±0.03 0.30±0.08 0.31±0.10 0.11±0.09	Comparison of CT with and without saddle shape of annulus. Results were not separated based on PM of origin. Conditions with significant differences are highlighted (p<0.05)

Author (Year) [Ref]	Study Type			<b>F</b>	<b>F<sub>p</sub></b>	Notes
		Chordal Type	Force (Mean ± SD)	Force (Mean ± SD)	Force (Mean ± SD)	
Nielsen (2005) [139]	<i>in vivo</i> , porcine MVs (N=9)	AA, Marginal	0.35±0.09	0.33±0.07	F <sub>p</sub> is the force normalized by LVP of 100mmHg. Chordal forces with IMR were also studied (Refer Table 7)	
		PA, Marginal	0.25±0.04	0.28±0.06		
		AP, Marginal	0.32±0.07	0.34±0.07		
		PP, Marginal	0.36±0.06	0.39±0.09		
Jimenez (2005) [143]	<i>in vitro</i> , human MVs (N=6)		<b>Flexible</b>	<b>Flat</b>	<b>Saddle</b>	Pathological forces with PM displacement (Table 7). Significant differences are highlighted (p<0.07)
		Marginal	0.14±0.05	0.20±0.06	0.23±0.06	
		Strut	0.66±0.17	0.78±0.19	0.65±0.13	
Jimenez (2005) [144]	<i>in vitro</i> , human MVs (N=6)	Basal	0.44±0.08	0.18±0.04	0.22±0.07	No significant differences found between porcine and human MVs.
		AA/PA, Marginal	0.26±0.08	0.41±0.09		
		AA/PA, Strut	1.02±0.27	1.16±0.23		
		AP/PP, Marginal	0.29±0.13	0.25±0.10		
		AP/PP, Strut	0.43±0.21	0.30±0.07		
He (2009) [147]	<i>in vitro</i> , porcine (N=22), ovine (N=4)	AP/PP, Basal	0.21±0.12	0.22±0.06		Peak systolic valve configuration was simulated using a static reservoir of fluid; full pulsatile loop was not used.
		CCT	0.06±0.01	0.21±0.11		
Grainer (2012)[146]	<i>in vitro</i> , porcine MVs (n=11)	AA/PA, Marginal	1.00±0.10	0.29±0.03	-	LVP generated using static pressure reservoir. 3 levels of LVP were generated, LVP=100mHg is reported here.
		AA/PA, Strut	0.10±0.01			
Grainer (2012)[146]	<i>in vitro</i> , porcine MVs (n=4)	0.69 ± 0.46 (PA, strut) 0.83 ± 0.41 (AA, strut)				Forces were not classified based on instrumented chord type
Grainer (2012)[146]	<i>in vitro</i> , porcine MVs (n=4)	0.66 ± 0.24 (AA/PA, strut)				

Overall, the anterior strut chordae carry the highest load amongst all chordal groups. The marginal chordal forces are lower than the strut forces, particularly if the marginal chordae insert into the coaptation zone of the leaflets [105,138,143,144]. Dynamic deformation of the mitral annulus increased basal chordal forces without affecting other chordae, demonstrating that the role of the basal chordae is to maintain a constant distance between the annulus and PMs [143]. The saddle shape of the native mitral annulus results in a more even distribution of forces among the chordae, which is expected to be mechanically beneficial. This is accomplished due to alterations in the physical distance between the PMs and various chordal insertions into the leaflet due to

the conferred 3D annular shape [105]. Among the anterior leaflet strut chordae, chordae originating from the posteromedial PM carry significantly higher forces [142]. Amongst marginal chordae, the origin of the chordae did not affect the magnitude of forces significantly, although the magnitude of forces measured *in vitro* were higher than the corresponding forces measured *in vivo*. This could be a result of the PM positions used to simulate normal geometry and the lack of a dynamic left ventricular complex in the *in vitro* studies [139,142].

Discrepancies in force measurements listed in Table 6 could be due to multiple reasons:

1. Variations in animal models, particularly in valve sizes and chordal distributions.
2. Variations in specific conditions used to simulate normal valvular function.
3. Chordal classifications are broad, and the differences exist in the specific leaflet insertions and branching of chordae. Any such differences in PM positioning and chordal anatomy across studies can result in alterations in chordal force distribution across valvular groups.

#### 2.2.3.3 Experimental measurement of chordal forces: Pathological conditions

The most commonly simulated pathological condition for chordal force measurement is annular dilation and papillary muscle displacement, as would be seen with functional or ischemic mitral regurgitation (Table 7). The specific changes in chordal force distribution are a consequence of the alterations in chordal insertion angles and distance from annular plane due to PM displacements [148]. The only *in vivo* study measuring IMR chordal forces showed an increase in force in the anterior leaflet marginal chordae originating from the anterolateral PM, while a decrease in force was noted in the

marginal chordae from the posteromedial PM, primarily due to the tethering caused by the IMR [139]. However, this study did not quantify PM positions and annulus size post-infarction.

**Table 1-7 Changes in chordal force due to pathological and surgical repair conditions as compared to normal physiology.**

Condition	Anterior Leaflet			Posterior Leaflet		
	Marginal	Strut	Basal	Marginal	Strut	Comm-issural
In vivo porcine IMR model [139]	↑/↓	N/A	N/A	=	N/A	N/A
(Lat.+Post.+Api.) PM displ. [141]	↑	N/A	N/A	↓	N/A	N/A
(Lat.+Post.+Api.) PM displ. [105]	=	↑	=	=	↑	↑
(Lat.+Post.) PM displ. [144]	=	=	↓	=	=	↓
(Lat.+Post.+Api.) PM displ. [144]	=	↑	↑	=	↑	↑
(Lat.+Post.+Api.) PM displ. + Annular Dilatation [149]	↑	N/A	N/A	↑	N/A	N/A

Multiple *in vitro* studies showed no changes in marginal chordal force due to isolated PM displacement, whereas the inclusion of annular dilatation causes an increase in the marginal chordal forces [143,144,149]. This suggests that these chordae can adapt better to geometric changes of the MV. The increase in force with annular dilatation could be due to increased mitral annular orifice area, resulting in a migration of the marginal chordal insertion points out from the leaflet coaptation zone into the pressure-bearing portion of the leaflet. Changes in forces in other chordae are directly related to the direction of PM displacement. Apical PM displacement causes increased forces in

most chordal groups due to leaflet tenting, which has been observed in human and animal models of IMR. Lateral and/or posterior PM displacement in isolation causes a redistribution of chordal loads such that the chordae near the displacement direction show a reduction in force. Basal and commissural chordae show higher sensitivity to PM displacement due to pre-straining of the chordae. Due to the non-linear mechanical response of chordae, PM displacement causes increases in chordal forces in pre-strained chordae.

Other pathological conditions studied include heart failure, where it was observed that changes in force could depend on several factors - reduction in coronary perfusion pressure reduced chordal force, ventricular pressure overload increased chordal force, while chordal force remained constant with ventricular volume overload [137]. Finally, hypertension is seen to increase chordal forces as expected, although this has only been shown in a statically pressurized system [147].

#### 2.2.3.4 Experimental measurement of chordal forces: Mitral Valve Repair

Most repair techniques for IMR focus on the annular level, with mitral ring annuloplasty (MRA) being the most common MV repair. With undersized MRA, the total amount of leaflet exposed to pressure load decreases, resulting in a reduction in the strut chordal tension; marginal chordae don't show any change in force since they are not the primary load bearing chordal structure [150]. Ostli et al (2012) showed a reduction in anterior leaflet strut chordal force after anterior leaflet patch repair compared to control in a static pressurization system [151]. However, the implantation of a patch without mitral annular dilatation can provide misleading results, since a dilated annulus should have a larger net pressure load on the leaflet, potentially causing an increase in strut chordal force. The

decrease in force was perhaps due to the patch relocating the strut chordal apically towards the free edge. This decreases the tension on the chords as their leaflet insertions are moved closer to the papillary muscles.

Chordal cutting, particularly of the strut chordae, has been proposed as a potential repair technique for alleviating leaflet tethering due to progressive PM displacement, which is expected to alter the chordal force distribution [152]. Using static pressurized porcine hearts, He et al showed increased marginal chordal forces as a result of strut chordal cutting, specifically on the marginal chordae originating from the same leaflet and PM [153]. Finally, the altered chordal force distribution in the marginal chordae as a result of strut chordal cutting depend on the specific manifestation of the disease, and is sensitive to direction of PM displacement [149].

## **2.2.4 Papillary Muscle Mechanics**

### 2.2.4.1 Experimental measurement of PM forces

The measurement of PM forces are critical to the understanding of the mitral valve force balance because of its force transfer to the left ventricle, and adverse LV remodeling is the most common chronic manifestation of MR. The three components of PM forces measured can be combined to obtain a total force magnitude, and this magnitude follows the transvalvular pressure very closely. Hashim et al reported PM force changes in an *in vitro* mitral valve model at two hemodynamic conditions – (1) High flow: 5L/min, 150mmHg peak transmitral pressure; (2) Low flow: 3.5L/min, 90mmHg peak transmitral pressure. These forces were measured with a strain gauge based transducer, capable of providing all three components of PM force. The peak force at high flow and low flow were measured to be 4.16N and 2.71N respectively [154]. Jensen et al utilized an

improved version of the same transducer and measured PM forces in normal and IMR conditions, simulated by PM displacement. Results of this study are presented in Table 8 [2].

**Table 1-8 Papillary muscle force measurements reproduced from [2]. P\*A is the product of transvalvular pressure (P) and leaflet surface area (A).**

PM Position	F <sub>T</sub> (N)	F <sub>M1</sub> (N)	F <sub>M2</sub> (N)	F <sub>rms</sub> (N)	P*A (N)
Normal	4.1	0.1	0.2	4.1±0.9	3.9±0.7
Apical	5.5	0.4	0.7	5.6±1.3	5.8±0.3
Apical+Posterior	6.9	1.6	2.4	7.5±1.8	8.1±0.6

This study demonstrated that there were no significant differences between the peak forces at normal condition between the APM and PPM. The total pressure force acting on the leaflets is very closely related to the total PM force, since the two forces should counteract each other. Particularly, this will hold true in *in vitro* simulators where confounders such as PM contraction and annular motion do not exist. With IMR, the PM forces increased due to two factors - increased force transmitted to the PMs from the larger leaflet area experiencing the transvalvular pressure; and increased tension of the chordae tendineae as shown in the previous sections, which are transmitted down to the PMs.

An *in vivo* study by Askov et al (2012) conducted in a normal porcine model (N=8) utilized a strain gauge based transducer designed to be implanted between the PM and the LV wall after dissecting the PM from the ventricle (Figure 2-9). PM forces rapidly increase during early systole, with the peak force occurring between early and

mid-systole, slightly lagging the LVP peak [9]. The peak values of  $F_{APM}$  and  $F_{PPM}$  were  $5.9 \pm 0.6N$  and  $5.8 \pm 0.7N$  respectively. These values were slightly higher than the forces observed *in vitro*, which could be related to the sizes of the valves used in this study, as well as due to differences between static and dynamic systems [2].

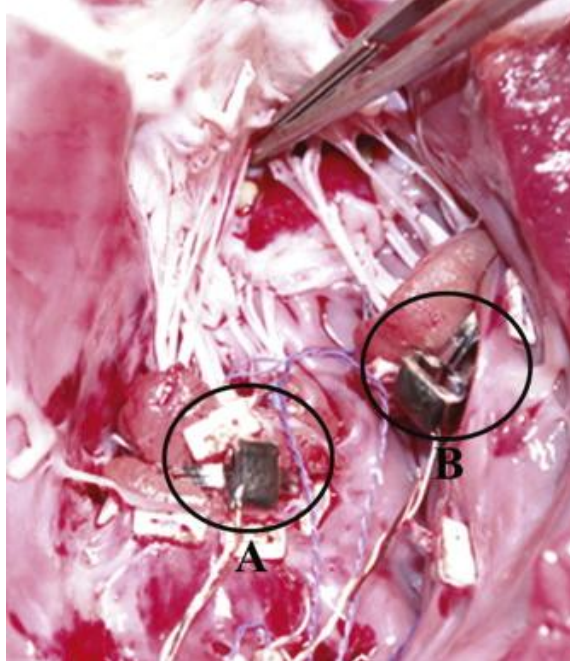


**Figure 2-9 Papillary muscle force transducers: Force transducers sutured between severed papillary muscles record forces throughout the cardiac cycle (Image adapted with permission from Askov et al. [9].)**

### 2.3 Mitral Valve Insufficiency

Mitral valve disease is often described as a complex and morbid condition which has challenged cardiologists and cardiac surgeons alike. There are two main classifications of mitral valve disease relating to the pathological effect of the valve's ability to regulate



flow: (i) mitral stenosis describes the total or partial obstruction of the mitral orifice affecting ventricular filling, and (ii) mitral insufficiency describes the valve's incompetency during systole which allows regurgitation, or backflow, into the left atrium. Mitral regurgitation can be further classified as congenital, degenerative, or functional. Functional mitral regurgitation occurs in the absence of structural valvular abnormalities and is the result of the geometric perturbations to the surrounding myocardium. It is the least understood of the valvular pathologies and is the most challenging to manage clinically; functional mitral regurgitation is the focus of the thesis herein, specifically ischemic mitral regurgitation.

The clinical burden of mitral regurgitation following ventricular ischemia has been well characterized. Doppler echocardiography studies report that the prevalence of mitral regurgitation following myocardial ischemia is between 13 and 59%, and approximately a third of these patients develop at least moderate regurgitation severity [155]. Ischemic mitral regurgitation is associated with a 2-fold increase in mortality [10,22] and with adverse patient prognosis [23]. Patients that develop mitral regurgitation following an ischemic event have a lower 5-year survival than those that do not (Figure 2-10) [10]. Mortality also increases even when ischemic mitral regurgitation is only mild [10,22,156]. Further, there is a graded relationship between regurgitation severity and reduced patient survival [10].

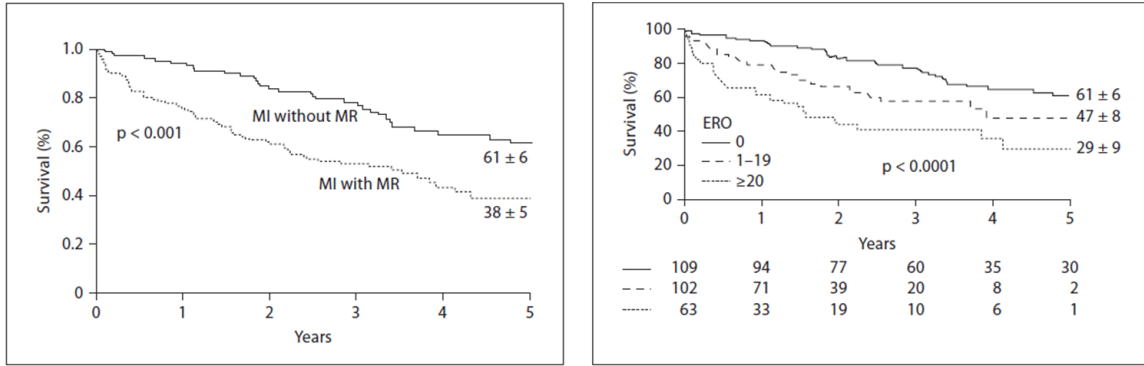


**Figure 2-10 (Left) Patient survival is significantly decreased with the presence of mitral regurgitation following myocardial ischemia. (Right) This relationship is proportional to regurgitation severity. [10]**

Functional mitral regurgitation may result from isolated left atrial dilation or more commonly with concomitant ventricular remodeling following myocardial infarction (also known as ischemic mitral regurgitation) or hypertrophy. These remodeling events induce dilation and flattening of the mitral annulus (Figure 2-11) [11], and displacement of the papillary muscles away from the mitral annular plane (Figure 2-12) [12]. Together, these geometrical changes restrict systolic leaflet closure (type IIIb Carpentier’s functional classification), ultimately resulting in mitral regurgitation.

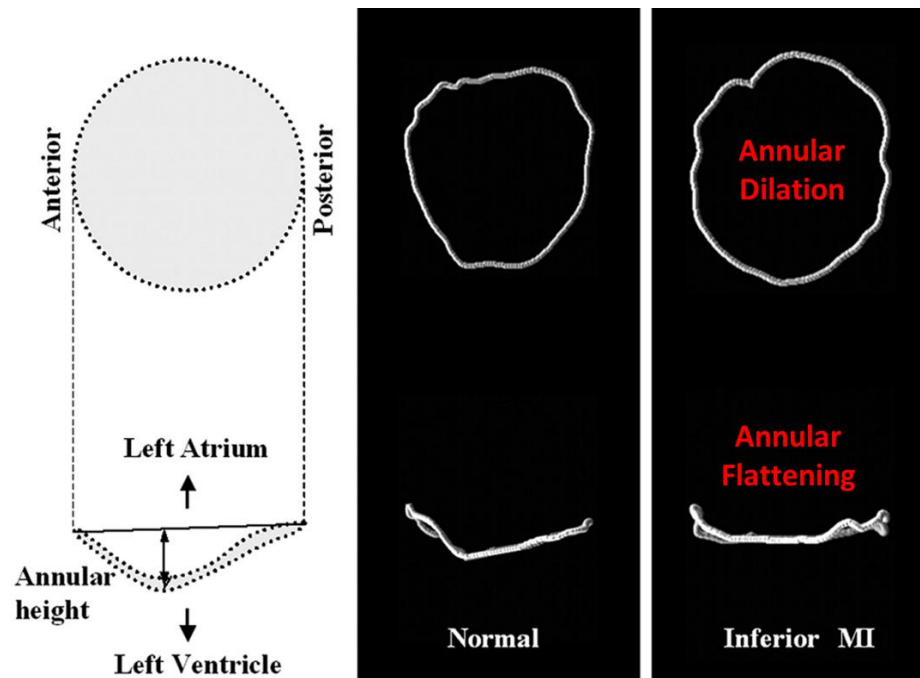


**Figure 2-11 Mitral annular dilation and flattening result from ischemic remodeling of the surrounding myocardium [11].**

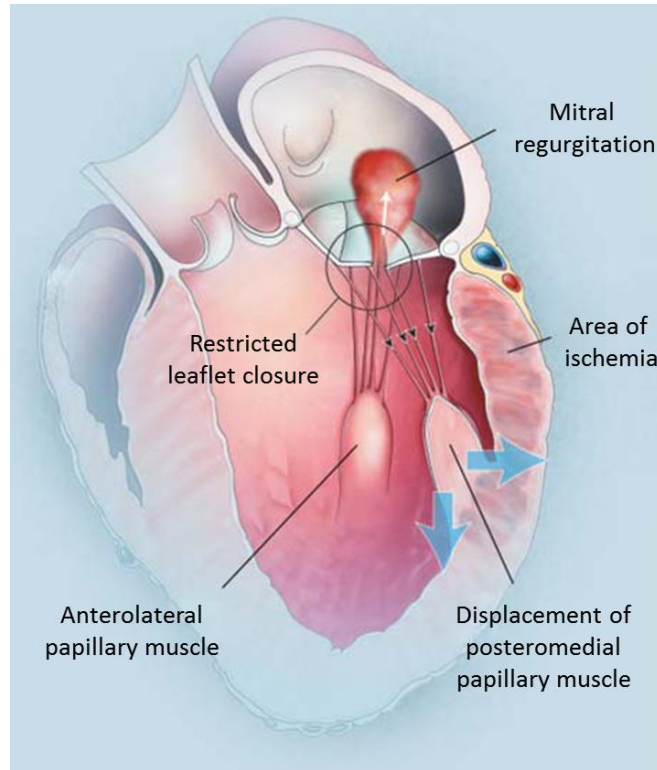


**Figure 2-12 Following myocardial ischemia, papillary muscle displacement away from the mitral annular plane results in restricted leaflet closure and mitral regurgitation [12].**

Changes in mitral annular geometry associated with ischemic mitral regurgitation have been well documented. Using three-dimensional echocardiography, Ahmad et al. quantified several dimensions along the human mitral annulus in patients with ischemic mitral regurgitation; these were compared to healthy control subjects [3] (Table 2-1). In a similar clinical study conducted by Watanabe et al. mitral annular circumference and area were found to be significantly different between control subjects and ischemic mitral regurgitation patients [11]. In another study, Watanabe et al. also reported significant mitral annular flattening and leaflet tenting with ischemic mitral regurgitation [157]. These changes to annular geometry were further corroborated by Vergnat et al.

[158], who additionally identified that papillary muscle to annular distance was significantly increased between control subjects and patients with myocardial infarcts. More comprehensive studies of the changes to the subvalvular apparatus were performed on large animal models using more invasive experimental techniques.

**Table 2-1 Changes in mitral annular dimensions associated with ischemic mitral regurgitation [3].**

Variable	Controls	IMR	p Value
Annular perimeter [cm]	8.6 ± 0.2	10.7 ± 0.7	0.03
Anterior annular perimeter [cm]	4.1 ± 0.2	5.0 ± 0.4	0.06
Posterior annular perimeter [cm]	4.5 ± 0.2	5.6 ± 0.5	0.06
Intertrigonal distance [cm]	2.1 ± 0.1	2.8 ± 0.3	0.06
Annular Area [cm <sup>2</sup> ]	5.7 ± 0.3	9.1 ± 1.2	0.03
Anterior annular area [cm <sup>2</sup> ]	2.5 ± 0.2	4.0 ± 0.7	0.08
Posterior annular area [cm <sup>2</sup> ]	3.2 ± 0.3	5.1 ± 0.9	0.08

Such quantitative studies were performed in parallel at the Stanford (Principle Investigator: Craig D. Miller) and University of Pennsylvania Labs (Co-Principle Investigators: Joe and Rob Gorman) using independently developed ovine ischemic mitral regurgitation models. Both groups strategically placed markers on the mitral annulus, ventricular myocardium, and papillary muscles, which were monitored before and after myocardial infarction. Figure 2-13 summarizes the statistically significant geometrical changes observed between animals that did (+) and did not (-) develop chronic ischemic mitral regurgitation (CIMR) in an ovine model following myocardial infarction [13].

### CIMR(+) vs. CIMR(-)

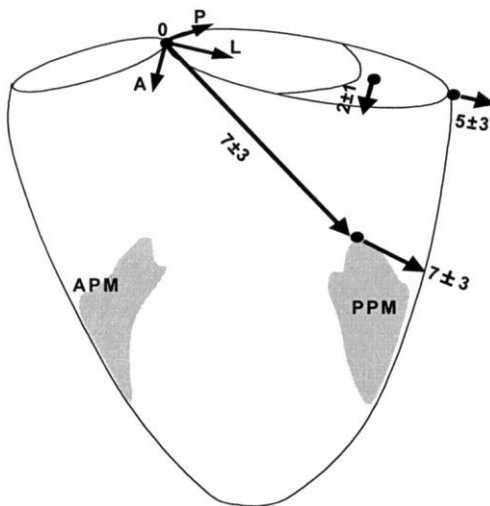


**Figure 2-13 Mitral annular dilation and posteromedial papillary muscle displacement was significantly different between animals that did and did not develop chronic ischemic mitral regurgitation after myocardial infarction [13].**

In these studies, it was not possible to isolate the independent effect of annular dilation and papillary muscle displacement on mitral valve function. Therefore, to understand the contribution of these geometrical changes towards mitral regurgitation, additional studies were necessary. In carefully controlled *in-vitro* studies using a pulsatile left heart simulator, He et al. showed that the mitral leaflets were sufficiently large to compensate for 80% mitral annular dilation in the absence of papillary muscle displacement (Figure 2-14) [14]. However, this compensatory mechanism was lost and significant mitral regurgitation occurred at smaller magnitudes of annular dilation in the presence of papillary muscle displacement, particularly asymmetric tethering. Mitral regurgitation was largest with posteromedial papillary muscle tethering, which is consistent with clinical evidence that suggests ischemic mitral regurgitation incidence is

highest with inferior myocardial infarction (localized to the posterior wall resulting in preferential displacement of posteromedial papillary muscle displacement) [159].

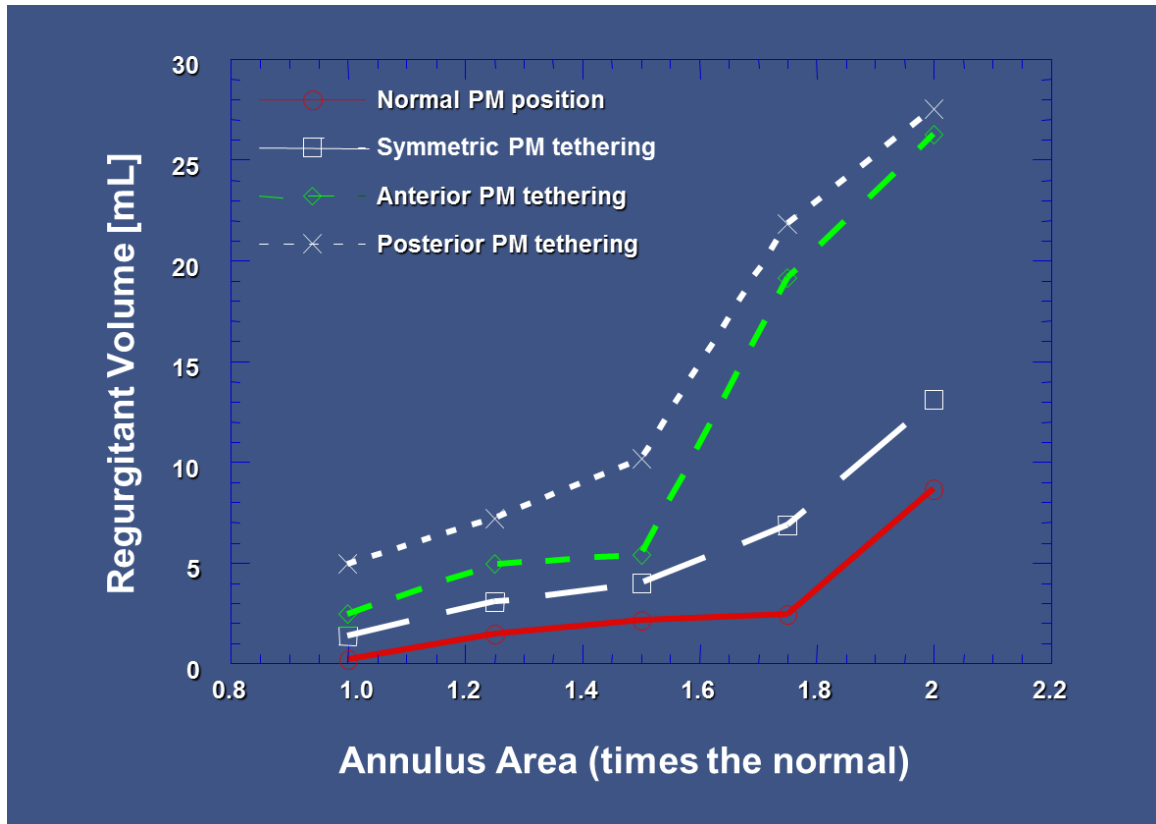


**Figure 2-14 Isolated and combined effects of annular dilation and papillary muscle displacement on mitral valvular function [14].**

### 2.4 Surgical Repair for Mitral Valve Insufficiency

Among treatment options for mitral regurgitation, surgical repair (over pharmacological therapy or surgical replacement) is the preferred mode, specifically ring mitral annuloplasty [48,160,161]. Ring mitral annuloplasty remodels the native mitral

annuloplasty through the use of an artificial band to restore its physiological shape and size (Figure 2-15). Annuloplasty rings are available in a wide spectrum of size, stiffness, and shape. More recently, etiology specific annuloplasty rings have targeted ischemic mitral regurgitation through rigid (titanium) complete rings that drastically undersize the septal-lateral diameter.

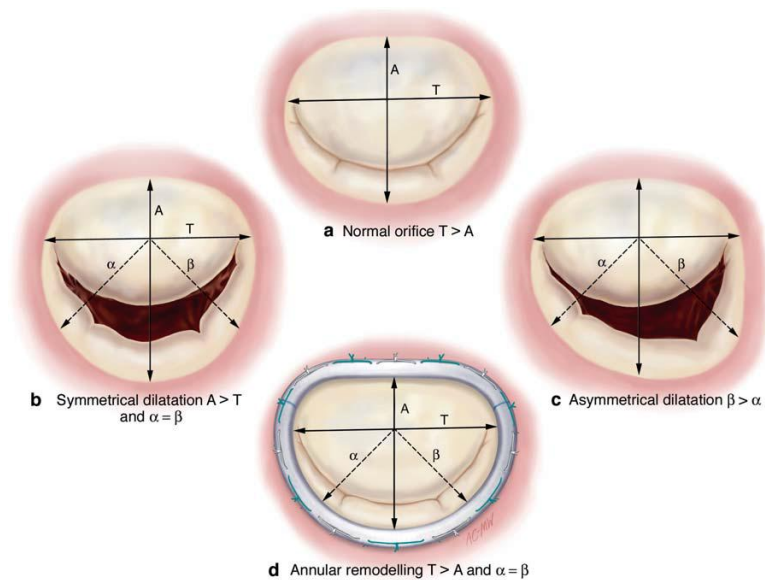


**Figure 2-15 Ring annuloplasty aims to surgically restore physiological size and shape of the native mitral annulus (image adapted from Carpentier’s Reconstructive Valve Surgery).**

Overall, clinical outcomes of mitral annuloplasty for functional mitral annuloplasty have been suboptimal. High rates of persistent or recurrent regurgitation have been observed in echocardiographic follow up as early as 3 years after surgical repair (Figure 2-16) [15]. This is further detailed by an excellent review by Magne et al., which shows that late regurgitant recurrence following annuloplasty repair can exceed 60% at 5 years follow up (Figure 2-17) [12].



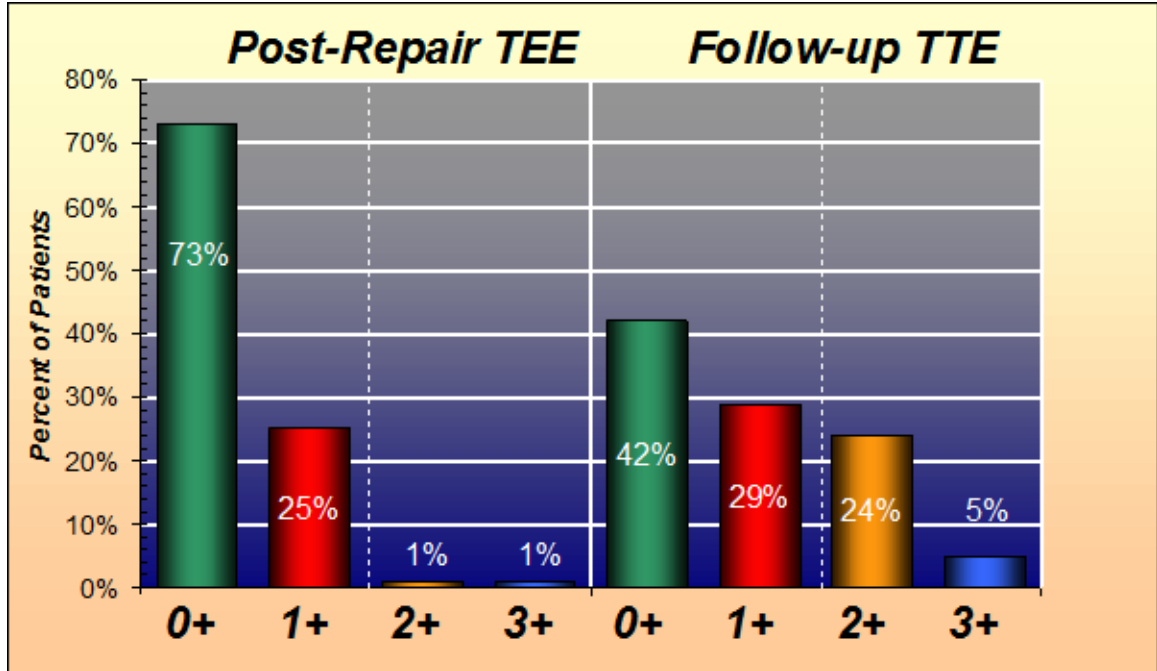


**Figure 2-16** Three year follow up of patients treated with mitral annuloplasty for functional mitral regurgitation reveals high rates of recurrence as early as 3 years. [15]

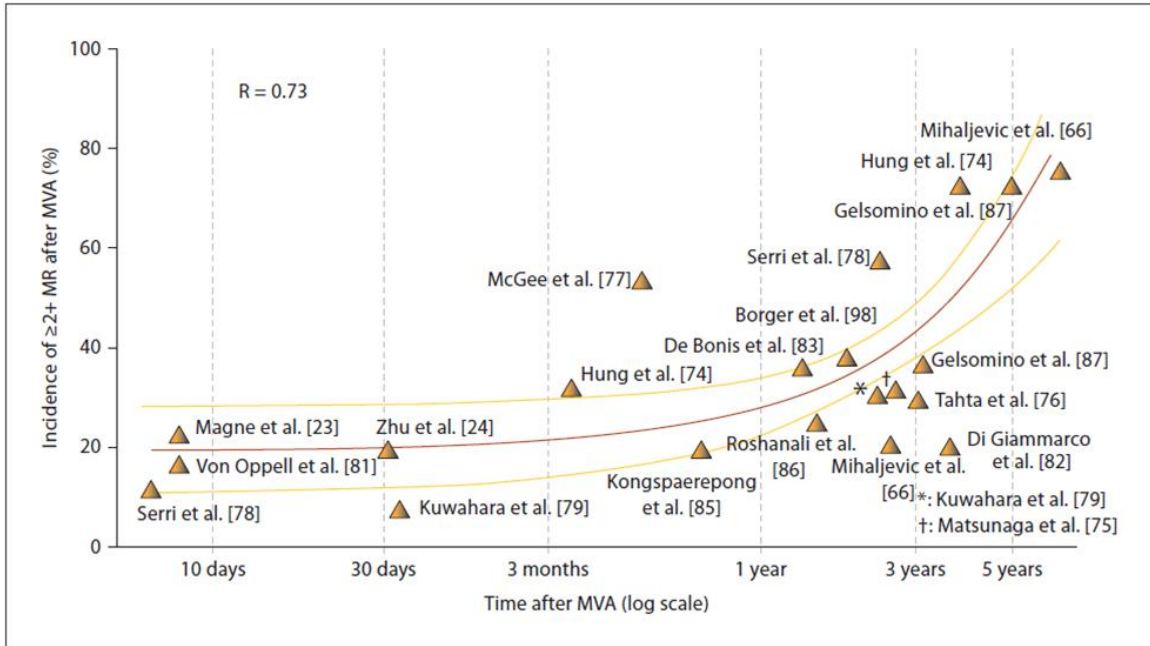


**Figure 2-17 Recurrent mitral regurgitation following ring annuloplasty of ischemic valve disease has been observed in a wide range of studies [12].**

It has long been purported that ring annuloplasty failure is a result of incompatible choice of mitral annuloplasty ring type for the functional pathology. To this point, recent studies systematically performed undersized (by two sizes) rigid complete annuloplasty have claimed long-term freedom of mitral regurgitation [48,160,162]. However, this success was limited by the patient's preoperative left ventricular geometry (end diastolic diameter < 65 mm). Excessive and late deleterious remodeling of the left ventricle have been identified as a key contributor to mitral annuloplasty ring failure [41,42,163]. These studies underscore the importance of addressing the pathologically tethered subvalvular apparatus in this setting of secondary mitral regurgitation.

Of note, anterior leaflet augmentation [57,58] and basal papillary muscle relocation (Kron Procedure) [17,56] have been recently demonstrated to restore leaflet

coaptation and mobility without the need to unnaturally undersize the mitral annulus while relieving subvalvular tethering. Anterior leaflet augmentation is performed by making an incision in the anterior leaflet parallel to the mitral annulus and letting the anterior leaflet “fall” into the ventricle (Figure 2-18). The height of the fall can be determined by the spread of the incision. As a result, the chordae which insert into the anterior leaflet also displace into the ventricle, which may help alleviate the pathological tethering from the displaced papillary muscles. A pericardial patch is then sutured to the anterior leaflet effectively increasing the available surface area to cover the mitral orifice and promote coaptation. In a pilot study by Kincaid et al., 25 patients with severe (84%) and moderate (16%) ischemic mitral regurgitation underwent anterior leaflet augmentation [57]. Post-operatively echocardiography revealed regurgitation was abolished in 80% of patients; the remaining 20% had moderate regurgitation. At 2 years follow-up, actuarial freedom from moderate or greater regurgitation was 81%. As this is a challenging surgical procedure, further mechanistic studies are needed to identify which patients would most benefit from such an adjunctive repair and to provide an understanding of the mechanical effects produced by displacing the anterior leaflet and its chordal attachments into the ventricle.

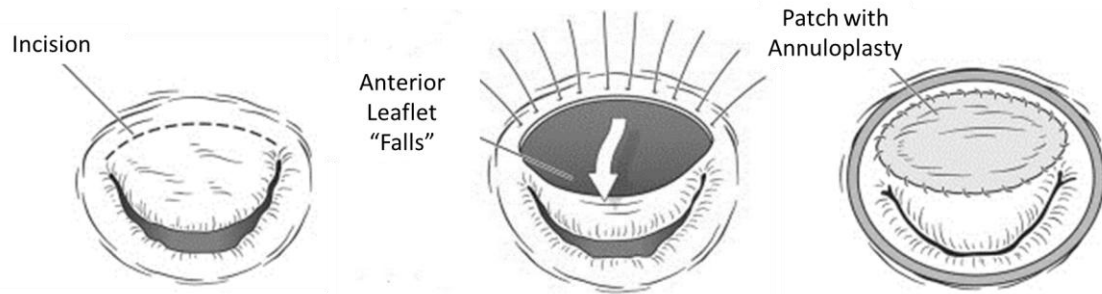
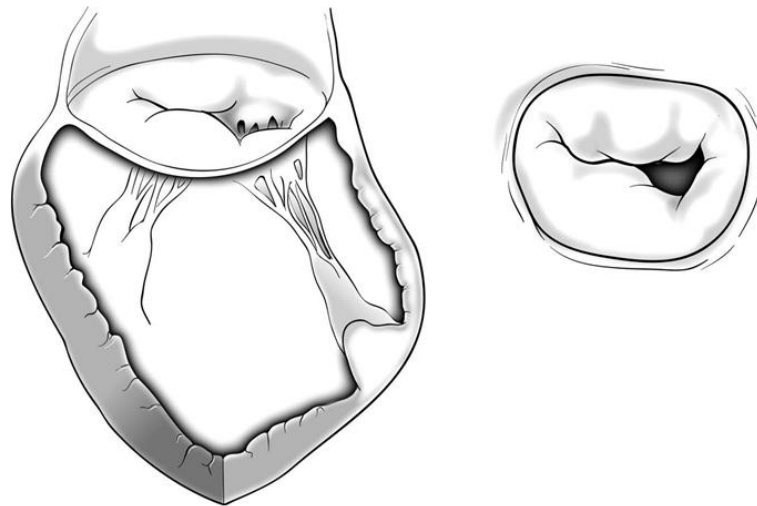


**Figure 2-18 Adjunctive leaflet augmentation results in larger anterior leaflet surface area to promote valve competency while displacing chordal insertion points [16].**

Similar to anterior leaflet augmentation, basal papillary muscle relocation aims to repair ischemic mitral regurgitation through a sub-annular adjunctive procedure (Figure 2-19). First pioneered by Dr. Kron, surgical relocation of the posteromedial papillary muscle was successfully performed in 18 patients with moderate to severe ischemic mitral regurgitation [56]. Prolene sutures were passed through the fibrous portion of the apically tethered posteromedial papillary muscle, which is then passed up through the adjacent mitral annulus at the right fibrous trigone. The papillary muscle was then drawn upwards towards the mitral annulus until sufficient coaptation was achieved through saline testing. In a 1:1 randomized study, Fattouch et al. compared repair efficacy of adjunctive papillary muscle relocation to the preferred surgical treatment, mitral annuloplasty [54]. At 5 years, recurrent regurgitation equal to or greater than moderate severity was significantly more prevalent in the isolated ring annuloplasty repair group (11.5%) as compared to the adjunctive papillary muscle repair group (3.7%). While these data are favorable, more detailed studies are needed to standardize this repair technique to maximize its clinical applicability. In particular, two questions need further

investigation: (i) to where on the mitral annulus should the papillary muscles be relocated, and (ii) how much basal relocation is needed to promote valve competency.

### Ischemic Mitral Regurgitation



### Kron Procedure with Ring Annuloplasty

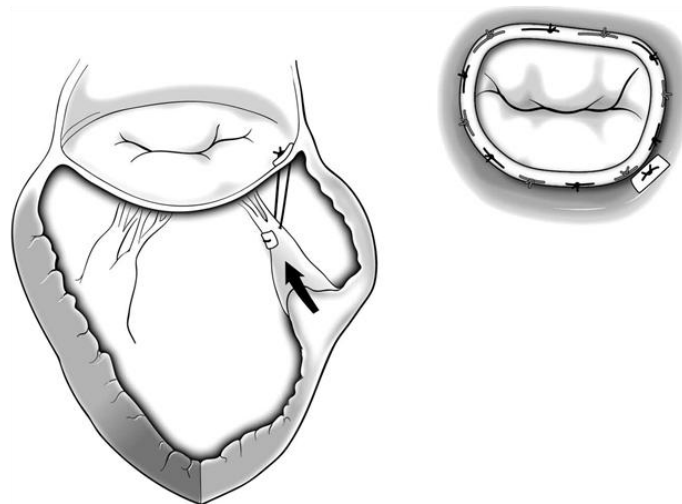


**Figure 2-19 In the Kron procedure, the posteromedial papillary muscle is surgically relocated to the adjacent mitral annulus to relieve subvalvular tethering caused by a severely dilated left ventricle [17].**

## 2.5 Quantification of Mitral Regurgitation

The first step in surgical indication for mitral valve repair is proper clinical referral through accurate diagnosis of mitral regurgitation severity and valvular dysfunction. The current guidelines utilize an integrative assessment of mitral regurgitation. The quantitative techniques include regurgitant volume, fraction, and orifice area. Using the clinical standard through noninvasive imaging, mitral regurgitation is quantified through the 2D color Doppler Proximal Isovelocity Surface Area measurement (PISA). The 2D proximal isovelocity surface area method is derived from the principle of conservation of mass: as blood approaches a regurgitant orifice, its velocity increases, forming concentric shells of increasing velocity and decreasing surface area [18,164-166].

Key assumptions of the PISA method are that the orifice is small and round, that the sourcing and sinking chambers are large (left ventricle and left atrium respectively), and that the location of the orifice is on a planar surface. If these conditions are met, the proximal flow will be axially symmetric, and locations of constant velocity will be hemispherical in shape.

Using continuity principles the volumetric flow rates on either side of the mitral regurgitation orifice are equal:

$$Q_1 = Q_2$$

Volumetric flow rate may be defined as:

$$Q = \text{Area} \times \text{Velocity}$$

From this, it follows that:

$$\text{Area}_1 \times \text{Velocity}_1 = \text{Area}_2 \times \text{Velocity}_2$$

Proximal to the regurgitant orifice (in the left ventricle), the surface area can be estimated during 2D color Doppler echocardiography assuming a hemispherical distribution of velocity vectors:

$$\text{Area}_1 = 2\pi R^2$$

The radius is determined from the 2D color Doppler echocardiography as the radial distance from the regurgitant orifice area to a predetermined isovelocity surface area. The isovelocity surface area is chosen by defining an Aliasing Velocity which gives a clear delineation of isosurfaces. From this, it follows that:

$$\text{Velocity}_1 = \text{Aliasing Velocity}$$

Downstream of the regurgitant orifice (in the left atrium), the area may be defined as the Effective Regurgitant Orifice Area:

$$\text{Area}_2 = \text{EROA}$$

The Effective Regurgitant Orifice Area is the cross-sectional area observed downstream of a nozzle at the point of the vena contracta. At this point, velocity is also the largest (as area is the smallest). Therefore, it follows:

$$\text{Velocity}_2 = V_{\max}$$

$V_{\max}$  can be determined using continuous wave (CW) color Doppler measure along the central axis of the regurgitant jet. Rearranging the continuity equation to solve for the effective regurgitant orifice area, the measurement of interest produces the following:

$$\text{EROA} = 2\pi R^2 \times \text{Aliasing Velocity} / V_{\max}$$

From this, regurgitant volume can be calculated by multiplying the effective regurgitant orifice area by the Velocity Time Integral, or the stroke distance over which blood travels in one cardiac cycle. VTI can be measured from the continuous wave color Doppler by integrating the velocities over the regurgitant portion of the cardiac cycle. Finally, regurgitant volume can be calculated as follows:

$$\text{Regurgitant Volume} = \text{EROA} \times \text{VTI, or}$$

$$\text{Regurgitant Volume} = 2\pi R^2 \times \text{Aliasing Velocity} \times \text{VTI} / V_{\max}$$

A schematic representation of the 2D PISA method can be seen in Figure 2-20.



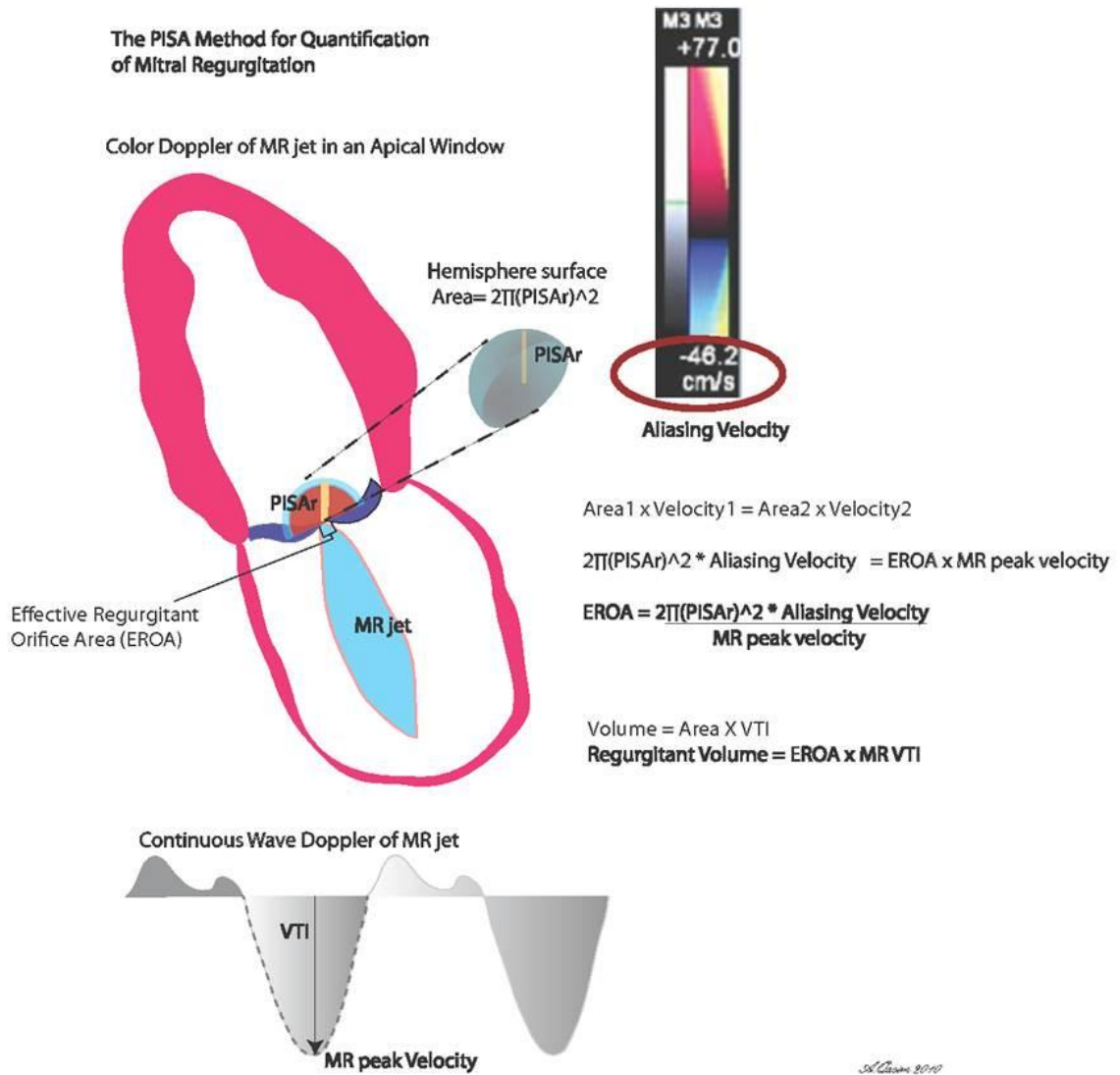


**Figure 2-20** The 2D PISA method is explained in this schematic from the [echocardiographer.org](http://echocardiographer.org).

This method is not without limitations. The most crippling of these limitations is the hemispherical assumption, which is often violated by mitral regurgitant orifices. The hemispherical assumption is derived from a pinhole source, or a small perfectly round orifice. Often times, the regurgitant orifices are elongated along the length of the mitral coaptation line. Therefore the flow convergence zone may not be defined by a

hemispherical approximation, which will result in systematic underestimation of true regurgitant volume.

A second major limitation is caused by the difficulty in accurately and reproducibly identifying the radial distance from the mitral regurgitant orifice to a defined isovelocity surface area. Small errors in this radial dimensions may cause large errors in calculate regurgitant volume due to squared weighting of the radial measurement.

A final major limitation is that Doppler ultrasound can only detect velocity components aligned with the direction of the ultrasound beam. It cannot detect velocities oriented perpendicular to the scan lines. Moreover, velocities observed by the ultrasound beam are a projection of the true velocity, that is, there is a loss of velocity magnitude defined by the scalar dot product. Observed velocities are modulated by the cosine of the angle between the ultrasound scan line and the direction of the velocity (Figure 2-21).

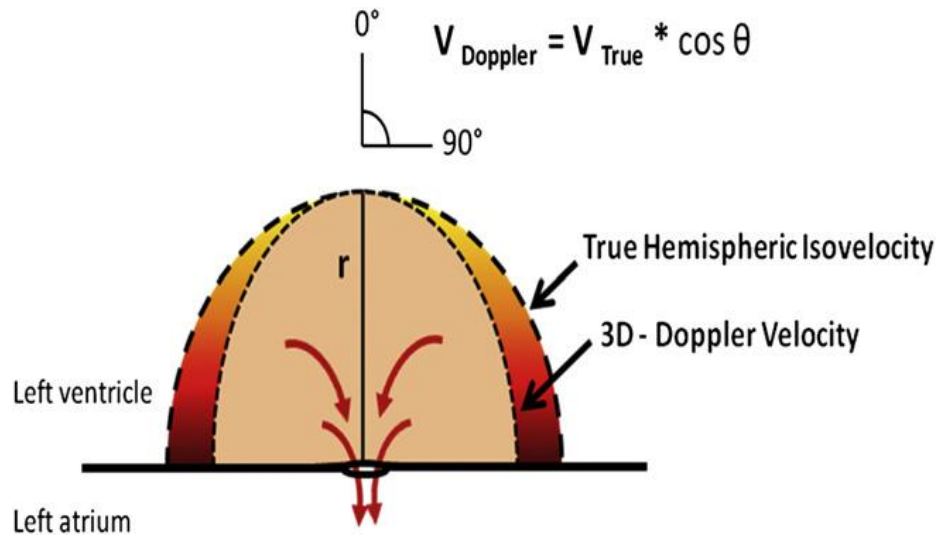


**Figure 2-21 The observed velocity vectors along the ultrasound scan lines have lower magnitudes than the true velocity field because of the cosine angle correction [18].**

Philips Healthcare recognized these limitations of 2D PISA and sought to create a simple new tool that uses 3D color Doppler echocardiography to improve quantification accuracy and robustness. Philips Healthcare developed a complex algorithm, herein known as the Field Optimization Method (FOM) to correct for differences in observed and true velocity magnitudes (Figure 2-22). The Field Optimization Method is initiated by an approximation of the true velocity vectors. Ultrasound physics are then applied to the guess of the true velocity fields to produce a calculated “observed” velocity field. The calculated and true “observed” velocity fields are then compared. This process is iterated until the error distribution between the calculated and true “observed” velocities are minimized. The velocities are then integrated in the flow convergence zone of the new true velocity field to calculate the overall regurgitant volume. This is done to all frames in the cardiac cycle. More detail on this method can be found here [167].

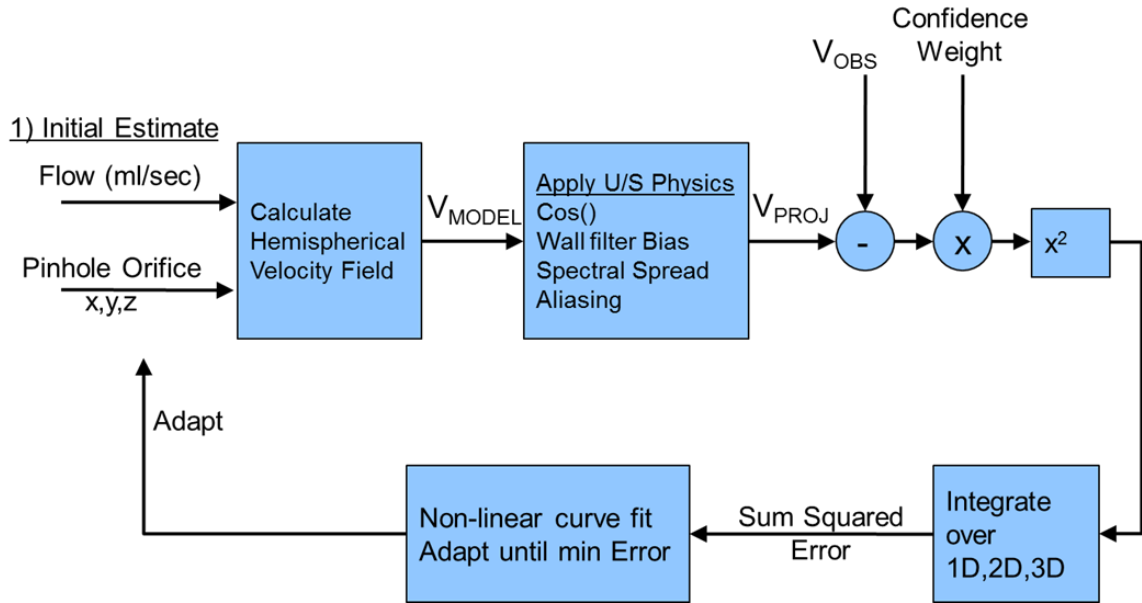


**Figure 2-22** The observed velocity vectors along the ultrasound scan lines have lower magnitudes than the true velocity field because of the cosine angle correction [167].

## 2.6 Computational Mitral Valve Models

Simplified numerical models of the mitral valve have been used for over 20 years to provide a unique and non-invasive analysis of function and biomechanics for direct surgical applications, such as annuloplasty [59-62], edge-to-edge[20,63] or neochordae [64,65] implantation, and stress analysis [66,67]. These models vary considerably in execution owing to differences in anatomical construction, material laws, boundary conditions, and preferred solvers.

Geometric mitral valve modeling has evolved from simple and idealistic annular, leaflet, and chordal profiles to patient specific models based on state of the art medical imaging, in particular ultrasound [20,67,168] and computed tomography [19] (Figure 2-

23). The mitral annulus and leaflets can be directly segmented from the resultant image stacks using manual or semi-automated techniques. Leaflet thickness must still be prescribed in the current models due to inconsistent image quality and relatively limited resolution [20]. Annular motion can be imposed to reflect in-vivo tracking [19,169,170].

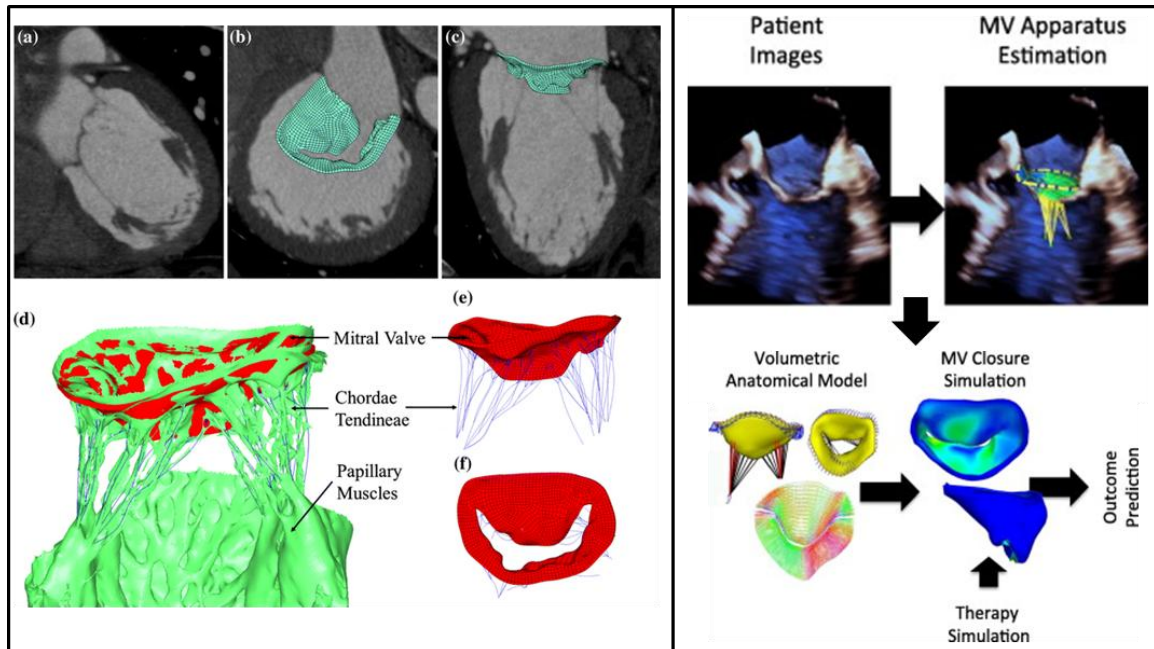


**Figure 2-23 Patient specific anatomical mitral valve models derived from CT (left) and three-dimensional echocardiography (right) imaging will ultimately be used for predictive surgical planning. CT imaging is better capable of capturing the detailed chordal structure. (Images adapted with permission from Wang et al. [19] and Mansi et al. [20].)**

Even greater challenges are presented by the chordae tendineae. Echocardiography, the standard of care modality, currently lacks the spatial resolution to accurately capture and segment the complex chordal branching and insertion. While computed tomography is capable of capturing chordal structures, it is not the standard of care, nor is it capable of finely resolving the cross-sectional areas [19]. As a result, it is

typical for chordae number, branching, and insertion to be approximated from literature derived data. This has been shown to lead to inaccurate closure simulations, which typically result in billowing mitral leaflets [19]. Additionally, implementing the chordal to leaflet transition region is a non-trivial problem. Point insertions are used for the chordal attachments to the leaflets and papillary muscles. However, physiologically, chords seamlessly fuse into the leaflets and the underlying collagen structures radially diffuse from the chordal core into the leaflet [108,171]. This can lead to uncharacteristically high stress magnitudes or leaflet kinking at the point of insertions. Furthermore, as the leaflets are passive membranes, their deformation and motion will be a balance of the interaction between the pressure driven flow and constraining chordal structure. Therefore, it is imperative for realistic simulations to develop a reliable strategy to physiologically implement the chordae. The tips of papillary muscles are normally modeled as the origins of the chordae, but are not given finite dimensions or physical properties; their position and motion can be imposed to reflect in-vivo tracking [169,172].

Material models for the mitral leaflets vary considerably, but should aim to capture the leaflets non-linear and anisotropic mechanical response [170,173,174]. The leaflets non-linear mechanical response may be neglected, mainly in modeling the isovolumic contraction/relaxation phases of the cardiac cycle, but will underestimate developed stresses [113,175]. The mitral chordae are typically modeled as hyperelastic or linear elastic tension only elements. However, regardless of material model implemented, the choice of material properties and microstructural fiber orientation remains difficult. These parameters can be approximated and iteratively refined such that

the computational solutions converge to match empirical data. Modeling disease tissue adds another level of complexity as the microstructure deleteriously remodels with altered mechanical loading. It is not known whether a given deformation can be achieved by a unique set of material parameters, which could yield misleading conclusions. Additionally, it is not enough to model the mitral valve in isolation, as the interplay with the left ventricle contributes strongly to mitral valve function. Efforts similar to the study by Wenk et al. will help target surgical riddles such as recurrent mitral regurgitation in patients with ischemic valve disease [176].

Initial and boundary conditions, as well as, preferred solver methods vary from group to group. Solvers range from in-house to commercial codes and execute structural or fluid-coupled simulations [174,177]. Nonetheless, direct one-to-one validation is needed against comprehensive, time resolved experimental data with multiple measured endpoints and well defined boundary conditions [37]. Additionally, systematic studies are needed to understand whether increasing model fidelity and complexity provides measured gains in assessing mitral valve function and structural mechanics, particularly as a patient specific surgical planning tool.

## CHAPTER 3

### OBJECTIVE AND SPECIFIC AIMS

Owing to its complex structure and dynamic mechanical loading, surgical repair of the heart's mitral valve poses a significant clinical challenge. Specifically, repair of ischemic mitral regurgitation, caused by the geometric disruption of the mitral apparatus in the setting of ventricular dysfunction, results in poor long-term patient survival[10,12,22,29,43,163,178]. Clinical data have shown that the preferred surgical treatment, restrictive mitral annuloplasty, may result in 15-30 % early (< 6 months) recurrence of mitral regurgitation ( $\geq 3$  and may exceed 70% after five years +) [178]. Studies have suggested isolated annuloplasty may not be a comprehensive repair suitable for all patients because ischemic pathology is multi-factorial and results in variable ventricular and valvular geometric distortions [11,157,179-182]. Recently, novel surgical repairs have been explored on a patient specific basis.

Consequently, it is important to improve clinical diagnostics to better identify patients that may benefit from these adjunctive surgical repairs. These complex repairs need to be carefully evaluated to understand their mechanical and functional benefits, particularly in maximizing leaflet coaptation and reducing subvalvular tethering. Finally, advances in predictive computational mitral valve modeling may make patient-specific surgical planning possible. To date, such tools are limited, however, without direct experimental validation to ensure their accuracy and reliability.



*Therefore, the central objective of this thesis is to develop and utilize an integrative experimental framework to improve mitral valve surgical repair outcome through multiple complementary approaches including: (i) advanced diagnostics, (ii) mechanistic evaluation of post-repair valvular function, and (iii) validation of novel computational surgical planning tools. These tasks are achieved through three specific aims:*

**Specific Aim 1: *In vitro* validation of the Philips 3D Field Optimization Method for the accurate quantification of mitral regurgitation.**

As patient outcome is correlated to mitral regurgitation severity, it is important to accurately quantify mitral regurgitation. Additionally, mitral regurgitation severity is associated with ventricular and valvular geometric distortions, which may not be easily quantifiable otherwise. More accurate quantification of valvular function and improved diagnostics may better guide surgical repair, particularly the need for more complex or adjunctive repair procedures. Current clinical practices, however, utilize a qualitative grading system, while quantitative techniques have been known to underestimate regurgitation severity. Therefore, in collaboration with Philips Healthcare, a novel mitral regurgitation assessment algorithm is systematically validated and compared against current clinical practices using the pulsatile Georgia Tech Left Heart Simulator. Multiple geometries of regurgitant orifices and flow rates are simulated over a range of pathological conditions to identify potential valvular lesions that may cause erroneous quantification. For direct comparison, the clinical standard, 2D PISA method, and a manual integrative 3D PISA method, are similarly compared. Consequently, the Field

Optimization Method will be adapted and refined by Philips Healthcare based on empirical observations. The data generated will be available for future evaluation of similar analysis techniques.

***Specific Aim 2: To elucidate the functional efficacy and mechanical benefit of novel adjunct surgical repairs for the treatment of ischemic mitral regurgitation.***

Since ischemic mitral regurgitation is a secondary pathology, or a result of left ventricular myocardial injury, we hypothesize that adjunct surgical procedures will restore leaflet coaptation and valve function while reducing subvalvular tethering. In particular, two novel adjunct surgical strategies that intend to compensate for severely dilated ventricles are investigated in this thesis: (A) anterior leaflet augmentation, and (B) basal papillary muscle relocation. Each targeted therapy is performed as an adjunct to true-sized mitral annuloplasty. Treatment efficacy is assessed using an integrative approach that combines (i) clinical measurements of valve function, (ii) direct flow measurements of regurgitation, and/or (iii) chordal force measurements of leaflet and subvalvular tethering. These repairs are expected to compare favorably against the current surgical preferred treatment for ischemic mitral regurgitation, restrictive or undersized mitral annuloplasty.

***Specific Aim 3: Development of an experimental framework and database for the direct validation and advancement of novel computational surgical planning platforms for mitral valve disease.***

Patient specific predictive surgical planning is a new frontier in mitral valve repair enabled by recent advances in computational modeling and medical imaging technology.

These models have evolved from simple two-dimensional approximations to complex three-dimensional fully coupled fluid-structure interaction models. To date, however, these models have lacked direct one-to-one experimental validation. Moreover, as computational solvers vary considerably, experimental benchmark data are critically important to ensure model accuracy. Moreover, these data need to be adaptable to provide a range of boundary conditions and measurable endpoints suitable for the various computational methods. To this end, a multi-modality in-vitro pulsatile left heart simulator is designed and developed. Comprehensive experimental data evaluating mitral valve function are acquired including:

1. Valvular geometry through state of the art micro-computed tomography and clinical standard of care echocardiography imaging
2. Geometric and hemodynamic boundary conditions
3. Ventricular flow fields through stereoscopic particle image velocimetry
4. Valvular mechanics (leaflet strain, chordal and papillary muscle force)

Taken together, the results from this thesis will lead to more accurate clinical diagnosis and improved surgical treatment for the management of ischemic mitral regurgitation. Specific Aim 1 will more accurately quantify valvular dysfunction, which may help to identify patients for adjunctive surgical intervention, where simple mitral annuloplasty may otherwise have failed. Specific Aim 2 will investigate novel adjunct surgical procedures which may provide new options for patients with pre-operative characteristics associated with simple annuloplasty repair failure. Furthermore, the experimental framework and database provided from Specific Aim 3 will be integral in improving the

accuracy and reliability of predictive patient specific surgical planning tools. Consequently, these validated computational mitral valve models can be used to explore and evaluate new surgical therapies.

## CHAPTER 4

### MATERIALS

In this chapter, the design and operating principles of the major equipment used in this thesis are described. Specifically, the pulsatile left heart simulator and its functional components, imaging systems, data acquisition systems and associated transducers, and instrument calibrations are detailed. Additionally, a novel modular left heart simulator specifically designed for micro-computed tomography and particle image velocimetry is described. Experimental methods and protocols are detailed in Chapter 5.

#### 4.1 Pulsatile Left Heart Simulator

All experiments for Specific Aim 1 and 2 were conducted in an *in vitro* pulsatile left heart simulator previously developed in the Cardiovascular Fluid Mechanics Laboratory. In section 4.5, a new modified left heart simulator is described specifically for completing the objectives of Specific Aim 3. The operating principles of the modified simulator are similar to those described herein. The simulator is a pulsatile, bladder pump driven system, in which physiological and pathological hemodynamic function of native mitral valves with complete subvalvular apparatus can be studied. As shown in Figure 4-1, the simulator consists of ten main components:

1. Low pressure atrial/pulmonary reservoir
2. Left atrial chamber

3. Mitral annular plate
4. Left ventricular chamber
5. Aortic outflow tract with mechanical valve
6. Papillary muscle positioning system
7. Pulsatile bladder pump
8. Programmable solenoid system (not pictured)
9. Compliances and resistances
10. Data acquisition system (not pictured)

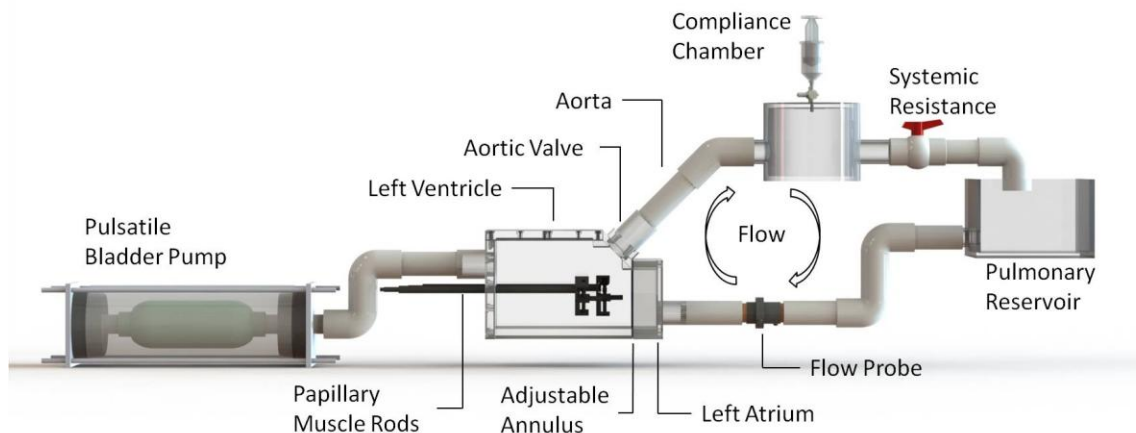


**Figure 4-1 Schematic representation of the pulsatile left heart simulator.**

An open air reservoir was used to maintain a static low pressure ( $\sim 10$  mmHg) head preceding the left atrium. This reservoir also functioned as a sink for aortic outflow distal to the systemic resistance. A clear, acrylic cuboid chamber was used as a left atrium. The chamber had a thin acrylic basal wall (3.5 mm) to minimize acoustic distortion of ultrasound waves and to provide optical access for en face and high speed

imaging of the functioning mitral valve. A second atrial chamber with a side inlet was used when needed to provide uninhibited optical and acoustic access to the valve for simultaneous high speed and ultrasound imaging (not shown). The left atrial chamber was designed such that its depth would position the functioning mitral valve between 10-12 mm away from an x7-2 transthoracic pediatric echocardiography probe (Philips Healthcare; Andover, MA).

An adjustable mitral annular plate was used to secure the native mitral annulus in the left heart simulator. The mitral annular plate consisted of an acrylic base plate and a tension spring with a metal wire core, which was embedded in silicone and wrapped in water proof cloth to form a D-shaped annulus (Figure 4-2). The core of the anterior portion of the synthetic annulus was constructed out of rigid tube material to prevent deformation. This region corresponds to the between the left and right fibrous trigones on the anterior annulus, which is often suggested to be more resistant to pathological mitral annular dilation [183]. By controlling the tension on the metal wire drawstring, the synthetic annular area can be incrementally adjusted.

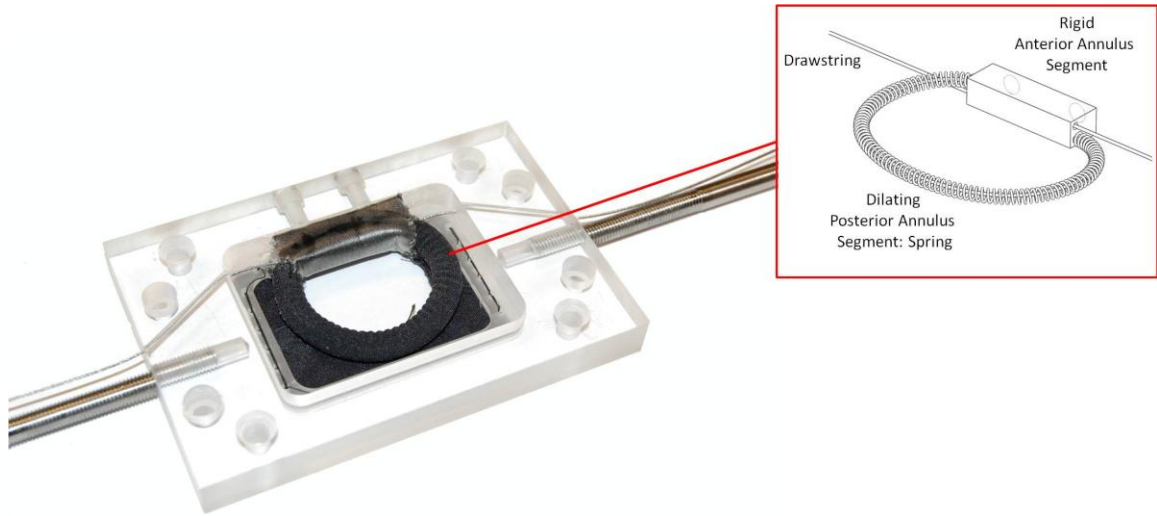


**Figure 4-2 Adjustable mitral annular plate.**

The synthetic annulus was designed such that the control, or physiologic, condition simulated a mitral annular area of 4.4 cm<sup>2</sup>, comparable to a size 30 Physio annuloplasty ring. This was achieved with septal-lateral and commissure-commissure dimensions of 19.2 and 34.9 mm respectively. These dimensions were chosen as they were a nominal representation of the ovine mitral valves procured from the local abattoir and are comparable to the most prevalent annuloplasty ring sizes used in human applications [184,185]. Control valves of different sizes may be used; however, range of annular dilation and under-sizing would need to be adjusted correspondingly.

The tension on the metal wire drawstring was adjustable to yield an undersized (or restrictive) mitral annuloplasty (increase tension), and increasing levels of pathological mitral annular dilation (decrease tension). See Table 4-1 for a summary of annular dimensions used.



**Table 4-1 Annular dimensions used for each experimental configuration.**

<b>Configuration</b>	<b>Physio Ring Size</b>	<b>Annular Orifice Area [cm<sup>2</sup>]</b>	<b>Septal-Lateral Diameter [mm]</b>	<b>Commissure-Commissure Diameter [mm]</b>
<b>Undersized Annuloplasty</b>	26	3.25	16.4	30.7
<b>Control</b>	30	4.40	19.2	34.9
<b>Oversized Annuloplasty</b>	34	5.72	22.0	39.1
<b>IMR</b>	38	7.22	24.8	43.2

The left ventricular chamber was a rigid acrylic chamber onto which the mitral annular plate was mounted (Figure 4-3). It was comprised of a left ventricular outflow tract that housed a 27 mm Bjork-Shiley convexo-concave mechanical valve in the aortic position. The outflow tract was designed at a 135° angle with the frontal face of the chamber to emulate the geometrical positioning of the mitral and aortic valves [186]. The apical wall of the chamber contained an inlet to the bladder pump and a through-wall connection bracket for the mechanical papillary muscle positioning system.

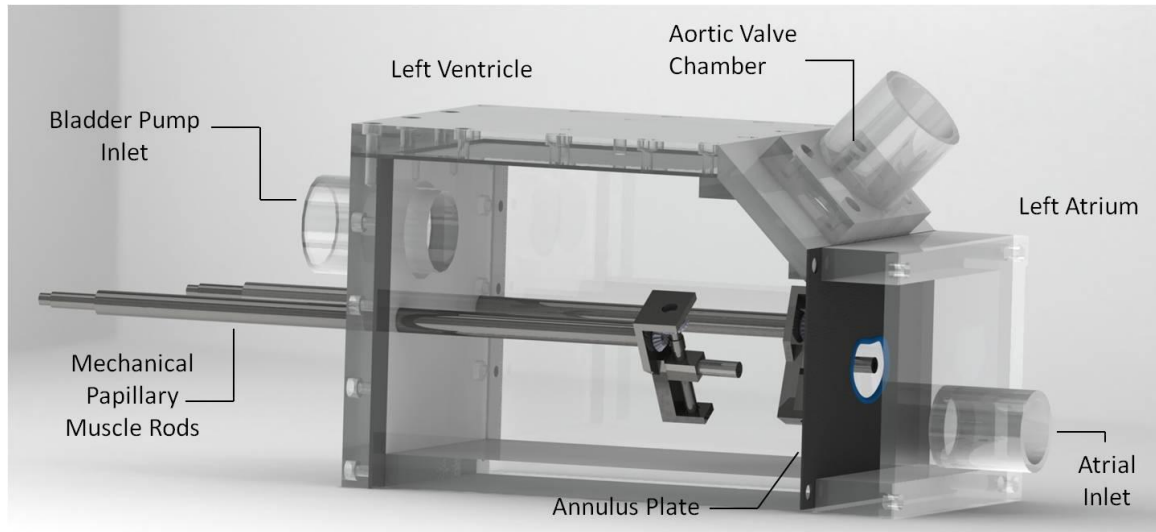


**Figure 4-3 The Left Heart.**

A mechanical papillary muscle positioning system was used to obtain accurate positioning of the native papillary muscles in the left ventricle to 0.9 mm resolution, which was a function of the bevel gear geometry (Miter Gear A-1X-4MY06020; SDP-SI; New Hyde Park, NY) (Figure 4-4). The positioning system was comprised of a main arm, a modified 90° pin-gear drive, and an elevator arm. The main arm was capable of translating into and out of the left ventricle for apical-basal positioning. A gear rotation rod coupled to the pin-gear drive induced displacement of the elevator arm. Combined rotations of the main arm and gear rotation rod were used for septal-lateral and anterior-posterior positioning. Native papillary muscles were mounted to the mechanical positioning system via a Teflon connector, which screwed into the end of the elevator arm. Further details on the papillary muscle positioning system can be found here [2,35].

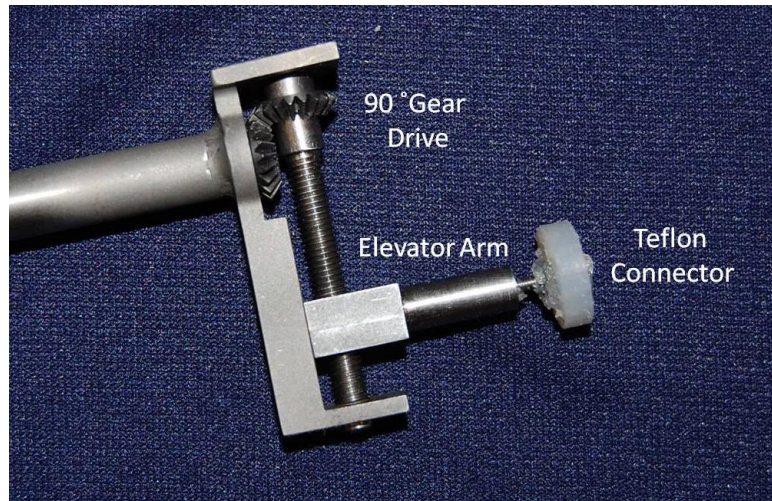


**Figure 4-4 Mechanical papillary muscle positioning rods.**

The left heart simulator used a pressure driven compressed air bladder pump, which was regulated by three 3-way air solenoid valves. One solenoid (A) was used to increase pressure around the bladder pump to generate a positive LVP. The remaining two solenoids (B and C) were used to evacuate the air around the bladder pump, decreasing ventricular pressure. The action of the solenoid valves was triggered by a computer controlled pulse generating system (TTL wave), which was also used to synchronize all data acquisition. Table 4-2 summarizes the timing used to cyclically compress the silicone bladder at a 70 beats per minute healthy adult (human) cardiac heart rate.

**Table 4-2 Timing and effect of air solenoid valves.**

Timing	Active Solenoids	Effect
0 – 220 ms	A	Bladder pump compressed, Positive LVP generated
220 – 820 ms	B and C	Bladder pump relaxes, Ventricular Diastole
820 – 860 ms	--	Mechanical Delay

In addition to controlling the timing of the pulsatile bladder pump, pressure regulators, and a lumped systemic resistance and compliance were used to tune the left heart simulator to adult physiological hemodynamics. The left heart simulator was tuned to 70 beats per minute heart rate (860 ms total cycle time, 530 ms diastole, 330 ms systole), 120 mmHg peak left ventricular pressure, and 5.0 L/min average cardiac output (70 mL stroke volume). Representative ensemble averaged (15 cardiac cycles) hemodynamic waveforms are shown in the Figure 4-5 below.

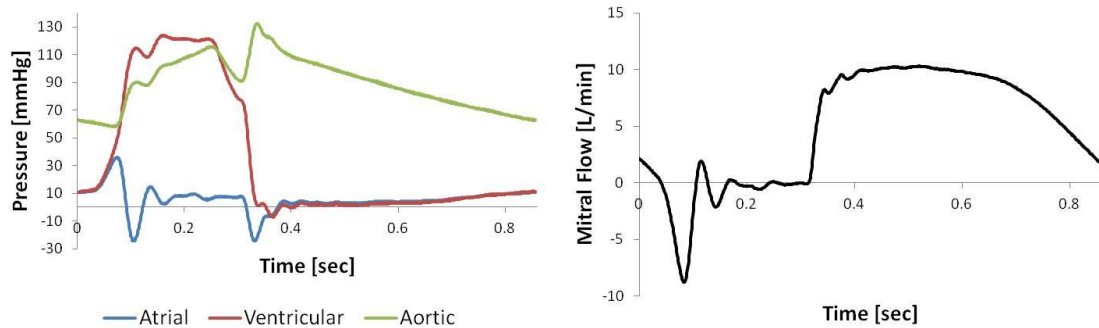


**Figure 4-5 Representative hemodynamic waveforms, ensemble average over 10 cardiac cycles, from the left heart simulator.**

Waveforms were monitored in real time using custom LabView Virtual Instruments (National Instruments Corp; Austin, TX). Pressures (TruWave Disposable Pressure Transducer; Edwards Lifesciences Corp; Irvine, CA) were acquired in the left atrium, left ventricle, and aortic root, while flow was acquired upstream of the mitral valve (In-Line Electromagnetic Flow Probe; Carolina Medical Electronics Inc.; East Bend, NC). Pressure transducers were coupled to Validyne Engineering Corp. (Northridge, CA) signal conditioners and strain gage amplifiers (SG297A) housed in an 8-channel module case (MC170-32). Electromagnetic flow probes were coupled to 500 Series flow meters (Carolina Medical Electronics Inc.). 10 cardiac cycles were acquired for off-line data analysis.

## **4.2 Echocardiography**

A Philips iE33 real-time 3D ultrasound imaging system (Philips Healthcare; Andover, MA) was used to evaluate valve performance. A 3D matrix array X7-2 pediatric transthoracic (TTE) probe was positioned on the left atrial window. Ultrasound gel was used to create a continuous air-free medium to transmit the acoustic waves.

Echocardiography was used to acquire: 2D and X-plane tissue and color Doppler, 3D tissue and color Doppler, and continuous wave (CW) Doppler. Image acquisition was gated using the common TTL trigger that synchronized all data acquisition. Images were transferred as .DICOM for offline analysis using Philips QLab software.

### 4.3 High Speed Imaging

A high speed imaging system was used to acquire en face imaging of the dynamically functioning mitral valve in the left heart simulator. The camera was positioned upstream of the left atrium, perpendicular to the mitral annulus. Images were acquired at 250 frames per second at 1280 x 1204 pixel resolution with a Basler a504k camera (Basler Vision Technologies, PA). The camera was outfitted with a 105 mm f/2.8D AF Micro-Nikkor lens (Nikon, USA). The camera was coupled to an EPIX high speed frame grabber (PIXCI CL3SD Frame Grabber; EPIX Inc.; USA). EPIX commercial software was used to acquire all images. Image acquisition was triggered using the common TTL waveform. Images were saved as .TIFF and processed offline.

### 4.4 Chordal Force Transducers

Strain gage based C-shaped transducers were used to measure the tension on individual chorda tendinae during dynamic valve testing (Figure 4-6). A C-shaped brass spring element (L x W x H x t: 6.5 x 2.0 x 5.0 x 0.5 mm) served as the parent geometry which sensed deformation. Two strain gages (EA-06-031DE-350; Vishay Measurements Group; Raleigh, NC) were attached to the inner and outer surfaces of the ring. These two gages were wired in a Wheatstone half-bridge configuration; the remaining half of the bridge was completed using a National Instruments cDAQ chassis (NI cDAQ-9174) with strain gauge modules (NI 9237). The transducers were coated using M-Bond 43 (Vishay Measurements Group) to maintain electrical stability during saline immersion. The transducers were sutured onto selected chordae; the portion of the chordae passing

between the measurement arms was bisected such that all chordal tensile loading was transferred to the brass spring element. Real time data monitoring and acquisition was performed using custom LabView Virtual Instruments. Data acquisition was synchronized using left ventricular pressure waveforms.

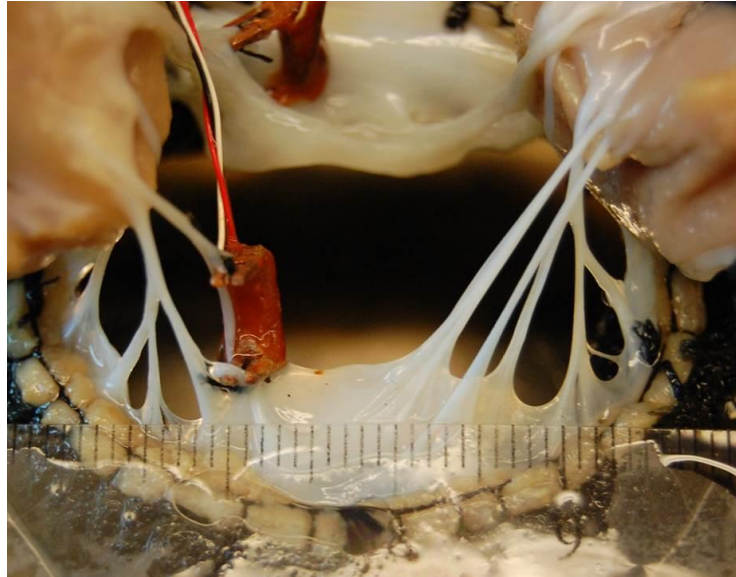


**Figure 4-6 Chordal force transducer sutured onto posterior leaflet secondary chordae. After securing the transducer, the chorea are bisected to transfer all load to the brass spring element (not shown).**

The sensitivity and linearity of individual transducers were tested prior to and after each experiment. The minimal measureable difference in tension for these transducers was 0.01 N. For all conditions tested, forces were baseline zeroed immediately preceding dynamic testing. Offline analysis was performed using custom MatLab (MathWorks; Natick, MA) scripts. Extensive information on c-ring design, manufacturing, calibration, and application can be found [187-189].

#### 4.5 Modified Left Heart Simulator

For the rigorous and comprehensive experimental validation of numerical mitral valve modeling (Specific Aim 3), design modifications were made to the existing left heart simulator to enable: (i) micro-computed tomography of the native mitral valve apparatus in its experimental configuration, (ii) stereoscopic particle image velocimetry of the native mitral flow fields, (iii) echocardiography (clinical imaging modality) of the dynamic mitral valve, (iv) carefully characterized boundary conditions, and (v) additional biomechanical evaluation of the mitral valve.

To meet these needs, the following key design constraints were identified: (i) micro-computed tomography field of view and bore size, (ii) uniform x-ray absorbance and scattering, (iii) minimal acoustic and optical distortions, and (iv) maintaining valvular geometry throughout complimentary experimental techniques.

The new modular design (Figure 4-7) allowed for complimentary experimental techniques to be performed on a singular mitral valve without perturbing the valvular configuration. The left heart consisted of a thin walled cylindrical (cross section  $\phi = 8.89$  cm) acrylic chamber ( $t = 6.35$  mm). A cylindrical design was preferred for use with the available micro-computed tomography system. With the VivaCT 40 system, the x-ray source and detector spiral around a fixed (or axially translating) sample. Any objects in the x-ray path, in this case, the left heart's walls, would affect the detected signal. Therefore, to ensure the absorbance was uniform, the chamber was cylindrical, and the valve was centrally mounted. The thin acrylic walls also minimized x-ray absorbance, as well as, optical distortions.



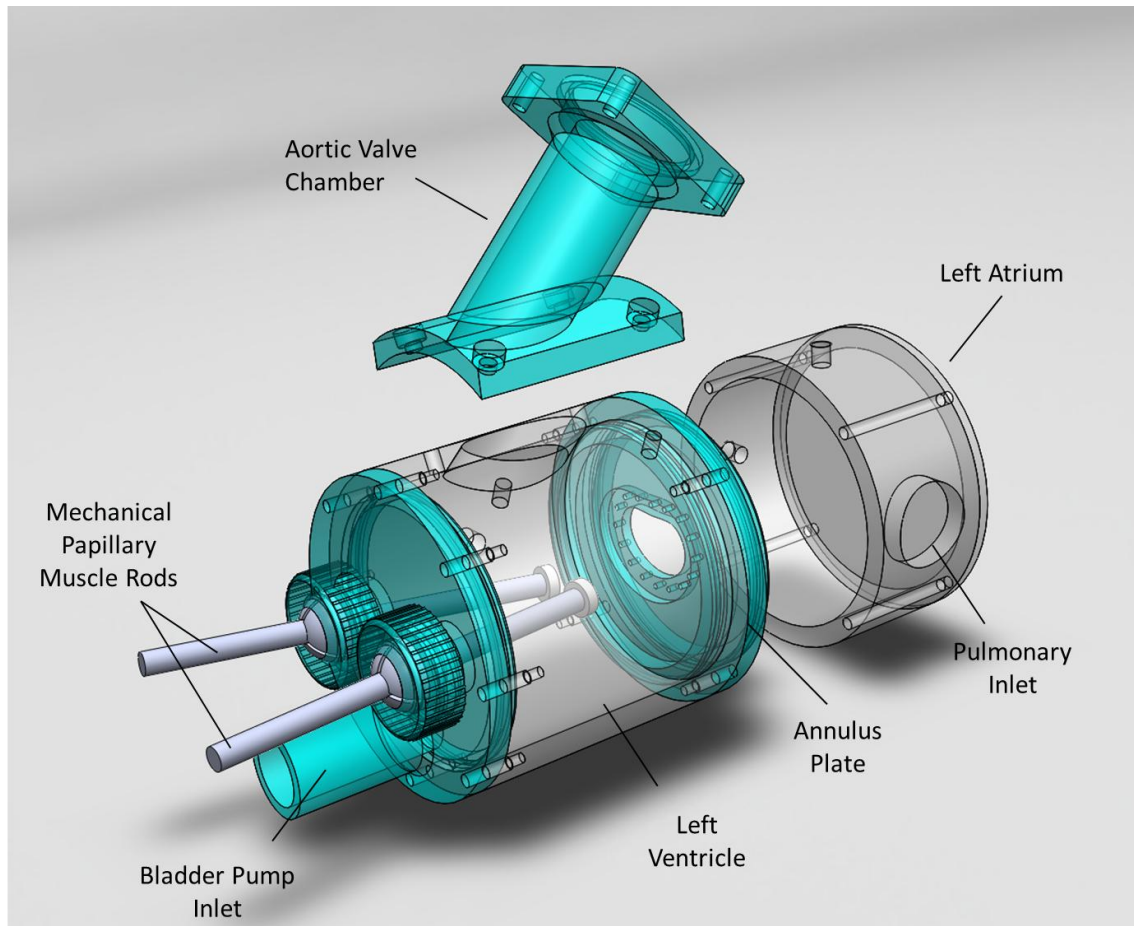


**Figure 4-7** A partially exploded view of the new modular left heart simulator is shown. The outflow tract with the aortic valve and the left atrium are removed for micro-computed tomography imaging.

En face imaging was possible through a thin, flat atrial (basal) wall. Stereoscopic particle image velocimetry was possible through the use of an outer rectangular chamber with inlets continuous with the left heart simulator. The outer chamber was filled with 36 % glycerin solution, which was the same working fluid used in the left heart simulator for particle image velocimetry. The combined effect of imaging through the flat side wall of the outer chamber and the use of the glycerin solution minimized optical distortions. Any

remaining mismatches in refractive indices were accounted for using a polynomial calibration mapping function in DaVis Imaging Software.

Two designs of the left atrial chamber were used; both employed a thin basal wall ( $t = 2.5$  mm). For particle image velocimetry, a direct flow inlet on the basal wall was employed. For all other experimental conditions, a side flow inlet was used. The ventricular chamber had a bladder pump inlet on its apical wall and a through-wall connection bracket for the mechanical papillary muscle positioning rods. An aortic flow outlet was machined into the left ventricle adjacent to the anterior mitral annulus. The outflow orifice was machined as a continuous projection of a 25.4 mm left ventricular outflow tract oriented at 135°. A removable left ventricular outflow tract and aortic valve chamber, which housed a 25 mm bi-leaflet mechanical heart valve (Medtronic Parallel; Minneapolis, MN) were designed.

A mitral annular plate was positioned between the atrium and ventricle. A D-shaped orifice was machined into the mitral annular plate with dimensions similar to a size 30 C-E Physio annuloplasty ring (see Table 4-1). The mitral annular orifice was centered on the annular plate. A silicon cloth ring was fixed to the mitral annular plate (as an analog for the Physio annuloplasty ring) onto which the native mitral annulus was sutured. The inner diameter of the silicon cloth ring aligned with the D-shape orifice. An additional mitral annular plate was fabricated to function as an analog for the highly saddle shaped Profile 3D annuloplasty ring. The core of this saddled ring was rapid prototyped out of ABS plastic, which was then covered in silicone and water proof cloth. The rapid prototyped geometry was created based on micro-computed tomography of a Profile 3D annuloplasty ring. This annulus plate did not utilize the spring and wire

drawstring construction as the metallic components effected the quality of the micro-computed tomography imaging acquisition.

The mechanical papillary muscle positioning rods were simplified (Figure 4-8); specifically the bulky modified 90° pin-gear drive system was replaced. The new papillary muscle position rods are simply a straight shaft with a papillary muscle attachment adapter at the end. The apical-basal, anterior-posterior, and septal-lateral positioning controls were moved to the apical plate of the left ventricle using a ball and socket joint. The ball and socket joint was designed as a mechanical collet. The papillary muscle shaft is passed through the slotted ball port design. To lock the position of the papillary muscle in place, the top is screwed down to tighten onto the ball, which in turn tightens onto the positioning rod. Rubber o-rings were used at all interfaces to create a leak-free seal and to increase the coefficient of friction between mates to prevent slippage. Accurate positioning can be obtained through simple trigonometry. The ball and socket joint was designed to achieve a ~30 degree maximum rotation. Based on the trigonometric relationships (25-30 mm shaft left distal to the ball and socket joint), a 14-17 mm maximum papillary muscle displacement in the septal-lateral or anterior-posterior directions can be attained. Apical-basal positioning is achieved by sliding the shaft into or out of the ball port.

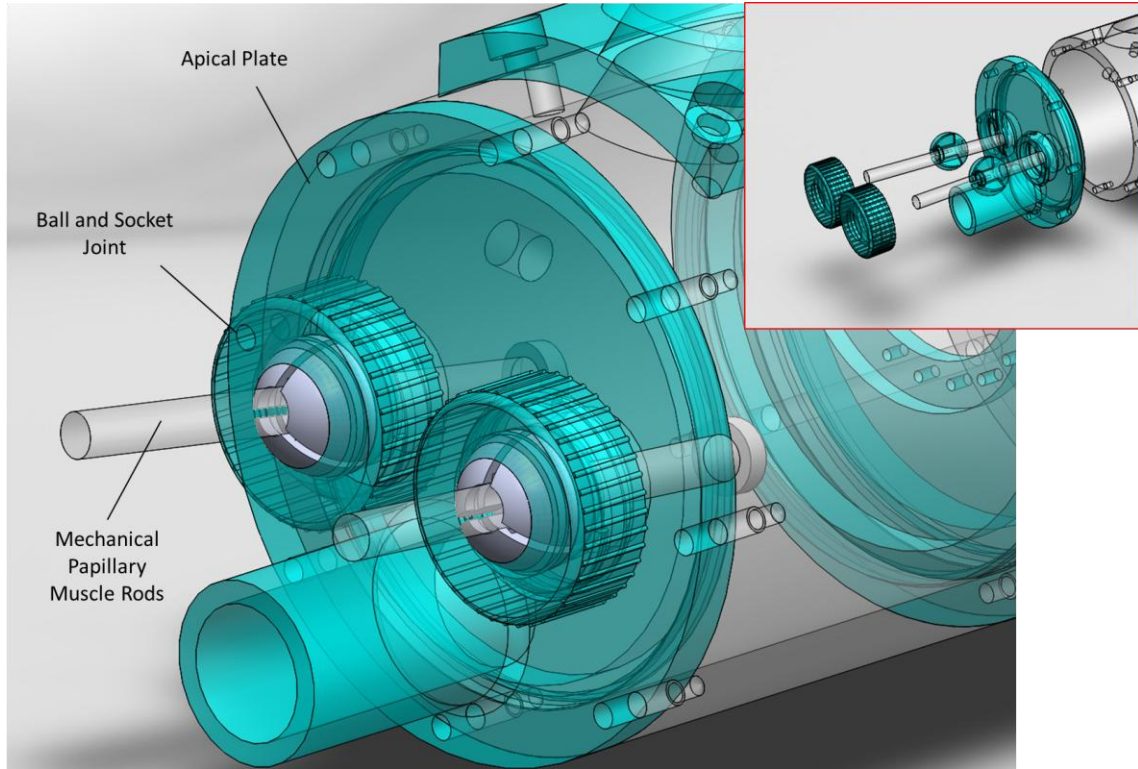


**Figure 4-8 Simplified papillary muscle positioning system uses a straight shaft rod with the native papillary muscle adapter at its end. The positioning mechanism was deferred to the ball and socket joint on the apical wall of the left ventricle. Inlay shows an exploded view of the ball and socket joint.**

#### 4.6 Particle Image Velocimetry

Stereoscopic digital Particle Image Velocimetry was performed to resolve the three components of velocity of the flow through and proximal to native mitral valves. Briefly, particle image velocimetry is a proven imaging technique which is able to acquire instantaneous measurements of velocity through a whole plane. A working fluid is seeded with neutrally buoyant 1- 20 micron size particles, which are illuminated by a high energy sheet of laser light. Two laser pulses separate by a short time ( $\Delta t$  chosen

based on expected particle displacement) are synchronized to high resolution CCD (charge coupled device) camera(s) to record paired images of the illuminated flow field. Statistical analysis (cross-correlation of the particles from each paired image) is used to calculate the average displacement and subsequent velocity within a subdivided region (interrogation window) of each image.

For these studies, a pair of 532 nm pulsed (9ns pulse duration) laser sources were used (Neodym:YAG, 17 mJ/pulse, ESI Inc.; Portland, OR). The laser beam was redirected and adapted with appropriate optics to create a laser sheet (~ 1 mm thickness) that bisected the mitral valve parallel to the septal-lateral long axis plane (Figure 4-9). The final mirror in the laser beam path (reflected the beam 90° upward into the chamber) was mounted on a traverse (Model # M1-102404; Lintech; Monrovia, CA) such that the target imaging plane could be accurately and incrementally displaced within the left heart (in the z-direction as denoted in Figure 4-9) to capture additional flow fields as needed.

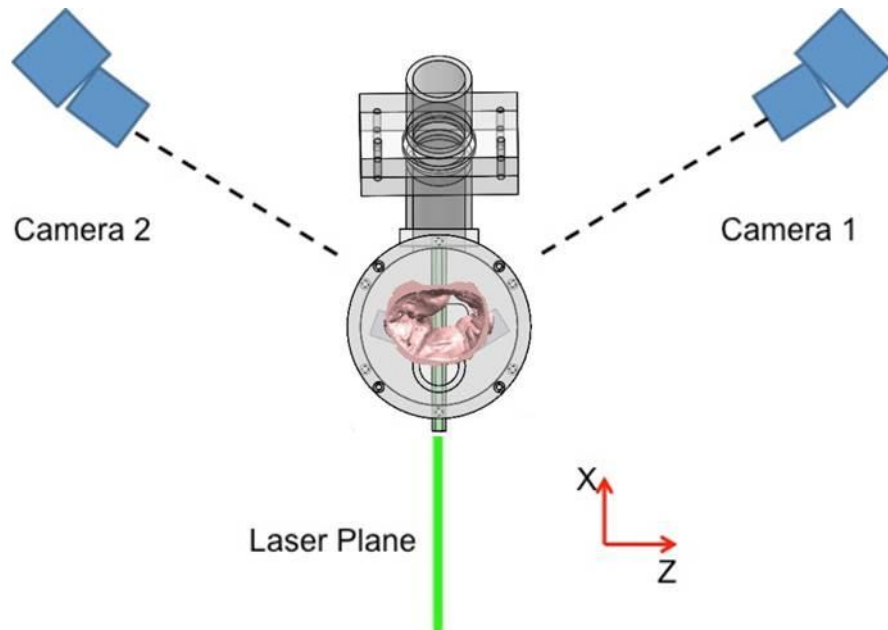


**Figure 4-9 Schematic representation of the stereo-photography and laser plane configurations.**

Two CCD cameras (Imager Pro, 1600 x 1200 pixels; LaVision GmbH; Goettingen, Germany) with a Nikon Micro-Nikkor 60 mm lens (Nikon Inc.; Melville, NY) were used for stereoscopic imaging. The cameras were mounted with Schiempflug adapters and an orange filter to eliminate reflected laser light (cut-off  $\lambda = 560$  nm; Hoya Optics, Santa Clara, CA). The Schiempflug adapters ensured the particles in the field of view were in focus when imaged at an angle. Neutrally buoyant polymethyl methacrylate (PMMA) fluorescent seeding particles (with Rhodium-B dye, 1-20  $\mu\text{m}$ , 580 nm emission; Dantec Dynamics, Denmark) were suspended in the working fluid. The CCD resolution was 16.6  $\mu\text{m}/\text{pixel}$  with particles sizes of 2-3 pixels. The field of view was 50 x 50 mm, which consisted of the flow region immediately down-stream and proximal to the mitral valve. 36% glycerin in water was used to match the kinematic viscosity of blood (3.5 cSt) and to minimize distortion errors from mismatching refractive indices. The

refractive index of the working fluid was 1.38, compared to 1.49 of the acrylic; this was corrected through calibration. For stereoscopic image calibration, a three-dimensional two-leveled target was used (Figure 4-10). The calibration target was 1 mm thick transparent acrylic with 1.5 mm laser printed markers aligned in a 5 mm x 5 mm grid on either side (dimensions L x W: 100 mm x 100mm ). PIV data acquisition was synchronized using the common TTL trigger. Data were processed off-line using DaVis 7.2 and custom MATLAB scripts; data were visualized using TecPlot (Bellevue, WA). For data acquired in the left atrium, a single camera arranged orthogonal to the laser plane was sufficient, as there were no obstructions to imaging (as compared to the papillary muscles and chordae tendinae).

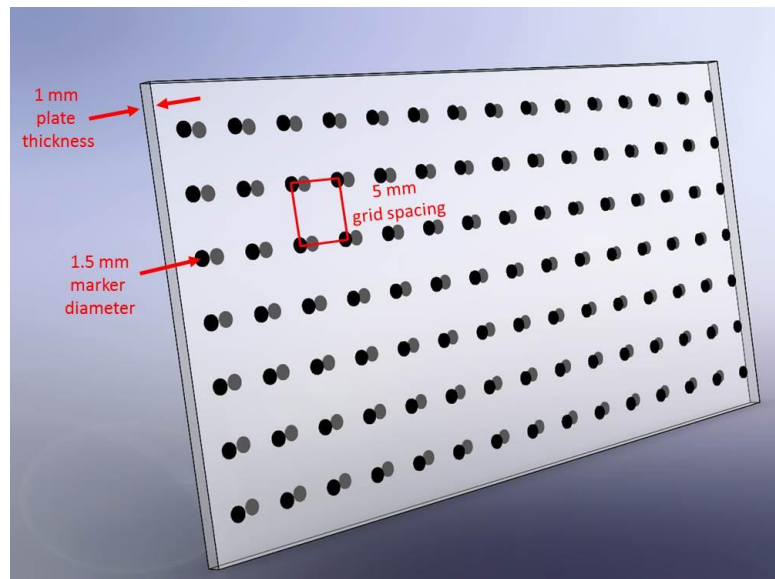


**Figure 4-10 Schematic representation of calibration target.**

#### 4.7 Micro-Computed Tomography

Micro-computed tomography ( $\mu$ CT) imaging of the entire mitral valve apparatus was performed using a VivaCT 40 system (Scanco Medical AG; Brüttisellen, Switzerland). The VivaCT 40 was an *in vivo* small animal live specimen scanner with a 90 mm diameter x 500 mm length bore size. This system provided a max scan field of view of 38.9 mm diameter x 145 mm length. At that diameter, 38.9  $\mu\text{m}^3$  isotropic voxel resolution was achieved. The system used a single x-ray source and detector, which spiraled around a stationary specimen. To capture a volume, the specimen was secured to a mechanical gantry, and linearly translated to expose new sections of volume for imaging.

The modified left heart simulator was mounted to the  $\mu$ CT gantry using a custom fabricated adaptor plate. The adaptor plate secured to the apical wall of the left ventricle. The adaptor did not interfere with the mechanical papillary muscle positioning rods nor the left ventricular pressure inlet.

When applicable, a flexible duct hose was connected to the left ventricular pressure inlet, snaked through the custom adaptor plate, and out of the  $\mu$ CT bore through an access port. The distal end of the flexible duct tubing was connected to a continuous compressed air pump. This system provided a constant 30 mmHg left ventricular pressure.



## 4.8 Instrument Calibration

### 4.8.1 Flow Probe Calibration

Flow probe calibration was performed regularly using a simple steady flow close circuit. The circuit consisted of a centrifugal pump, an in-line electromagnetic flow probe, and sink/source reservoir. The flow output of the pump was controlled by a rotary transformer. Calibration was performed in increments (5 L/min) over a range of flow rates: 5 L/min to 30 L/min. Voltage output from the flow meter was monitored in real time using a voltmeter. At each flow rate, volume collected in a reservoir for specified time duration was recorded. Simultaneously, voltage output from the flow meter was recorded. Calibration was typically repeated three times. Separate flow calibrations were performed for saline and glycerin working fluids. Flow rates were plotted versus voltage output (Figure 4-11); linear regressions were fit to the data. Typical coefficients of regressions showed a strong correlation ( $R^2 = 0.97 - 1.0$ ).

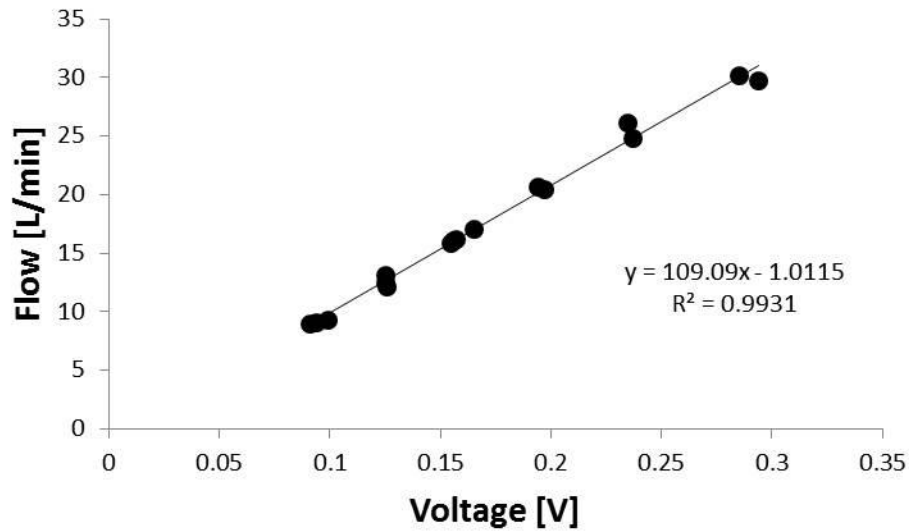


**Figure 4-11 Representative flow probe calibration.**

#### **4.8.2 Pressure Calibration**

Pressure calibration was performed using a Utah Medical Delta-Cal system (650-950; Utah Medical; Midvale, UT). The Delta-Cal system is capable of simulating pressure to  $\pm 350$  mmHg. A range of 0 to 140 mmHg in 15 mmHg increments was used for calibration; calibration was repeated three times. At each pressure value, a voltage output was recorded. Pressures were plotted versus voltage output (Figure 4-12); linear regressions were fit to the data. Typical coefficients of regressions showed a strong correlation ( $R^2 = 0.98 - 1.0$ ).

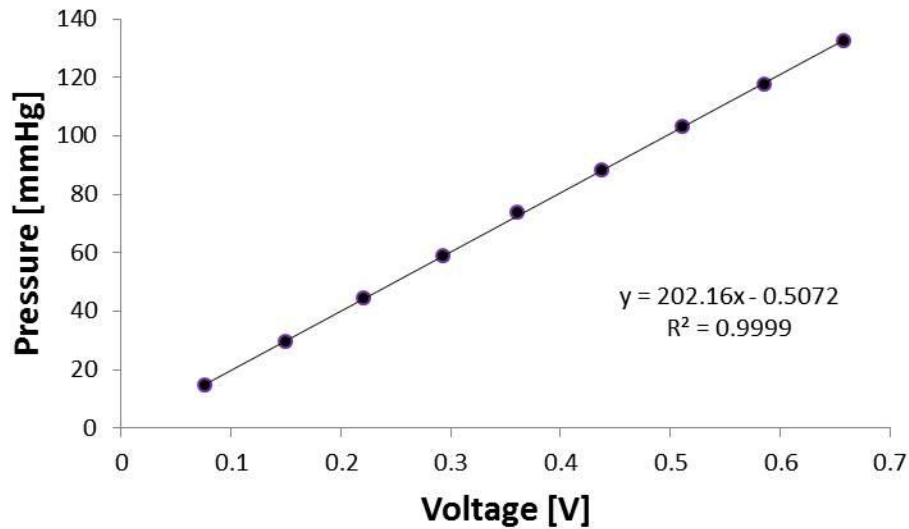


**Figure 4-12 Representative pressure calibration.**

#### **4.8.3 Viscosity Calibration**

Viscosity of the 36 % water glycerin solution was measured using a Cannon-Fenske size 50 glass viscometer (Dakota Instruments; Monsey, NY). The water glycerin solution was titrated to yield a kinematic viscosity similar to blood ( $3.5 \pm 0.02$  cSt). Viscosity measurements were repeated three times.

#### **4.8.4 Papillary Muscle and Chordal Force Transducer Calibration**

Papillary muscle and chordal force transducers were calibrated using a similar technique: known weights were suspended from the transducers and resultant voltage output was noted. The papillary muscle force transducers were affixed at their base using a table clamp. To isolate each directional component of force, the orientation of the affixed transducers was changed between calibrations. To calibrate for pure tension, the known load was applied along the central axis of the transducer. The two out of plane bending

directions were calibrated by applying a load perpendicular to the central axis of the transducer. One end of each arm of the c-ring chordal force transducers was suspended from a ring stand using 2-0 prolene sutures. From the other end, loads were incrementally applied over a select range. The papillary muscle force transducers were calibrated over of 0.1 to 10 N in the axial direction. The bending directions were calibrated over a range of 0.1 to 5 N. A lower range was applied in this direction because the resultant deformations would otherwise exceed the operating limits of the strain gauges. Similarly, chordal force transducers were calibrated over a range of 0.05 to 5 N. This is within the range of expected chordal forces.

## CHAPTER 5

### EXPERIMENTAL METHODS AND PROTOCOLS

#### 5.1 Common Experimental Techniques

##### 5.1.1 Mitral Valves Excision

Fresh ovine explanted hearts were procured from a local abattoir; ovine hearts are structurally and functionally very similar to the human heart [184,185]. The mitral valves were sized using standard techniques: Carpentier-Edwards Physio annuloplasty ring sizer measured to the ovine mitral anterior leaflet (Figure 5-1). Size 30 valves were selected for the studies herein. Only valves with Type I or Type II papillary muscles were included in the studies. Other types were difficult to mount to the left heart simulator due to their diffuse or multiple head geometry. Valves were excluded if their chordae did not have a clear delineation into marginal, basal, and strut groupings.

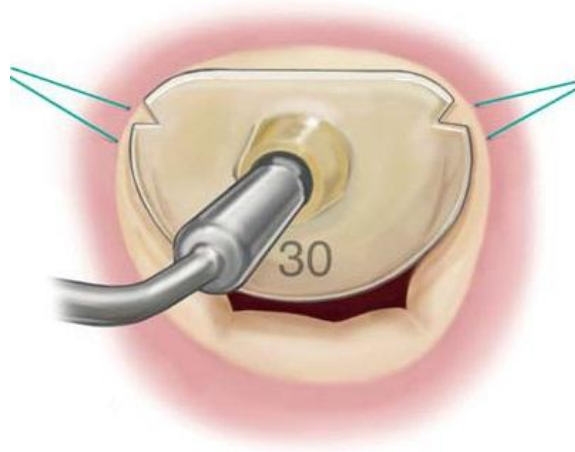


**Figure 5-1 Mitral valve sizing is performed with a C-E Physio annuloplasty ring sizer measured to the anterior leaflet. (Image adapted from Carpentier's Reconstructive Valve Surgery)**

Ovine mitral valves were excised using techniques previously described [34,35,39]. In short, an incision was made through the aortic valve and down the left anterior descending coronary artery (through the thickness of the myocardium). This exposed the subvalvular apparatus for inspection. The entire valve apparatus was preserved and removed from the left ventricle and stored in 0.9% physiological saline for later use. 1-2 mm of supra-annular and 10-15 mm of papillary muscle tissue were preserved for mounting to the left heart simulator (Figure 5-2).

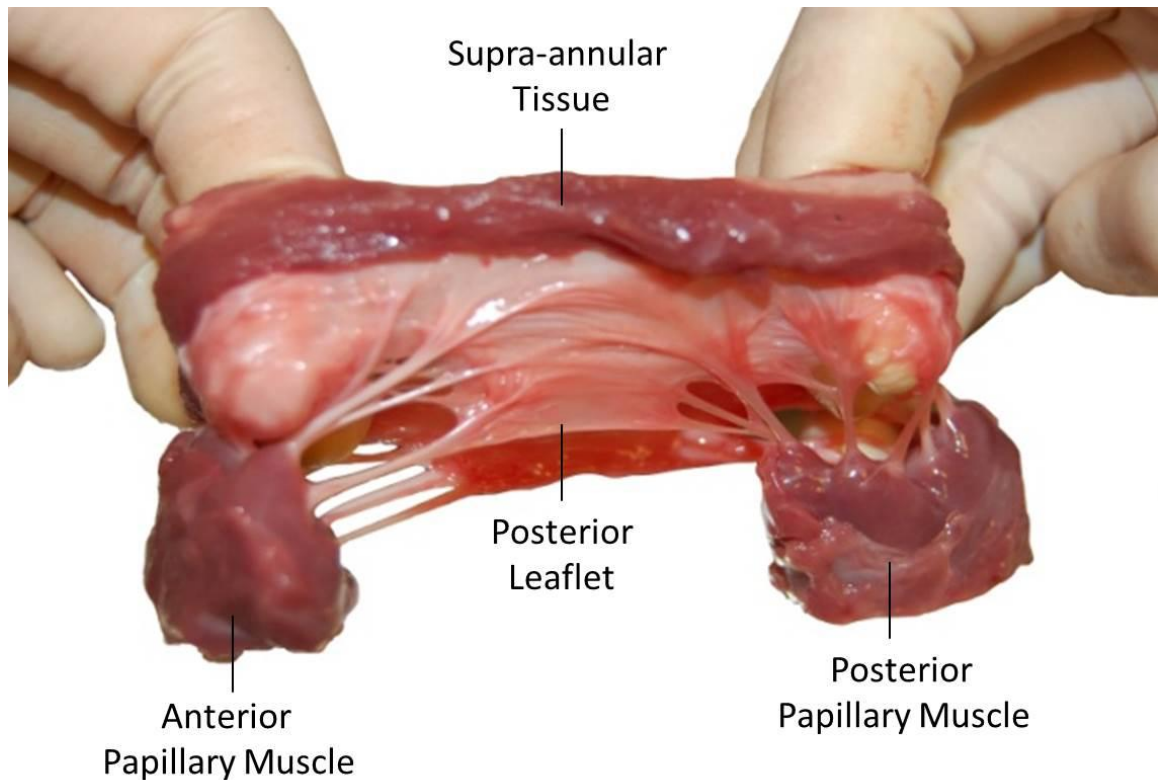


**Figure 5-2 Excised mitral valve apparatus.**

### **5.1.2 Mitral Valve Preparation**

Excised mitral valves were mounted to the left heart simulator at the annulus and the papillary muscles. The native mitral annulus was sutured to the adjustable mechanical annulus in a two-step process. First, the native annulus was positioned using eight interrupted knot sutures carefully placed 1-2 mm above the leaflets' natural hinge. These were positioned in the following order:

1. Left fibrous trigone
2. Right fibrous trigone
3. Center of the anterior annulus
4. Posterior annulus at P1

5. Posterior annulus at P3
6. Posterior annulus at P2
7. Anterior commissure
8. Posterior commissure

These locations of the native annulus were sutured to their corresponding location on the mechanical adjustable annulus (Figure 5-3). Care was taken to respect normal annular geometrical relationships: (i) intertrigonal distance, (ii) anterior leaflet occupying one third of the annular circumference, and (iii) the anterior and posterior commissures aligned at the 10 and 2 o'clock positions respectively. A Ford interlocking stitch was run from the left fibrous trigone, clockwise around the mitral annulus to create a tight seal between the native annulus and the mechanical adjustable annulus.

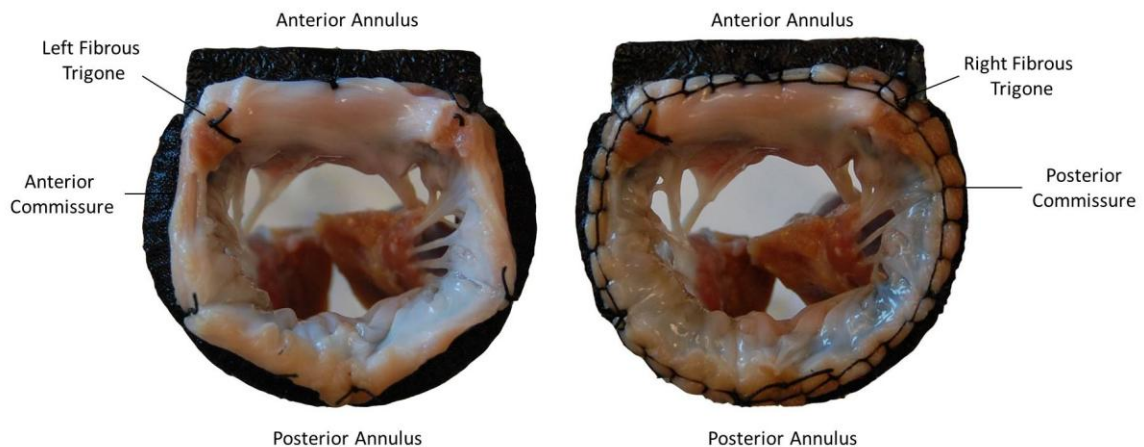


**Figure 5-3 Left: Interrupted knots strategically placed to position the mitral annulus. Right: Continuous Ford interlocking stitch secures the native mitral annulus to the silicon annulus.**

After the annulus was secured, the papillary muscles were wrapped in Dacron cloth to prevent tearing. The cloth covered 3-5 sides of the papillary muscles, only



leaving the tips and chordal insertions exposed. Care was taken to ensure the cloth did not interfere with chordal function, i.e., the cloth and sutures were positioned away from the chordal insertion sites. A Teflon connector with 2-56 stainless steel screw was sutured to the distal end of each papillary muscle for mounting in the left heart simulator (Figure 5-4).

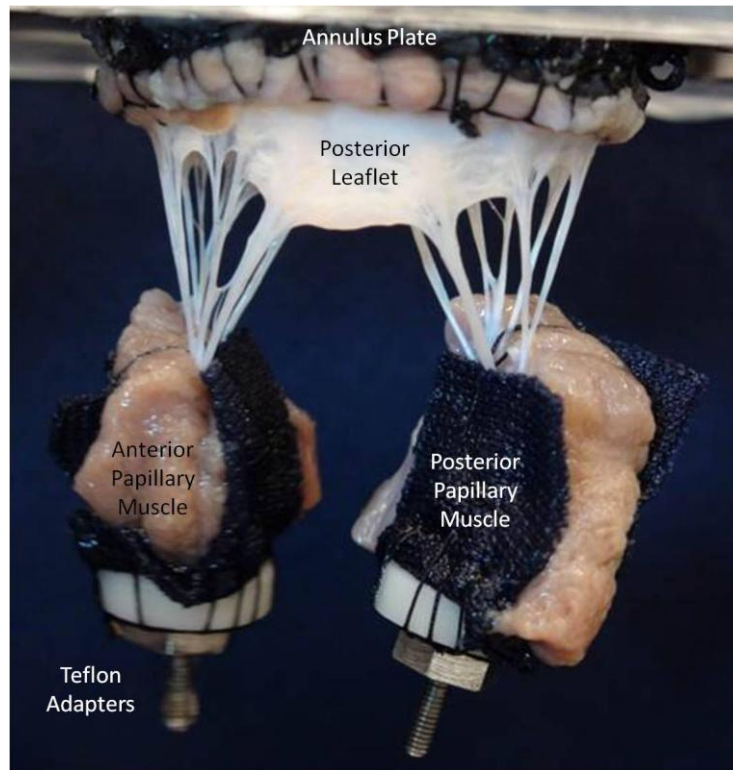


**Figure 5-4 Mitral valve mounted onto annulus plate.**

### **5.1.3 Establishing a Control**

Next, the valve was mounted into the left heart simulator and normal mitral annular and papillary muscle configurations were established as described below. The tension on the wire drawstring was adjusted such that the mitral annulus achieved its

control size; this corresponded to a size 30 Physio annuloplasty ring. Annulus size was confirmed by taking a short axis echocardiography slice along the mitral annular plane. The annular area was measured with the ultrasound caliper tool; for control, this was ~ 4.40 cm<sup>2</sup>.

Once the annulus control was established, the papillary muscles were set to their normal physiological position, as previously described [35]:

1. Lateral: The papillary muscles were arranged parallel to each other and with the chordal insertion points directly positioned behind their respective commissure. The commissural chords should insert perpendicularly to the annular plane.
2. Septal-lateral: The papillary muscles were moved septal-laterally until an even extension of the commissural chords inserting into the annulus was observed.
3. Apical-basal: The papillary muscles were adjusted apical-basally until a balance was observed in chordal tension. No slack should be observed, and the chords should be under minimal tension.

Minor adjustments were made to the papillary muscles positions under dynamic valvular evaluation (70 bpm heart rate, 120 mmHg peak LVP, 5.0 L/min average cardiac output) to ensure normal leaflet closing characteristics were observed, mainly: (i) the anterior leaflet spanned approximately two-thirds of the mitral orifice, (ii) adequate coaptation length (5 – 6 mm) along the central long-axis plane (A2P2), and (iii) minimal tenting (height < 1 mm) (Figure 5-5), and (iv) minimal mitral regurgitation (< 10 mL, no observable jets). More detail of how these measurements were taken can be found in sections 5.2.1.3.

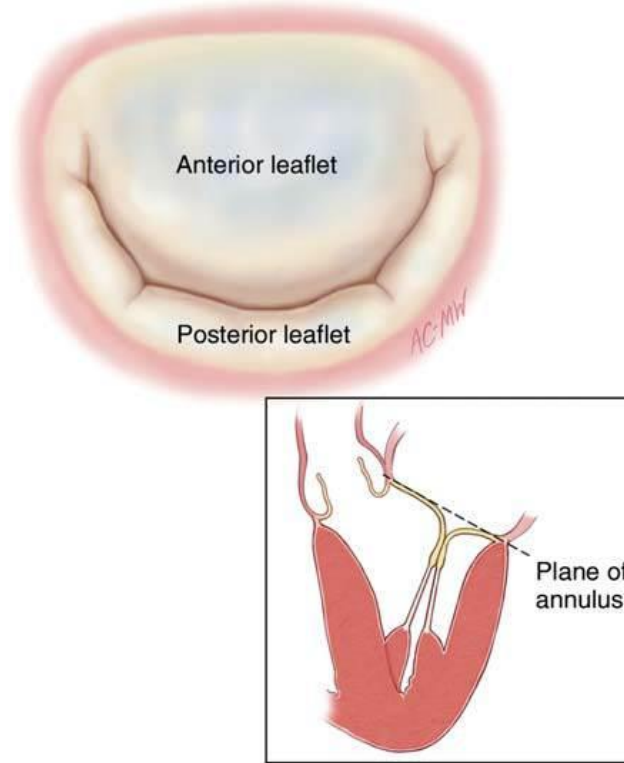


**Figure 5-5 An en-face view of the normal mitral valve closure. Inlay: Apical-basal long axis view of normal mitral valve closure. (Images adapted from Carpentier's Reconstructive Valve Surgery.)**

## 5.2 Specific Aim 1 – Accurate Quantification of Mitral Regurgitation

The objective of this study was to evaluate the accuracy of clinical techniques to quantify mitral regurgitation in a pulsatile left heart simulator using native ovine mitral valves. Direct flow (Gold Standard) measurements were compared to 2D PISA, Integrative 3D PISA, and Philips 3D FOM analyses. Data were further subdivided based on orifice type (round or slit) and mitral regurgitant grade (mild, moderate, or severe) to identify problematic patient subsets.

### 5.2.1 Experimental Protocol

Size 30 native ovine mitral valves were mounted into the left heart simulator with an adjustable annulus plate and mechanical papillary muscle positioning rods. A calibrated in-line electromagnetic flow probe was positioned upstream of the mitral valve. Normal, or control, mitral valve function was established using the previously described methods. Mitral insufficiency was created by selective adjustment of the mitral annular circumference and papillary muscle positioning. Combinations of mitral annular dilation, anterolateral and/or posteromedial papillary muscle displacement were performed as necessary to achieve round and slit orifices as determined from direct visual observation and high speed imaging (Figure 5-6). Each experiment (one valve) contained 4-6 orifices. Additionally, mild, moderate, and severe mitral regurgitation were targeted (MR range: 10 – 70 mL/beat); regurgitation was monitored in real-time. For a given orifice, baseline mitral regurgitation was varied by adjusting peak left ventricular pressure and downstream aortic/systemic resistance. Typically, this was performed to provide 3-4 regurgitant volumes for a given geometric condition (baseline MR  $\pm$  15 mL). In summation, each experiment provided 10-15 analogs of patient data. This was performed using empirical observations of the regurgitant orifices and flow rates in real time.

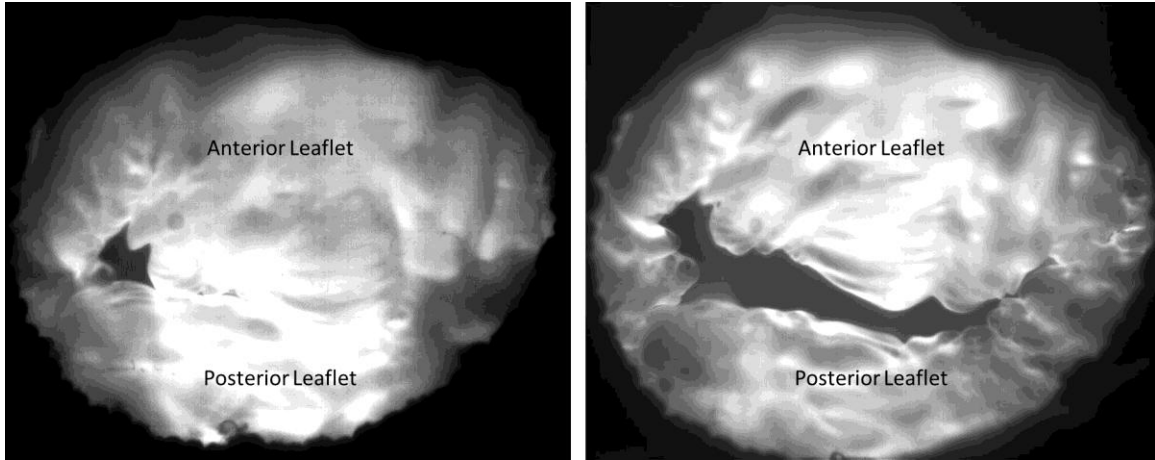


**Figure 5-6 Left: “Round” regurgitant mitral orifice. Right: “Slit’ regurgitant mitral orifice”**

0.9% saline (speed of sound: 1502 m/s) was used as the working fluid and blood analog. En face high speed imaging (250 fps) was performed to capture each orifice’s geometry. After high-speed imaging, corn starch (1% by total volume) was added to the working fluid as a suspended particulate to enhance color Doppler signal. An x7-2 TTE probe was mounted on a traverse (1 mm linear translation) and positioned onto the basal left atrial wall. The traverse was used to position the apical-basal long axis slice to best capture the largest regurgitant radius in the 2D plane (Figure 5-7). 2D, X-plane, and 3D tissue and color Doppler echocardiography, as well as continuous wave (CW) were acquired for all conditions. After ultrasound data were acquired, the flow loop was drained, and clean saline working fluid was added. This step was necessary as cornstarch the cornstarch mixture was opaque, rendering visual observation impossible. A new orifice was produced and the experimental protocol repeated.

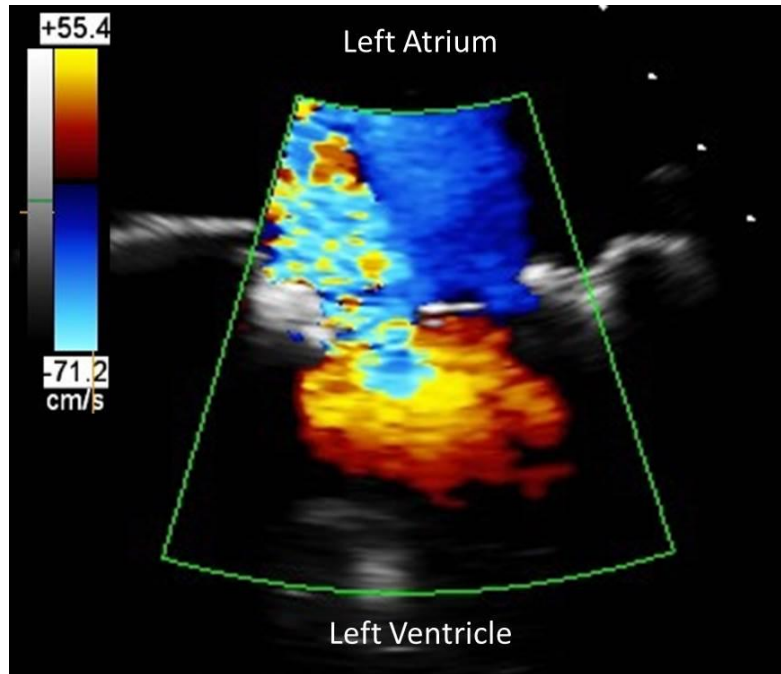


**Figure 5-7 2D apical-basal long axis echocardiography shows a large regurgitant jet and proximal isovelocity surface area.**

All baseline conditions were performed at 70 bpm heart rate, 120 mmHg peak LVP, and 5.0 L/min average cardiac output. Hemodynamic data acquisition, high-speed imaging, and echocardiography were synchronously triggered by a central mock QRS signal (TTL wave).

### 5.2.2 Data Analysis

Ten cardiac cycles of direct flow data were ensemble averaged. Mitral regurgitation was quantified by integrating the reverse (negative flow) during the regurgitant portion of the cardiac cycle; closing volume was excluded from this measurement (Figure 5-8). Closing volume was denoted between the first zero crossing following end diastole and the next local maxima. Regurgitation was quantified by integrating flow this local maximum to the next zero crossing at end systole.

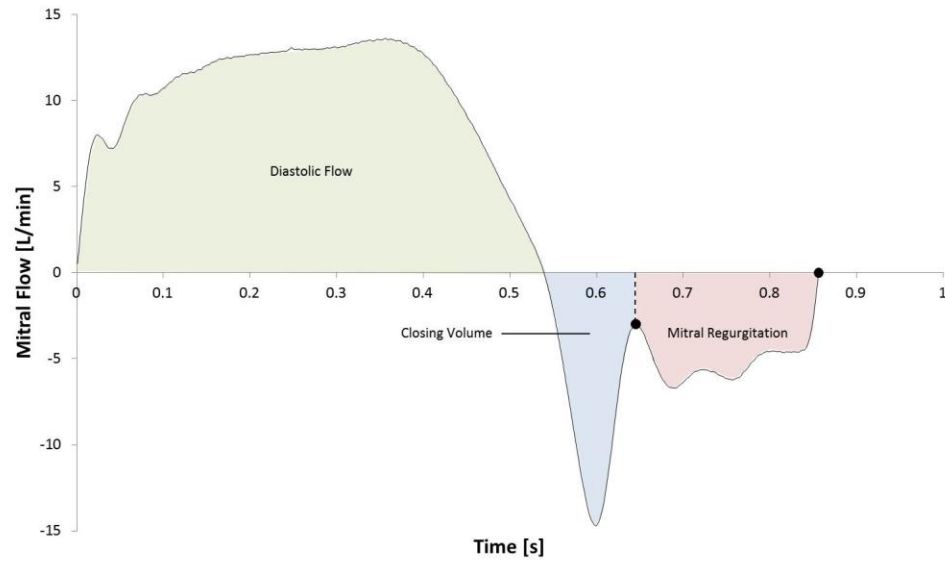


**Figure 5-8** A representative mitral flow waveform shows. Mitral regurgitation is calculated by integrating over the late systolic portion of the flow curve.

Philips Qlab was used for 2D PISA analysis, which was performed in three main steps for a given experimental condition: (i) the PISA shell was identified, and a shell radius for a given aliasing velocity was measured, (ii) the velocity time integral (VTI) was measured from the CW data, and (iii) regurgitant volume was calculated based on PISA assumptions and conservation of mass principle.

1. The frame with the largest PISA shell is identified in the apical-basal long-axis 2D color Doppler sequence.
2. Aliasing velocity is adjusted (typically ~ 40 cm/s) to achieve a clearly delineated corresponding thin shell (Figure 5-9).
3. The radius of the aliasing velocity shell is measured.
4. The velocity time integral is measured from the corresponding continuous wave (CW) echocardiography data (Figure 5-10).

5. Mitral regurgitant volume was calculated as follows:

$$EROA = \frac{2\pi r^2 \times V_{alias}}{V_{max}} \quad (\text{Equation 1})$$

$$MR_{VOL} = EROA \times VTI \quad (\text{Equation 2})$$

EROA = Effective Regurgitant Orifice Area

MR<sub>VOL</sub> = Mitral Regurgitant Volume

r = PISA Shell Radius for Selected V<sub>alias</sub>

V<sub>alias</sub> = Aliasing Velocity

V<sub>max</sub> = Maximum Velocity

VTI = Velocity Time Integral

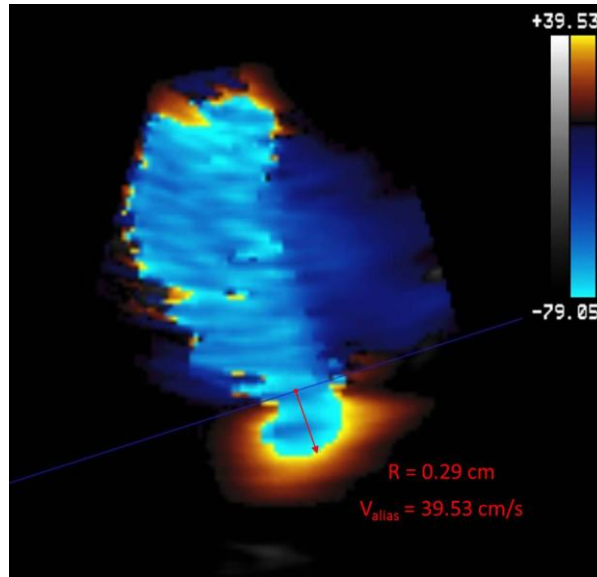
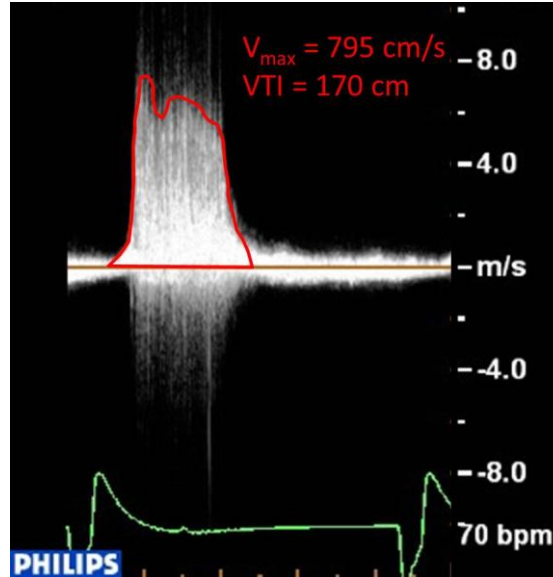


Figure 5-9 PISA radius and V<sub>alias</sub> are determined.





**Figure 5-10 Vmax and VTI are measured from continuous wave echocardiography.**

A second analysis technique was performed to improve on the 2D PISA method. In this integrative 3D PISA method, the assumption of a hemispherical regurgitant proximal isovelocity surface area was not used. The actual isovelocity surface area was manually traced in several slices to reconstruct the true geometry. This was performed through the following steps:

1. The frame with the largest PISA shell is identified in the apical-basal long axis 2D color Doppler sequence.
2. Aliasing velocity was adjusted to achieve a clearly delineated corresponding thin shell.
3. Using the “ginput( )” MATLAB function, points along the PISA shell were manually selected in the apical basal long axis slice (Figure 5-11 and 5-12).
4. Step 3 was repeated until the entire regurgitant jet was segmented (3 mm slice spacing, approximately 9 slices).

5. Point clouds were calibrated using lines of known distances drawn in Qlab using the caliper tool (0.217 mm/pixel).
6. Point clouds were imported into Geomagic Studio, where a triangulated surface mesh was fit to the data (Figure 5-12).
7. Erroneous facets were removed, and any holes in the mesh were filled. Light smoothing was applied to remove sharp peaks.
8. Surface area was computed using built in tools.
9. Regurgitant volume was calculated using equations 1 and 2 above.  $2\pi r^2$  was replaced with the true area measured in step 8.

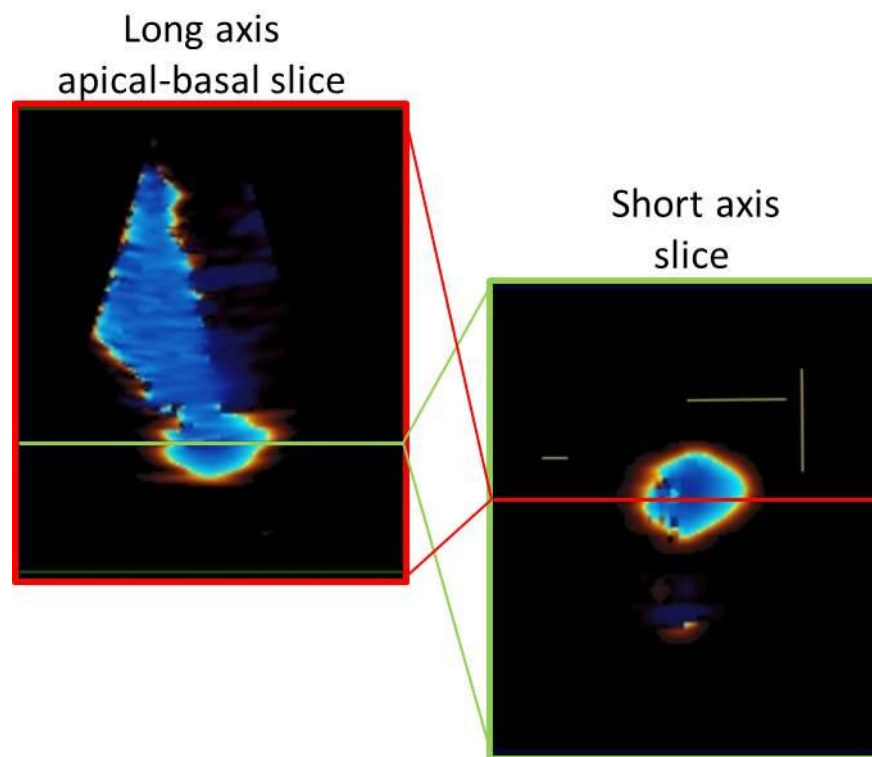


**Figure 5-11** Representative long (left) and short (right) axis slices of the regurgitant jet. The short axis slice was used to position the long-axis slices, from which the PISA shell was manually segmented.

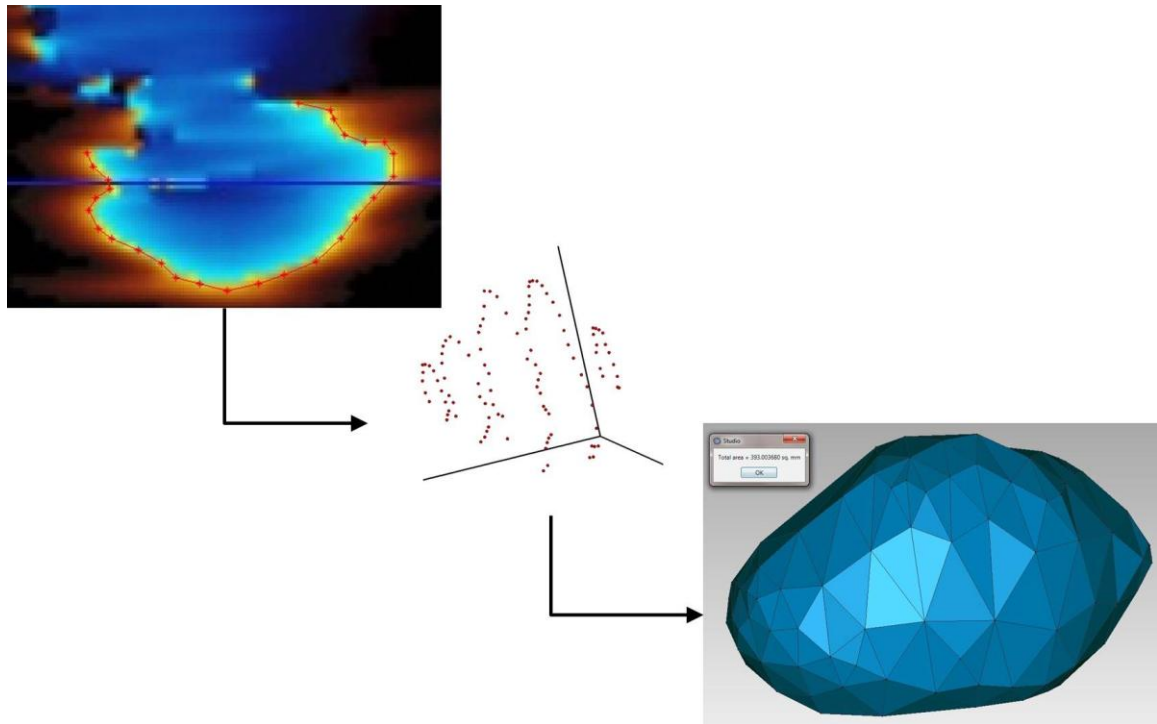


**Figure 5-12 Points along the PISA for a given aliasing velocity were manually selected. A surface mesh was fit to the resulting point cloud using Geomagic Studio. Total surface of the mesh was computed to provide the effective regurgitant area.**

A third analysis technique was performed using Philips Qflow software to quantify mitral regurgitation through the 3D Field Optimization Method (FOM). The FOM was limited to the portion of the cardiac cycle where a distinct PISA shell was observed (typically 4-5 frames). The analysis was initiated in the frame where the PISA shell was largest. The four quadrant view was optimized to best display the regurgitant jet. The “Flow Only” setting was applied (Figure 5-13). The regurgitant orifice origin was selected and the regurgitant volume was calculated using the automated FOM method. To better identify the regurgitant orifice, the color data could be turned off, using the “color suppress” toggle. A second analysis was performed using the “Flow Only” setting with the “Enable Adjust Orifice and Flow Band” setting. A final analysis was performed

using the “Flow + Z” setting with the “Enable Adjust Orifice and Flow Band” enabled. More detail on the different preferences is found in Chapter 6.

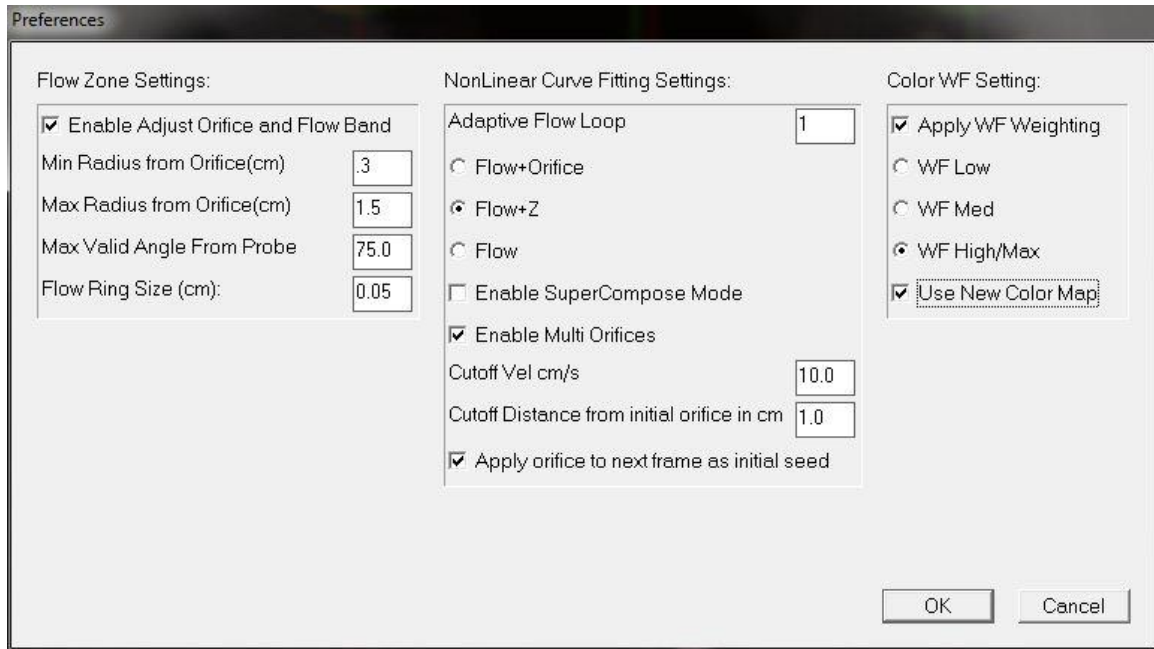


**Figure 5-13** Screen capture of the QFlow preferences. “Flow” and “Flow + Z” analysis were performed with and without the “Enable Adjust Orifice and Flow Band” options.

Intra-user variability was assessed for both 2D PISA and 3D FOM. A single expert user trained with a subset of data to refine their technique. User was blinded to true regurgitant volumes to avoid measurement bias. Measurements were repeated five times.

Mitral regurgitation quantified from 2D PISA, 3D PISA, and 3D FOM were plotted against direct flow measurements. Linear regressions were fit to the data. A 1:1 agreement line was overlaid on the data. Data were grouped with all possible combinations of orifice type and MR grade.

## **5.3 Specific Aim 2 – Evaluating the Efficacy of Surgical Repair for Ischemic Mitral Regurgitation**

### **5.3.1 Papillary Muscle Relocation**

The objective of this study was to evaluate the efficacy of basal papillary muscle relocation as a targeted surgical therapy for ischemic mitral regurgitation. The study intended to elucidate two key sources of procedural ambiguity: (i) what location of the mitral annulus is best for traction suture placement, and (ii) by how much does a papillary muscle need to be relocated to restore normal valvular function

#### 5.3.1.2 Experimental Protocol

The experimental protocol was performed in five main steps:

1. Control
2. Acute Myocardial Infarction (MI) - ischemic mitral valve dysfunction
3. Mitral Annuloplasty (Acute MI with MA)
4. Progression of mitral valve dysfunction (Chronic MI with MA)
5. Basal papillary muscle relocation with true sized mitral annuloplasty

The control condition was established as previously described. For all conditions, the left heart simulator was tune to 70 bpm, 120 mmHg peak left ventricular pressure, and 5.0 L/min average cardiac output. Ischemic mitral valve dysfunction was simulated with combined mitral annular dilation and papillary muscle displacement to achieve Carpentier type IIIb restricted leaflet motion. The mitral annulus was dilated to 180% of its normal area. The papillary muscles were symmetrically displaced 5 mm in the apical, posterior, and lateral directions. This was the acute myocardial infarction (Acute MI)

condition. Next, annuloplasty repair was simulated by returning the annulus back to its normal size, while the papillary muscles remained displaced (Acute MI with MA). Subsequently, further left ventricular dilation post mitral annuloplasty was simulated by displacing the papillary muscles an additional 3 mm in the posterior and lateral directions (Chronic MI with MA). The papillary muscles were displaced to mimic the effect of progressive left ventricular geometric changes on the mitral leaflets following surgical repair [44,45,47,180].

Papillary muscle relocation was performed as an adjunct to mitral annuloplasty to relieve mitral leaflet tethering. The papillary muscles were relocated toward either the ipsilateral commissure or trigone, representing two variants of possible annular suture anchors (Figure 5-14). Four targeted repair strategies were performed in conjunction with the simulated true-sized mitral annuloplasty: (i) both PMs were relocated toward their respective commissures, (ii) both PMs were relocated toward their respective trigones, (iii) the posteromedial PM was relocated toward its ipsilateral commissure, and (iv) the posteromedial PM was relocated toward its ipsilateral trigone. Repairs were performed in 2 mm increments. Mathematical unit vectors were calculated from the chronic MI papillary muscle positions to each annular anchor (see Appendix for further details) (Figure 5-15). These vectors were resolved into their apical, posterior, and lateral components to define the corrective displacements for each targeted repair. After each repair, the papillary muscles were returned to their pathological (progressive left ventricular dilation) position.

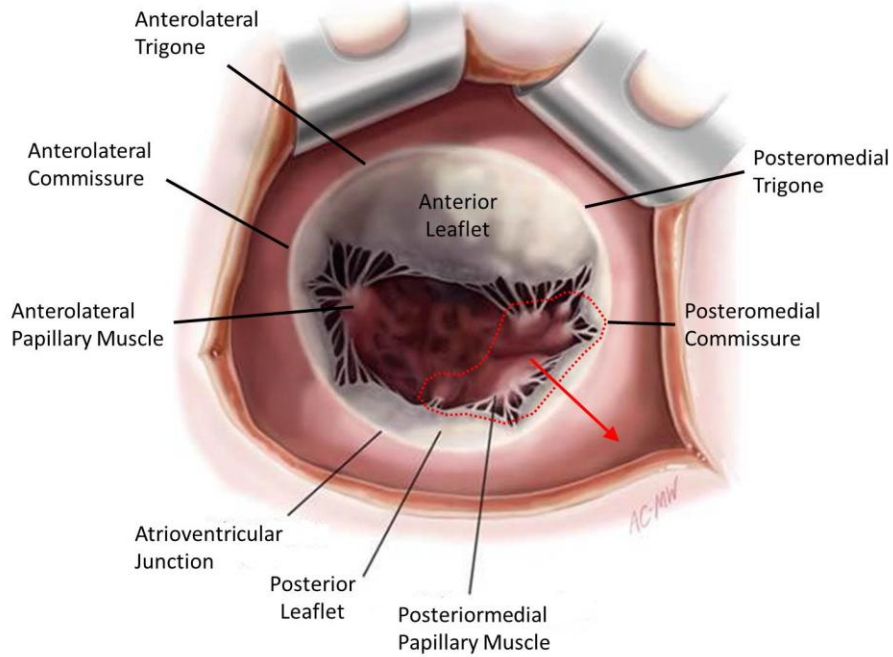


**Figure 5-14 Annular landmarks depict targets for traction suture. Highlighted in red is the pathologically displaced postero-medial papillary muscle.**

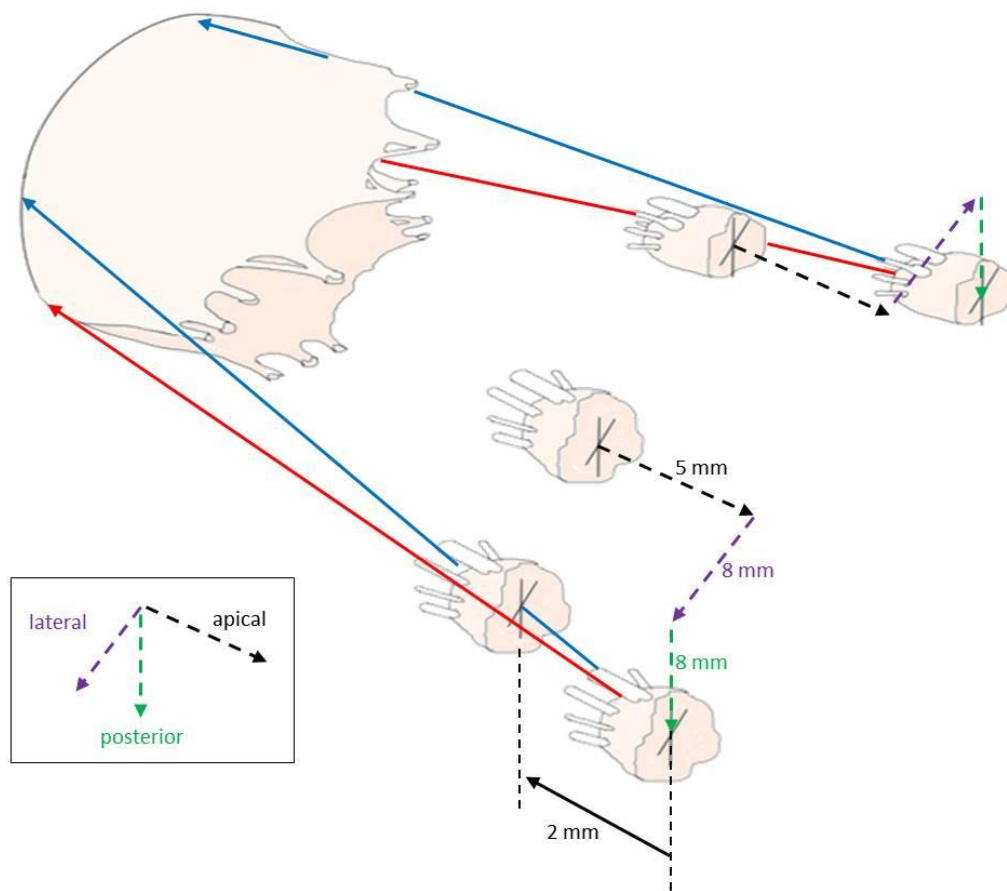


**Figure 5-15 Basal papillary muscle relocation was performed in 2 mm increments to either the trigone (blue vector) or the commissure (red vector). Pathological papillary muscle displacement was performed in the apical (black dashed vector), lateral (purple dashed vector), and the posterior (green dashed vector) directions.**

### 5.3.1.3 Data Analysis

For all conditions, three-dimensional (full volume tissue Doppler) echocardiography was performed; .DICOMs were evaluated offline using Philips Qlab software. Clinical metrics of valvular function were analyzed at all three lines of coaptation, A1-P1, A2-P2, and A3-P3 (Figure 5-16). Coaptation length (CL) was measured as the distance from the point of coaptation to the leaflets' free edge. Tenting



area (TA) was measured as the area entrained between the annular plane and the leaflets' surfaces (Figure 5-17).

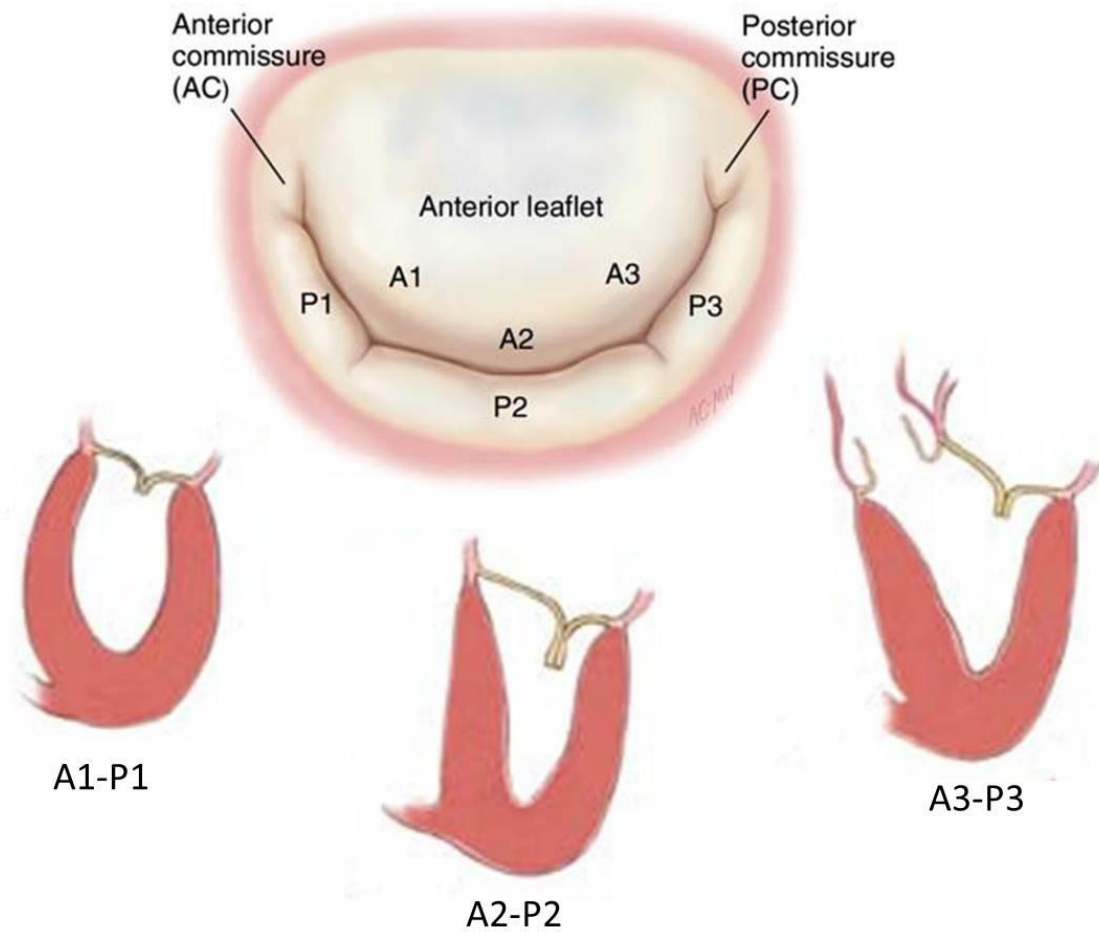


**Figure 5-16 Three lines of coaptation are shown: A1-P1, A2-P2, and A3-P3.**

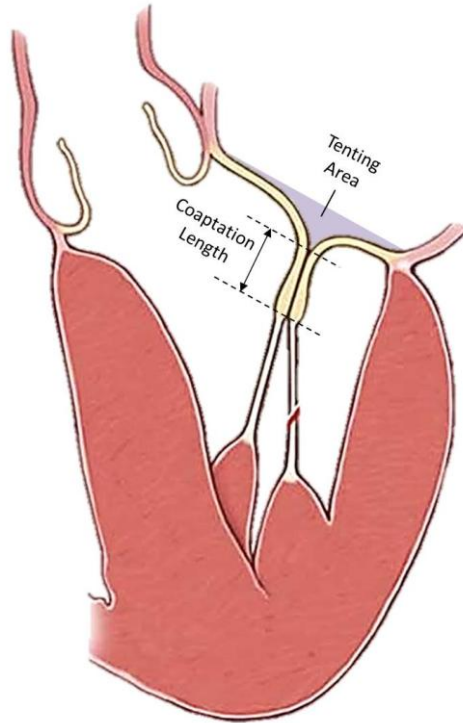


**Figure 5-17 Coaptation height and tenting area are depicted.**

Statistical analysis was completed using Minitab 16 (Minitab Inc.; State College, PA) and data were expressed as the mean  $\pm$  1 standard deviation. An Anderson Darling test was performed to assess data normality, and an F test was used to check for equality of variances. Each valve served as its own control, that is, echocardiographic measurements (CL and TA) of disease and repaired conditions were compared with those made on the same valve for a given experimental sequence. Thus, a repeated measures analysis of variances (ANOVA) was used as the samples were not independent.

If a significance of differences was present ( $p < 0.05$ ), a Dunnett's post hoc analysis was used to assess which experimental groups had CL or TA that varied from the control condition. A Tukey's post hoc test was used to assess differences in CL and TA within experimental groups.

Leaflet geometric variables (CL and TA) were plotted as a response to PM distances. Measured variables were normalized by anterior leaflet height to remove the influence of valve size. A linear regression was used to determine the relationship between PM distance and closed leaflet geometry; the characteristic equations and fit (coefficient of determination,  $R^2$ ) were recorded.

### **5.3.2 Anterior Leaflet Augmentation**

The objective of this study was to investigate the efficacy of anterior leaflet augmentation as a viable surgical therapy for ischemic mitral regurgitation. Treatment efficacy was assessed using an integrative approach that combined: (i) clinical measurements of valve function, (ii) direct flow measurements of valve regurgitation, and (iii) chordal force measurements of leaflet tethering. Leaflet augmentation was compared against the current surgical gold standard treatment for ischemic mitral regurgitation, undersized or restrictive mitral annuloplasty. Surgical treatment was randomized to either a moderate or large size pericardial augmentation.






#### 5.3.2.1 Experimental Protocol

This study involved the use of miniature chordal force transducers to capture the dynamic tension on four main chordae throughout the cardiac cycle: (i) anterior leaflet strut chordae from the anterolateral papillary muscle, (ii) anterior leaflet strut chordae from the posteromedial papillary muscle, (iii) posterior leaflet strut chordae from the anterolateral papillary muscle, and (iv) the posterior leaflet strut chordae from the posteromedial papillary muscle. These chordae were chosen as they are the main load bearing chordae for each leaflet [187,188].

Prior to each experiment, miniature force transducers were sutured to each of these selected chordae, without altering the chordae's native length. The section of chordae that passed between the measurements arms of the transducer was bisected to transfer chordal load into the transducer. The voltage output of the transducers was zeroed before the start of each experimental condition (0 mmHg of transmitral pressure).

The experimental protocol was performed in 4 main steps (Figure 5-18):

1. Control
2. Ischemic mitral regurgitation
3. Undersized, or restrictive, mitral annuloplasty
4. Leaflet augmentation

	Healthy Control	IMR	RMA	TSA with Small Leaflet Patch	TSA with Large Leaflet Patch
<b>Condition</b>			 <i>Repair 1</i>	 <i>Repair 2</i>	 <i>Repair 3</i>
<b>Annular Size</b>	Size 30	Size 38	Size 26	Size 30	Size 30
<b>PM Position</b>	Normal	IMR Configuration	—————→		

**Figure 5-18 Annular sizes and pm positions for repair protocol. Repairs were randomized to either small or large patch treatments**

The control condition was established as previously described in section 5.1.2. Ischemic mitral regurgitation was simulated with asymmetric annular dilation and papillary muscle displacement, representative of an inferior myocardial infarction. Specifically, the mitral annulus was dilated to 150% of the control valve area (7.22 cm<sup>2</sup>). The antero-lateral

papillary muscle was displaced 3 mm apically and 2 mm anteriorly, while the postero-medial papillary muscle was displaced 4 mm apically, 4 mm posteriorly, and 8 mm laterally. These changes were consistent with data previously measured in chronic ischemic mitral regurgitation studies [13,190,191].

Following IMR, undersized mitral annuloplasty was performed; the valve was downsized from a size 30 to a size 26 (C-E Physio). Next, anterior leaflet augmentation was performed using a pericardial patch (Bovine, 0.5% in Gluteraldehyde). Augmentation repair was randomized to either a moderately sized (major  $\phi$  x minor  $\phi$ : 1.77 x 0.65 cm) or large (major  $\phi$  x minor  $\phi$ : 2.68 x 1.07 cm) pericardial patch (Figure 5-19). An incision was made in the anterior leaflet parallel to and 1 - 2 mm from the anterior mitral annulus. For the large augmentation procedure, the incision was made from commissure to commissure. For the moderate augmentation, the incisions stopped short of either commissure by ~ 4- 5 mm. The pericardial patch was positioned in place with 4 interrupted knots in the 3, 6, 9, and 12 o'clock positions. A running mattress suture was used to secure the pericardium to the leaflet and create a leak free seal. For each augmentation procedure, the mitral annulus was stepped through three mitral annuloplasty ring sizes (undersized 26, true-sized 30, and over-sized 34), in addition to the 150% mitral annular dilation from the IMR condition.



**Figure 5-19** Atrial (left) and ventricular (right) views of an anterior leaflet augmented with a pericardial patch. Two chordal force transducers can be seen attached to the anterior strut chordae.

#### 5.3.2.2 Data Analysis

All hemodynamic and force data were ensemble averaged over 10 cardiac cycles. Mitral regurgitation was quantified by integrating the negative (or reverse) flow over the systolic portion of the cardiac cycle. The presence of MR was confirmed with Doppler echocardiography. Qlab was used to quantify mitral valve leaflet coaptation as the distance from the point of coaptation to the leaflets' free edge. Chordal forces were measured as the difference between peak systolic and diastolic force. Due to inherent drift of the transducers, absolute forces were not reported.

A two-way repeated measures analysis of variance (ANOVA) was used to assess the effects of experimental condition (Control, IMR, Repair) and patch size (moderate, large). A general linear model was performed using Minitab 16. Significance was determined at a 95% confidence interval ( $p < 0.05$ ). A Tukey post hoc test was used to determine between group significant differences. All data were reported as mean  $\pm$  1 standard deviation.

## **5.4 Specific Aim 3 – Developing an Experimental Database to Advance Mitral Valve Surgical Planning Tools**

The objective of this study was to develop an experimental workflow and potential database to help advance mitral valve surgical planning computational models. For each experiment, multiple complimentary techniques were performed:

5. Mitral valvular geometry was provided from: (i) state of the art micro-computed tomography, and (ii) clinical standard of care echocardiography
6. Geometric and hemodynamic boundary conditions were carefully defined
7. Stereoscopic particle image velocimetry captured native mitral flow fields
8. Valvular mechanics (leaflet strain, and papillary muscle force) were quantified

### **5.4.1 Experimental Protocol**

The work of this aim was performed in the new, modified left heart simulator. A native ovine mitral valve was mounted to the left heart simulator and a control was established as previously described. For all conditions, the left heart simulator was tuned to 70 bpm heart rate, 120 mmHg peak left ventricular pressure, and 5.0 L/min average cardiac output.

#### 5.3.1.1 Hemodynamic Boundary Conditions

Hemodynamic boundary conditions were acquired using in-line electromagnetic flow probes positioned upstream of the left atrium, downstream of the bladder pump (upstream of the left ventricular inlet), and downstream of the aortic valve. Pressure transducers were mounted to the left atrium, left ventricle, and the aortic outlet.

#### 5.4.1.2 Clinical Imaging and Biomechanical Evaluation

Full volume tissue and color Doppler echocardiography was performed using an x7-2 TTE probe and a Philips iE33 ultrasound system. Images were acquired over 5 cardiac cycles at ~ 20 Hz. Papillary muscles forces were acquired over ten cardiac cycles. Baseline forces (axial, two directions of out of plane bending) were zeroed before pulsatile pressures were applied to the left heart simulator. Forces were acquired over 10 cardiac cycles. More detail on papillary muscle force transducers and acquisition system can be found here [2,192]. Dual camera stereo-photogrammetry was performed to acquire leaflet dynamics throughout the cardiac cycle. Tissue marker dye was applied to the atrialis of the anterior and posterior leaflets in a 2 mm array. These markers were tracked and digitized throughout the cardiac cycle using custom MatLab scripts. The pixel coordinates of each marker from the two cameras were transformed using a Direct Linear Transformation into 3D Cartesian space. A 10 mm cube imaged from each camera was used for the calibration function. Anterior and posterior leaflet strain were calculated from the marker deformation using techniques described here [36,118,120,193,194].

#### 5.4.1.3 Micro-computed Tomography

Following clinical imaging and biomechanical evaluation, the modified left heart simulator was adapted for micro-computed tomography. The mitral annulus and papillary muscle positions were unperturbed from their experimental configuration. The left atrium and out flow tract with aortic valve housing were removed. The aortic outlet was sealed with a flush mounted acrylic plate and rubber gasket. The atrial side of the annulus plate was exposed to atmosphere. All pressure transducers were removed and



ports sealed with flush mounted nylon set screws. An adaptor plate was mounted to the apical wall of the left ventricle to secure the left heart for micro-computed tomography gantry. Humidity was maintained in the left heart by a wet sponge.

Scanning parameters were optimized to image the mitral valve (low density soft tissue) in air; a control file (no. 204) was created and saved for future acquisitions (See Appendix for more detail). The key parameters were: 55 keV energy, 109  $\mu$ A intensity, and 300 ms integration time. The field of view was set to its maximum diameter, 38.9 mm, which resulted in 38.9  $\mu$ m isotropic voxel resolution. Typically, 600 – 1000 image slices were acquired in 30 – 40 min. A Scout-View was performed to ensure the valve was properly positioned within the field of view. Axial scanning boundaries were set to ~ 1-2 mm supra-annularly and ~1-2 mm distal to the papillary muscles. Inclusion of these additional geometric features was used to register the mitral valve to the surface mesh of the left heart simulator.

Two scans were typically performed to capture: (i) diastolic or open configuration of the mitral valve geometry, and (ii) systolic or closed configuration. The first scanned was performed under ambient pressure, and ~ 0 mmHg of transmitral pressure. Following the first scan, a continuous compressed air pump was connected to the left ventricular inlet using a flexible duct hose, which was snaked through the adapter plate and out of the micro-computed tomography system via an access port. The left ventricle was pressurized to ~ 30 mmHg; the atrial side of the valve remained exposed to ambient pressure. Higher pressure could not be obtained with the continuous air pump used. The scan was repeated with identical parameters.

#### *5.4.1.2.1 Paraformaldehyde Pressure Fixation*

As an alternative to pressurizing the left ventricle with a compressed air pump, the valve was pressure fixed using para-formaldehyde (PFA) treatment. A 4 % PFA fixative was prepared ahead of time using the manufacturer's suggested protocol (Biocare Medical; Concord, CA) (See Appendix for protocol detail). Fixative was prepared fresh and used within two weeks (stored at 4° C).

Valves were fixed under static left ventricular pressure (~ 70 mmHg) to provide a closed configuration valve. Pressure was dictated by maximum allowable height inside of a fume hood. Static left ventricular pressure was maintained using a peristaltic pump (Masterflex Model # 7518-10; Cole-Parmer; East Bunker Court Vernon Hills, IL) and speed controller. Speed was set to offset any leakage such that a static PFA pressure head was maintained. Fixation took place overnight for ~ 10 - 12 hrs. Valves were subsequently scanned in air using parameters previously described. PFA fixation was performed as the terminal experimental step.

#### *5.4.1.2.2 Phosphotungstic Acid Contrast Enhancement*

X-ray contrast was enhanced using phosphotungstic acid (PTA). Fresh 1% PTA solution was prepared using a previously outlined protocol [195] (see Appendix for protocol detail). The valve was submerged in PTA solution overnight (~ 10 – 12 hrs) at 4° C. Valves were subsequently scanned in air as previously described.

#### 5.4.1.4 Stereoscopic Particle Image Velocimetry

Stereoscopic particle image velocimetry was performed to capture flow fields through and proximal to the mitral valve. The laser plane was initially set to bisect the mitral valve in the central apical-basal long axis slice. Cameras were positioned equidistant on either side of the ventricular chamber. Using the Schiempflug adapters, the cameras were

angled ( $\sim 30^\circ$ ) to increase optical access to the mitral flow field (avoiding the bulk of chordae tendinae) (Figure 5-20).

Data were acquired at room temperature for adult pulsatile hemodynamic conditions. 50 phase locked image pairs were acquired every 25 ms in the cardiac cycle (Figure 5-21). The time difference (dt: 200-1000  $\mu$ s) between image pairs was optimized for each sampled point in the cardiac cycle to capture high fidelity velocity vectors (target particle displacement: 5-8 pixels, or 25% of the size of the interrogation window) (Table 5-1). 4 flow field planes were acquired in the ventricle. The planes were spaced by 4, 8, and 15 mm from the central plane using the traverse. One central plane was used in the left atrium. Each plane was independently calibrated. Calibration was performed using a three-dimensional two-level target positioned in the laser plane and imaged from both cameras. A 3<sup>rd</sup> order polynomial fit of the calibration points was utilized, which corrects for the velocity vectors based on the distortion observed with the calibration target.

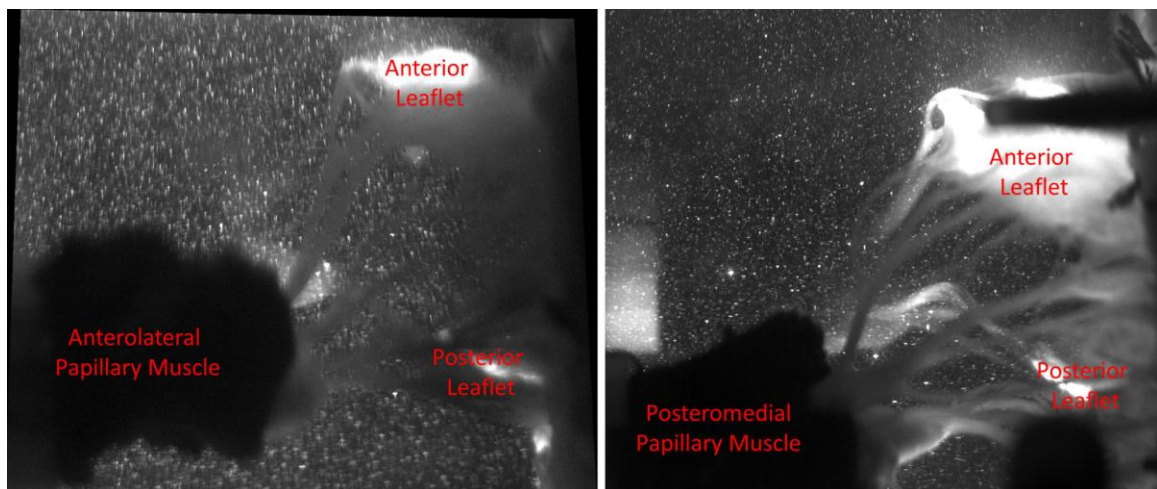


**Figure 5-20 Representative paired images acquired during peak systole.**

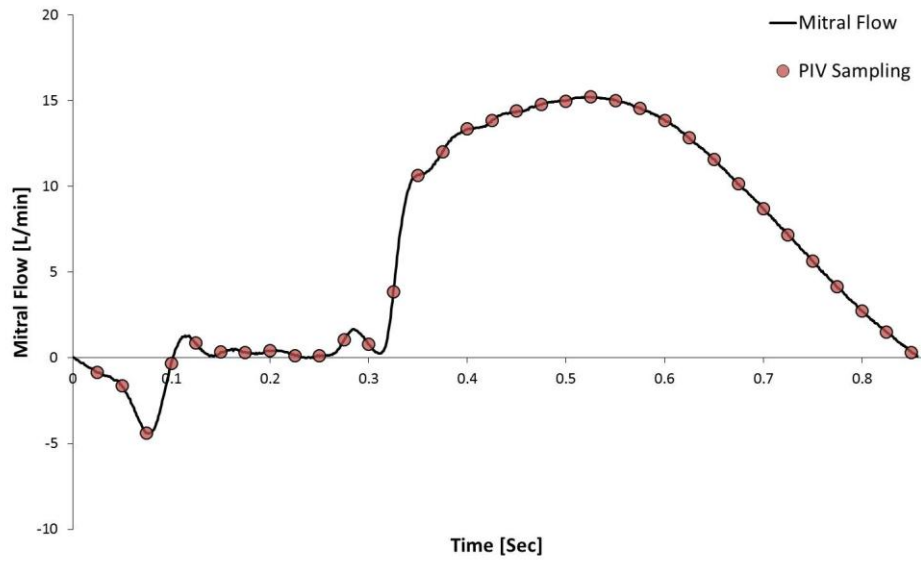


**Figure 5-21 Representative mitral flow curve depicting time points sampled for particle image velocimetry.**

**Table 5-1 Time difference between image pairs for various segments of the cardiac cycle.**

Mitral Valve State	dt ( $\mu$ s)	Flow State
<b>Opening</b>	200 - 300	Highest velocity flow through mitral valve
<b>Open</b>	300 - 400	Continued high velocity flow through mitral valve
<b>Closing</b>	1000	Low magnitude reverse flow
<b>Closed</b>	400 - 500	Systolic ejection through outflow tract

#### 5.4.1.5 Geometric Boundary Conditions

The geometry of the left heart simulator was modeled using SolidWorks computer aided design (CAD). As a geometric boundary condition, only the surfaces that contacted the blood analog were modeled. In essence, a “negative” of the left heart assembly was created as one solid part (Figure 5-22). The SolidWorks part was exported as a stereolithography (.STL) model for further manipulation; specifically, a surface mesh could be applied and optimized for computational implementation. Additionally, inlets and outlets can be extended to promote fully developed for computational model stability.

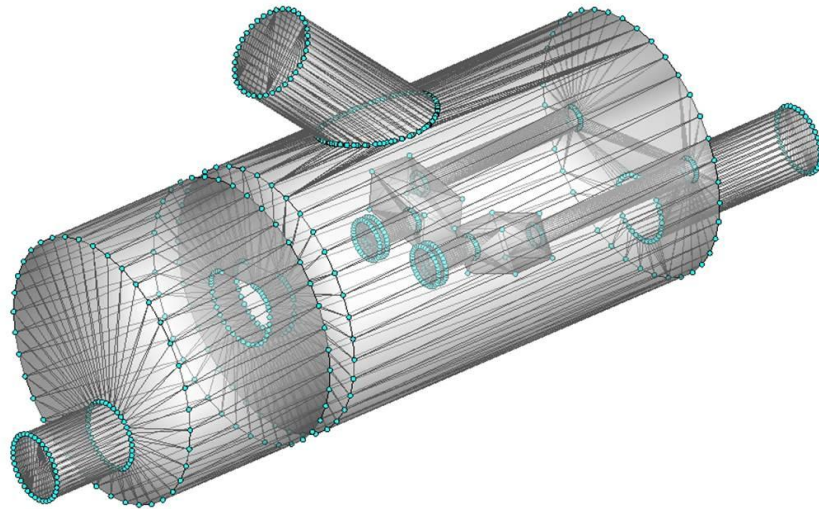


**Figure 5-22 Surface mesh of the left heart simulator.**

## 5.4.2 Data Analysis

### 5.4.2.1 Geometric Reconstruction from Micro-computed Tomography

The image data were reconstructed using multiple complimentary techniques. A Gaussian filter ( $\sigma = 1.2$ , support = 2) was applied to improve signal to noise and edge enhancement. Slice by slice user initialized contouring was performed to define the valve anatomy to be included in image segmentation (Figure 5-23). Area(s) for inclusion was manually traced in every 40-60 slices. A dynamic morphing algorithm interpolated the area(s) between slices. The raw gray scale images were filtered and converted to binary images using upper and lower bound thresholds [196]. Thresholds were manually identified via the histogram composition of intensities and adjusted based on empirical observation. An in-house MATLAB script was used to segment mitral valve anatomy through canny edge detection; this produced a point cloud of the valve surface. Geomagic Studio (company information) was used to mesh, smooth, and visualize resultant mitral valve geometry. The mitral valve geometry was also registered to the surface mesh of the left heart using overlapping segments. Boolean addition was used to fuse the segments together at the mitral annulus and papillary muscles.

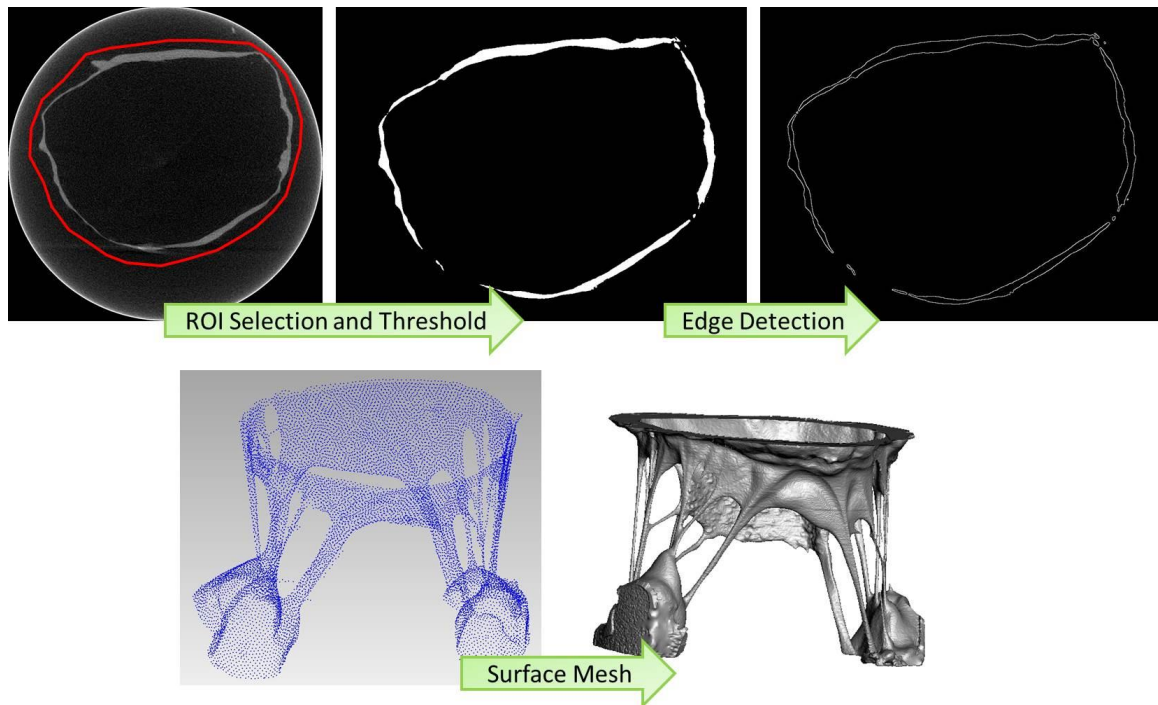


**Figure 5-23 Micro-CT segmentation protocol is outlined.**

#### 5.4.2.2 Geometric Reconstruction from Echocardiography

A validated in-house MATLAB script was used to extract the mitral leaflet geometry [197]. J-splines were used for semi-automatic segmentation of the posterior and anterior mitral leaflets during peaks systole. 15-20 long axis apical-basal slices across a valve were used for segmentation (slice thickness ~ 2.8 mm). Data were interpolated using an algorithm which was based on the weighted positions of the surrounding points (Butterfly mesh refinement) [198]. Leaflet geometry was post-processed in GeoMagic Studio and visualized in TecPlot.

#### 5.4.2.3 Velocity Field Reconstruction

After raw image pairs were acquired, a background intensity subtraction was performed to enhance image contrast. Next, individual image masks were created for each time

point in the cardiac cycle. A mask was created from representative images from each camera (for a given time point) (Figure 5-23). A single mask was created by manually superimposing one masked image onto its corresponding pair. This ensured velocity vectors were only calculated in regions where flow was visible from both cameras. A 3<sup>rd</sup> order polynomial mapping function was performed in DaVis 7.2, which also corrected for image distortion [199]. Particle cross-correlation was performed on the calibrated masked images using multi-pass interrogation with decreasing window size (64 x 64 to 32 x 32 pixels). Erroneous vectors were rejected based on signal to noise ratio and a median filter which detected outliers. Resultant vector fields were ensemble averaged and three-dimensional velocity fields across the cardiac cycle were obtained. Vorticity ( $\omega_z$ ) was calculated as the curl of the velocity vectors:

$$\omega_z = \frac{\partial V}{\partial x} - \frac{\partial U}{\partial y}$$

PIV processing is outlined by the flow chart in Figure 5-24.



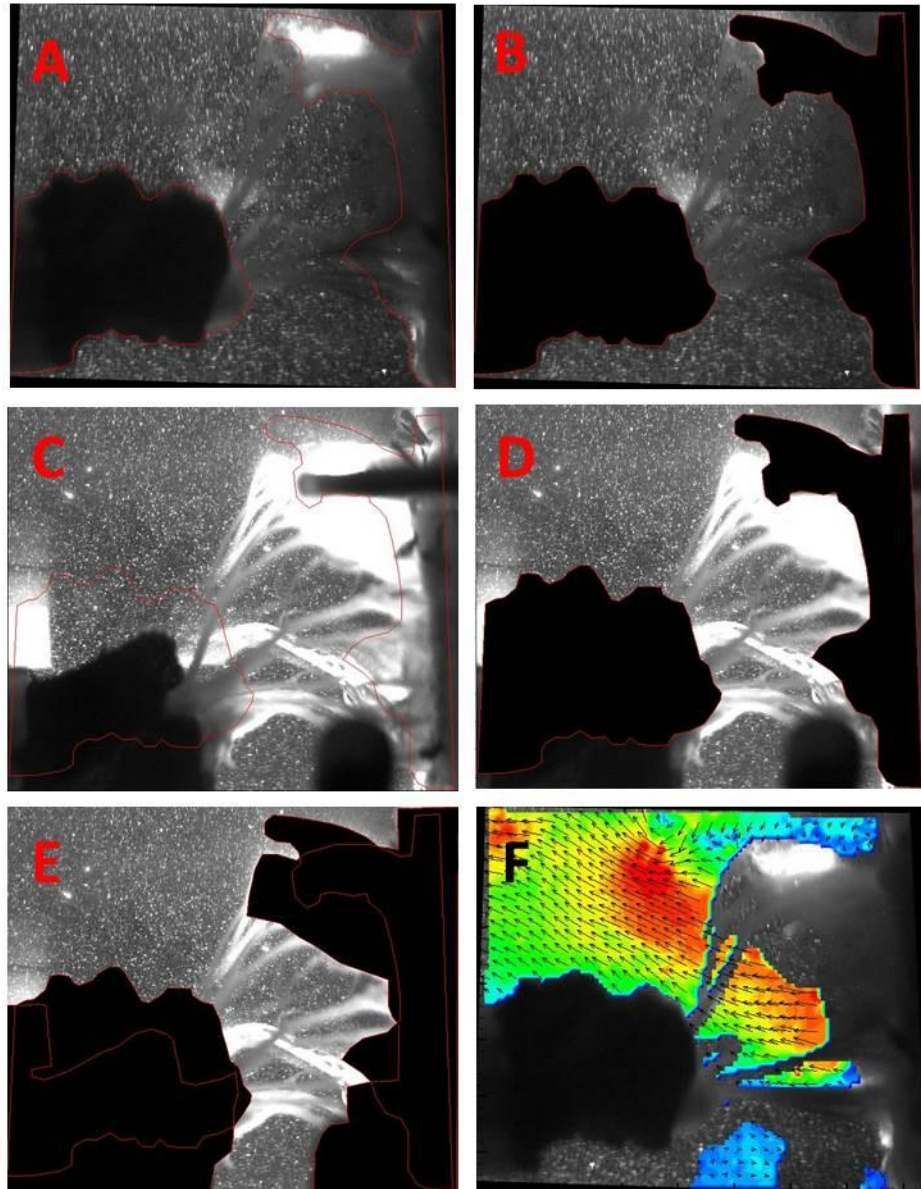


**Figure 5-23** Mask creation for PIV data processing was performed in the following steps: a mask was created (A) and applied (B) to the image in Camera 1; mask from Camera 1 was overlaid (C) and applied (D) to image from Camera 2; an additional mask was created for Camera 2 (E), and velocity vectors were calculated for remaining flow field (F).

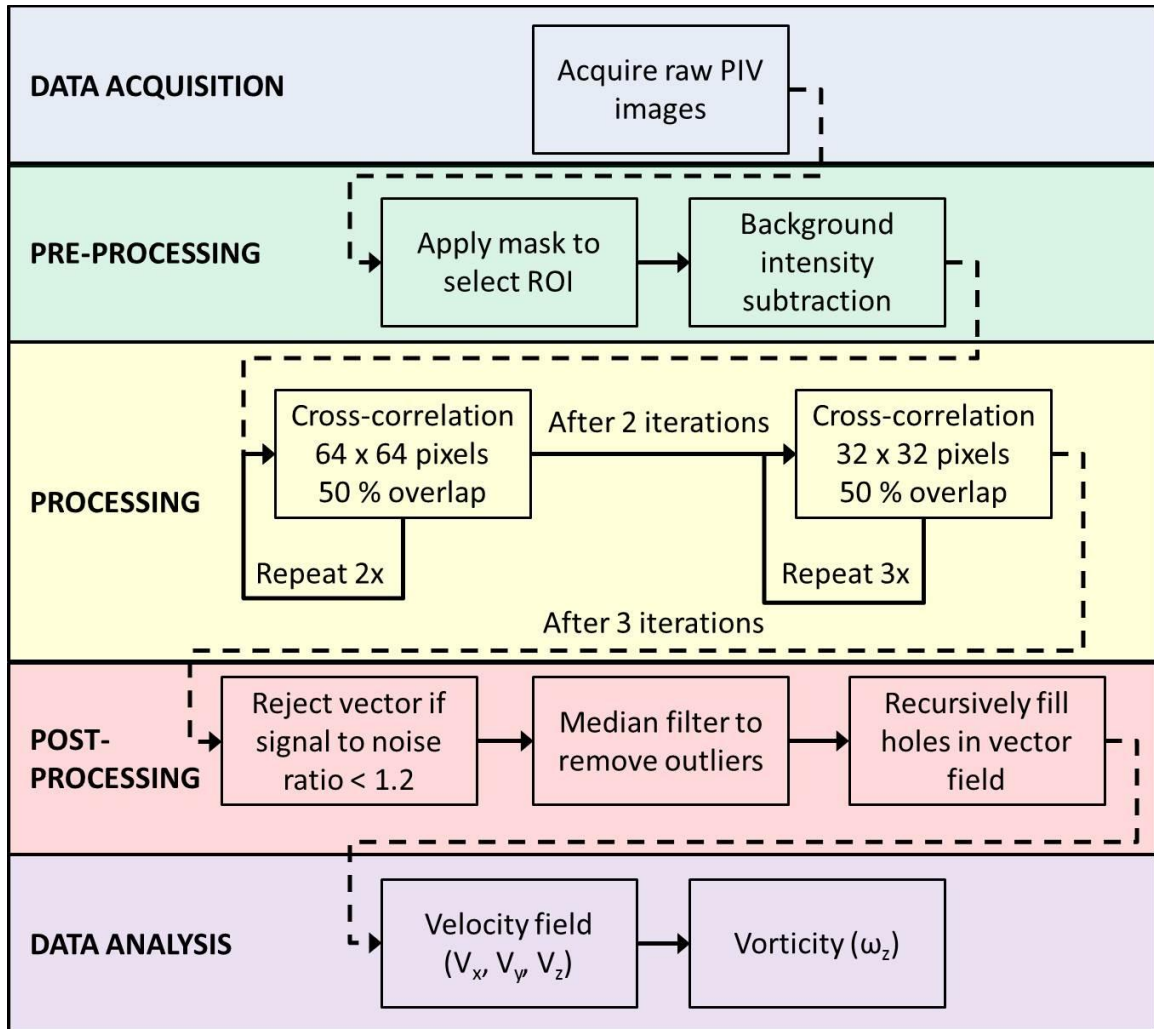


Figure 5-24 Particle image velocimetry processing flow chart.

## CHAPTER 6

### SPECIFIC AIM 1: *IN-VITRO* VALIDATION OF THE PHILIPS 3D FIELD OPTIMIZATION METHOD

#### 6.1 Introduction

Quantitative assessment of mitral regurgitation can help remove the uncertainty associated with characterizing mitral valve disease and improve on the current qualitative methods outlined by the ACC/AHA guidelines [24]. However, these quantitative methods have met clinical resistance challenging their accuracy [18,164-166]. The most common of these methods is the 2D color Doppler Proximal Isovelocity Surface Area (PISA) measurement. Proximal isovelocity surface area is derived from the principle of conservation of mass: as blood approaches a regurgitant orifice, its velocity increases, forming concentric shells of increasing velocity and decreasing surface area [18,167]. This surface area can be estimated during 2D color Doppler echocardiography assuming a hemispheric distribution of velocity vectors proximal to the regurgitant orifice. Unfortunately, this 2D PISA is saddled with limitations.

The source (left ventricle) and sink (left atrium) chambers need to be sufficiently large to develop hemispherical axisymmetric flow convergence. Controlled *in-vitro* experiments using a flail regurgitant mitral valve model demonstrated that proximity to the left ventricular wall will elongation of the shape of the isovelocity contours and cause overestimation of the regurgitant flow [200,201].

A second limitation is due to the variable shape of the regurgitant orifice and the non-planarity of the opposing mitral leaflets. Hemispherical axisymmetric flow convergence requires single point source, which is rarely observed in clinical practice. In vivo, in-vitro and in-silico studies have shown that with elongated or c-slit orifices this the hemispherical assumption of the flow convergence is violated and regurgitant flows are underestimated [164-167,202,203]. Levine et al. were the first to suggest that a correction factor is needed to account for leaflet non-planarity [204]. This was later confirmed by studies by Yamachika et al[205] and Cape et al [206], which showed regurgitant volume was underestimated when leaflets came together in an angle greater than 180 degrees. Flow was overestimated when the leaflets came together in an angle less than 180 degrees.

A final limitation, which may cause overestimation of flow is a result of proximity of the regurgitant flow to the outflow tract. It is assumed that the flow observed proximal to the mitral orifice is directed through the insufficient mitral valve into the left atrium (continuity principle). However, a combined computational and *in-vitro* study found that isosurfaces at larger radii may be effected by neighboring aortic outflow, causing their distortion and elongation [202,203]. In that same series of study, it was demonstrated that, a correction for this and the previous limitations could be made by approximating the shape of the isosurfaces as hemi-elliptical. A novel hemi-elliptical curve-fitting algorithm [207] was used to accurately quantify mitral regurgitation through two standard orthogonal 2D color Doppler views.

This has led to recent improvements of the 2D methodology, which aim to identify the true geometry of the regurgitant isosurfaces for more accurate quantification

[164-167]; one such technique is the Philips 3D Field Optimization Method (FOM). The Field Optimization Method utilizes a complex algorithm to correctly identify the proximal isosurface volume over which it integrates all the flow convergence velocities to calculate true mitral regurgitant volume. Unlike other 3D PISA methods, the FOM is the first to correct for the Doppler angle effect, which may cause the observed magnitude of velocities, particularly along the lateral shoulders of the regurgitant zone, to be underestimated by as much as 40% [18]. However, this and other quantitative measurements still need rigorous validation to ensure their clinical accuracy.

To this end, in this thesis, a regurgitant mitral valve model was developed for which multiple regurgitant orifices and flow rates were simulated. Transmitral flow was measured directly upstream of the left atrium using an electromagnetic flow probe sampled at 1kHz, as a true gold standard. Regurgitant volume was measured using three echocardiography methods: (i) 2D PISA, (ii) 3D FOM, and (iii) an Integrative 3D PISA. The algorithm of the 3D FOM was iterated three times based on empirical insights.

## **6.2 Results**

### **6.2.1 Mitral Regurgitation Model**

Mitral regurgitation was created using isolated and combined annular dilation and papillary muscle displacements. Mitral regurgitation was created empirically under pulsatile conditions through live monitoring of the hemodynamics and direct visual observation of the systolic mitral closure. In total, 42 regurgitant orifices were created yielding 18 round orifices and 24 slit orifices. Orifice shape was binned into round and slit based on en face high speed imaging of mitral leaflets during systole and the shape of

the PISA shell through echocardiography (Figure 6-1). PISA shell shape was determined in the C-plane 1-3 mm sub-annularly. Mitral regurgitation per beat ranged from 13.8 mL to 71.2 mL (median: 37.9 mL) (Figure 6-2). Similarly, mitral regurgitation was graded into mild, moderate, and severe based on direct flow measurements acquired with the electromagnetic flow probe (Table 6-1). Grades were determined in accordance with guidelines on valvular disease [24].

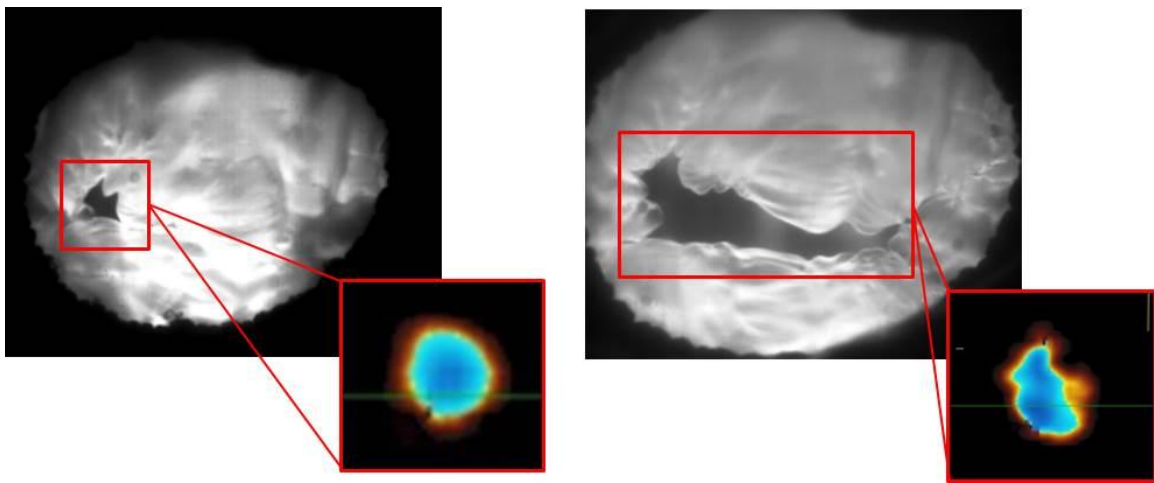


**Figure 6-1 Representative images of round (Left) and slit (Right) regurgitant orifices. Inlays shows corresponding C-plane echocardiography of proximal isovelocity surface are observed 1-3 mm sub-annularly.**

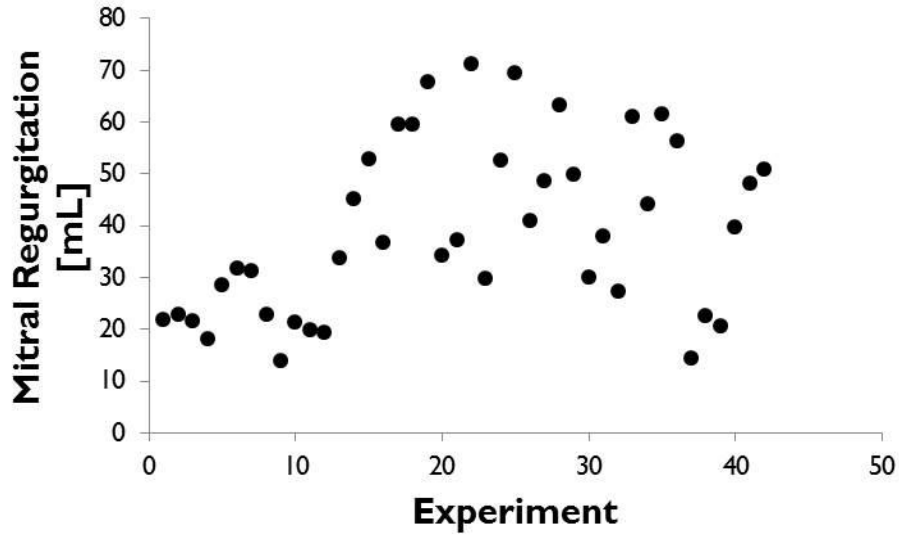


**Figure 6-2** Scatter plot of mitral regurgitation shows a range of volumes from 10 to 70 mL.

**Table 6-1** Mitral regurgitation was binned into mild, moderate, and severe based on clinical guidelines.

Mitral Regurgitation Grade	N (%)	Regurgitant Volume [ml]
Mild	15 (35.7)	< 30
Moderate	21 (50)	30 – 59
Severe	6 (14.3)	> 60

### 6.1.2 2D PISA Analysis

2D PISA analysis was performed as it is the currently used quantitative clinical measurement. 2D PISA analysis was performed on all data sets with corresponding Continuous Wave Doppler echocardiography (N = 30). CW data was not available for all 42 data sets acquired. For each condition, the CW data analysis was repeated 5 times and

averaged to measure maximum velocity ( $V_{max}$ ) and the velocity time integral (VTI). Similarly, the 2D PISA radius measurement was repeated five times and averaged from the 2D Color Doppler images. For each independent observation ( $N = 5$ ), 15 cardiac cycles were available for analysis. Subsequently, mitral regurgitation was calculated as described above (Chapter 5.2.2). The intra-observer variability was captured using the coefficient of variation, which is the non-dimensional ratio of the standard deviation to the mean. The average standard deviation between regurgitant volume measurements was relatively large (9.1 mL), and the coefficient of variation was 0.26 (a value less than 0.05 is desirable).

Regurgitant volume calculated from 2D PISA was plotted against regurgitant volume measured through direct flow analysis (Flow Probe Gold Standard) (Figure 6-3). 2D PISA analysis underestimated mitral regurgitation over all data sets, regardless of leakage severity and orifice type. On average, 2D PISA underestimated true regurgitation by  $9.8 \text{ mL} \pm 9.3 \text{ mL}$ ; however this was not statistically significant ( $p = 0.014$ ). A measurement bias of -5.84 (underestimation) was calculated using Bland-Altman analysis (Figure 6-4). The data were further grouped by round and slit orifices.



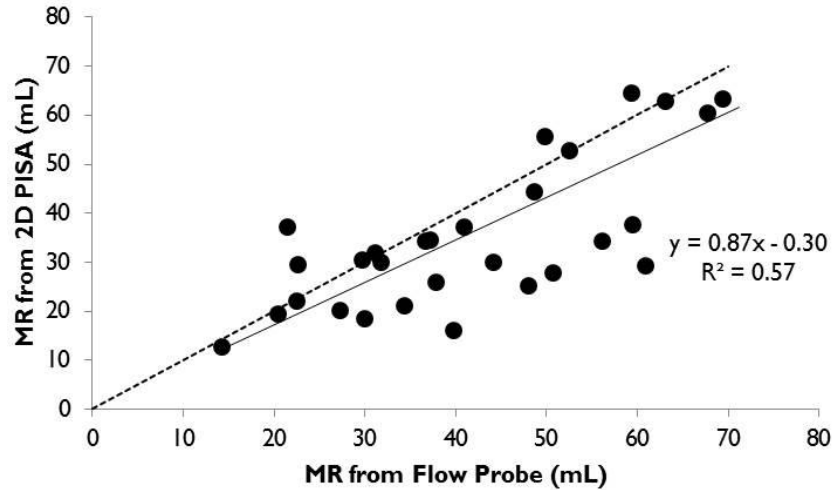


**Figure 6-3 Mitral regurgitation volume quantified through 2D PISA underestimated true mitral regurgitation. Dashed line represents 1:1.**

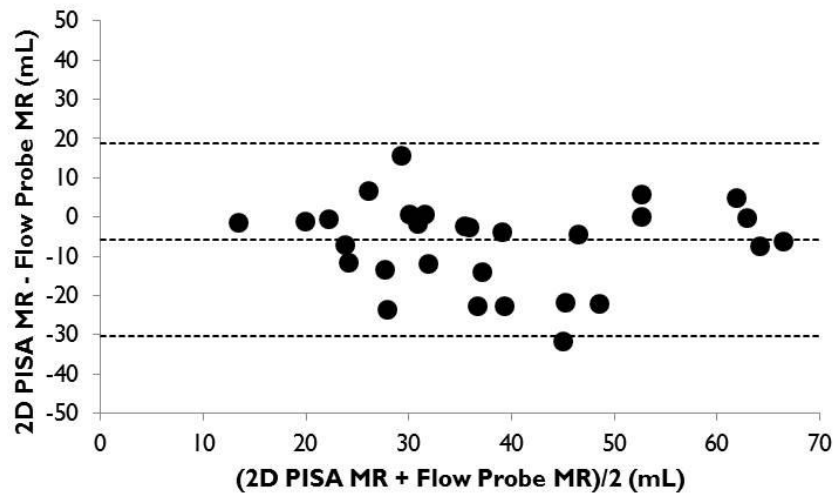


**Figure 6-4 Mitral regurgitation volume quantified through 2D PISA underestimated true mitral regurgitation. Dashed lines show mean  $\pm$  2 standard deviations.**

Data were further analyzed by orifice type as it was expected that 2D PISA analysis would be accurate for round orifices, but otherwise inaccurate (systematic underestimation) for slit orifices (Figure 6-5). For the round orifice, the average error by

2D PISA analysis was reduced to  $2.7 \pm 2.3$  mL; regurgitant volume measured by both techniques was not significantly different ( $p = 0.668$ ). Similarly, the measurement bias was reduced to 0.63 mL. However, for the slit orifice, systematic underestimation was observed, and the measurement bias was -7.81 mL. The average error was  $12.0 \pm 9.6$  mL; this was nearly statistically significant and is clinically impactful. These results confirm that the hemispherical assumption of the 2D PISA analysis was violated for the slit orifices. Mitral regurgitation was underestimated for 69.6% percent of the slit orifice data ( $N = 16/23$ ). Intra-observer repeatability was equally poor for both orifice conditions (coefficient of variation: round 0.27; slit 0.25).

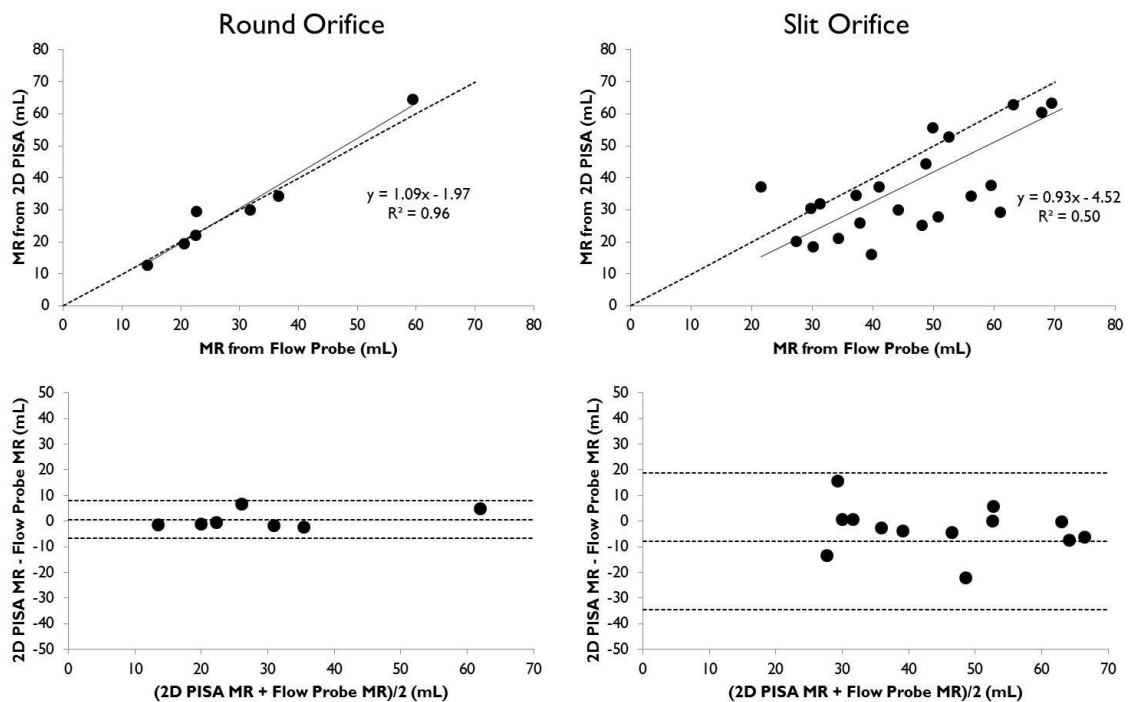


**Figure 6-5** Data were grouped for round and slit orifice. 2D PISA was accurate for the round data, but systematically underestimated regurgitant volume for the slit orifice data.

Average error was further subdivided by regurgitation severity (Table 6-2). Average error for the round orifice types remained low (< 5 mL) for mild and moderate grades. No data were available for severe regurgitant through a round orifice. Average error for the slit orifice increased with regurgitation severity.

**Table 6-2 Reported errors for the 2D PISA method grouped by orifice type and regurgitant severity.**

<b>Mitral Regurgitation Grade</b>	<b>Total</b>	<b>Round</b>	<b>Slit</b>
Mild	6.1 ± 4.8	4.8 ± 2.1	3.4 ± 6.0
Moderate	10.9 ± 9.1	3.1 ± 1.7	12.8 ± 9.1
Severe	14.1 ± 13.5	--	14.1 ± 13.5
<b>Total</b>	<b>9.8 ± 9.3</b>	<b>2.3 ± 2.3</b>	<b>12.0 ± 9.6</b>

Misdiagnosis incidence was reported as the frequency of erroneous regurgitation grading by 2D PISA (Table 6-3). Hard cutoffs were applied to regurgitation grades as measured through the direct flow gold standard. In total, there were 10 events of misdiagnosis; the majority of these were underestimation of regurgitation severity (N = 7, 70% of total misdiagnosis). The most frequent misdiagnoses were in the moderate mitral regurgitation grade. As these techniques aim to move away from qualitative guidelines, it may be better to bin the data by their percent error from truth (Figure 6-6). 60 percent of the 2D PISA analysis resulted in less than 10% error from truth. The largest errors

were all a result of the slit conditions; this can be noticed in the histogram distributions. The round orifice data have a tight clustering for low errors, whereas the data are more equally distributed for the slit orifices.

**Table 6-3 Misdiagnosis incidence by regurgitant grade was reported.**

<b>Mitral Regurgitation Grade</b>	<b>Total</b>
Mild	2 (↑)
Moderate	1 (↑) 6(↓)
Severe	1(↓)
<b>Total</b>	<b>3(↑) 7(↓)</b>

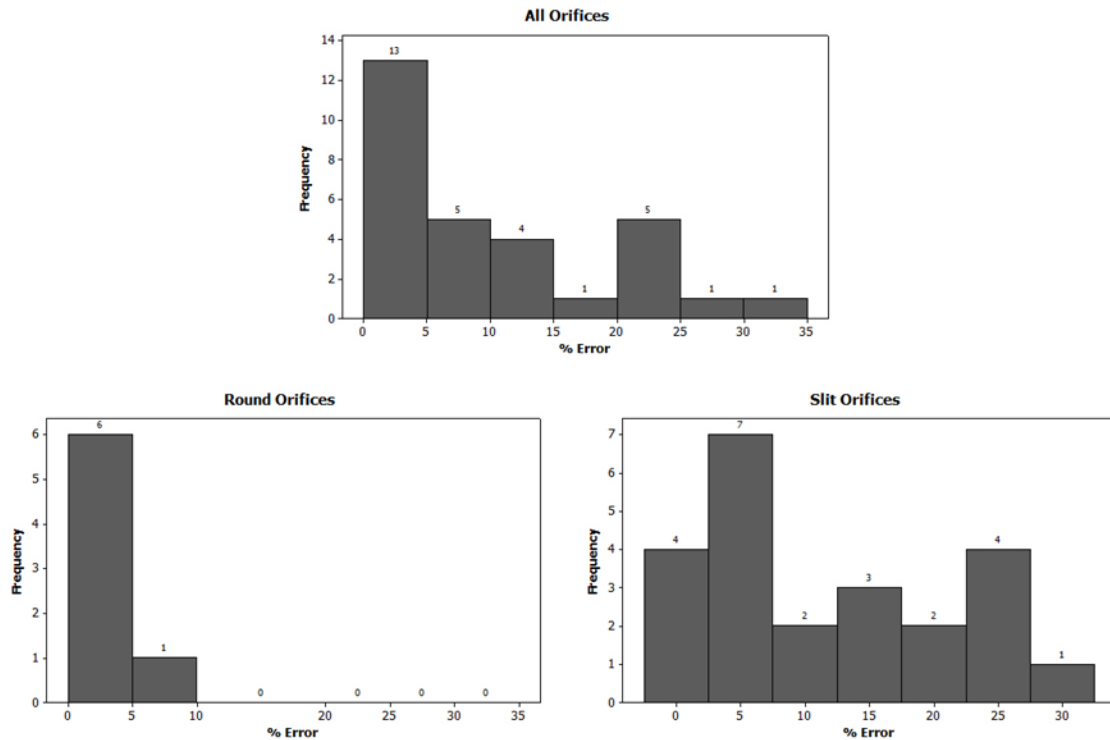


**Figure 6-6 Histogram distribution of percent errors were grouped for round and slit orifice data.**

### 6.2.3 Philips 3D Field Optimization Method

Three iterations of the 3D FOM were assessed. In the first iteration, velocities in the flow convergence zone were integrated over fixed, pre-defined radii across all conditions and frames in the cardiac cycle. In the second and third iteration, the radii of velocity integration were actively adjusted by the automated algorithm for each frame of the cardiac cycle, as well as, for each regurgitant condition. In addition to adaptively adjusting the radii for velocity integration, in the third iteration, the z-height of a regurgitant orifice was actively adjusted from frame to frame. For all three iterations, 3D FOM was performed on all data sets ( $N = 42$ ). For each condition, 3D FOM was repeated 5 times.

### 6.2.3.1 Iteration 1: Fixed Radii of Velocity Integration

The average standard deviation between measurements was a robust 1.4 mL. The coefficient of variability was an acceptable (0.06). The average error, however, was a relatively large  $12.6 \pm 13.3$  mL; the difference between measured values and truth were statistically significant ( $p < 0.005$ ). On average, 3D FOM underestimated true regurgitant volume, and a -9.4 mL measurement bias was observed. As identified in the scatter (Figure 6-7) and Bland Altman (Figure 6-8) plots, the errors were largest for regurgitant volumes greater than 30 mL per beat, which were typically associated with the slit orifices. Therefore, the data were further grouped by round and slit orifice.

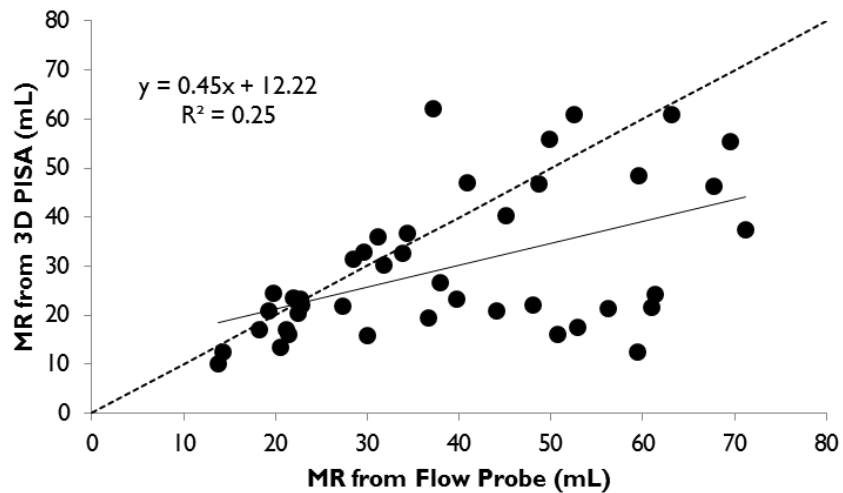


**Figure 6-7 Mitral regurgitation volume quantified through 3D FOM underestimated true mitral regurgitation. Dashed line represents 1:1.**

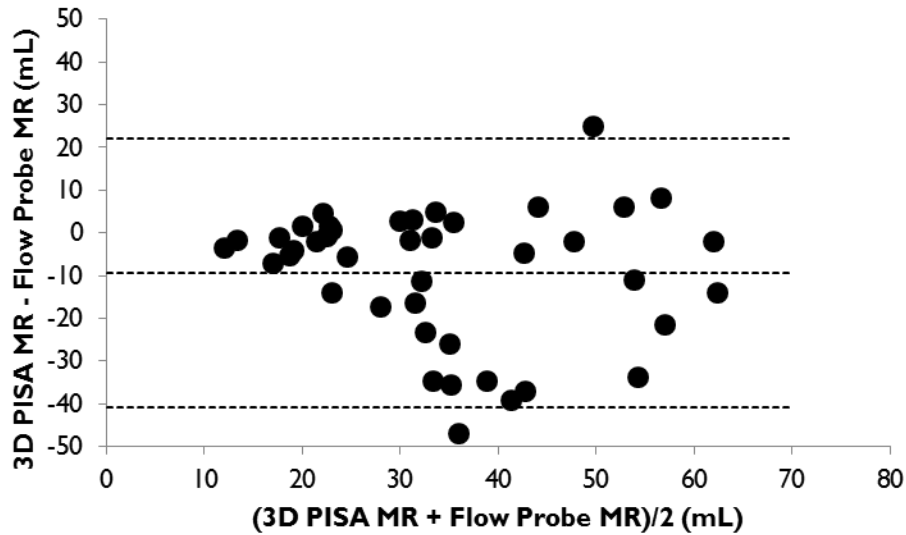


**Figure 6-8 Mitral regurgitation volume quantified through 3D FOM underestimated true mitral regurgitation. Dashed lines show mean  $\pm$  2 standard deviations**

Three data points were identified as outliers (red points on scatter plot in Figure 6-9). The error associated with these three points (17.3, 35.5, and 47.0 mL) was greater than 1.5 times the interquartile range (4.3) added to the third quartile (5.91); outlier cut off value was 13.6 mL. Error was defined as the regurgitant volume difference between direct flow measurement and 3D FOM calculation. Each of the three data points originated from the same mitral orifice condition. These points were excluded from statistical analysis, but were identified for further investigation with the 2<sup>nd</sup> and 3<sup>rd</sup> iteration of the 3D FOM. 3D FOM accurately measured regurgitant volume for the round orifices (average error:  $2.6 \pm 1.9$  mL) (Figure 6-9); the difference between measured values and truth were not statistically significant ( $p = 0.186$ ). Tight scattering was observed in the Bland-Altman plot, and measurement bias was -1.1 mL. Large average errors ( $16.2 \pm 12.6$ ) were observed for the slit orifices; the difference between measured

values and truth were statistically significant ( $p < 0.005$ ). Systematic underestimation was observed for the slit orifices (measurement bias: -11.6 mL).

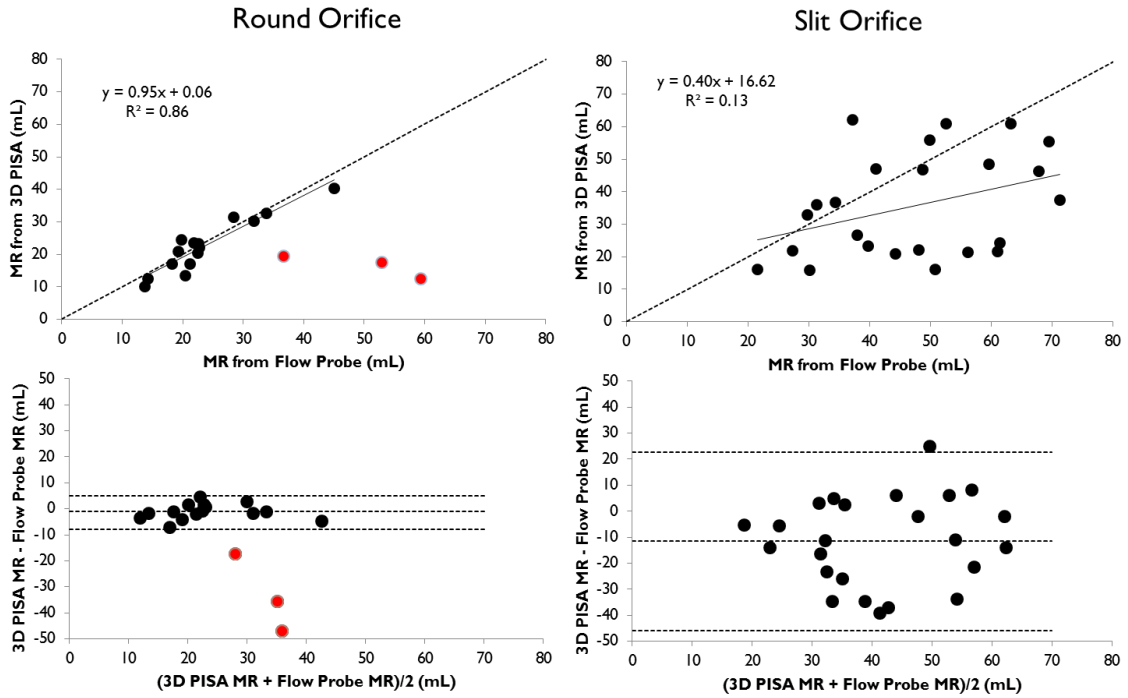


**Figure 6-9** Data were grouped for round and slit orifice. 3D FOM was accurate for the round data, but systematically underestimated regurgitant volume for the slit orifice data.

Average error was further subdivided by regurgitation grade (Table 6-4). Average error for the round orifices remained low (< 5 mL) regardless of regurgitation severity. No data were available for severe regurgitation through a round orifice. Average error for the slit orifices increased with mitral regurgitation grade.



**Table 6-4 Reported errors for the 3D FOM grouped by orifice type and regurgitant severity.**

<b>Mitral Regurgitation Grade</b>	<b>Total</b>	<b>Round</b>	<b>Slit</b>
Mild	3.1 ± 2.0	2.7 ± 1.9	4.7 ± 1.4
Moderate	11.0 ± 10.6	3.1 ± 2.3	13.8 ± 11.0
Severe	24.7 ± 14.7	--	24.7 ± 14.7
<b>Total</b>	<b>12.6 ± 13.3</b>	<b>2.6 ± 1.9</b>	<b>16.2 ± 12.6</b>

Misdiagnosis incidence was reported as the frequency of erroneous regurgitation grading by 3D FOM (Table 6-5). There were 19 total events of misdiagnosis; the majority of these were underestimation of regurgitation severity (N = 15, 79% of total misdiagnosis). The most frequent misdiagnoses were in the moderate mitral regurgitation grade. Histogram analysis further reveals that the largest errors are associated with the slit orifice conditions (Figure 6-10). Errors were acceptably low for the round orifice data, but a high frequency of large errors were observed for the slit orifice conditions.

**Table 6-5 Misdiagnosis incidence by regurgitant grade was reported.**

Mitral Regurgitation Grade	Total
Mild	2 (↑)
Moderate	2 (↑) 10(↓)
Severe	5(↓)
Total	4(↑) 15(↓)

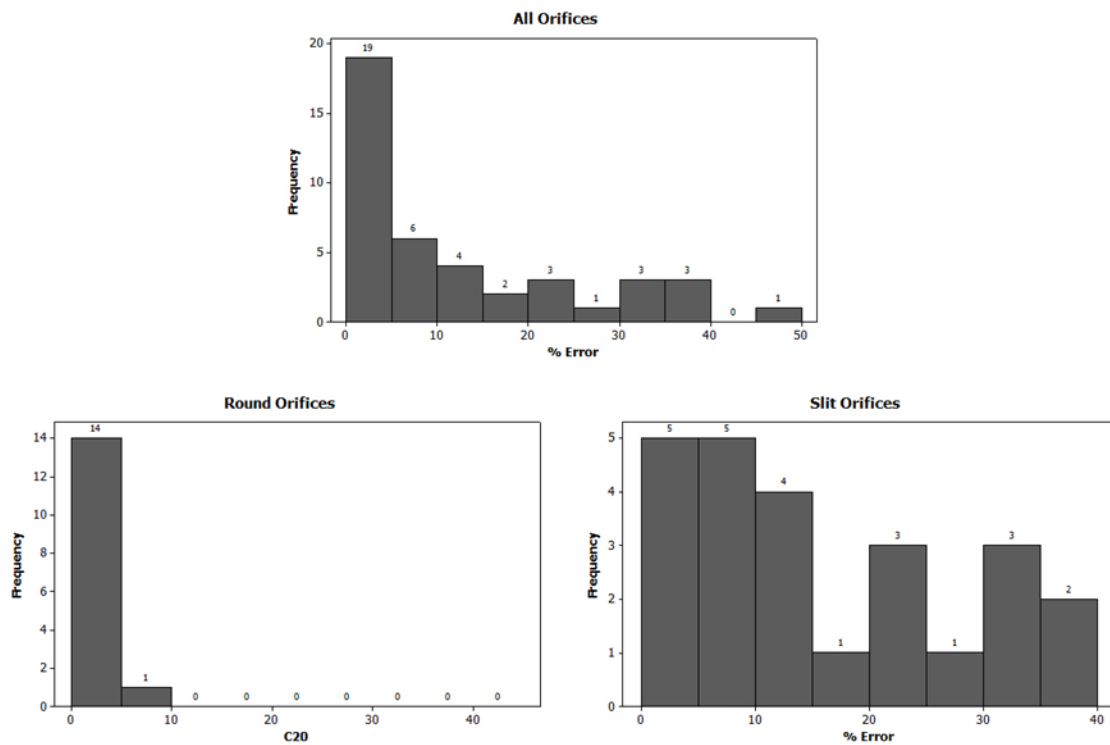


**Figure 6-10 Histogram distribution of percent errors were grouped for round and slit orifice data.**

### 6.2.3.2 Iteration 2: Adaptive Adjustment of Radii for Velocity Integration

Previously, this was pre-defined, and the radii chosen were applied to all frames of the cardiac cycle (Figure 6-11). This is a non-trivial undertaking as the minimum selected radius is known to have a large effect on the calculated regurgitant volume.

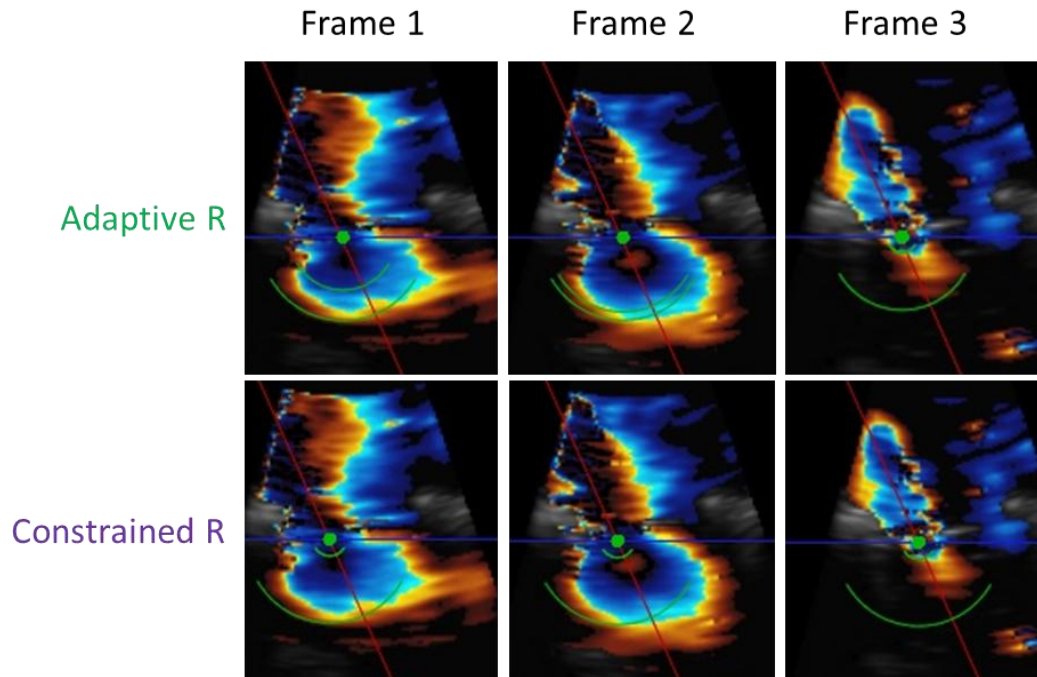


**Figure 6-11** The top panels show the radius is adjusted between frames of the cardiac cycle. This is most clearly observed as the minimum radius increases then decreases from frame 1 to 2 and then from frame 2 to 3. In the bottom panel, the radius is predefined and constrained. (Green dot is the origin of the flow convergence. The two curved bands are the minimum and maximum radius over which the velocities are integrated).

The analysis was first performed on the 3 data points identified previously as outliers for the round orifice data. In all three cases, the new measurement was more accurate, as can be seen in Table 6-6. Previously, the FOM analysis severely underestimated the regurgitant volume. With the adaptive radii implementation, two of the three measured regurgitant volumes were accurate to within 3 mL. The third case

overestimated the true regurgitant volume. While the new method was more accurate, the results were slightly more variable. The average measurement standard deviation for these three cases increased from 1.2 to 3.5 mL per beat from the initial method to the new adaptive radii measurement. Similarly, the coefficient of variability slightly increased from 0.053 to 0.065. This underscores the difficulty of accurately and repeatedly identifying the necessary radii over which the velocity vectors should be integrated to calculate the regurgitant volume.

**Table 6-6 Reanalysis of round orifice outliers.**

Case	Initial FOM	Adaptive R	True
1	17.4 ± 1.5	51.2 ± 5.8	52.9
2	19.4 ± 1.3	52.8 ± 2.3	36.6
3	20.5 ± 0.2	62.8 ± 2.4	59.4

All slit orifice conditions were reanalyzed (Figure 6-12). Measured regurgitant volumes using the new adaptive radii algorithm were on average more accurate than previously measured over all flow rates (adaptive radii: 7.6 ± 7.8 mL; old FOM: 16.8 ± 13.1 mL), a statistically significant improvement. The difference between measured values between the new adaptive radii FOM and truth were not statistically significant (p = 0.081). Mitral regurgitation was no longer systematically underestimated as most data points lay onto or above the 1:1 line (regurgitant volume measured through ultrasound : regurgitation volume measured through flow probe). Contrarily, at higher regurgitant

volumes (60+) mitral regurgitation was overestimated. The average error was relatively low for both mild ( $2.8 \pm 2.0$  mL) and moderate ( $6.2 \pm 6.2$  mL) mitral regurgitation severity. Average error increased with severe mitral regurgitation to  $13.5 \pm 10.3$  mL. Overall, there was a slight overestimation measurement bias of 3.8 mL observed by Bland Altman analysis.

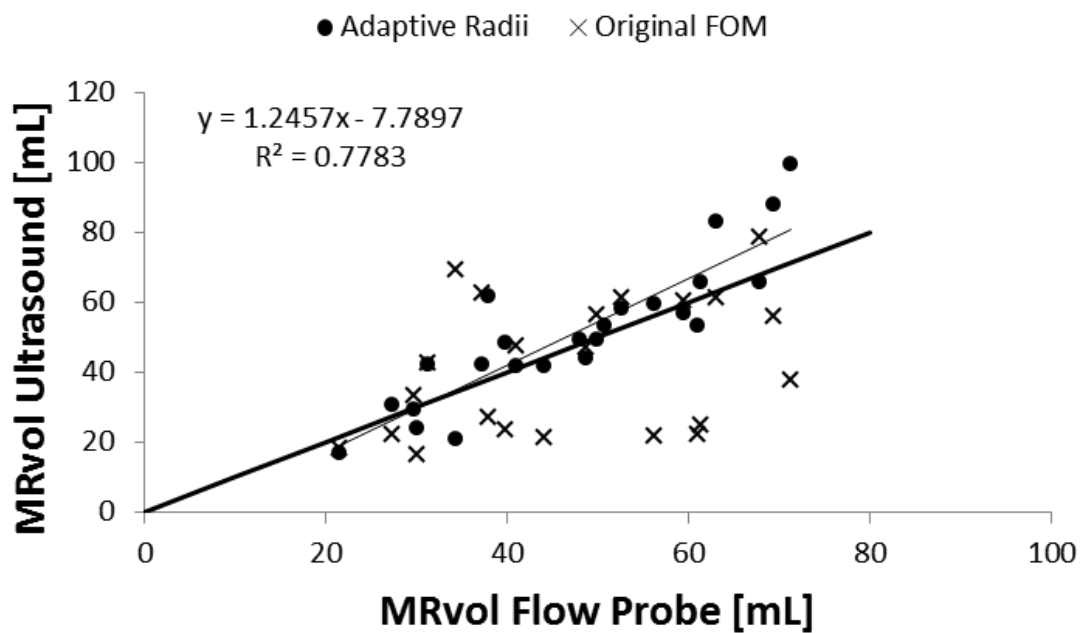


**Figure 6-12 Mitral regurgitation volume quantified through adaptive radii 3D FOM slightly overestimates the data. Dashed line represents 1:1.**

Additionally, as seen in Table 6-7 incidence of misdiagnosis was relatively low; only a total of 5 cases were identified. Of these five, there were two observed cases of underestimation of moderate mitral regurgitation, and one observed case of overestimation of mild mitral regurgitation. A histogram distribution shows 79% of the measured mitral regurgitation volumes were in an acceptable range ( $< 10\%$ ) (Figure 6-

13). This is a reversal from previously slit orifice analysis which contained equal distribution of errors.

**Table 6-7 Misdiagnosis incidence by regurgitant grade was reported.**

Mitral Regurgitation Grade	Total
Mild	1(↑)
Moderate	1 (↑) 2(↓)
Severe	1(↓)
Total	2(↑) 3(↓)

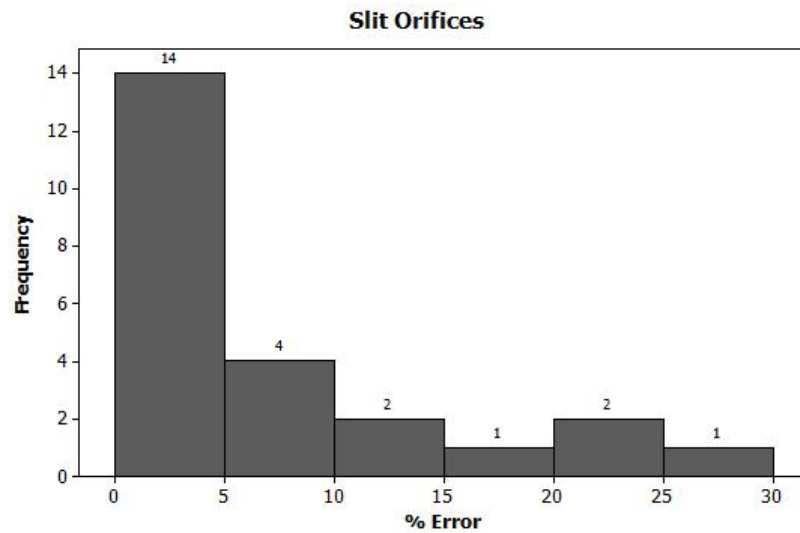


**Figure 6-13 Histogram distribution of percent errors between measured and truth regurgitant volumes for slit orifices.**

Finally, the algorithm proved relatively robust. For each condition, the measurement was repeated five times; the average and median standard deviation were 4.9 and 3.0 mL, respectively. The coefficient of variability increased slightly to 0.094 from 0.060 (comparison of adaptive radii to constrained radii), but this is still within an acceptable range. Collectively, these data show the updated 3D FOM can accurately measure mitral regurgitation over a wide range of regurgitant mitral orifices and flow rates.

#### 6.2.3.3 Iteration 3: Adaptive Adjustment of Regurgitant Orifice Z-height

All slit orifice conditions were reanalyzed (Figure 6-14). Measured regurgitant volumes using the new adaptive algorithm were on average more accurate than previously measured by the original FOM over all flow rates (adaptive z:  $8.2 \pm 7.2$  mL; old FOM:  $16.8 \pm 13.1$  mL), a statistically significant improvement ( $p < 0.005$ ).

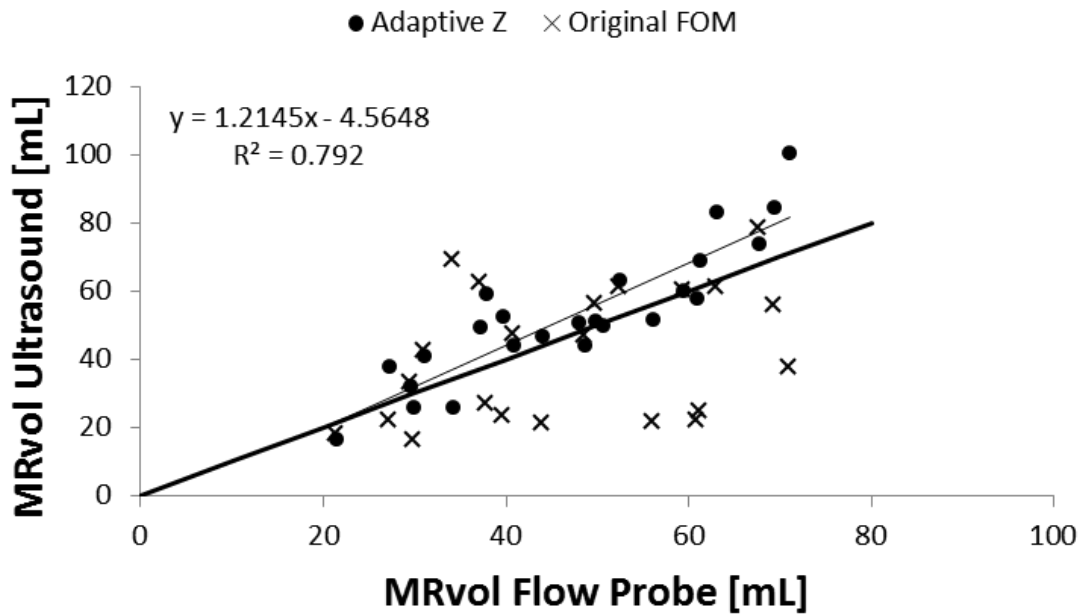


**Figure 6-14 Mitral regurgitation volume quantified through adaptive z-height 3D FOM slightly overestimates the data. Dashed line represents 1:1.**

However, this method had slightly reduced accuracy ( $p = 0.036$ ) as compared to the adaptive radii method without automated z-height adjustment (adaptive z:  $8.2 \pm 7.2$  mL; adaptive radii without adaptive z:  $7.6 \pm 7.8$ ). The overall trend in data were similar as well as observed by the linear regressions (adaptive z:  $1.22x - 4.5$ ,  $R^2 = 0.79$ ; adaptive radii without adaptive z:  $1.25x - 7.79$ ,  $R^2 = 0.78$ ). Surprisingly, these two adaptive algorithms were comparatively robust. The median and mean measurement standard deviation for the adaptive z-height method were 3.9 and 4.7, respectively (compared to 3.9 and 4.9 for the constrained z-height). The coefficients of variability were not statistically different (CV adaptive r: 0.094; CV adaptive z: 0.090;  $p = 0.805$ ).

The difference between measured values between the new adaptive z-height FOM and truth were statistically significant ( $p = 0.009$ ). This was mostly a result of the



relatively large errors at the higher regurgitant volumes. The average error was relatively low for both mild ( $5.9 \pm 4.2$  mL) and moderate ( $6.6 \pm 5.9$  mL) mitral regurgitation severity. These were both negligibly larger than the previous iteration of the Field Optimization Method. Average error increased with severe mitral regurgitation to  $13.5 \pm 9.8$  mL, which was comparable to the second iteration and better than the measurements from the initial algorithm. However, because this error was due to overestimation, clinically this would have minimal effect on patient diagnosis. Overall, there was a slight overestimation measurement bias of 5.6 mL observed by Bland Altman analysis. Mitral regurgitation was rarely underestimated as most data points lay on or above the 1:1 line (regurgitant volume measured through ultrasound : regurgitation volume measured through flow probe). Contrarily, at higher regurgitant volumes (60+) mitral regurgitation was overestimated.

As seen in Table 6-8 incidence of misdiagnosis was relatively low; only a total of 6 cases were identified. Of these six, there were two observed cases of underestimation of moderate mitral regurgitation, and two observed case of overestimation of mild mitral regurgitation. A histogram distribution shows 67% of the measured mitral regurgitation volumes were in an acceptable range ( $< 10\%$ ) (Figure 6-15). This is an improvement over the initial algorithm, but is worse than the adaptive radii algorithm.

**Table 6-8 Misdiagnosis incidence by regurgitant grade was reported.**

Mitral Regurgitation Grade	Total
Mild	2 (↑)
Moderate	1 (↑) 2(↓)
Severe	1(↓)
Total	3(↑) 3(↓)

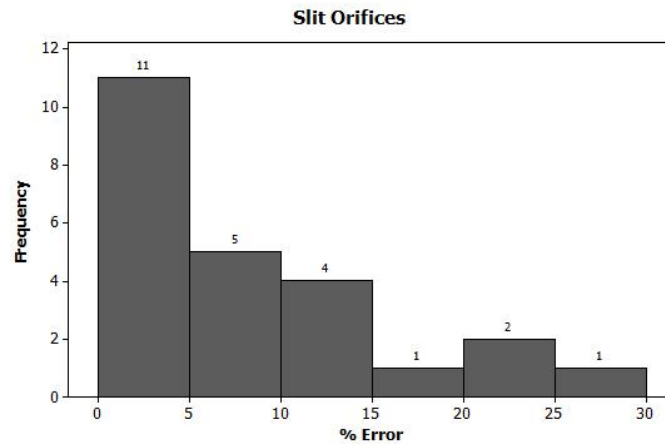


**Figure 6-15 Histogram distribution of percent errors between measured and truth regurgitant volumes for slit orifices.**

Collectively, these data show the updated 3D FOM can more accurately measure mitral regurgitation over a wide range of regurgitant mitral orifices and flow rates as compared to the initial algorithm. However, the updated algorithm did not perform as well as the adaptive radii only algorithm.

### 6.3 3D Integrative PISA

3D Integrative PISA was performed on all data sets with available Continuous Wave Doppler echocardiography (N = 30) (Figure 6-16). As previously noted in 6.1.2, CW data was not available for all 42 data sets. Previously measured  $V_{\max}$  and VTI from the 2D PISA analysis were retained for the 3D Integrative PISA analysis. Average error across all data points was low ( $5.9 \pm 3.3$  mL). The difference between measured values by the integrative 3D PISA method and truth were not statistically significant ( $p = 0.625$ ). Measurement bias was similarly low ( $-0.6$  mL) (Figure 6-17).

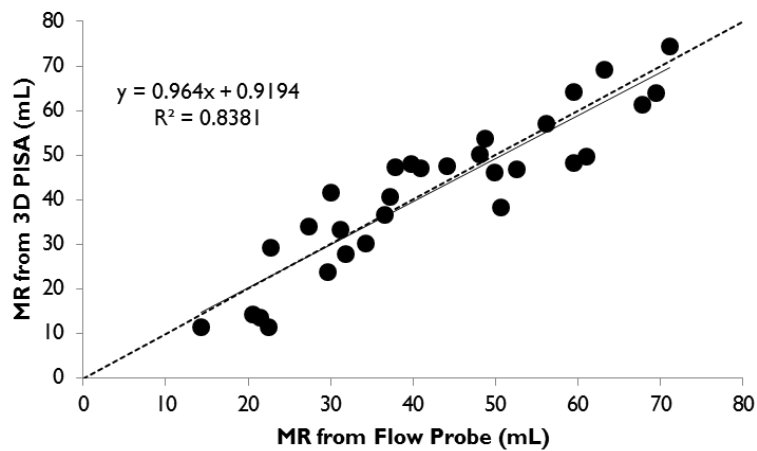


**Figure 6-16 Mitral regurgitation volume quantified through the integrative 3D PISA method correlates closely to the truth data. Dashed line represents 1:1.**

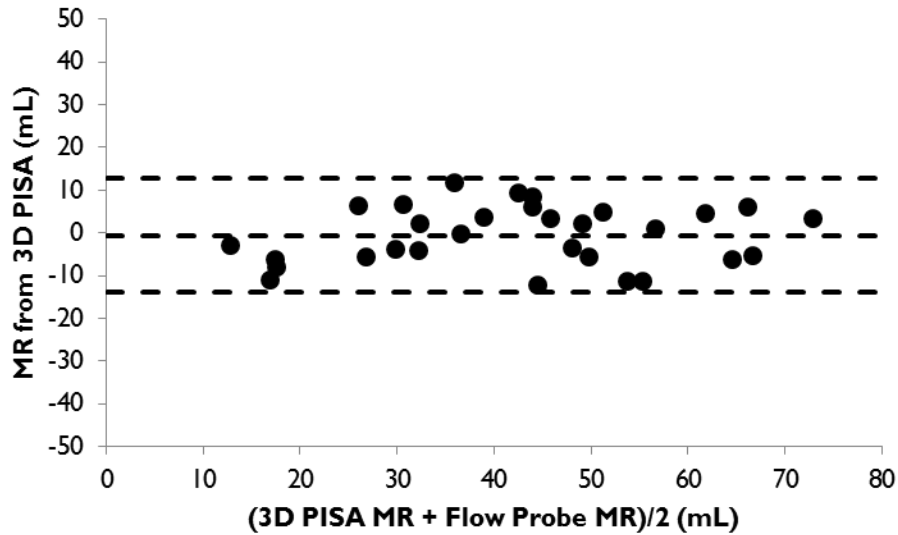


**Figure 6-17 Mitral regurgitation volume quantified through the integrative 3D PISA method has a minimal measurement bias. Dashed lines show mean  $\pm$  2 standard deviations**

These trends were consistent across both round and slit orifices (Figure 6-18). Average error for the round orifice was  $6.0 \pm 4.1$  mL with a measurement bias of  $-4.1$  mL (Table 6-9). Average error for the slit orifice was  $5.9 \pm 3.1$  mL with a measurement bias of  $0.4$  mL. Average error across all regurgitant grades was low for both orifice types. No data were available for severe regurgitation through a round orifice.

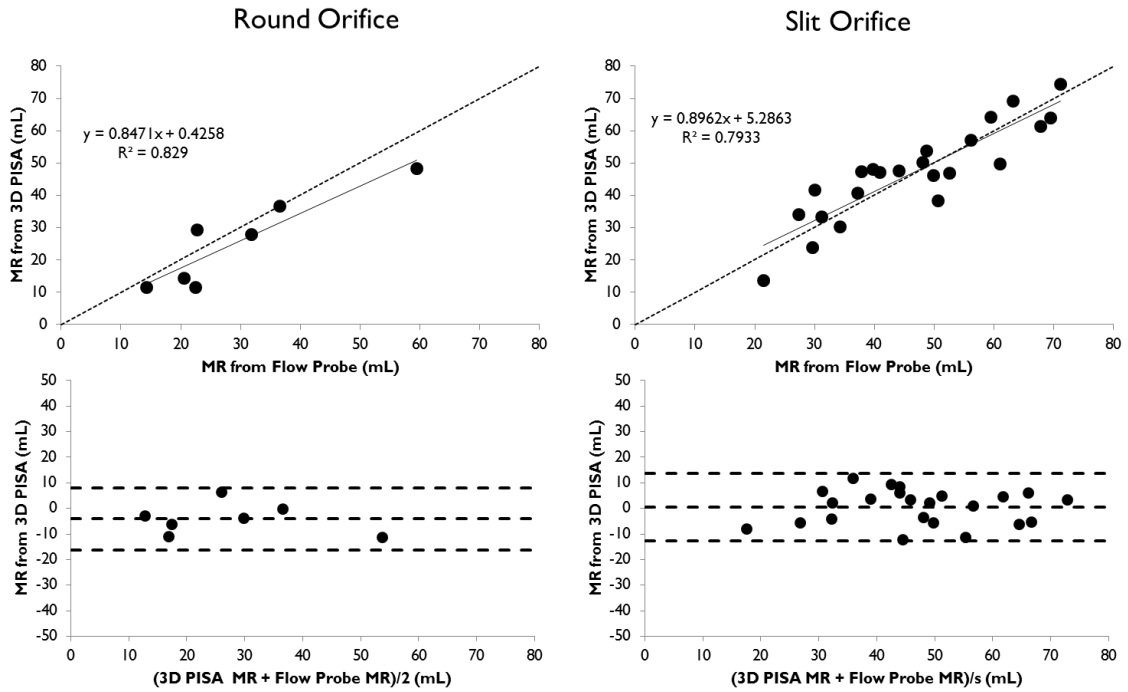


**Figure 6-18** Data were grouped for round and slit orifice. The Integrative 3D PISA method was comparably accurate for the round and slit orifice data.

**Table 6-9** Reported errors for the Integrative 3D PISA method grouped by orifice type and regurgitant severity.

Mitral Regurgitation Grade	Total	Round	Slit
Mild	7.3 ± 2.8	6.6 ± 3.4	7.9 ± 2.5
Moderate	5.5 ± 3.6	5.5 ± 3.4	5.5 ± 3.4
Severe	6.5 ± 3.0	--	6.5 ± 3.0
Total	5.9 ± 3.3	6.0 ± 4.1	5.9 ± 3.1

Misdiagnosis incidence was reported as the frequency of erroneous regurgitation grading by 3D Integrative PISA (Table 6-10). There were four total events of misdiagnosis; over- and underestimation occurred at the same frequency. The most frequent misdiagnoses were in the moderate mitral regurgitation grade. 83% of the data (N = 26/30) have an acceptable percent error from the truth (Figure 6-19). All of the errors fall below 15% on a histogram distribution.

**Table 6-10 Misdiagnosis incidence by regurgitant grade was reported.**

Mitral Regurgitation Grade	Total
Mild	1(↑)
Moderate	1(↑) 1(↓)
Severe	1(↓)
Total	2(↑) 2(↓)

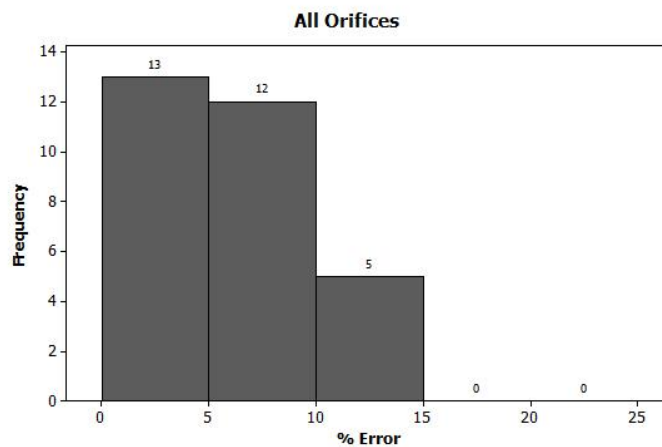


**Figure 6-19 Histogram distribution of percent errors between measured and truth regurgitant volumes for slit orifices.**

## 6.4 Discussion

An *in-vitro* pulsatile mitral valve regurgitation model using native ovine heart valves was successfully developed. A wide range of mitral regurgitation conditions were created for maximal clinical relevance. The higher flow rates were all associated with the comparatively larger slit orifices. Geometric orifice area of a round orifice was the limiting factor. To produce large orifices, the mitral annulus was dilated; however, because annular dilation was performed globally throughout the circumference of the annulus, leaflet coaptation was equally lost throughout the line of closure. This resulted in a slit orifice, making it impossible to create severe regurgitation through a round orifice. Mild (35.7%) and moderate (50%) severity was created with greater frequency as they are associated lower quantification accuracy [167]. Moreover, accurately determining mild and moderate regurgitation severity may affect surgical indication. Surgical intervention may be delayed for asymptomatic patients presenting with mild regurgitation, whereas patients with moderate to severe regurgitation would be more readily referred for surgery.

Mitral regurgitation was quantified using three general methods. 2D PISA analysis was performed as it is the currently used quantitative clinical measurement. 2D PISA is a simple well established method and its limitations are also well understood. Consequently, more complicated 3D PISA techniques should be comparable to or more accurate and robust than the 2D PISA method to establish clinical efficacy.

As expected, there was very little error in measured regurgitant volume by 2D PISA for round orifices. This is consistent with previous validation studies [164]. However, there was a systematic underestimation of regurgitant volume for the slit

orifices. This underestimation is consistent with previous studies, and is a result of the hemispherical assumption of the isovelocity surface areas. The violation of this assumption was later confirmed through the integrative 3D PISA method which extracted the isovelocity surface area at a given aliasing velocity.

In addition to characterizing the accuracy of 2D PISA, measurement robustness was explored. It was found that intra-observer repeatability was equally poor for both orifice conditions. This is a known issue associated with the difficulty of manually identifying the regurgitant orifice (Figure 6-20) [18,167]. Subsequently, the radial measurement made from the orifice to the isovelocity surface area is affected. As the calculated regurgitant volume from the 2D PISA method is proportional to  $R^2$ , small errors in radius measurements may have large effects. This lack of measurement robustness is a key challenge in the development of the Philips FOM, as well as other 3D PISA methods.

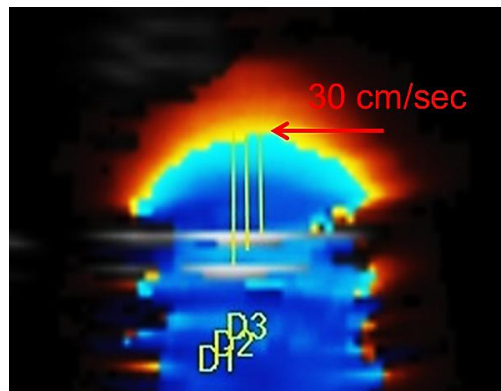


**Figure 6-20** There is an uncertainty associated with identifying the origin of flow convergence and the subsequent radial measurement to the velocity isosurface.



The Philips 3D Field Optimization Method has been previously validated in an idealized *in-vitro* setting against nominal planar pin hole and c-slit regurgitant orifices created in acrylic plates [167]. However, this simplistic model is limited; native mitral regurgitant orifices are three-dimensional and non-planar (the z-height of the orifice may change across its lateral spread and the leaflets rarely oppose each other at a 180° angle) and dynamic throughout the cardiac cycle. Identifying the location of the regurgitant orifice in each frame is non-trivial, particularly by automated techniques. For these reasons, in collaboration with Philips Healthcare, the accuracy of the 3D FOM was assessed in a pulsatile native mitral valve left heart simulator.

Three successive iterations of the 3D FOM were investigated. In the first iteration, velocities in the flow convergence zone were integrated over a fixed, pre-determined radius. Subsequently, in an effort to improve the accuracy of the Field Optimization Method, the algorithm was adjusted to automatically identify the correct radii over which to integrate velocities of the flow convergence zone. A final adjustment to the Field Optimization Method was to implement an algorithm to adaptively locate the orifice in each frame of the cardiac cycle. In the two previous iterations, the orifice was constrained to the location initialized by the user in the chosen ultrasound frame (typically selected as the frame with the largest proximal isovelocity surface area).

The fixed radii 3D FOM was as accurate as the 2D PISA method for round orifices. Three cases were identified as outliers in the round orifice data and excluded from this statistical comparison. These three data points corresponded to three of the four largest regurgitant flow rates created for the round orifice and warranted further investigation. Additionally, there was a decrease in accuracy for the slit orifices,

particularly those at higher regurgitant volumes. Reanalysis of these conditions identified that the calculated regurgitant volume was strongly sensitive to the pre-defined radii chosen and applied to all frames of the cardiac cycle. Specifically, for these data, the calculated regurgitant volume was most sensitive to the minimum defined radius.

This is because flow closest to the orifice has the highest velocities and enters what is known as the “decorrelation zone” [167]. In the decorrelation zone, flow is unpredictably turbulent and the velocity profile is no longer inversely proportional to the radius squared ( $V \propto 1/R^2$ ) (Figure 6-21). The decorrelation zone is larger at greater flow rates adding to the complexity of empirically pre-defining the minimum radius. This will be a point of emphasis in future studies utilizing highly-resolved velocity data from particle imaging velocimetry (see future studies, 9.3.1).

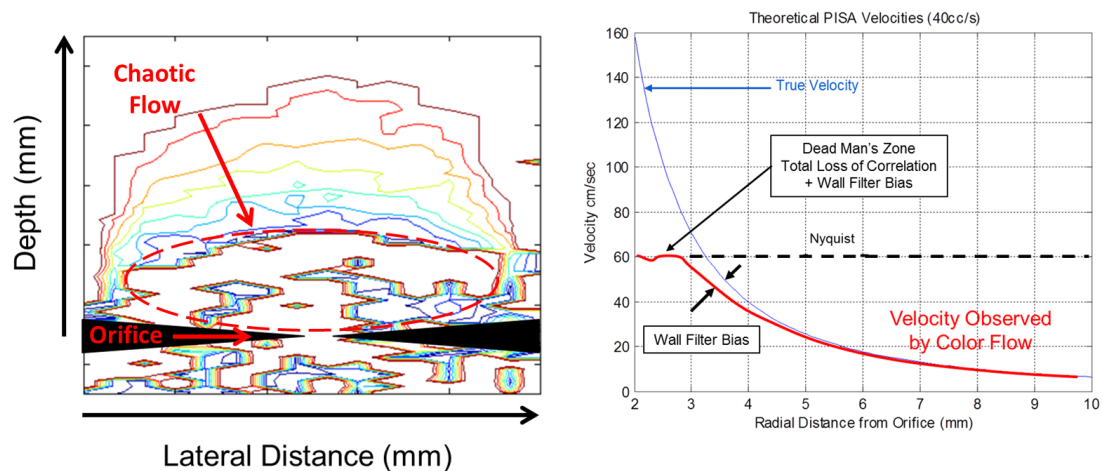


**Figure 6-21 (Left) Near to the mitral orifice, highly turbulent and chaotic flow defines the decorrelation zone. (Right) In the decorrelation zone, the velocity profile no longer follows the expected relationship ( $V \propto 1/R^2$ ) [167].**

It is easier, however, to identify the maximum radius as the calculated regurgitant volume is not as sensitive to small changes in this dimension. This is because of the inverse relationship described above; velocities at larger radii are smallest. Therefore, the exclusion of this low velocity flow does not impact the total regurgitant volume calculated. However, it should be noted that large noise near the outer border of the isovelocity surface area may erroneously increase the regurgitant volume calculated. Additionally, proximity of the left ventricular outflow to the regurgitant flow may cause these velocities to be incorrectly included for analysis.

Implementation of the adaptive radii algorithm increased the overall accuracy of the 3D FOM to calculate regurgitant volume for both round and slit orifices. For the round orifice conditions, the adaptive radii 3D FOM was comparably accurate to the 2D PISA method. However, there was a marked improvement in analysis accuracy for the slit orifice conditions, particularly for the mild and moderate regurgitant severities. Most of the observed large errors corresponded to severe mitral regurgitation. Fortunately, for these cases, the adaptive radii 3D FOM overestimated total regurgitant volume. Clinically, this would have minimal effect on patient diagnosis; surgery would be correctly indicated.

A final iteration to the 3D FOM was implemented to account for the dynamics of the heart and mitral apparatus throughout the cardiac cycle. These motions may cause apical-basal translation of the regurgitant orifice from frame to frame. If the location of the orifice were restrained in a case when migration was present, mitral regurgitation would be erroneously calculated due to the under- or over-estimation of the isosurface area (Figure 6-22).

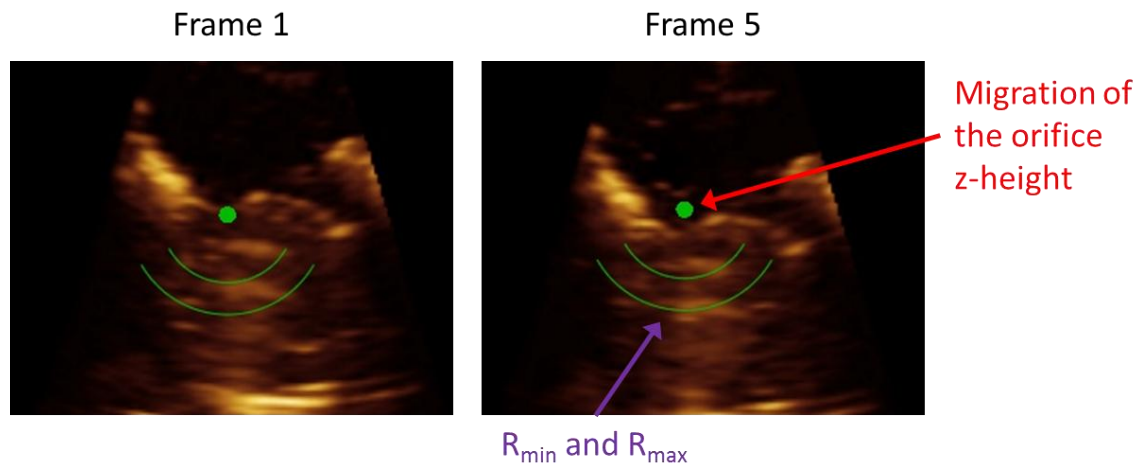


**Figure 6-22 Erroneous migration of the apical-basal position of the mitral orifice is seen between two frames in the cardiac cycle.**

The adaptive z-height 3D FOM algorithm was observed to be comparably accurate as the adaptive radii 3D FOM. Additionally, as with the adaptive radii iteration, the adaptive z-height method was more accurate for slit orifice conditions than 2D PISA. Similar to the previous iteration of the 3D FOM, the large errors were predominantly localized to over-estimation of severe mitral regurgitation. Again, this would have minimal clinical impact, as surgical would remain correctly indicated.

Of note, however, each of the 3D FOM iterations demonstrated intra-observer measurement repeatability. Each of these three techniques was more robust than the 2D PISA measurements. Between 3D FOM techniques, the initial constrained radii algorithm was the most robust, but this was associated with unacceptable accuracy. Both of the adaptive algorithms were comparably and acceptably robust.

It should be noted however, that data corresponding to very large discrepancy (greater than 3 mm) between automated z-height orifice location and true orifice location

were rejected during initial observations; these measurements were repeated. This artificially improved the robustness of the adaptive z-height algorithm. This erroneous migration of the adaptive z-height orifice location was easily identifiable. Such a selection criteria could be readily applied in the clinic to advise a trained user. However, it is recommended that further studies should be performed on the intra-observer variability in a more dynamic system. In the present left heart simulator, there is minimal apical-basal translation of the regurgitant orifice. Specifically, the left heart simulator does not mimic annular motion or the apical-basal contraction of the heart. Moreover, the position of the ultrasound probe to the mitral annular plane was fixed. These limitations could underscore the similarity in the accuracy and robustness of the two iterations.

A final source of error was explored for the 3D Field Optimization Method following empirical observation of the limited temporal frequency of the echocardiography acquisition. For all 3D FOM analysis, only 3-5 frames of the cardiac cycle (250 msec regurgitation period) were available during systole; typical acquisition frame rate was 20 Hz (1/50 msec). Due to discrete sampling, the regurgitation period may have been under-sampled by 1-2 frames (or 50- 100 msec). Regurgitation period as measured by 3D FOM and through direct flow measurements were compared. On average, 3D FOM underestimated regurgitation period by  $9.3 \pm 27.2$  msec. A simple case study shows the effect of offsetting the initial and final time frame due to discrete sampling, which could cause up to a 20 mL underestimation of true regurgitant volume (Table 6-11). This may be worse for clinical data were acquisition frequency can be as low as 11 Hz and only 1-2 frames comprise the regurgitant period.

**Table 6-11 Discrete temporal sampling by the ultrasound system may affect regurgitation quantification by up to 20 mL per beat. These values were extracted from a representative hemodynamic waveform.**

Offset		Total
Initial Time Point [msec]	Final Time Point [msec]	Mitral Regurgitation [mL]
0	0	54.3
+50	0	38.2
0	-50	44.7
+50	-50	28.7

One source of error not investigated in these studies is the effect of the initial hemispherical guess performed in the FOM analysis (as mentioned in section 2.5). As previously explained, the FOM uses an initial hemispherical estimation of the proximal flow; this is an estimation of the true velocity field. Next, the FOM applies ultrasound physics to calculate an “observed” velocity field. This corrects for the cosine angle projection of the true velocity vectors projected onto the ultrasound scan lines. Subsequently, the true velocity vectors are iterated until the error field between the calculated and true observed velocities is minimized. Once the error is minimized, the velocity vectors are integrated to calculate the regurgitant volume. However, this process is limited by the initial estimation applies a hemispherical velocity field.

Pioneering work by Hopmeyer et al. suggests a hemi-elliptical model of the isovelocity surface areas may be better suited for this initial estimation [202,203]. In their studies, Hopmeyer et al. used hemi-elliptical curve fitting applied to digitized isovelocity flow data from two perpendicular long-axis color Doppler planes. From each plane, the

height and widths of the isovelocity contour were extracted. Next, the total surface area was computed using elliptical integrals as described in [208]. This method demonstrated promise in accurately quantifying regurgitant volumes over a range of flow rates, and was more accurate than a hemispherical assumption in their in-vitro studies. With the advances of three-dimensional echocardiography, this hemi-elliptical curve fitting may be applied to additional lateral planes of the proximal convergent flow. This will improve the estimation of the isovelocity surface area. Such a technique may be implemented in future iterations of the FOM to more accurately represent the isovelocity surface areas. This may be performed in place of the initial hemispherical assumption currently used.

A final analysis technique was performed using a manual method. The intention of this was to confirm the utility of the experimental three dimensional echocardiography data as a gold standard by which similar analyses could be developed and validated. This was performed in parallel with the Philips collaborative studies.

3D Integrative PISA method was based on several previously published studies which sought to specifically improve on the hemispherical assumption of 2D PISA [165]. In this technique, a single frame with the largest isosurface was identified; subsequently, the isosurface was manually segmented through several lateral slices. A surface mesh was fit to the generated point cloud and the total surface area was calculated. A key benefit of this technique is that the location of the regurgitant orifice does not have to be identified (nor is a radius measurement explicitly taken). This removes errors associated with this uncertainty. It must be noted, however, that this technique was manually intensive and time consuming (~ 30 min), which makes it unsuitable for clinical use.

3D Integrative PISA was observed to very accurate over the range of regurgitation flow rates and orifices. Overall, the 3D Integrative PISA method was the most accurate of the analyses performed; this was somewhat unexpected. This technique did not correct for the Doppler angle effect. Therefore, in theory, a systematic underestimation (potentially up to 40%) should have been observed. It's quite possible that the expected underestimation was offset by measuring only the single largest PISA instead of integrating over multiple frames in the cardiac cycle. Potentially, this can be confirmed through a more thorough manual analysis, but is currently unnecessary for the intent of developing and validating the Philips FOM.

There are three insights which were gained from the 3D Integrative PISA method which could be applied to future iterations of the Field Optimization Method. First, it is comparatively easier to identify the isoveLOCITY surface area (isosurface at a defined aliasing velocity) than it is to identify the origin of the regurgitant orifice. This also removes uncertainty associated with the subsequent radius measurements from said orifice. Second, it is not necessary to integrate the regurgitant volume over several frames. It is sufficient to analyze the regurgitant isosurface in a single frame (preferably the frame with the largest identifiable PISA) and utilize information for Continuous Wave Doppler to complete the measurement. This removes limitations associated with temporal frequency, which can manifest in clinical data where only 1-2 frames may represent the entire regurgitant period. Finally, by performing the PISA analysis using a single frame, uncertainty associated with a dynamic or migrating regurgitant orifice is removed.



These insights are consistent with the pioneering observations by Hopmeyer et al. In each method, the focus was to identify the isovelocity surface area, regardless of the location of the regurgitant orifice. As explained above this reduces errors associated with identifying the dynamic orifice. Both techniques were accurate in resolving regurgitant flows using only one frame of the cardiac cycle, which identified the single largest regurgitant jet. While not investigated in this study, it is expected that the proximity of the flow convergence zone to the left ventricular myocardium and outflow tract would not affect the accuracy of the 3D Integrative PISA. This was a motivating factor the hemi-elliptical assumption. It is now known however, if the FOM would be susceptible to such flows due to its current use of the hemispherical model. Finally, the generated surface meshes of the 3D Integrative PISA method can be used to refine the approximation of the hemi-elliptical model, which may then be implemented in the FOM.

## 6.5 Conclusions

A mitral regurgitation model using native (ovine) heart valves in a pulsatile left heart simulator was established. This model was able to create several regurgitant orifices and flow rates representing a wide range of valvular insufficiencies. For all conditions, a true gold standard measurement was acquired, which may be used for analysis development and validation. The accuracy and repeatability of the Philips FOM was assessed over three algorithm iterations, and were compared to truth as well as the current clinical quantitative standard, 2D PISA. The Philips FOM using an adaptive radii algorithm was accurate and robust over a wide range of regurgitant offices and flow rates. However, the

FOM algorithm performed worse when the z-height was automatically adjusted from frame to frame, suggesting further development may be needed.

## CHAPTER 7

### SPECIFIC AIM 2: SURGICAL MANAGEMENT OF ISCHEMIC MITRAL REGURGITATION

#### 7.1 Introduction

In the previous chapter, improved patient diagnosis was explored through novel quantitative methods; this is the first step in optimizing patient surgical management. In this chapter, two adjunctive surgical repairs are evaluated for their functional benefit and their effect on leaflet-subvalvular tethering. Through evaluating these surgical repairs in an *in-vitro* and carefully controlled experimental environment, a mechanistic understanding of their efficacy can be gained. This, in turn, will add to the surgical toolbox from which patient specific surgical repairs may be performed based on preoperative diagnosis.

Ischemic mitral valve disease is one particular landscape for which new and targeted surgical repair is believed to be needed. Ischemic mitral regurgitation is a complex disease process stemming from a multifactorial pathology [13,180,191,209]. Myocardial infarction or chronic ischemia results in left ventricular remodeling, dilation and dysfunction. These combined effects disrupt mitral valve geometric relations leading to mitral annular flattening and dilation and papillary muscle displacement. Collectively, this causes Carpentier's type IIIb valvular dysfunction, or restricted systolic leaflet motion, and insufficiency, or mitral regurgitation. If left untreated, ischemic mitral

regurgitation is associated with a two-fold increase in patient mortality [12]. Moreover, ischemic mitral regurgitation severity has a graded relationship with reduced survival and increased heart failure [12].

While significant knowledge of ischemic mitral regurgitation and its physiological impact exists, its surgical management remains controversial [55,56,58,160,210-212]. Amid this controversy, restrictive mitral annuloplasty, performed with a complete rigid ring has been regarded as the preferred surgical repair [160,162]. While typically effective, approximately 10-15 % patients, specifically those presenting with severe left ventricular dilation, suffer from recurrent or persistent mitral regurgitation, have low rates of reverse left ventricular remodeling, and exhibit poor survival [13-17].

Several studies have identified pre-operative characteristics which are predictive of simple annuloplasty failure, including: mitral regurgitation grade [49] and jet characteristics [46], coaptation length [51,52], interpapillary muscle distance [53], and left ventricular dilation [48,50]. These studies have identified excessive leaflet restriction through tethered chordae and pathologically displaced papillary muscles as a key contributor to repair failure. Additionally, it is believed that further tethering may be produced through the unnatural downsizing of the mitral annulus by restrictive mitral annuloplasty . Downsizing annuloplasty hoists the posterior annulus directionally away from pathologically displaced papillary muscle (Figure 7-1). In turn, valvular function effectively becomes unicuspid, as the posterior leaflet is “chordalized” and immobile [38]. The anterior leaflet becomes solely responsible for maintaining valvular

competency and overall coaptation redundancy is reduced. Ultimately, the valve is susceptible to any further left ventricular remodeling [44-47,213].

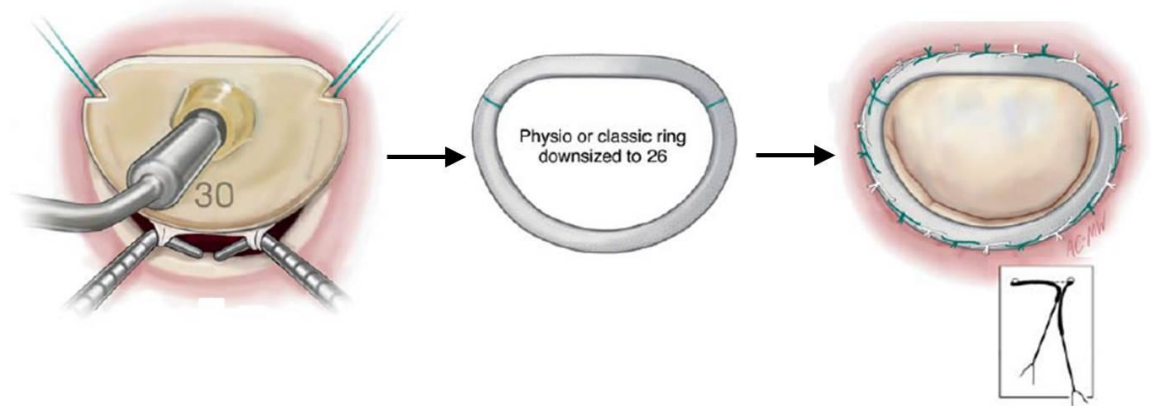


**Figure 7-1 Restrictive mitral annuloplasty is performed by systematically downsizing the mitral annulus by two sizes using a rigid ring. As a result, mitral coaptation is dominated by the anterior leaflet; the posterior leaflet is chordalized.**

Consequently, new adjunct surgical strategies have been attempted to compensate for severely dilated left ventricles [17,54-58]. When completed with mitral annuloplasty, these adjunct strategies are hypothesized to further alleviate chordal-leaflet tethering, improve leaflet mobility, and maximize leaflet coaptation. Of note, anterior leaflet augmentation [57,58] and basal papillary muscle relocation (Kron Procedure) [17,56] have been recently demonstrated to restore leaflet coaptation and mobility without the need to unnaturally undersize the mitral annulus . While preliminary studies have demonstrated the potential benefits of these two adjunct procedures, little knowledge exists of what mechanistic improvements in valve function can be expected.

In this chapter, the functional benefit and effect on leaflet-subvalvular tethering of anterior leaflet augmentation and basal papillary muscle relocation as adjunctive

procedures to true-size mitral annuloplasty for the repair of ischemic mitral regurgitation will be presented. As it is hypothesized that surgical repair should aim to restore normal physiology, each surgical repair will be compared to control (or healthy mitral valve) function. Additionally, improvements in mitral valve function as compared to the preferred surgical technique, isolated mitral annuloplasty, are explained.

## 7.2 Anterior Leaflet Augmentation

Anterior leaflet augmentation is an adjunctive procedure to mitral annuloplasty, in which pericardial tissue is used to increase the surface area of the anterior leaflet. The increased anterior leaflet area is expected to provide greater leaflet redundancy to promote valve competency.

Anterior leaflet augmentation was performed with either a small or large pericardial patch to further elucidate the potential effects of procedural technique, i.e. does the size of the pericardial patch determine its efficacy. It is hypothesized that anterior leaflet augmentation will achieve comparable leaflet coaptation to restrictive mitral annuloplasty, while yielding significant improvements in leaflet tethering as measured by chordal forces.

### 7.2.1 Results

The results of this section are subdivided into (i) development of the ischemic mitral regurgitation model, and (ii) surgical repair. Surgical repair was performed as undersized mitral annuloplasty, and anterior leaflet augmentation with true-sized annuloplasty. The

main experimental endpoints are mitral regurgitation grade, leaflet coaptation length, and chordal forces

#### 7.2.1.1 Ischemic Mitral Regurgitation

Ischemic mitral regurgitation was successfully simulated with asymmetric annular dilation and papillary muscle displacement for all experimental conditions (3+ MR grade: N = 4; 4+ MR Grade: N = 11) (Table 7-1).

**Table 7-1 Mitral regurgitation grade of N = 15 experiments for the ischemic mitral regurgitation model.**

<b>Mitral Regurgitation Grade</b>	<b>N</b>	<b>Volume Fraction [regurgitation/stroke]</b>
< 3+	0	< 29 %
3+	4	30 – 59 %
4+	11	> 60 %

Mitral regurgitation was graded based on the volume fraction of regurgitation to forward flow (stroke volume ~ 70 mL) [24]. This normalized any potential differences in total regurgitation volume due to possible variations in pulsatile hemodynamics. A volume fraction of 30-59% is graded as 3+ mitral regurgitation; a volume fraction greater than 60% is characterized as 4+ [24]. The combined annular and papillary muscle alterations did not produce mitral regurgitation lower than 3+.

Further, mitral regurgitation was confirmed through color Doppler echocardiography. Large, asymmetric regurgitant jets were observed in combination

with severely tethered mitral leaflets (Figure 7-2). It should be noted that mitral regurgitation was not quantified through echocardiography, but solely through the direct flow measurements taken immediately upstream of the left atrium through the electromagnetic flow probe.

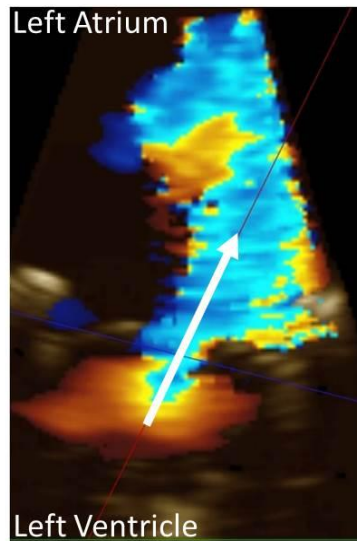


**Figure 7-2 Large asymmetric regurgitant jet. White arrow indicates flow direction.**

Noticeable leaflet tethering was observed in both the anterior and posterior leaflets, consistent with severe papillary muscle displacement [157]. This can be seen in Figure 7-3. The overlaid red lines trace the centerline of the mitral leaflets. Localized tethering points by the restricted mitral chordae are indicated by the white arrows. The green line denotes the mitral annular plane at which physiological coaptation takes place. As seen in Table 7-2, the anterior leaflet coaptation length was significantly decreased from the control condition (Control:  $4.8 \pm 0.5$  mm; IMR:  $3.2 \pm 0.5$  mm;  $p < 0.005$ ) at the central A2-P2 coaptation plane. It should be noted that all coaptation data were analyzed



at the central coaptation plane as chordal force transducers cause acoustic shadowing which prohibited accurate measurements in the off-center planes (A1-P1, A3-P3).

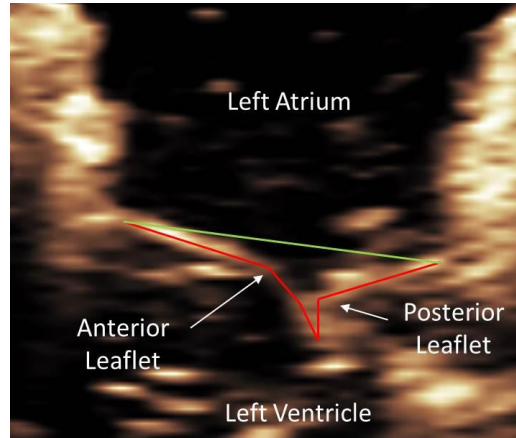


**Figure 7-3 Minimal coaptation is observed at the A2-P2 coaptation line. Anterior and posterior leaflets are tethered apically into the ventricle. A notable kink in each leaflet is observed due to chordal tethering.**

**Table 7-2 Coaptation length was significantly decreased from Control to IMR.**

	<b>Control</b>	<b>Ischemic Mitral Regurgitation</b>	<b><i>p value</i></b>
<b>Sample Size</b>	15	15	--
<b>Coaptation Length [mm]</b>	4.8 ± 0.5	3.2 ± 0.5	0.001

Chordal force data are summarized in Figure 7-4 and Table 7-3. Significant increases in tethering forces compared to the control group were observed for both the anterior strut and posterior intermediate chordae originating from the posteromedial papillary muscle. While modest increases were observed, no statistically significant

differences were observed for the anterior strut and posterior intermediate chordae originating from the anterolateral papillary muscle.

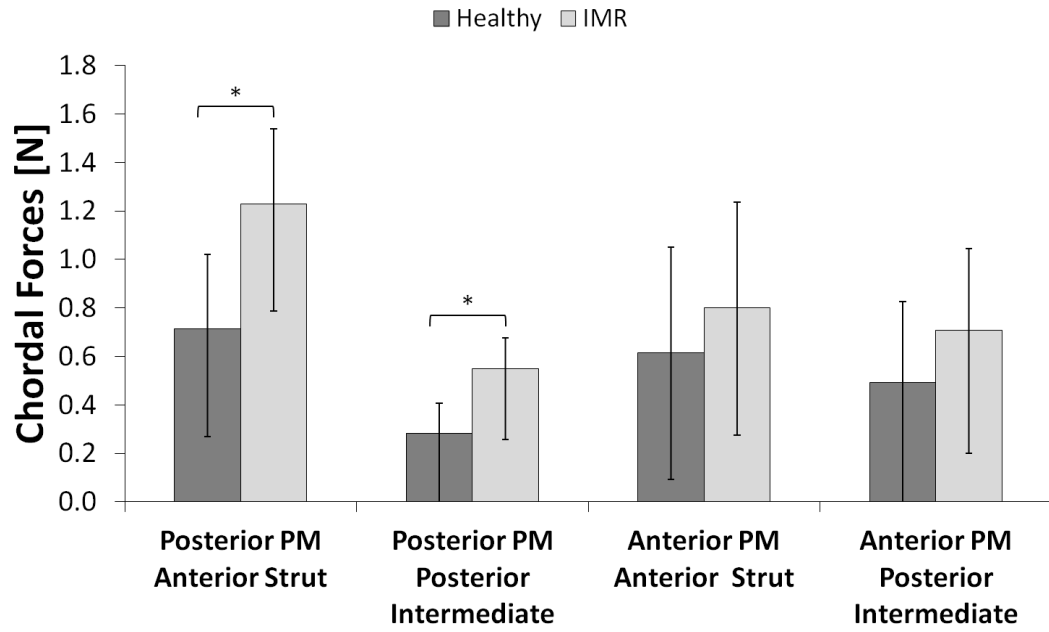


**Figure 7-4 Chordal forces were increased from the healthy to the IMR conditions. \* denotes significance between conditions at  $p < 0.05$ .**

**Table 7-3 Chordal forces for all four instrumented chordae in the control and Ischemic Mitral Regurgitation group.**

Papillary Muscle	Chordae	Control [N]	Ischemic Mitral Regurgitation [N]	<i>p value</i>
Posterior	Anterior Strut	0.71 ± 0.31	1.23 ± 0.44	0.001
	Posterior Intermediate	0.29 ± 0.13	0.55 ± 0.29	0.006
Anterior	Anterior Strut	0.62 ± 0.44	0.80 ± 0.52	0.304
	Posterior Intermediate	0.49 ± 0.34	0.71 ± 0.51	0.181

7.2.1.2 Undersized Annuloplasty versus Anterior Leaflet Augmentation with True-Size Annuloplasty

Surgical repairs were performed as undersized mitral annuloplasty (N = 15) and anterior leaflet augmentation with true sized mitral annuloplasty. Anterior leaflet augmentation was randomized to small (N = 8) and large (N = 7) pericardial patch procedures. The changes in anterior leaflet size due to pericardial patch insert are shown in Table 7-4.

**Table 7-4 Dimensions of the small and large anterior leaflet patch inserts.**

	<b>Small Patch N = 8</b>	<b>Large Patch N = 7</b>	<b><i>p</i> value</b>
<b>Length [cm]</b>	1.77 ± 0.10	2.68 ± 0.25	0.001
<b>Height [cm]</b>	0.65 ± 0.14	1.07 ± 0.10	0.001
<b>Area [cm<sup>2</sup>]</b>	0.86 ± 0.29	2.26 ± 0.36	0.001

All surgical repairs alleviated mitral regurgitation; no regurgitant jets were observed postoperatively through Color Doppler echocardiography. Additionally, all repairs significantly ( $p < 0.005$ ) increased coaptation length from ischemic mitral regurgitation (MR) back to or greater than control levels (Table 7-5). The large patch procedure resulted in an additional 1 mm gain in coaptation length, as the large patch significantly increased the anterior leaflet surface area available for coaptation.

**Table 7-5 Coaptation length was significantly increased by all three repairs compared to the IMR condition. \* Denotes significance ( $p < 0.05$ ) between large patch and both RMA and small patch.**

	<b>RMA</b>	<b>Small Patch</b>	<b>Large Patch</b>
<b>Sample Size</b>	15	8	7
<b>Coaptation Length [mm]</b>	4.7 ± 0.6	4.8 ± 0.5	5.8 ± 1.0 *

For heightened clinical relevancy, coaptation length is also shown as a percent increase from the ischemic mitral regurgitation condition to each repair (Figure 7-5). By

evaluating repair efficacy as a percent increase from the pathological condition, this data can be most readily translated to the clinic, where patient healthy levels are not known. Additionally, repair efficacy can be viewed in this normalized perspective to remove effects of variable valve size and geometry.

The large patch procedure with true-sized mitral annuloplasty resulted in the greatest improvement in coaptation length ( $98.3 \pm 31.0\%$  increase) as compared to ischemic mitral regurgitation. Restrictive mitral annuloplasty ( $51.0 \pm 21.3\%$  increase) and the small patch with true-sized annuloplasty ( $43.2 \pm 16.5\%$  increase) treatments resulted in similar improvements in coaptation length as compared to ischemic mitral regurgitation. Further, postoperative coaptation length for the large patch procedure was significantly greater than the restrictive mitral annuloplasty ( $p = 0.006$ ) and the small ( $p = 0.003$ ) patch repairs.

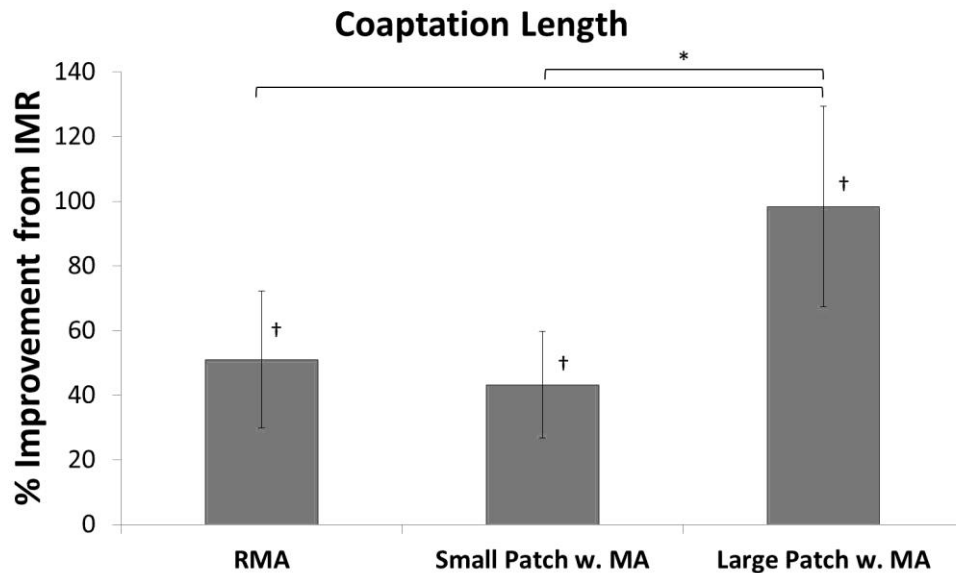


**Figure 7-5 % improvement in coaptation length of each repair as compared to IMR. \* Denotes significance between repairs. † Indicates significance as compared to IMR condition.**

Forces in all four chordae for all of the surgical repairs are found in Table 7-6. Figure 7-6 shows the percent improvement in chordal forces for all chordae for each repair as compared to the ischemic mitral regurgitation condition.

**Table 7-6 Chordal forces for all four instrumented for the surgical repair conditions. \* denotes significance ( $p < 0.05$ ) as compared to IMR. † indicates significance between groups.**

Papillary Muscle	Chordae	RMA [N]	Small Patch [N]	Large Patch [N]
Posterior	Anterior Strut	$0.89 \pm 0.33$ *	$0.91 \pm 0.37$ *	$0.74 \pm 0.31$ *
	Posterior Intermediate	$0.51 \pm 0.26$ †	$0.39 \pm 0.18$	$0.45 \pm 0.25$ †
Anterior	Anterior Strut	$0.66 \pm 0.39$	$0.78 \pm 0.43$	$0.94 \pm 0.60$
	Posterior Intermediate	$0.54 \pm 0.33$	$0.46 \pm 0.24$	$0.63 \pm 0.45$

Compared to the ischemic mitral regurgitation condition, the large patch procedure significantly reduced the force in the anterior strut chordae ( $20.5 \pm 20.0$  %), and the posterior intermediate chordal chordae ( $25.2 \pm 18.0$  %) originating from the posteromedial papillary muscle. Similar improvements were observed for the small patch procedure as compared to the ischemic mitral regurgitation condition:  $34.8 \pm 33.5$  % reduction in anterior strut chordae and  $15.8 \pm 23.9$  % reduction in posterior intermediate chordae originating from the posteromedial papillary muscle. Restrictive mitral

annuloplasty only resulted in significant reduction ( $27.0 \pm 16.6\%$ ) in chordal force in the anterior strut chordae originating from the posteromedial papillary muscle. Forces in the posterior intermediate chordae originating from the posteromedial papillary muscle remained elevated ( $3.7 \pm 23.9\%$  reduction).

Conversely, there was a slight increase in the tethering force for both the small ( $20.5 \pm 69.4\%$ ) and large ( $11.8 \pm 27.2\%$ ) patch treatments as compared to ischemic mitral regurgitation for the anterior strut chordae originating from the anterolateral papillary muscle. Restrictive mitral annuloplasty resulted in a slight reduction in chordal force for the anterior strut origination from the anterolateral papillary muscle.

None of the repairs had an effect on posterior intermediate chordae originating from the anterior papillary muscle as compared to ischemic mitral regurgitation (RMA:  $4.7 \pm 48.4\%$  reduction; Small Patch:  $1.5 \pm 48.4\%$  increase; Large Patch:  $0.7 \pm 88.1\%$  reduction).

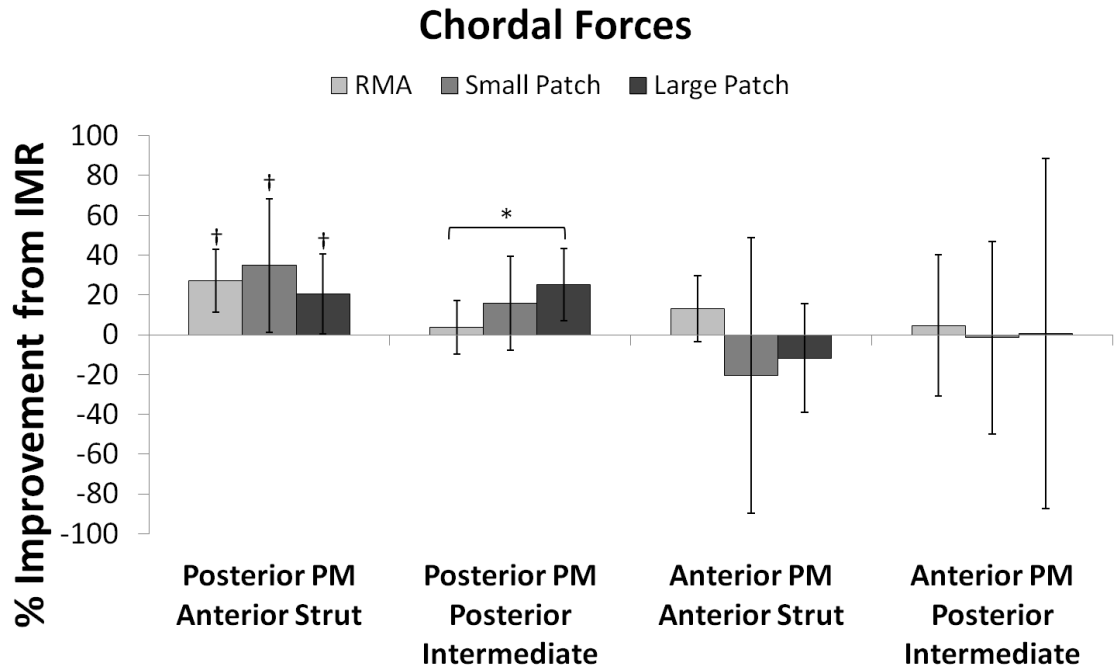


**Figure 7-6 % improvements in chordal forces for all repairs as compared to IMR. †denotes significance ( $p < 0.05$ ) as compared to IMR. \* indicates significance between groups.**

### 7.2.2 Discussion

Ischemic mitral regurgitation was successfully simulated with pathological annular dilation and papillary muscle displacement that consistent with well-established large animal models and patient data [13,209,214]. Inferior myocardial infarction was chosen as the basis for simulating ischemic mitral valve disease as this is associated with greater mitral valve regurgitation severity and incidence, and valvular geometric distortion [11,157,159]. Mitral regurgitation severity was consistent with previously published data for inferior myocardial infarction [13,39,209,214].

Leaflet-chordal tethering was quantified using miniature force transducers instrumented onto the major load bearing chordae (anterior strut, posterior intermediate)



from both the anterior and posterior leaflets [138,153,215]. The anterior strut and posterior intermediate chordae are also known to be the most sensitive to changes in papillary muscle displacement [215].

In the inferior myocardial model, asymmetric papillary muscle displacement was performed. Specifically, greater papillary muscle displacement was performed for the posteromedial papillary muscle, particularly in the lateral direction. Overall, the posteromedial papillary muscle was displaced a total of 9.8 mm as compared to 3.6 mm from the anterolateral papillary muscle. This is nearly a 3 fold increase in extension the chordae need to account for to maintain normal coaptation. This explains why significant increases in chordal forces were observed for the chordae originating from the posteromedial papillary muscle, but not for the anterolateral papillary muscle.

Between repairs, anterior leaflet augmentation with a large pericardial patch resulted in the best improvement in length; anterior leaflet augmentation also resulted in the best improvement in coaptation length compared to ischemic mitral valve disease. Overall, this creates additional redundancy in coaptation to maintain proper valvular competency, which may have the potential to withstand late ventricular remodeling. These data demonstrate that large patch procedure has the greatest impact on mitral valve functional efficacy, whereas both the restrictive mitral annuloplasty and small patch procedures have comparable improvements in clinical valve performance. To further delineate between these repairs, leaflet-chordal tethering was investigated.

The large patch procedure, which resulted in the greatest improvements in leaflet coaptation length, was expected to be associated with deleterious increases in cyclic chordal forces. This relationship was expected due to the significantly larger exposed

leaflet surface area (Force = Pressure X Exposed Leaflet Surface Area) created by the pericardial augmentation; the anterior leaflet bellowed above the annulus plane, similar to a sail. However, this was not observed for the anterior strut and posterior intermediate chordae originating from the pathologically displaced posteromedial papillary muscle. The opposite was observed as both the anterior strut and posterior intermediate chordae originating from the posteromedial papillary muscle experienced lower force after repair as compared to disease.

The reduction in anterior strut chordal force is most likely due to two mechanisms (Figure 7-7): (i) leaflet insertion points of the anterior strut chordae were displaced apically, towards the papillary muscles, by use of the patch. This effectively shortened the distance between the leaflet insertion point and the papillary muscles, which reduced the overall extension needed from the chordae to maintain proper coaptation. (ii) Echocardiography showed that the anterior strut chordae were moved into or near to the coaptation zone (Figure 7-8) [216]. This site is known to experience relatively low chordal force as it is not actively engaged in resisting transmitral pressure [149,150,215,217].

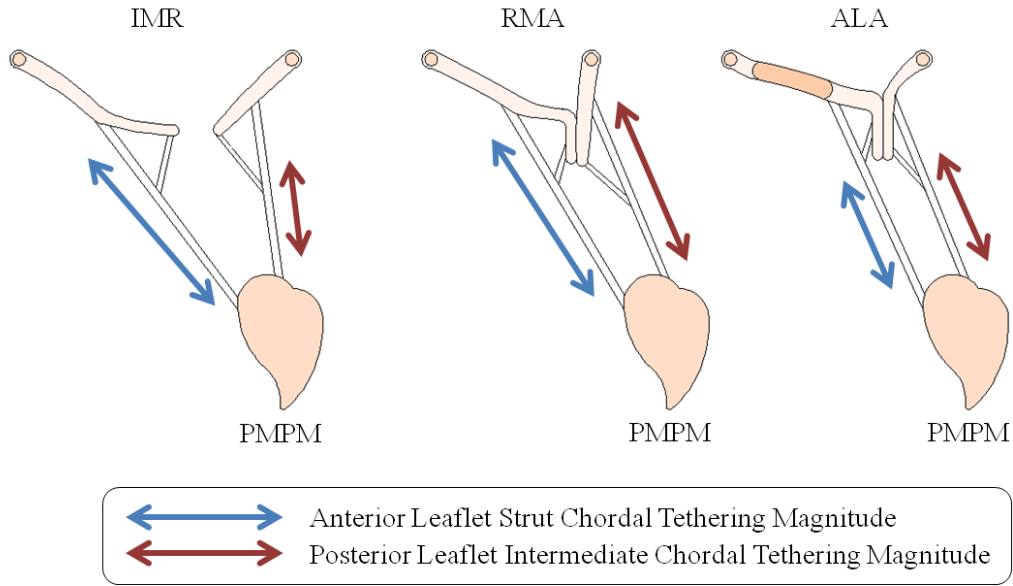


**Figure 7-7 Schematic representation of the effects Ischemic Mitral Regurgitation (IMR), Restrictive Mitral Annuloplasty (RMA) and, Anterior Leaflet Augmentation (ALA) has on chordal tethering. PMPM: posteromedial papillary muscle.**

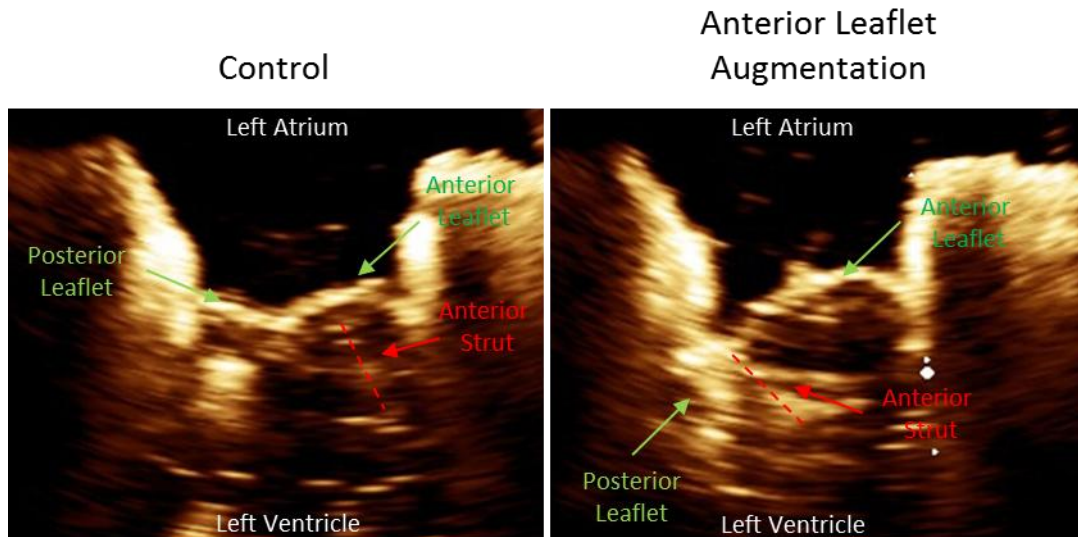


**Figure 7-8 Echocardiography shows that the anterior strut chordae have been translocated apically with the insertion of an anterior leaflet patch. This moved the chordae into the coaptation zone and away from the belly of the leaflet.**

Three mechanisms are suspected for the reduction of posterior intermediate chordal force. First, the increased anterior leaflet mobility reduced the overall loading of the posterior leaflet, such that the posterior leaflet did not traverse as far to oppose the anterior leaflet. This effectively limits the elongation of the chordae from diastole to systole. Second, more of the posterior leaflet was involved with coaptation, effectively displacing the posterior intermediate chordae near to, or into the coaptation zone; a site known to experience lower chordal forces. Finally, the posterior annulus was not hoisted directionally away from the pathologically displaced papillary muscles as is done with restrictive, or undersized, mitral annuloplasty [41]. This effectively shortened the distance between the leaflet insertion point and the restraining papillary muscle, limiting the extension of the chordae.

These mechanisms are likewise applicable to the significant reduction in anterior strut chordal force and moderate reduction in posterior intermediate chordal force observed for the small patch procedure. It is believed that the larger reduction in anterior strut chordal force in the small patch procedure compared to the large patch procedure is a result of smaller exposed surface area in the small patch procedure. Both repairs are performed in conjunction with true-sized annuloplasty, i.e. their mitral annular area is the same. However, for the large patch procedure, the anterior leaflet more greatly dominates coaptation and results in mild billowing (leaflet area above the mitral annular plane). This results in greater exposed surface area. However, these same mechanisms yield better reductions in posterior intermediate chordal force for the large patch repair as compared to the small patch repair as the posterior leaflet is not as involved in coaptation.

Restrictive mitral annuloplasty also results in a significant reduction in chordal force in the anterior strut chordae originating from the posteromedial papillary muscle. This was expected as restrictive mitral annuloplasty undersizes the mitral annular area. While the anterior leaflet still dominates coaptation, the mitral orifice it spans is the smallest of all conditions.

Conversely, there was no measured change in posterior intermediate tethering forces for the restrictive mitral annuloplasty repair treatment. An increase of force was expected due to the hoisting of the posterior annulus. However, it is likely this was offset by the creation of a functionally unicuspid valve, which resulted in minimal posterior leaflet area exposed to a transmitral pressure gradient. Nonetheless, posterior chordal forces remained elevated at pathological levels. Because of this elevated tension, the posterior leaflet remains susceptible to further perturbations in papillary muscle positioning. This is an often cited mode of failure for restrictive mitral annuloplasty which may be explained by these data [41,163].

Anterior strut chordae originating from the anterior papillary muscle did not benefit from anterior leaflet augmentation. Contrarily, there was a slight increase in tethering force for both the small and large patch treatments as compared to ischemic mitral regurgitation. Restrictive mitral annuloplasty showed a moderate improvement in chordal force as compared to ischemic mitral regurgitation.

These data suggest that significant papillary muscle displacement (as seen with the posteromedial papillary muscle) has a compensatory effect on the tethering forces in the presence of leaflet augmentation. Without papillary muscle displacement, the anterior leaflet freely billowed into the left atrium, which further exposed surface area to

transmitral pressure. In this setting, restrictive mitral annuloplasty resulted in modest improvement in tethering force, which is attributed to the smaller mitral orifice. These data support the notion that these complex and adjunctive leaflet augmentation procedures should be targeted in cases of enlarged left ventricles associated with severely displaced papillary muscles.

None of the repairs had an effect on posterior intermediate chordae originating from the anterior papillary muscle as compared to ischemic mitral regurgitation. Without significant papillary muscle displacement, hoisting of the posterior annulus did not exacerbate posterior leaflet tethering. The leaflet remained mobile and spanned more of the mitral orifice to oppose the anterior leaflet.

In this work, it is assumed a reduction in chordal forces, specifically from the ischemic condition, towards normal, control levels is beneficial. It may be possible that a significant reduction in chordal forces below physiological levels may lead to decreased ventricular function, as seen with non-chordal sparing mitral valve replacement [218]. However, with these repairs, it is not expected that the intricate valvular-ventricular balance will be disrupted.

### **7.2.3 Conclusions**

This study demonstrated that in the setting of ischemic mitral regurgitation due to severe left ventricular geometric distortion, anterior leaflet augmentation is a viable surgical option. The data from each patch size suggest that augmentation dimensions do not need to be precisely tailored as sufficient repair is achievable within a range. An oversized patch can be targeted as it provided the best gains in coaptation length and reduction in chordal tethering. Although all repairs abolished mitral regurgitation

acutely, repairs that create the greatest coaptation may conceivably produce a more robust and lasting repair in the chronic stage. However, there is still a clinical need to best identify which patients with altered mitral valve geometry would most benefit from an adjunct procedure over a simple restrictive mitral annuloplasty (refer to section 9.3.2 for more detail).

### 7.3 Basal Papillary Muscle Relocation

Basal papillary muscle relocation was first pioneered by Dr. Kron and colleagues to surgically relocate the papillary muscles towards the mitral annular plane to combat left ventricular dilation [17,56]. In this technique, as an adjunct to mitral annuloplasty, prolene sutures are passed through the fibrous portion of the posteromedial papillary muscle and looped through the mitral annulus at the right fibrous trigone. The posteromedial papillary muscle is subsequently pulled basally until a surgeon-desired level of leaflet coaptation is thought to be achieved. This is typically done on a non-beating, flaccid heart during bypass, and subsequently confirmed with saline testing. Therefore there is some procedural uncertainty associated with translating the geometric relationships between an arrested heart during bypass and the beating heart postoperatively.

Using this procedure, improved leaflet coaptation, alleviated subvalvular tethering, and a reinforcement of the left ventricle have been demonstrated [17,56]. While the potential benefits of this technique have been described, several challenges remain in demonstrating papillary muscle relocation as an effective and reproducible adjunct to mitral annuloplasty. Mainly, where on the mitral annulus should the papillary

muscle(s) be relocated, and how much basal relocation is necessary to promote valve competency.

In this study, basal papillary muscle relocation was performed to two locations on the mitral annulus. For each annular anchor, the posteromedial papillary muscle was relocated in isolation, or both papillary muscles were relocated symmetrically. Finally, basal papillary muscle relocation was performed with 2, 4, and 6 mm displacements, for each repair group.

### **7.3.1 Results**

The results of this section are subdivided into: (i) development of the ischemic mitral regurgitation model and subsequent annuloplasty repair, and (ii) basal papillary muscle relocation. The experimental conditions are (refer to section 5.2.1 for more detail):

1. Control
2. Acute myocardial infarction (MI)
3. Acute MI with mitral annuloplasty (MA)
4. Chronic MI with MA
5. Posteromedial papillary muscle (PM) repair to either the commissure (Comm) or trigone (Trig)
6. Both PMs to either the Commissure or Trigone.

The main end points are Coaptation Length (CL), Tenting Area (TA), and Tenting Height (TH) as measured through three-dimensional echocardiography, and are presented as mean  $\pm$  1 standard deviation. Statistical significance was determined at  $p < 0.05$ . For all conditions, a total of  $N = 6$  experiments were performed.

#### 7.3.1.1 Disease Progression and Ring Annuloplasty



Annular dilation and papillary muscle displacement (Acute MI) resulted in significant decreases in coaptation length and tenting area compared to control (Table 7-7, Figure 7-9). Mitral annuloplasty improved leaflet geometry, but did not restore coaptation, nor relieve leaflet tethering compared to Control. Further papillary muscle displacement following mitral annuloplasty (Chronic MI with MA), as seen with late left ventricular remodeling [41,42,163], resulted in moderately worsened coaptation, and leaflet tethering. Coaptation and tenting deleteriously returned to Acute Myocardial Infarction levels, indicating long-term repair failure. These data are consistent with clinical observations, which identify continued left ventricular dilation as a mechanism of ring annuloplasty failure [41,42,163].

**Table 7-7 Coaptation length and tenting area for the disease progression and mitral annuloplasty repair.**

<b>N = 6</b>	<b>Control</b>	<b>Acute MI</b>	<b>Acute MI with MA</b>	<b>Chronic MI with MA</b>
<b>Coaptation Length [mm]</b>	5.58 ± 1.42	3.96 ± 0.98	4.74 ± 1.22	3.98 ± 0.71
<i>p value to control</i>		0.002	0.024	0.001
<i>p value to previous condition</i>			0.453	0.069
<b>Tenting Area [mm<sup>2</sup>]</b>	18.3 ± 12.0	30.9 ± 9.3	26.9 ± 12.3	41.6 ± 19.8
<i>p value to control</i>		0.001	0.046	0.001
<i>p value to previous condition</i>			0.073	0.002

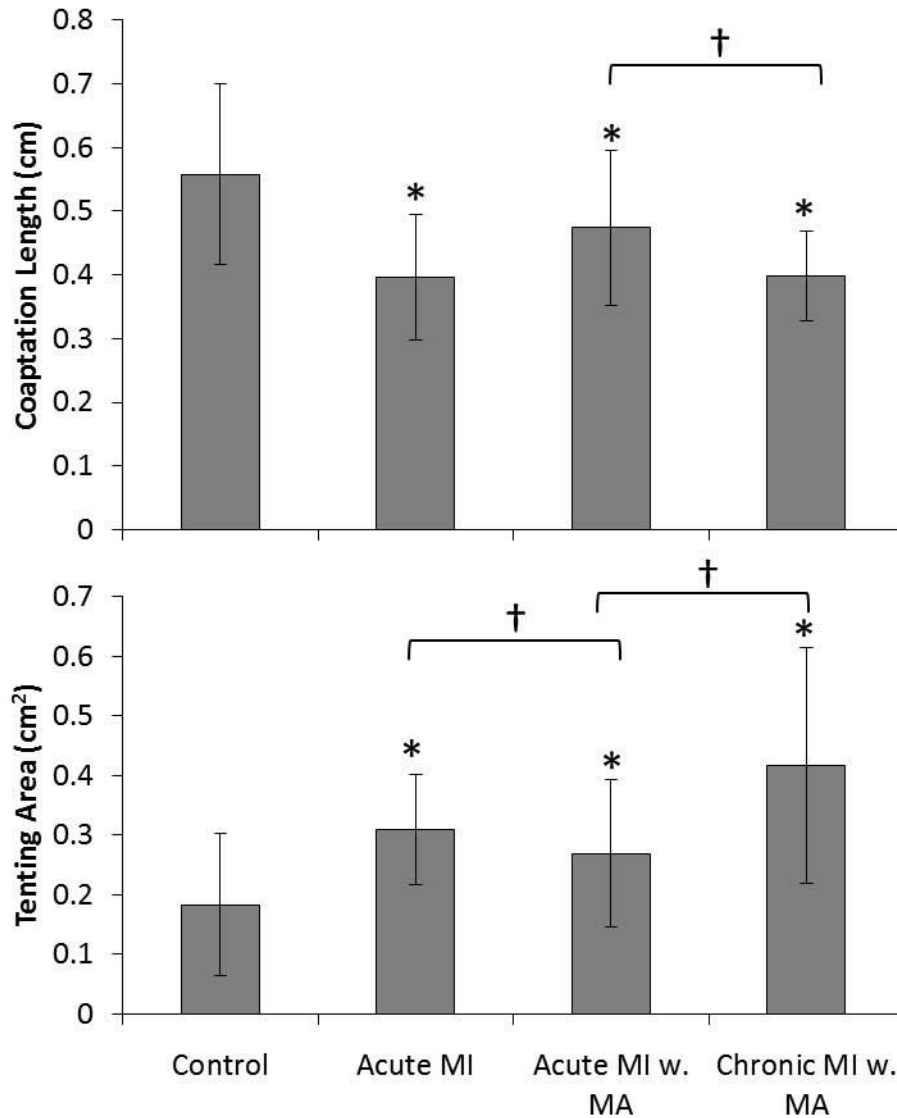


**Figure 7-9** Coaptation length and tenting area are shown for the disease progression and mitral annuloplasty conditions. \* denotes significance to control ( $p < 0.05$ ). † indicates significance between conditions ( $p < 0.05$ ).

### 7.3.1.2 Basal Papillary Muscle Relocation

For the 6 mm basal papillary muscle relocation, all repairs significantly improved coaptation and relieved leaflet tethering compared to isolated mitral annuloplasty (Chronic MI with MA) (Table 7-9, Figure 7-10). No significant differences in coaptation

length and tenting area were observed between any of the 6mm repair groups and the control group, suggesting papillary muscle relocation was able to restore natural physiological function of the mitral valve. Additionally, no statistical significance was observed when comparing coaptation length and tenting area within any of the 6 mm repair groups.

**Table 7-9 Coaptation length and tenting area for all four repairs at the 4mm and 6 mm increments. The 2mm repair increment is not shown as this level of repair did not improve leaflet closure.**

N = 6	Repair	Posteromedial Papillary Muscle		Both Papillary Muscles	
		Commissure	Trigone	Commissure	Trigone
Coaptation Length [mm]	6 mm	5.96 ± 1.46	6.23 ± 1.84	6.23 ± 1.58	6.26 ± 1.80
	4 mm	4.96 ± 1.25	5.31 ± 1.27	5.58 ± 1.39	5.75 ± 1.82
Tenting Area [mm <sup>2</sup> ]	6 mm	19.7 ± 11.6	21.7 ± 10.7	20.4 ± 12.0	19.8 ± 10.2
	4 mm	32.9 ± 20.3	34.5 ± 21.6	27.9 ± 15.4	23.6 ± 9.8

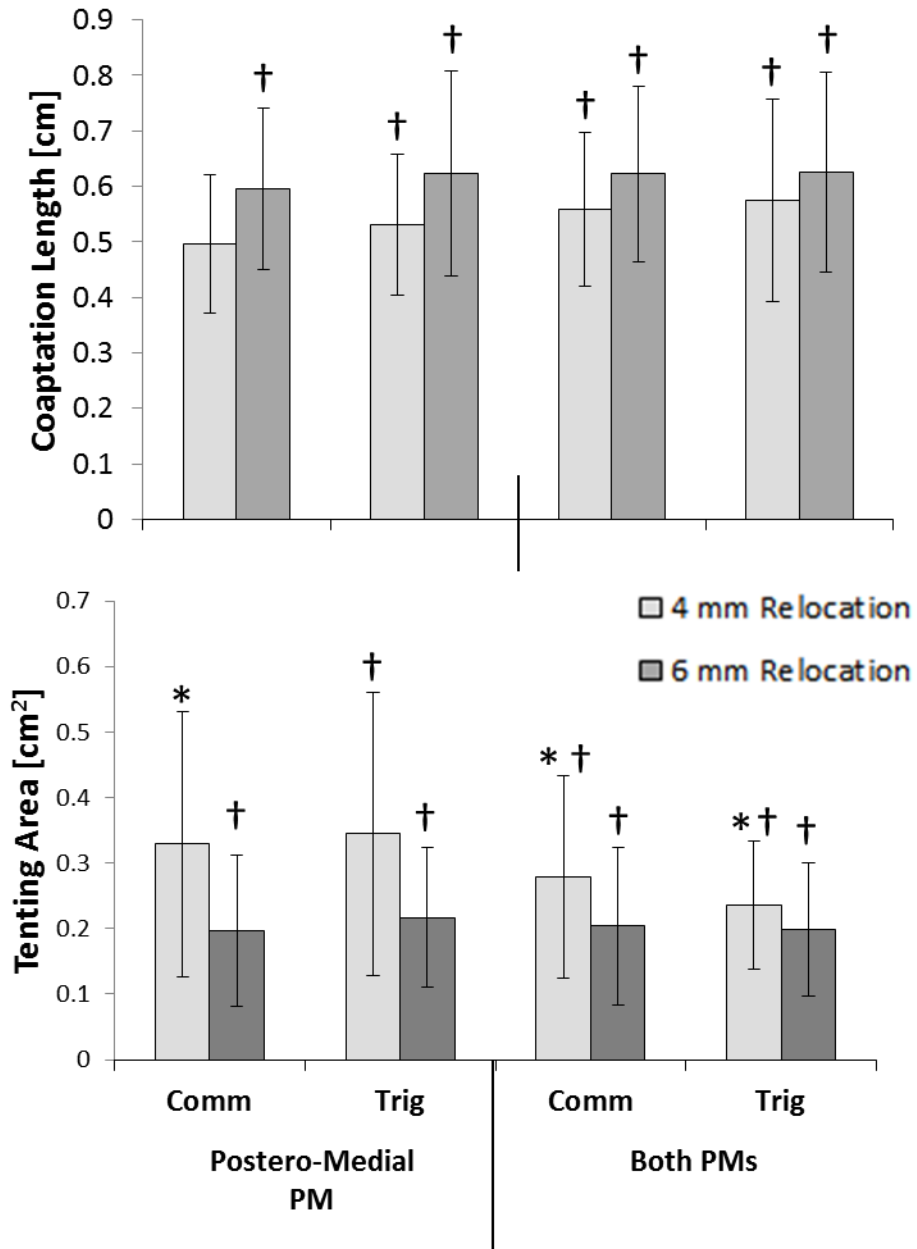
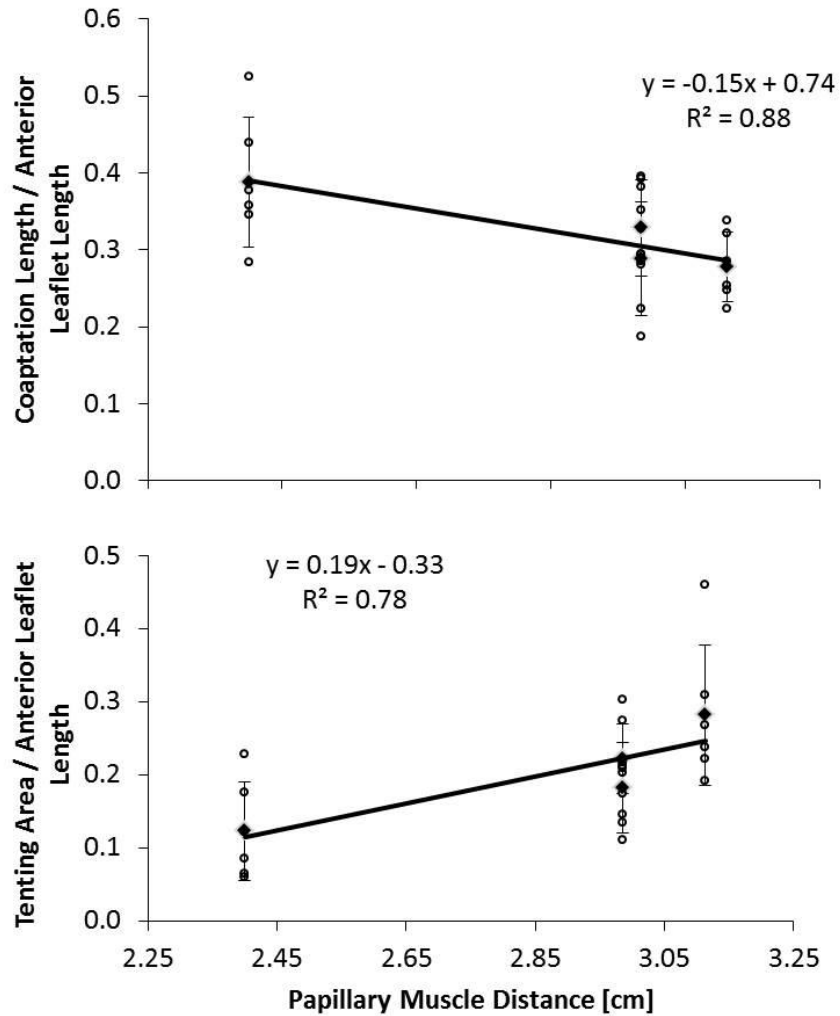


Figure 7-10 Coaptation length and tenting area for all four repairs at the 4mm and 6 mm increments. \* denotes significance from Control, while † denotes significance from Chronic MI with MA. 2mm repair increment is not shown as this level of repair did not improve leaflet closure.

For a 4 mm basal papillary muscle relocation, displacing both papillary muscles towards either annulus anchor significantly improved coaptation length and relieved leaflet tenting compared to isolated mitral annuloplasty (Chronic MI with MA). The resulting coaptation length and tenting area were not statistically significant from Control. Additionally, there was no statistical significance between the two annular anchor groups. Relocating only the posteromedial papillary muscle did not significantly improve coaptation length or tenting area from the Chronic MI with MA grouping. Leaflet tenting area was significant from control for either of the annular anchor groups. Again, there was no statistical significance observed between the repair groups. 2mm repair increment data were not shown as there were no improvements from pathology.

Leaflet coaptation geometry was plotted as a function of papillary muscle distance (Figure 7-11) for the Control to the IMR conditions. Papillary muscle distance was measured as the absolute distance from the tip of the papillary muscle to the adjacent commissure on the mitral annular plane. This is a different measurement than papillary muscle displacement which was a relative magnitude from the control geometry. Leaflet geometry was normalized against anterior leaflet length to eliminate effects of valve size variability. A scatter points were used to show the data for all six experiments for the plotted conditions; similar trends were observed between all experiments.

With disease progression, normalized coaptation length was observed to have a linearly proportional (inverse) relationship with papillary muscle distance. Conversely, normalized tenting area linearly increased with papillary muscle distance. Characteristic equations and goodness of fit for are presented in Table 7-9.



**Figure 7-11 Normalized coaptation length has an inverse relationship with papillary muscle distance. Tenting area is linearly proportional to papillary muscle distance. Papillary muscle distance is measured from the tip of the papillary muscle to the mitral annular plane. Scatter points show consistent trends between experiments.**

**Table 7-9 Coaptation length was significantly decreased from Control to IMR.**

<b>Parameter/Anterior Leaflet Length</b>	<b>Characteristic Equation</b>	<b>Fit [R<sup>2</sup>]</b>
<b>Coaptation Length</b>	$-0.15*PM + 0.74$	0.88
<b>Tenting Area</b>	$0.18*PM - 0.33$	0.78

Similarly, a strongly linear relationship existed between normalized coaptation geometry and papillary muscle distance for the individual papillary muscle repair groups. This can be observed in Figure 7-12. From right to left, papillary muscle position is basally improved from the Chronic Myocardial Infraction condition by 2, 4, and 6 mm (x-axis shows absolute papillary muscle distance decreased by 2 mm for each increment of repair). Normalized coaptation length was linearly and inversely proportional to papillary muscle distance. Characteristic equations and fits for all linear regressions were tabulated (Table 7-10)

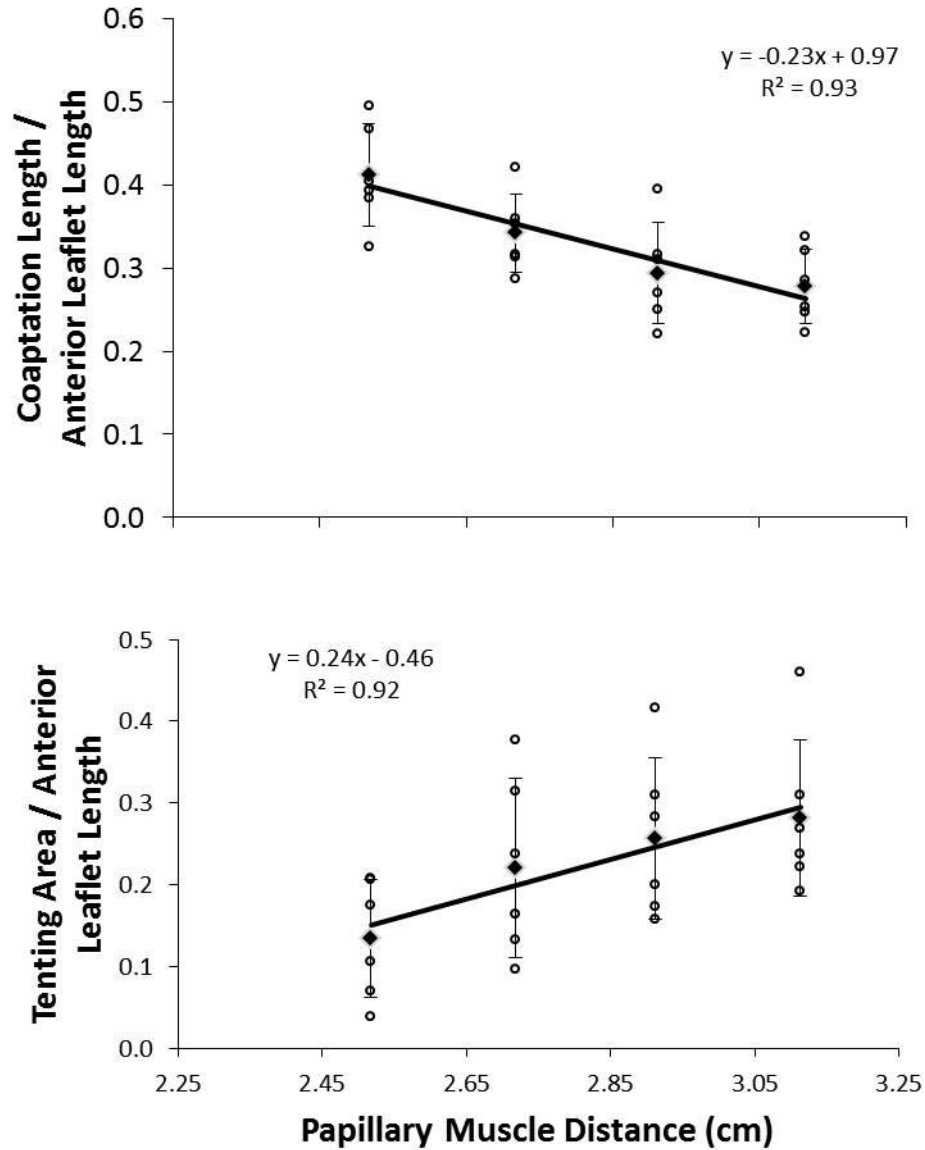


**Figure 7-12** Normalized coaptation length has an inverse relationship with papillary muscle distance. Tenting area is linearly proportional to papillary muscle distance. Papillary muscle distance is measured from the tip of the papillary muscle to the mitral annular plane. Scatter points show consistent trends between experiments.



**Table 7-10 Relationships between leaflet parameters and papillary muscle distance are tabulated. Coefficients are comparable between repair groups.**

		Parameter/Anterior Leaflet Length	Characteristic Equation	Fit [R <sup>2</sup> ]
Both Papillary Muscles	Commissure	Coaptation Length	$-0.26*PM + 1.10$	0.97
		Tenting Area	$0.24*PM - 0.48$	0.96
	Trigone	Coaptation Length	$-0.30*PM + 1.20$	0.98
		Tenting Area	$0.26*PM - 0.52$	0.97
Postero-medial PM	Commissure	Coaptation Length	$-0.23*PM + 1.97$	0.93
		Tenting Area	$0.24*PM - 0.46$	0.91
	Trigone	Coaptation Length	$-0.30*PM + 1.71$	0.96
		Tenting Area	$0.34*PM - 0.75$	0.75

It was observed that isolated postero-medial papillary muscle repair in the anterior myocardial infarction model failed to alleviate tethering at the contralateral, A1-P1, coaptation line (Table 7-11, Figure 7-13). Tenting area was significantly different from control for both commissural and trigonal repairs. The ipsilateral A3-P3 coaptation line showed no significant tethering for either annular anchors compared to control.

**Table 7-11 Tenting area at the off-center coaptation lines.**

	Control		Contralateral [A1P1]		Ipsilateral [A3P3]	
	A1P1	A3P3	Comm	Trig	Comm	Trig
<b>Tenting Area [mm<sup>2</sup>]</b>	13.0 ± 7.9	12.7 ± 6.7	31.9 ± 13.5	29.2 ± 9.2	16.9 ± 10.4	14.4 ± 11.7

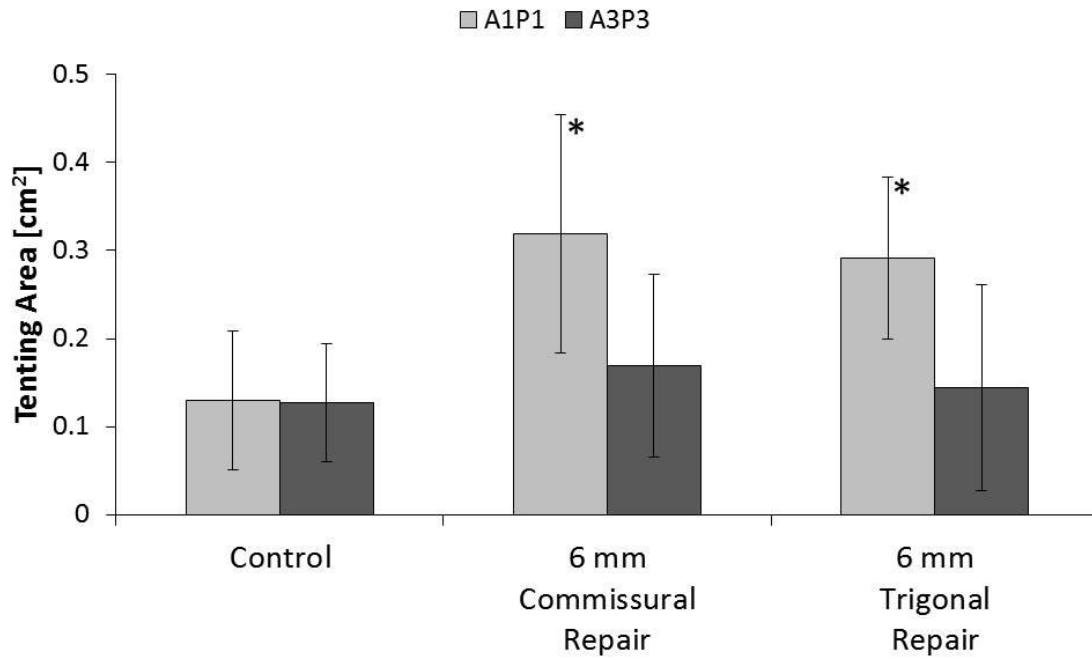


**Figure 7-13 Tenting area at the off-center coaptation lines.**

## 7.3.2 Discussion

### 7.3.2.1 Efficacy of Basal Papillary Muscle Repair

Within this study, the 4 and 6 mm basal papillary muscle relocations restored leaflet coaptation and alleviated leaflet subvalvular tethering when performed as an adjunct to true-sized mitral annuloplasty. This adjunctive repair was more efficacious than isolated mitral annuloplasty, which showed a regression in valvular competency in the presence of chronic left ventricular dilation.

Moreover, these data suggest that there is a viable range to which the papillary muscles can be relocated which yield physiological valvular function. This is important as a patient's normal papillary muscle position is not known, thus making it difficult to pre-operatively determine the exact papillary muscle relocation required for a competent long-term repair. Fortunately, the results herein indicate this may not be necessary as normal coaptation can be obtained within a given range of papillary muscle relocation positions. This redundancy is due to the natural functional reserve of the mitral valve, which has been previously characterized in *in-vitro* studies of annular dilation and papillary muscle displacement [14,34].

By exploiting this redundancy a surgeon can restore leaflet function with a more durable repair. Specifically, forces on traction sutures and consequently the papillary muscles have recently been shown to be proportional to the applied repair distance [219]. Logically, it follows that lesser stress on the papillary muscles would be beneficial for optimizing repair durability and avoiding potential long term papillary muscle distension or rupture.

The data also suggest that undersized mitral annuloplasty, or the unnatural downsizing of the mitral annulus, is not necessary when adjunctive papillary muscle repair is performed. This is consistent with recent work published by Fattouch et al. in which patients receiving papillary muscle relocation with concomitant true-sized annuloplasty demonstrated favorable outcomes compared with isolated undersized annuloplasty at 5 year follow up [54]. However, it is unclear where there is an added benefit of combining undersized annuloplasty with papillary muscle relocation.

#### 7.3.2.2 Effect of Annular Anchor Selection

Basal papillary muscle relocation was performed to two annular landmarks based on their physiological structure and function: the commissures and the fibrous trigones. In normal physiology, each papillary muscle lays behind its corresponding commissure (Figure 7-14). Therefore, it is believed that relocating the papillary muscle towards its respective commissure will restore natural physiology. The fibrous trigones, due to their dense collagenous structure, are believed to serve as more secure anchors from which the papillary muscles can be suspended. Also, relocating the papillary muscles towards the trigones is expected to result in additional corrective lateral displacement of the papillary muscles. This would further resist the outward tethering of the left ventricle.

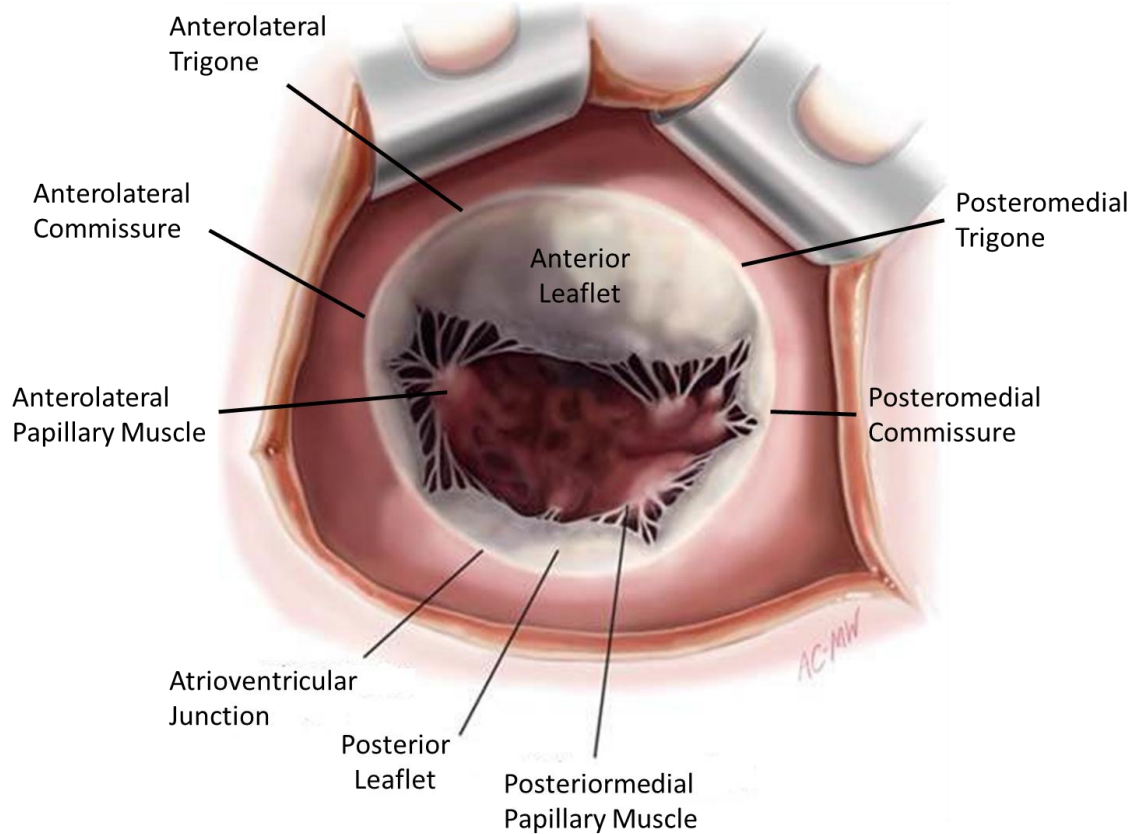


**Figure 7-14 Papillary muscles and annular landmarks are shown.**

The anchor position of the traction suture did not affect valve function as determined by leaflet coaptation. No statistically significant differences in mitral leaflet coaptation and tethering were observed between repairs. At 6 mm displacement, coaptation was entirely restored and tenting was alleviated as compared to control for either the trigonal or commissural repair group.

The similarity between trigonal and commissural repair efficacies was attributed to the relatively small spatial differences between the two annular landmarks. Annular dimensions were defined by annuloplasty geometry. For size 28 to 32 annuloplasty rings, this corresponds to approximately 5 to 7 mm in the lateral direction (Figure 7-15). However, when this is projected onto the direction of the surgical repair, there is a

minimal affect. For each repair, the main direction of papillary muscle relocation is an apical-basal correction. This can be seen in Table 7-8 below, which shows the residual papillary muscle displacement for each repair throughout the 2 mm increments. With either annular location, the apical component of papillary muscle displacement was entirely corrected. Posterior and lateral components of the pathological displacement largely remained with either annular anchor repair. This is consistent with previous *in-vitro* investigations, which found apical papillary muscle displacement can be primarily responsible for mitral insufficiency, and exacerbates regurgitation in the presence of posterior and lateral displacement [14,220]. Clinically, these results are favorable as the data suggest that the procedures are robust to variations along the mitral annulus.

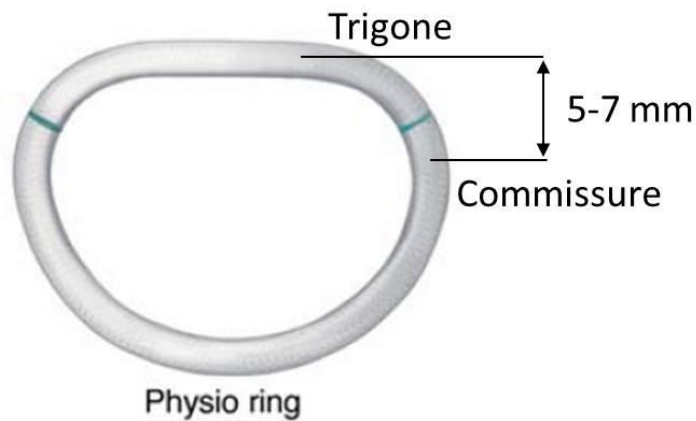


**Figure 7-15 Physio annuloplasty ring demarked with difference in trigone and commissure dimensions.**

**Table 7-12 Residual papillary muscle displacement after each incremental basal repair.**

			Normal	Chronic MI	2 mm	4 mm	6 mm
Commissural Repair	Papillary Muscle Displacement [mm]	Lateral	0	8	7.3	6.6	5.9
		Posterior	0	8	7.4	6.7	6.1
		Apical	0	5	3.2	1.5	<b>-0.3</b>
Trigonal Repair	Papillary Muscle Displacement [mm]	Lateral	0	8	7.2	6.5	5.7
		Posterior	0	8	6.9	5.7	4.6
		Apical	0	5	3.5	2.1	<b>0.6</b>

### 7.2.2 Clinical Parameters to Inform Papillary Muscle Relocation Distance

Simple clinical correlates between papillary muscle position and leaflet geometry were identified, which may be used to pre-operatively determine a favorable basal papillary muscle relocation range.

The formulae derived from the linear regressions may be used clinically to determine papillary muscle distance as measured through an easily obtained surrogate leaflet parameter (e.g. coaptation length); papillary muscle position is difficult to capture with current clinical imaging modalities. These relationships can be exploited to pre-operatively plan papillary muscle relocation. That is, given the diseased and the desired repaired coaptation length, the difference in papillary muscle distance can be determined.

Subsequently, that distance can be surgically applied to the papillary muscle relocation. Follow up studies are necessary to quantify the predictive value of these parameters more comprehensively (refer to section 9.3.3 for more detail).

#### 7.3.2.3 Effect of Papillary Muscle Selection

By analyzing the changes in leaflet closure geometry at the off-center coaptation lines (A1-P1, and A3-P3), the localized effect of papillary muscle relocation was investigated. Isolated repair of the posteromedial papillary muscle only improved leaflet closure at the ipsilateral (A3-P3) and the adjacent (A2P2) coaptation line. As the anterolateral papillary muscle remained displaced, localized tethering was observed at the A1P1 coaptation line. This indicates that basal papillary muscle relocation should be targeted to the displaced papillary muscle, which can be identified by local leaflet tethering measured through full volume echocardiography.

In this study, symmetric papillary muscle displacement was performed, which most closely simulated anterior myocardial infarction [11,157,213]. For this model, both papillary muscles require correction to improve leaflet function. However, the data are readily extrapolated to single papillary muscle repairs in a posterior myocardial infarction model. For such a case, left ventricular dilation and papillary muscle displacement is asymmetric, resulting in mostly isolated posterior papillary muscle displacement. Based on the improvement in leaflet closure observed by correcting both papillary muscles in the symmetrically displaced anterior myocardial infarction model, it is expected that repairing only the posteromedial papillary muscle in an asymmetric inferior myocardial infarction model will be sufficient. In an inferior myocardial infarction model, the



anterolateral papillary muscle only experiences mild displacement. Furthermore, this displacement is not in the apical direction.

### 7.3.3 Conclusions

In this systematic controlled *in-vitro* study, basal papillary muscle relocation was found to be insensitive to the choice of annular suture location and exploits natural leaflet redundancy, demonstrating great surgical repeatability and robustness. Papillary muscle distance was linearly proportional to changes in leaflet geometry as measured by coaptation length and leaflet tenting. This relationship indicated that leaflet geometry could be used as a surrogate for papillary muscle positioning to inform surgical repair.

These published findings [38] were recently appreciated in an invited commentary Dr. Ulrik Hvass, “These essential findings should make surgeons more confident by the various imperfections they fear to produce, and that controlling the mitral regurgitation by intervening on the subvalvular anatomy does not require a high degree of precision.” The simplicity of basal papillary muscle relocation (as opposed to anterior leaflet augmentation) combined with its demonstrated robustness suggests this adjunctive repair may be performed by lesser experienced cardiovascular surgeons.

## CHAPTER 8

### **SPECIFIC AIM 3: NOVEL LEFT HEART SIMULATOR FOR THE DEVELOPMENT AND VALIDATION OF COMPUTATIONAL MITRAL VALVE SIMULATIONS**

#### **8.1 Introduction**

In the past ten years, numerical models of the heart's mitral valve have evolved from simple, two-dimensional mathematical approximations to three-dimensional patient specific models with couple fluid-structure interaction [221]. These evolving methods can provide unique and non-invasive analysis of mitral valve function and biomechanics while evaluating fluid flow characteristics pre- and post-operatively [221,222]. More recently, medical imaging has been employed to extract patient specific annuloplasty ring design, MitraClip implantation and closure, and predict virtual modification of the mitral annulus and chordae [223-230].

However, as numerical mitral valve models have grown in complexity, most still lack direct one-to-one experimental validation. Typically, the computed endpoints of the numerical solvers are compared to previously published data, for which only mean values are available, and often result in mismatches in valve geometry and boundary conditions. As computational solvers can vary considerably, experimental benchmark data are important to ensure model accuracy [231]. Without such validation against benchmark

data, the computation model is of “questionable” value in its clinical utility. As rightly pointed out by Einstein et al. “...three-dimensional in-vitro flow, deformation and strain data with a native mitral valve are sorely needed” [232].

Herein, a novel left heart simulator designed specifically for the validation of mitral valve finite element and fluid structure interaction models is presented. Several distinct and complementary techniques were collectively performed to resolve mitral valve geometry and biomechanics. In particular, micro-computed tomography and three-dimensional echocardiography were used to obtain high-resolution valvular anatomy and systolic leaflet geometry, while stereoscopic digital particle image velocimetry provided detailed characterization of the mitral flow field. In addition, physiologic hemodynamic boundary conditions were defined and all data were synchronously acquired through a central trigger.

The results presented below are a demonstration of the capabilities of the novel left heart simulator and further subdivided by experimental technique: (i) hemodynamic data (ii) echocardiography, (iii) micro-computed tomography, (iv) stereoscopic particle image velocimetry, and (v) valve and subvalvular biomechanics. Finally, current uses of the experimental data are explored.

## 8.2 Results

### 8.2.1 Hemodynamic Boundary Conditions

Hemodynamic boundary conditions (pressure and flow) were obtained in the left atrium, left ventricle, and aortic outflow tract. Data were acquired at 1 kHz over ten cardiac cycles and subsequently ensemble averaged to remove cycle to cycle variability.

Representative adult physiological hemodynamics are presented below (Figures 8-1, 8-2, and 8-3). The ensemble averaged mitral flow was  $4.8 \pm 0.1$  L/min, corresponding to a stroke volume of  $69.9 \pm 2.1$  mL; the closing volume was  $6.5 \pm 0.6$  mL. Peak mitral flow rate was 13.2 L/min. Left ventricular pressure peaked at  $125.6 \pm 1.7$  mmHg, and the rate of LVP (dLVP/dt) increase was  $1506 \pm 52.8$  mmHg/sec. Aortic pressure was  $122 \pm 1.8/52 \pm 0.9$  mmHg (systole/diastole). Diastole lasted approximately 560 msec (as denoted by positive flow through the mitral valve); the remaining 300 msec comprised systole. The mitral valve closed in approximately 100 msec (as observed in the retrograde flow) and remained closed for the final 200 msec (zero flow) of the cardiac cycle.

The atrial, ventricular, and aortic pressures and the mitral flow were stable (as noticed by the low standard deviation) and well simulated [233]. Additionally, the waveforms are easily tunable to simulate various pathologies such as tachycardia (elevated heart rate), hypertension (elevated systemic pressure), or congestive heart failure (depressed cardiac output). Pressures and flows at all inlets and outlets were acquired as various computational techniques require different boundary conditions as an input. For example, finite element solvers may require transmitral pressure [19,234], whereas fluid-structure interaction models, such as smooth particle hydrodynamic may require flows [221].

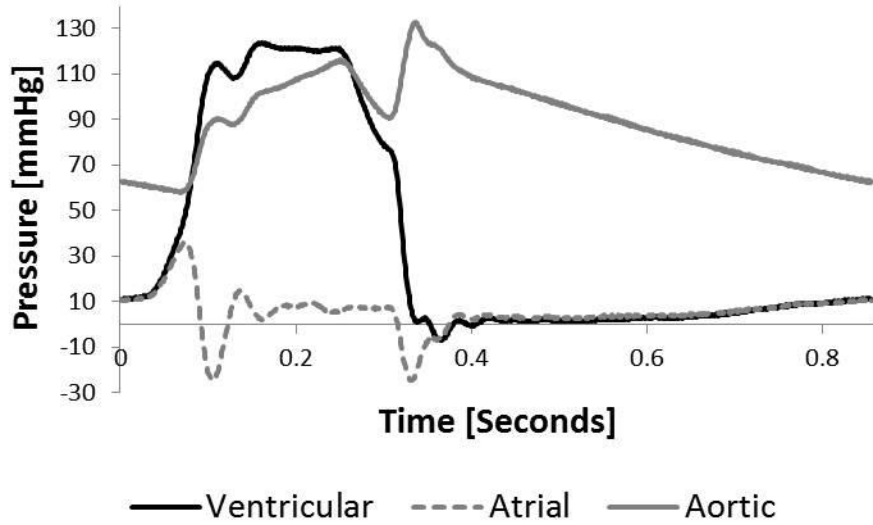


**Figure 8-1** Representative pressure waveforms in the Atrium, Ventricle, and Aorta as acquired from the modified heart simulator.

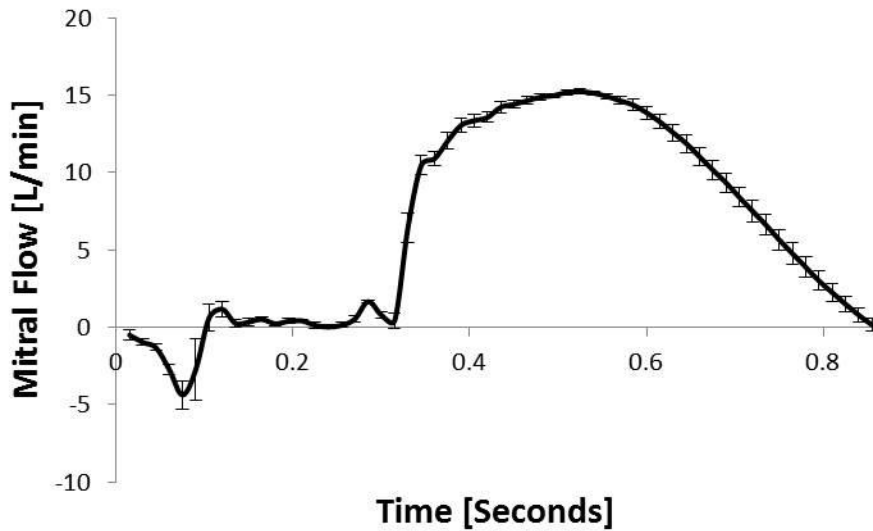


**Figure 8-2** Representative mitral flow has low cycle to cycle variability as denoted by  $\pm 1$  standard deviation.

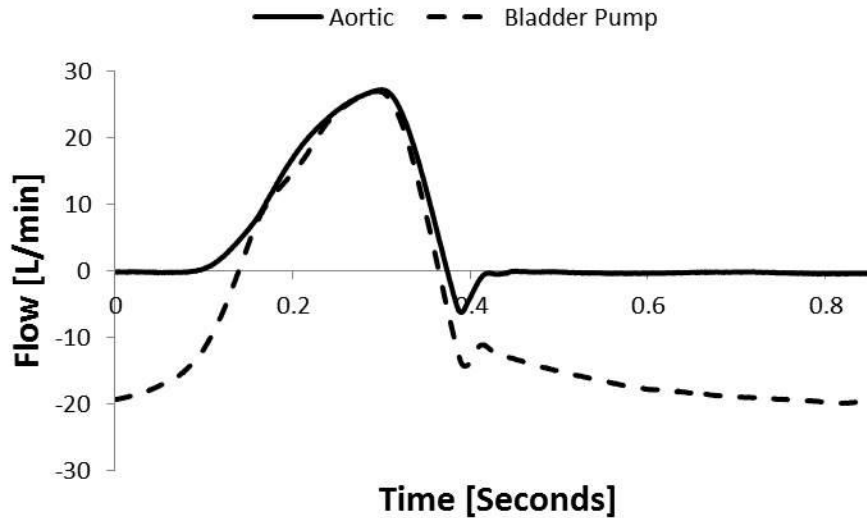


**Figure 8-3 Representative aortic outflow and bladder pump inlet flow.**

### 8.2.2 Geometric Characterization

Peak systolic anterior and posterior leaflet geometries segmented from three-dimensional echocardiography are shown in Figure 8-4. Echocardiography images were analyzed using a previously validated in-house MATLAB tool [197]. The leaflets demonstrated good closure curvature and functional redundancy creating a competent seal. Annular area was  $4.5 \text{ cm}^2$ . Coaptation length at the center of the valve was 5.0 mm; this decreases to 2.0 mm near the commissures. The point of coaptation was 9.3 mm from the anterior annulus and occurred 2.3 mm from the annular plane. Different time points in the cardiac cycle may be similarly segmented for distinct comparison of leaflet-motion with numerical simulation across the cardiac cycle. This has previously been accurately performed for the opening and closing phases, where the leaflets are most dynamic [197]. As the ultrasound acquisition had a temporal frequency of  $\sim 20 \text{ Hz}$ , 16-17 frames may be

analyzed. This technique has been previously shown to be accurate for segmenting the highly dynamic motion of valve closure and opening [197].

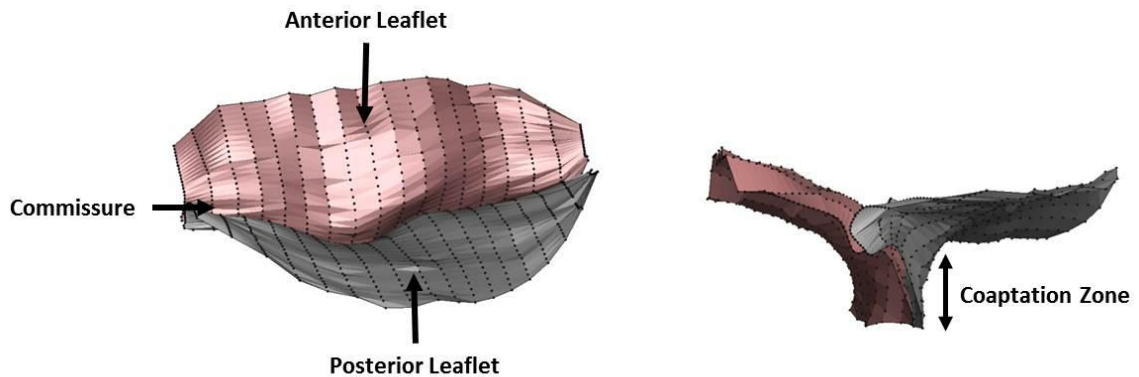


**Figure 8-4 Segmented mitral valve leaflets reconstructed from full volume echocardiography.**

As echocardiography is the clinical standard of care imaging modality, it was important for the experimental platform to provide clear acoustic windows which capture dynamic mitral leaflet geometry. The in-house segmentation tool demonstrated the mitral leaflets can be clearly and easily extracted from the data [197]. The anterior and posterior leaflets and annulus were extracted from 18 apical-basal long axis slices in the peak systolic echocardiography frame. A butterfly mesh interpolation scheme was used to create smooth surface topology. Ongoing development is aimed at providing improved acoustic windows to capture subvalvular geometry. Representative echocardiography images through the new acoustic window show the subvalvular apparatus can be captured throughout the cardiac cycle (Figure 8-5).

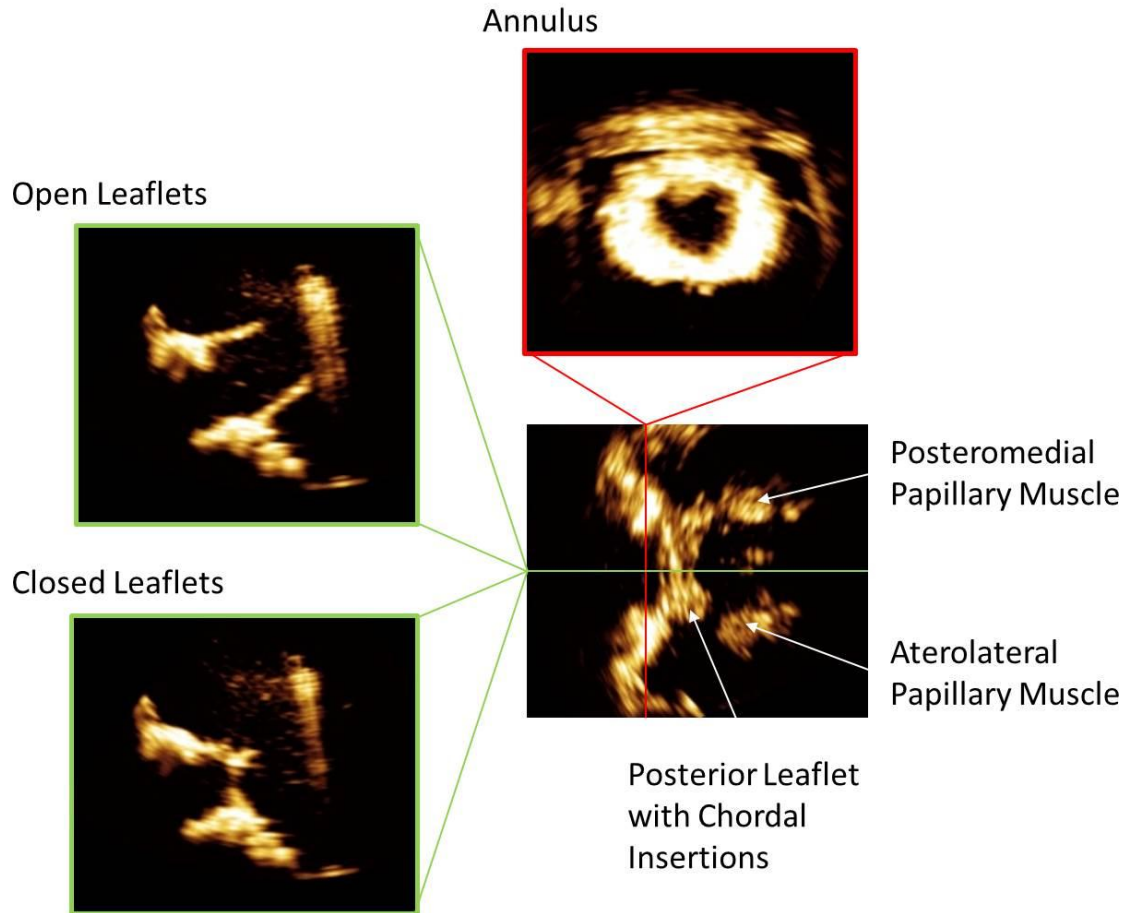


**Figure 8-5 Full volume echocardiography images acquired through new acoustic imaging windows capture subvalvular apparatus. The green lines indicate a long axis slice taken through the central A2-P2 zone. The red line indicates a short axis slice taken at the mitral annulus.**

### 8.2.3 Micro-Computed Tomography

In the novel left heart simulator, high resolution micro-computed tomography was performed to acquire experimental mitral valve geometry. That is, valvular anatomy, particularly the mitral annulus and papillary muscles, were unperturbed from their experimental configuration. This ensures that experimentally measured endpoints directly correspond to acquired mitral valve apparatus geometry; this is a key distinction between data generated herein as compared to previously published data.



Micro-computed tomography derived geometry is shown in Figure 8-6. Imaging the valve in air provided excellent contrast for reconstruction. Due to the low-density of the biological tissue and its high water content, scanning in solution provided low contrast. The left ventricular chamber had minimal interference, which allowed a high quality segmentation to be performed. Two defined leaflets with small commissural scallops were observed. Chordae tendinae, derived from each papillary muscle, insert into the mitral leaflets. The chordal structures are well defined and show continuous insertions into the free edge, belly, and base of the mitral leaflets. Leaflets and chordal structure are asymmetric and have varying lengths and thicknesses. Comparatively, numerical simulations often assume symmetric and homogenous thickness in mitral anatomy. Additionally, unlike present numerical approximations, the chordae do not originate from a singular point on the papillary muscles; chordal insertions vary along the body of each papillary muscle. Chordae also appear to branch or diffuse radially into the mitral leaflet, which is typically not represented in computer simulated models. The reconstructed annulus and papillary muscles can be registered to the CAD model of the left heart simulator using Boolean algebra for use in computational modeling (see Chapter 5.4.1.6).

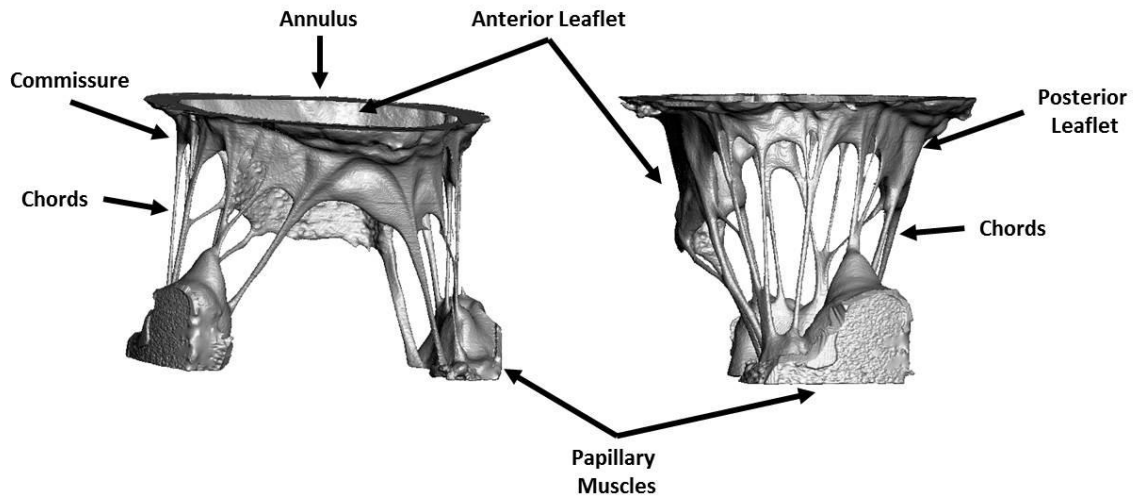


**Figure 8-6 Mitral valve apparatus as reconstructed from micro-computed tomography imaging.**

The high spatial resolution (39  $\mu\text{m}$ ) micro-computed tomography data were necessary to accurately resolve the detailed and intricate chordal branching. In particular, no other modality is currently capable of reliably imaging the marginal chordae, which control leaflet coaptation, and are thus critical to numerical modeling accuracy. Recent studies have shown the effect of modeling mitral valve closure with approximated chordal structure as compared to more realistic image derived geometry [19]. Specifically, in models of approximate chordal structure, the mitral leaflets bellow unnaturally above the mitral annular plane.

Mitral valve anatomy was also acquired in closure, representing ventricular systole. This was done at two pressures. Using a continuous air pressure pump connected to the left ventricle, approximately 30 mmHg of pressure was obtained. This was suitable to maintain valve closure. Further, based on its collagenous microstructure, leaflet strain plateaus during closure suggesting this is suitable to capture accurate systolic mitral valve geometry [118]. Greater pressure may be obtained with a more

powerful air pump; however, with this technique, the valve may dry out making further experimentation difficult. Pressure fixation was also performed using dilute aqueous Paraformaldehyde (PFA). PFA fixation was limited to 70 mmHg; this was determined by the largest pressure column possible in the fume hood. Mitral valve anatomy obtained by each complementary imaging modality (micro-computed tomography: off-white; full volume echocardiography: cyan) at peak systole is compared in Figure 8-7. Strong agreement in leaflet geometry was observed. Similarly, diastolic, or open, leaflet geometry may be compared. With the mitral valve scanned in air, the mitral leaflets appear shorter after micro-computed tomography reconstruction as compared to echocardiography (Figure 8-8). This suggests a method is needed to unfurl the mitral leaflets during scanning (water tension may be causing retraction of the leaflets). This can be circumvented by using the systolic geometry (already shown to agree well between echocardiography and micro-computed tomography) or by scanning the leaflets in solution. For the latter, the Phosphotungstic Acid staining (contrast agent) should be performed overnight, and the valve should be scanned in ethanol (see Chapter 5.4.1.4.2). Micro-computed tomography imaging was limited to these two time points. Transient valvular anatomy during opening or closing was only obtained through echocardiography.

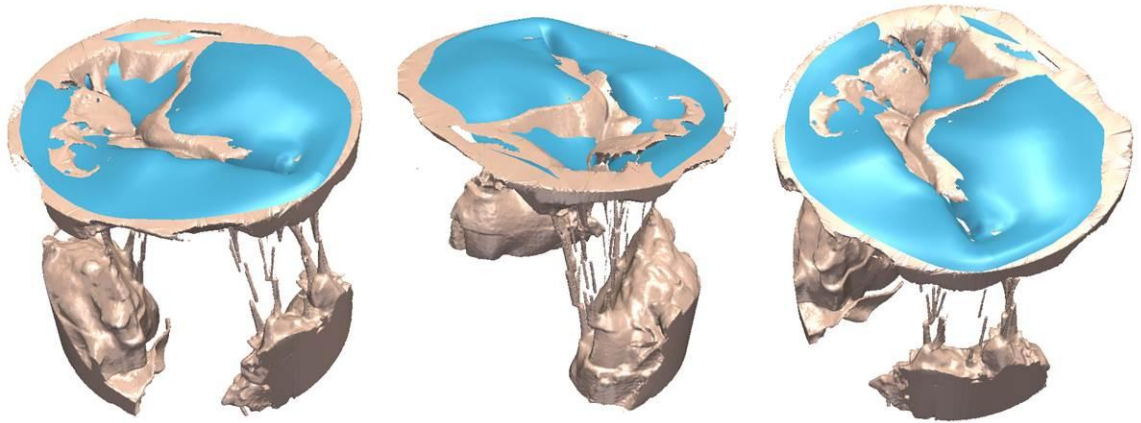


**Figure 8-7 Comparison of mitral valve anatomy obtained through micro-computed tomography imaging (off-white) and full volume echocardiography (cyan).**

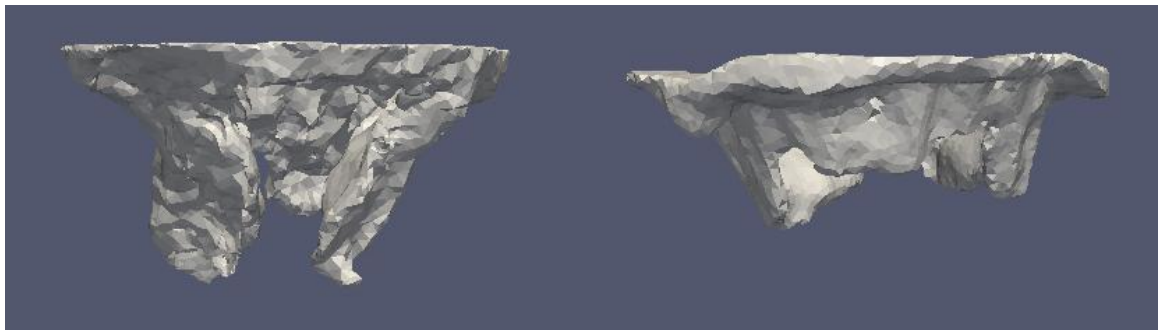


**Figure 8-8 Comparison of open mitral leaflets reconstructed from echocardiography (left) and micro-computed tomography (right).**

Ongoing developments are aimed at improving micro-computed tomography image acquisition. Recent availability of a Siemens Inveon (Siemens Medical Solutions USA, Inc.; Malvern, PA) micro-computed tomography system will provide higher resolution data (up to 21  $\mu\text{m}$  vs. 39  $\mu\text{m}$ ), faster image acquisition (<20 min vs. ~45 min), and larger field of view (56 mm diameter vs. 39 mm) (Figure 8-9). With higher resolution images, smaller marginal chordae can be captured. Faster data acquisition can help ensure the valve does not dry out, making further experimentation possible if

necessary. The larger field of view makes data analysis more streamlined, as the limited field of view of the Scanco system caused a high intensity ring artifact at the borders the valve anatomy. This had several drawbacks: (i) valve size was limited by the field of view and made simulating annular dilation impossible, (ii) the ring artifact was of similar intensity as the valve structure prohibiting simple thresholding from being effective, and (iii) automated segmentation techniques required manual user manipulation to be effective. Additionally, there is a large field of view in the axial direction, which allows the valve to be scanned from the annulus to the papillary muscles in one pass. Previously, the Scanco system required translation of the sample into the bore, which resulted in motion artifacts.

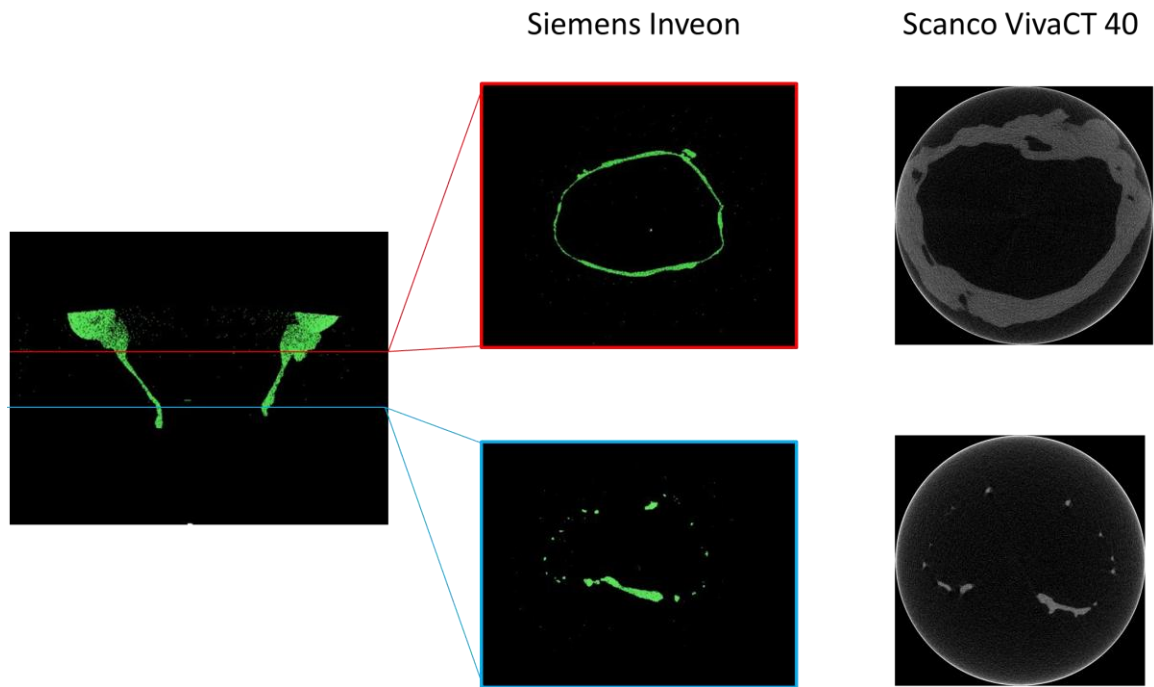


**Figure 8-9 Comparable image slices from Siemens Inveon and Scanco micro-computed tomography systems. Data from the Siemens system have lower signal to noise and a larger field of viewing. A simple band-pass threshold is sufficient (applied in images as green) for the Siemens data sets.**

#### 8.2.4 Stereoscopic Particle Image Velocimetry

For the first time, stereoscopic digital particle image velocimetry was performed on a native mitral valve with intact subvalvular apparatus to quantify the fluid fields through and proximal to the mitral valve. This well-established technique is capable of measuring velocity vectors with high spatial resolution at any point in the cardiac cycle, which is necessary for the direct quantitative validation of computational fluid dynamics. Stereoscopic particle image velocimetry was performed at 27 time points in the cardiac cycle. Four flow fields were captured in the left ventricle at 4, 8, and 15 mm lateral spacing from the central plane. An additional central plane in the left atrium was captured using a single camera orthogonal to the flow field.

Because of the complex subvalvular apparatus, stereoscopic particle image velocimetry was necessary to acquire the best field of view in the left ventricle. The mitral chordae and the papillary muscles obscured the optical access of a single orthogonal camera as would be performed with typical 2D PIV. To improve this, first the native papillary were closely trimmed to minimize their thickness without affecting their function. Next, the camera was angled with the use of a Schiempflug filter to minimize optical distortion (Figure 8-10). However, the use of a single camera in a 2D configuration led to the underestimation of the velocity vectors; observed velocities were a projection of the true velocity vectors onto the imaging plane. To compensate for this, a second camera in a stereo configuration was added. This also provided the added benefit of allowing the third component (out of plane) velocity to be resolved.

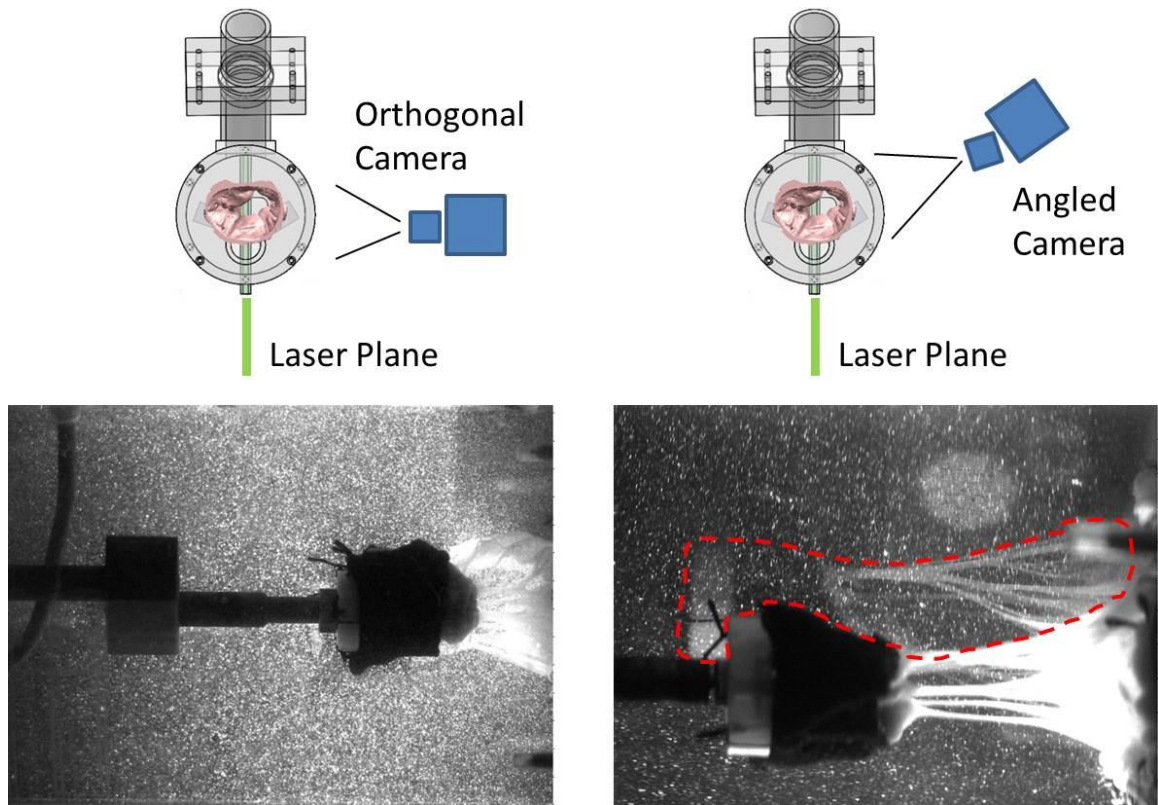


**Figure 8-10 Comparison of PIV optical access from orthogonal and angled camera configurations. Dotted red line highlights increased field of view, which captures flow through and proximal to the mitral valve.**

Flow fields at key points in the cardiac cycle are presented below. During early systole, the flow field was mostly quiescent when both the mitral and aortic valves were closed (Figure 8-11). During early diastole, the mitral valve opens and flow begins to accelerate through the mitral valve. This is indicated by the velocity vectors into the ventricle originating from the mitral orifice. Flow is primarily orientated perpendicular to the mitral annular plane. Some entrainment of fluid from the quiescent portions of the ventricle, particularly near the top and bottom of the image (Figure 8-12), was observed. The peak velocity of flow through the valve is about 0.4 m/s in the center of the filling jet.

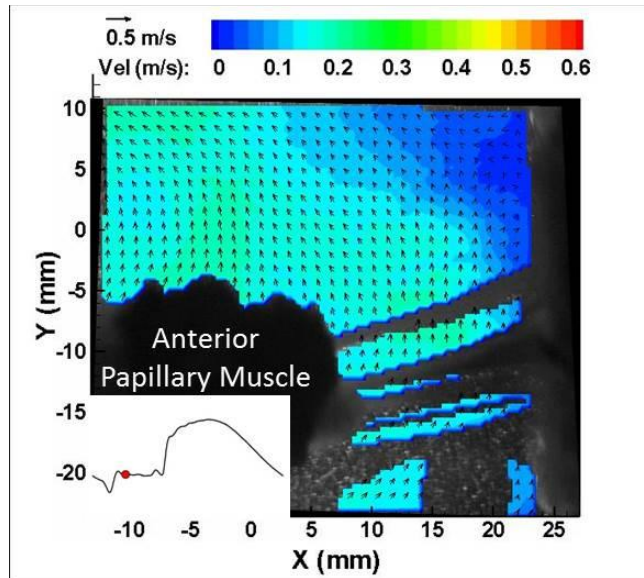


**Figure 8-11** Flow field during early systole is mostly quiescent. Mitral annular plane is to the right in the image. Inlay shows the point on the cardiac cycle demarked on the mitral flow curve.

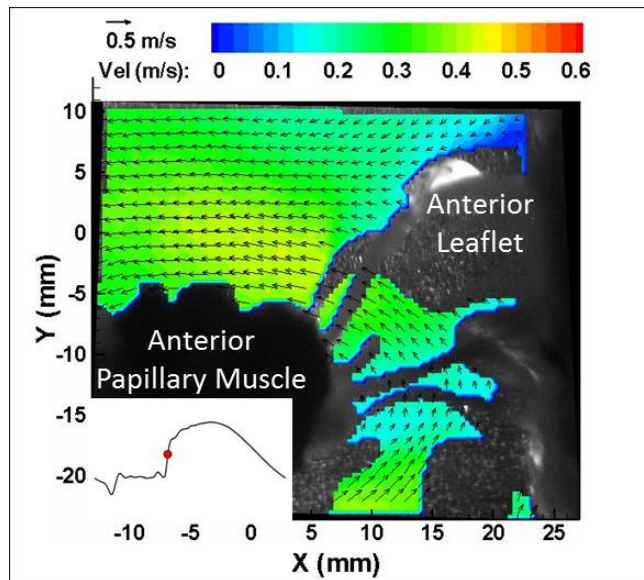


**Figure 8-12** Flow field during early diastole shows the onset of left ventricular filling through the mitral valve. Mitral annular plane is to the right in the image. Inlay shows the point on the cardiac cycle demarked on the mitral flow curve.



At peak diastole, a strong central filling jet was observed (Figure 8-13). The peak velocity observed in this jet was  $\sim 0.6$  m/s, which is similar to the velocities observed in flow through the mitral valve in clinical studies using echocardiography and in in-vitro studies on native mitral valves [235-237]. The mitral filling jet appears anteriorly oriented, as indicated by the velocity vectors overlaid on the contour plot. This is a result of the anterior leaflet having slightly higher mobility (and opening). This is similar to jets observed in clinical studies using Phase Contrast Magnetic Resonance Image and echo-PIV [238-240]. As suggested by Kilner et al. [238], the dominant direction of flow through the mitral valve is observed to be towards the anterior mitral leaflet free edge. The diastolic jet also causes some entrainment of fluid from the quiescent region near the aortic outflow, indicated by the redirection of flow towards the central jet. The peak Reynolds number of the flow through the mitral valve, based on the flow at peak diastole (15 L/min) and mitral annular area ( $4.5 \text{ cm}^2$ ) was  $\sim 3370$  (kinematic viscosity = 3.5 cSt).

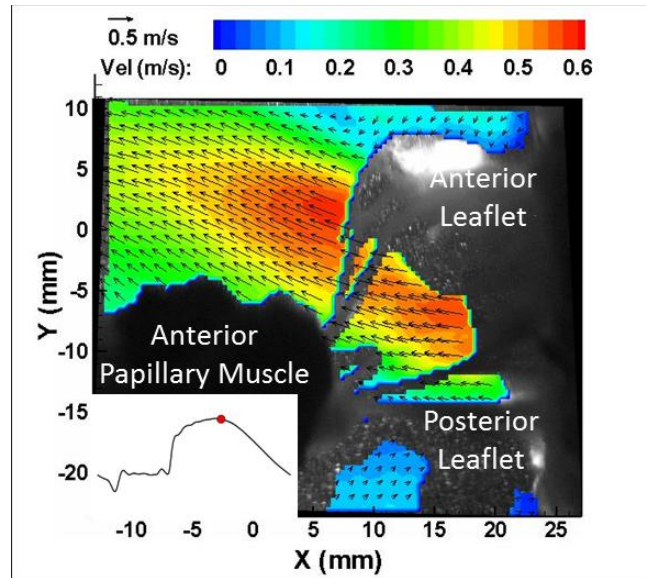


**Figure 8-13** Flow field during peak diastole shows a strong, anteriorly oriented central filling jet through the mitral valve. Mitral annular plane is to the right in the image. Inlay shows the point on the cardiac cycle demarked on the mitral flow curve.

During end diastole, ventricular pressure increases, slowing and reversing flow through the mitral valve and ultimately forcing it shut. This is indicated by the velocity vectors oriented towards the mitral annulus (Figure 8-14). There is minimal flow in the remaining portions of the ventricular chamber during this time point in the cardiac cycle. No flow was observed when the mitral valve was closed since the valve was competent.

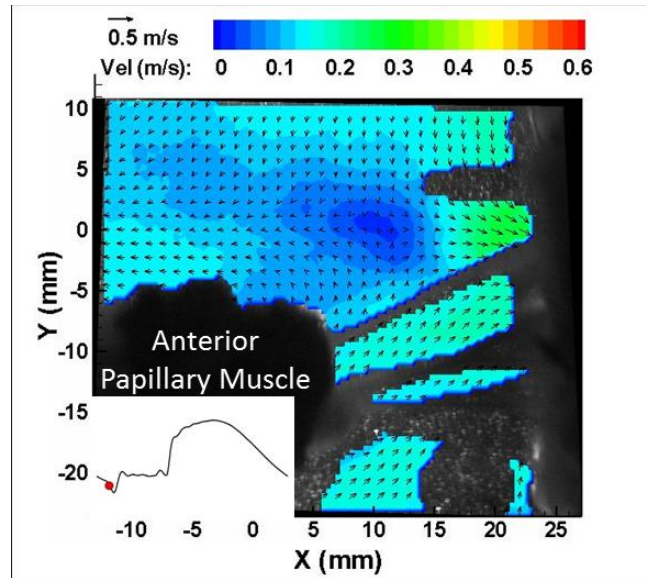


**Figure 8-14** Flow field during end systole shows mostly quiescent flow with low velocity flow reversal, which helps drive the valve closed. Mitral annular plane is to the right in the image. Inlay shows the point on the cardiac cycle demarked on the mitral flow curve.

Figure 8-15 shows contours of the out-of-plane velocity ( $W$ ) at peak diastole. The low magnitude of  $W$  throughout the entire field of view indicates that the flow is predominately two dimensional through the native valve, which can be expected in the cylindrical axisymmetric left ventricular chamber. Similar low out-of-plane velocities were observed at all points in the cardiac cycle that were studied (not shown). Figure 8-16 shows the out-of-plane vorticity during peak diastolic filling through the mitral valve. As expected, the highest magnitudes of vorticity are observed at the edges of the central filling jet. The region of clockwise fluid rotation, indicated by the negative vorticity values, appear stronger and more coherent compared to the positive vorticity observed near the papillary muscle.

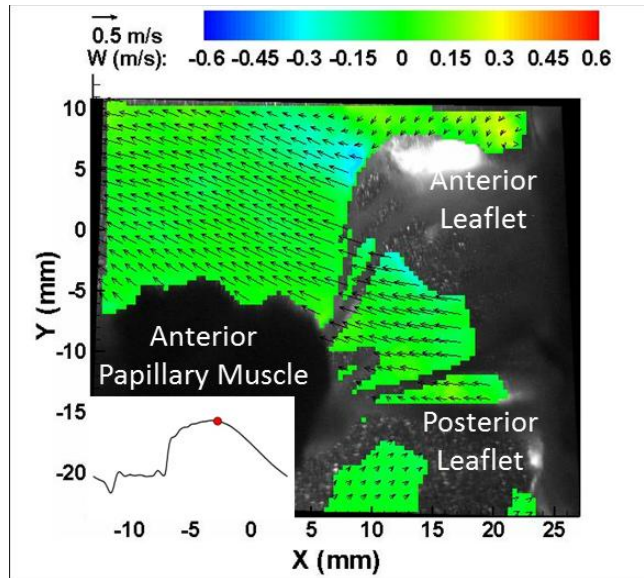


**Figure 8-15** Contour plot of out of plane velocity during peak diastole confirms flow through mitral valve is mostly two-dimensional. Mitral annular plane is to the right in the image. Inlay shows the point on the cardiac cycle demarked on the mitral flow curve.

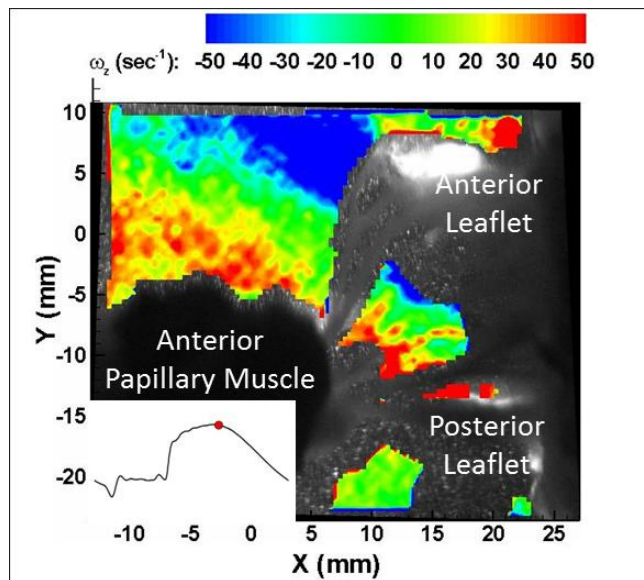


**Figure 8-16** Out of plane vorticity is strongest at edges of central filling jet during peak diastole. Mitral annular plane is to the right in the image. Inlay shows the point on the cardiac cycle demarked on the mitral flow curve.

An additional central plane in the left atrium was captured using a single camera orthogonal to the flow field. Stereoscopic particle image velocimetry was not performed as the flow was expected to be mostly two-dimensional in the axisymmetric cylindrical atrium. Further, direct optical access to the desired field of view could be obtained with a single orthogonal imaging plane. Figure 8-17 shows a strong central jet filling the left atrium through the pulmonary venous return; velocity vectors are directed towards the mitral orifice. Figure 8-18 shows a low velocity retrograde jet. As the valve was competent, this was the closing volume advecting away from the mitral annular. This suggests a regurgitant jet could be accurately resolved in the left atrium in cases of simulated mitral valve insufficiency

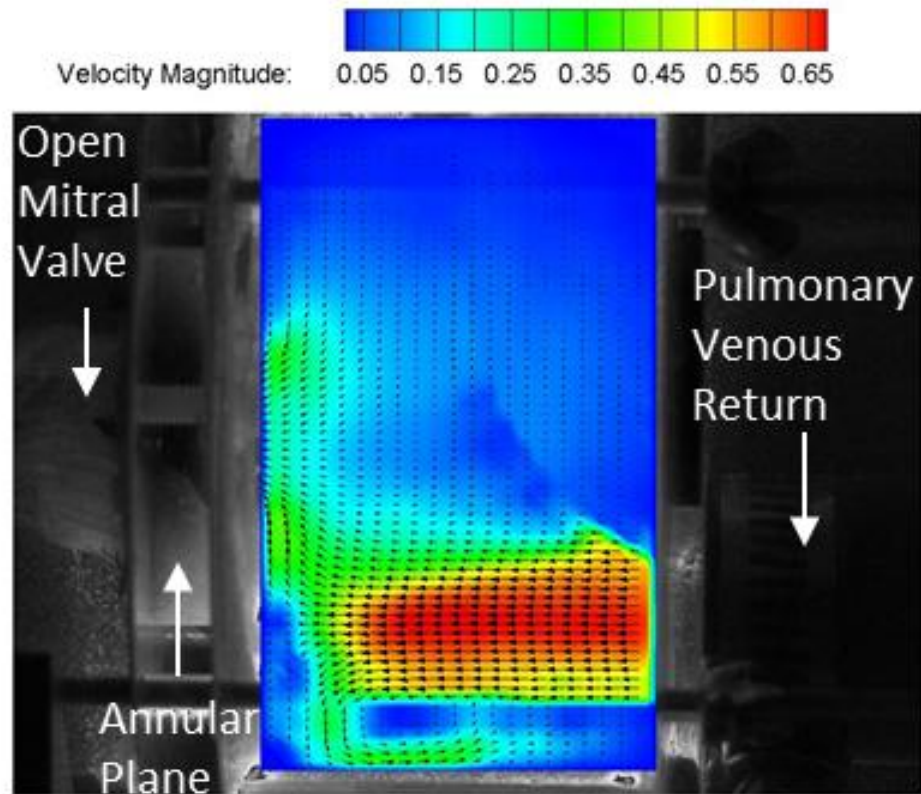


**Figure 8-17** Flow in the left atrium during diastole shows a strong pulmonary venous return jet. Velocity vectors are directed towards the mitral orifice. Mitral annular plane is to the left in the image.

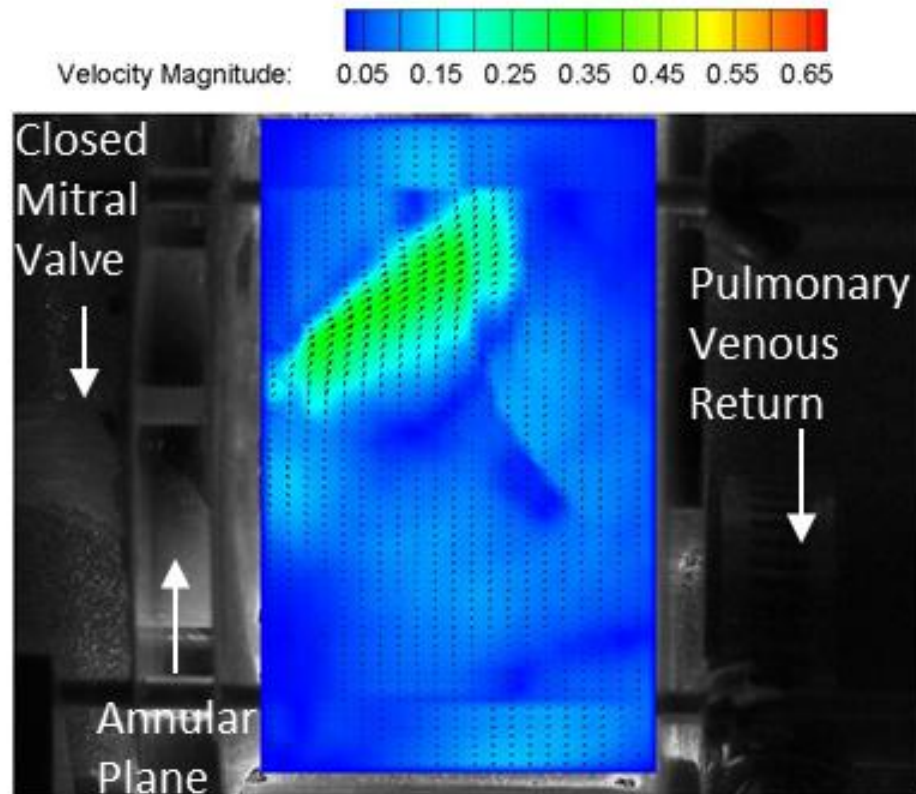


**Figure 8-18** Flow in the left atrium early systole shows a low velocity retrograde jet; as this valve was competent, this was the closing volume. Mitral annular plane is to the left in the image

### 8.2.5 Valve Biomechanics

Finally, experimental measurements of valve biomechanics can be used to tune material properties prescribed to computational mitral valve models. Of paramount importance, complex mitral leaflet deformation needs to be characterized. Mitral leaflets are non-linear anisotropic membranes that experience large deformation due to their intricate microstructure [4,106,110,134]. To this end, mitral leaflet strain was calculated throughout the cardiac cycle through a well-established experimental technique [118,194].

Surface markers on the anterior and posterior leaflets were digitized from dual camera photogrammetry in a reference and systolic configuration (Figure 8-19). The reference configuration was chosen at the lowest left ventricular pressure when surface markers were easily visible. Peak systolic closure was determined by selecting the frame which corresponded to peak left ventricular pressure (image and pressure acquisition were synchronously triggered). 51 nodes were tracked for the anterior leaflet; 23 for the posterior leaflet. Markers were tracked over the entire anterior leaflet and the P2 (central) scallop of the posterior leaflet. A triangulated shape function was applied to the nodes (71 elements for the anterior leaflet; 28 for the posterior leaflet). Green area, circumferential and radial strains were calculated based on methods described in [118,194].



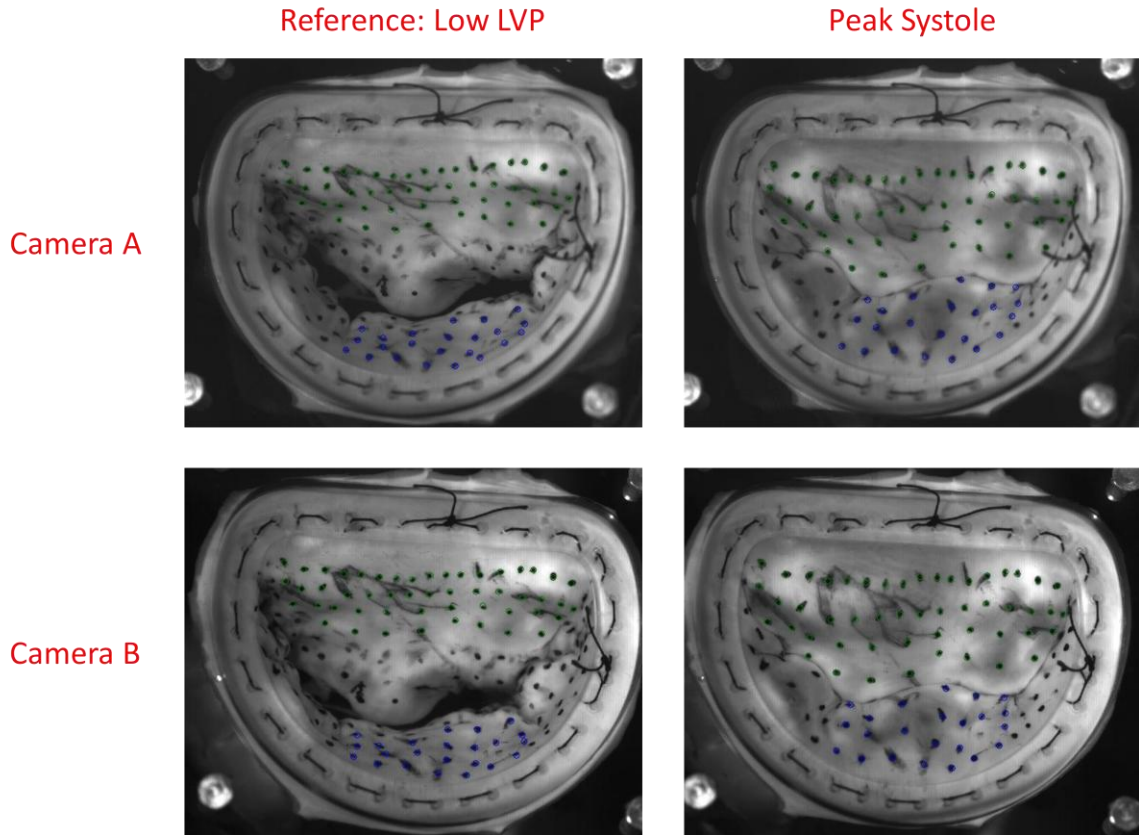


**Figure 8-19** Surface markers on the anterior (green circles) and posterior (blue circles) leaflets were digitized from dual camera photogrammetry in a reference and systolic configuration.

Spatially averaged anterior and posterior strains were consistent with previous *in-vitro* studies (Figure 8-20) [36,118,193,194]. Anterior leaflet areal strain ( $0.577 \pm 0.288$ ) was greater than posterior leaflet areal strain ( $0.404 \pm 0.360$ ). Radial strain was the largest contributor (anterior leaflet:  $0.118 \pm 0.107$ ; posterior leaflet:  $0.311 \pm 0.208$ ). Circumferential strain was comparatively low for both leaflets (anterior leaflet:  $0.123 \pm 0.103$ ; posterior leaflet:  $0.040 \pm 0.150$ ). This is expected as the native mitral leaflets extend radially to create competent valvular closure. Additionally, it is well known that the load bearing collagenous fibers preferentially orient in the circumferential direction [106].

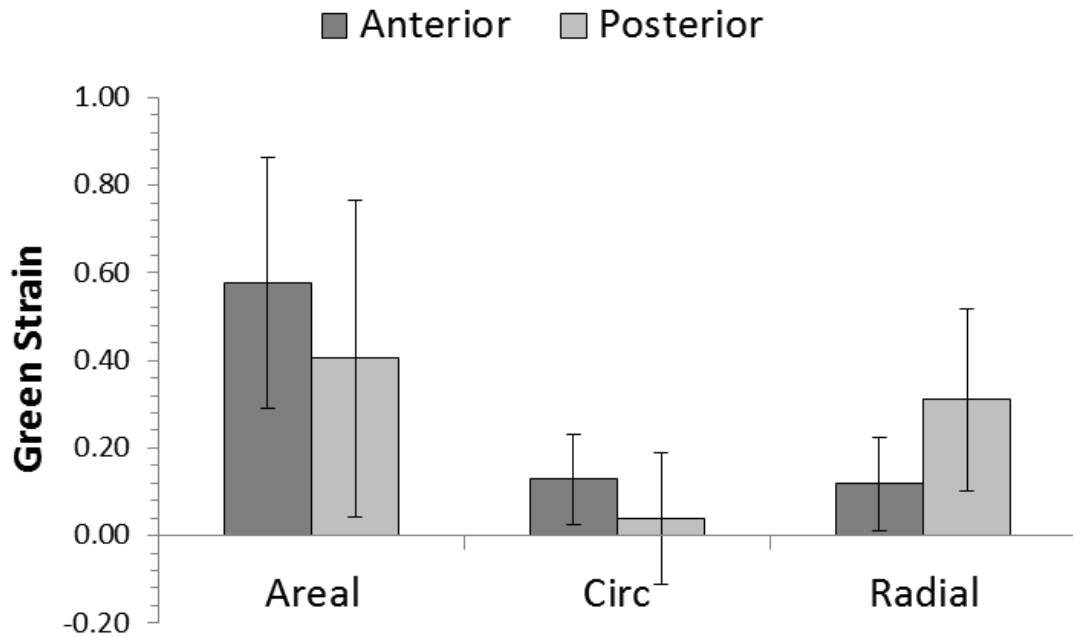


**Figure 8-20 Anterior and posterior areal, circumferential and radial strains.**

Local areal (Figure 8-21), circumferential (Figure 8-22), and radial (Figure 8-23) strains were additionally characterized to identify regional gradients of leaflet deformation. This is necessary to understand the complex mitral leaflet deformation because of the unique scallops and closures geometries. The anterior leaflet shows preferentially larger strains closer to the anterior commissure. In this region, the coaptation line appears to skew towards the posterior annulus, suggesting the anterior leaflet undergoes larger deformation as necessary to maintain valve competency. Posterior leaflet strain is largest at the central region of the P2 scallop. Both the posterior and anterior leaflets appear to have lower strains towards the posterior commissure.

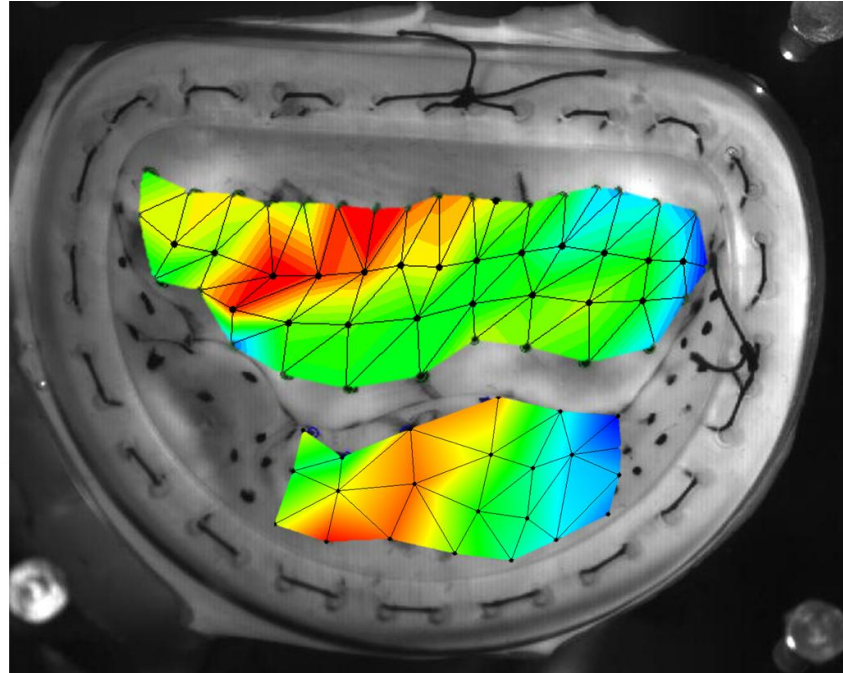
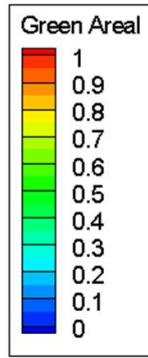


Figure 8-21 Anterior and posterior areal strain.

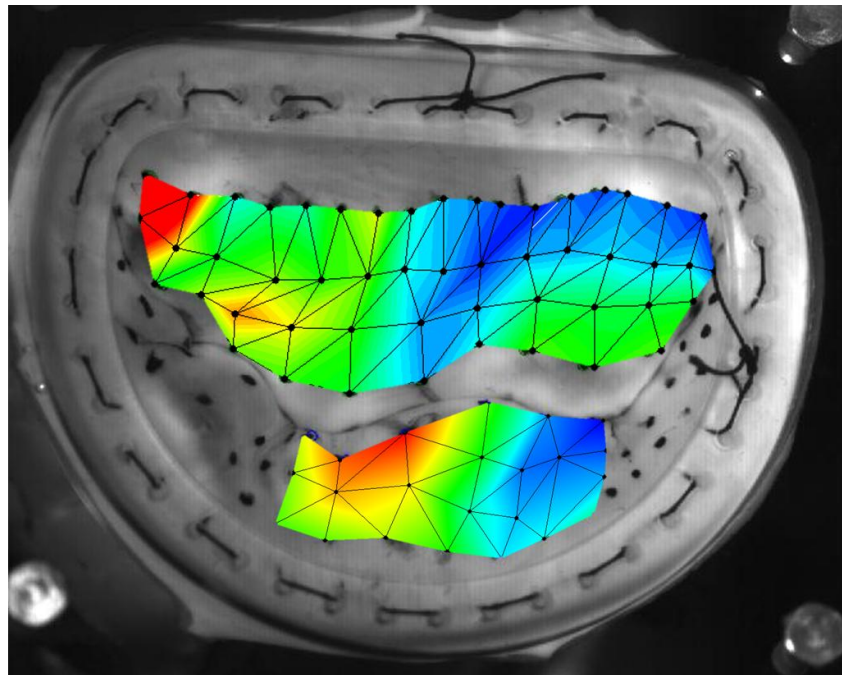
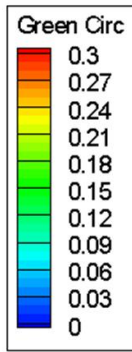
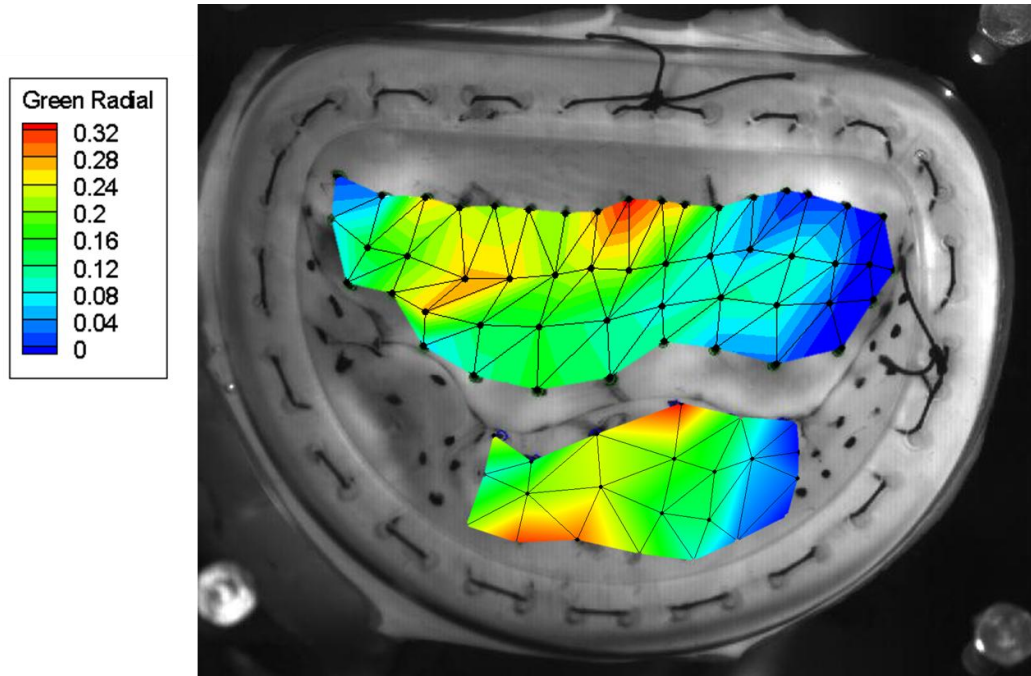
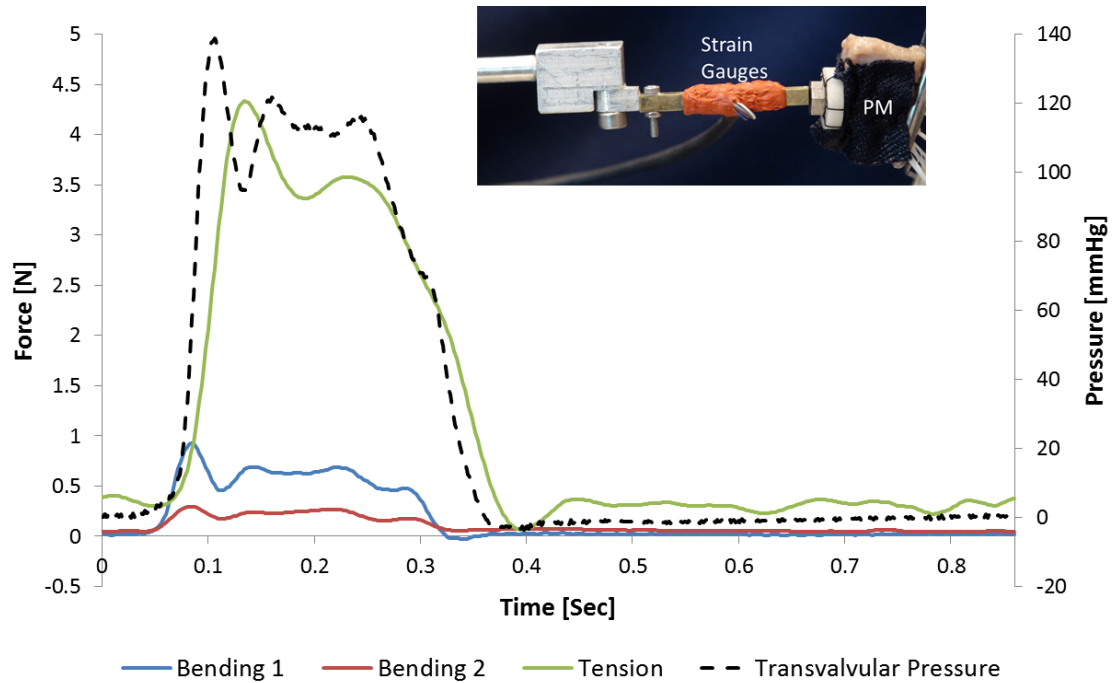


Figure 8-22 Anterior and posterior circumferential strain.



**Figure 8-23 Anterior and posterior radial strain.**

In addition to mitral leaflet strain, forces can be resolved at each papillary muscle using in-house built strain gauge transducers [2]. These transducers are the last link between the mechanical positioning rods and the native papillary muscles. Forces can be resolved in the tensile and bending components throughout the cardiac cycle. The largest component of force in the normal valvular configuration is in the tensile direction (Figure 8-24). Understanding the resultant forces at each papillary muscle provides an additional metric to validate subvalvular computational modeling. Resultant papillary muscle forces will be affected by the implementation of chordal anatomy. While it's not possible to experimentally measure forces on all potential chordae, it is comparatively easy to quantify the resultant force of all the chordae on each papillary muscle.



**Figure 8-24 Forces at each papillary muscle can be resolved in the tensile and bending directions throughout the cardiac cycle. Force profiles follow the transmitral pressure waveform. The largest force component is in the tensile direction.**

### 8.3 Discussion

These representative data, along with additional data acquired through further experimentation, have become available to the scientific community through a central online repository. This repository is accessible through a password protected secure shell client. The currently available data are tabulated below (Table 8-1). Micro-computed tomography imaging for open (N = 6; MV\_1-6) and closed (N = 2; MV\_5-6) mitral valves are available. Two of these data sets have corresponding full volume echocardiography (N = 2; MV\_1-2). Of these, there are papillary muscle forces (N = 1;

MV\_1) and leaflet strains (N = 1; MV\_1) for one geometry. For this geometry, hemodynamic (120 mmHg peak LVP, 70 bpm heart rate, 5.0 L/min cardiac output, N = 1; MV\_1) and particle image velocimetry (4 flow fields in the left ventricle, 1 flow field in the atrium, each sampled every 25 ms in the cardiac cycle, N = 1; MV\_1) data are also available. Additional steady flow particle image velocimetry data are available at four flow rates for all conditions. A single valve (N = 1; MV\_7) was tested with normal papillary muscle positioning and papillary muscle displacement. Papillary muscle displacement was performed in the apical, lateral, and posterior directions for the anterolateral papillary muscle, the posteromedial papillary muscle, and both papillary muscles simultaneously. A second iteration of papillary muscle displacement was performed with only lateral and posterior displacement.

**Table 8-1 Currently available data. Repository population is ongoing.**

<b>Experimental Technique</b>	<b>Sample Size</b>	<b>Notes</b>	<b>Serial #</b>
<b>Micro-Computed Tomography</b>	Open (N = 6) Closed (N = 2)	Closed geometry obtained at > 30 mmHg.	MV_1-6 MV_5-6
<b>Echocardiography</b>	N = 2	Dynamic.	MV_1-2
<b>Papillary Muscle Forces</b>	N = 1	Dynamic.	MV_1
<b>Leaflet Strains</b>	N = 1	Anterior and Posterior Leaflets. Dynamic.	MV_1
<b>Particle Image Velocimetry</b>	N = 1	Sampled every 25 ms in the cardiac cycle. 4 LV planes, 1 LA plane.	MV_1
<b>Steady Flow Particle Image Velocimetry</b>	N = 1	4 Flow rates at 7 PM configurations.	MV_7

Data can be selectively mined based on the methods and objectives of the implemented computational solver. Three such examples of independent research groups having made use of the experimental data for their computational model development and validation are described below. Each of these research institutions has a unique approach to leverage their particular expertise.

Siemens Healthcare is placing a priority in the development of anatomically accurate models that can be virtually rendered in real time using advanced machine learning algorithms [20,21,225]. Because their model generation is exceptionally fast, there is an associated loss in patient specific geometric features. Their mitral valve models are developed from a large statistical database, which causes smoothing of unique features, such as the indentations between leaflet scallops. Additionally, their database is

populated solely from clinical imaging modalities, which are not capable of accurately resolving the complex chordal structure. As a result, chordae are assumed based on representative literature data.

The data generated from the novel left heart simulator have been paramount to improving their model accuracy. In particular, Siemens Healthcare is utilizing high-resolution micro-computed tomography data, full-volume echocardiography, and pressure boundary conditions for their model development. Computational simulations of mitral valve closure from high-resolution micro-computed tomography imaging were compared to similar such models generated from lower resolution clinical imaging (echocardiography) (Figure 8-25). For each model, experimental pressure boundary condition was applied as the driving force to leaflet motion and valve closure. The discrepancy in resultant valve closure geometry was used to parametrically tune the anatomical model generated from the lower resolution medical imaging to ultimately develop a strategy for simulating patient specific geometry (Figure 8-26).

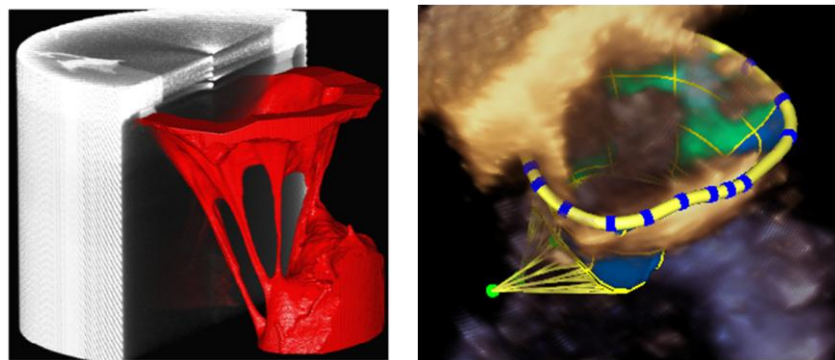


**Figure 8-25 Mitral valve anatomy reconstructed from micro-computed tomography imaging (Left) and full volume echocardiography (Right). Notice the idealized chordal structure in the echo generated model. [21]**



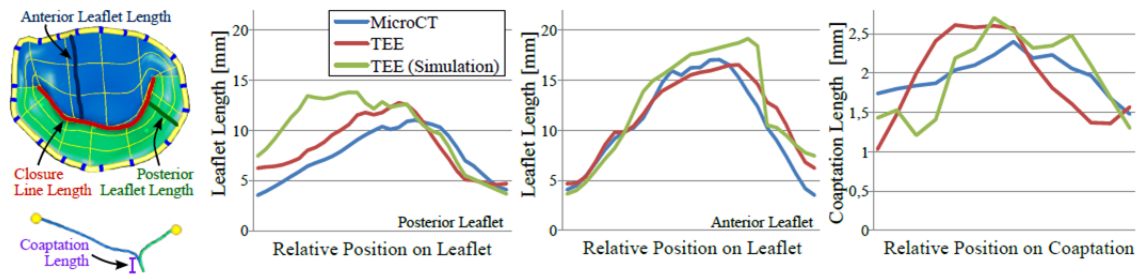


**Figure 8-26 Simulated mitral valve closure is compared for models generated from micro-computed tomography and echocardiography imaging. [21]**

In particular, by combining the state of the art imaging with the standard of care imaging, Siemens healthcare is attempting to develop a new empirically derived strategy to computationally model the mitral chordae. A simple workflow is proposed in Figure 8-27. As an initial guess, the computational model should assume chordal architecture derived from literature. Subsequently, the chordal anatomy can then be iterated until the simulated and experimental endpoints are agreeable. This may first be performed for the control valve; however, these generated models should be further tested under a range of hemodynamic and geometric conditions. Hemodynamic changes may be applied as altered heart rate (brachy/tachy-cardia), left ventricular pressure (hyper/hypo-tension), and cardiac output (heart failure/exercise). Detailed comparisons between valvular mechanics can be performed using leaflet strain and subvalvular force measurements. Geometric conditions may be applied as annular dilation and papillary muscle displacement (neither of these perturbations affects leaflet or chordal structure). These additional conditions will help assess the accuracy and predictive capabilities of the computational models.

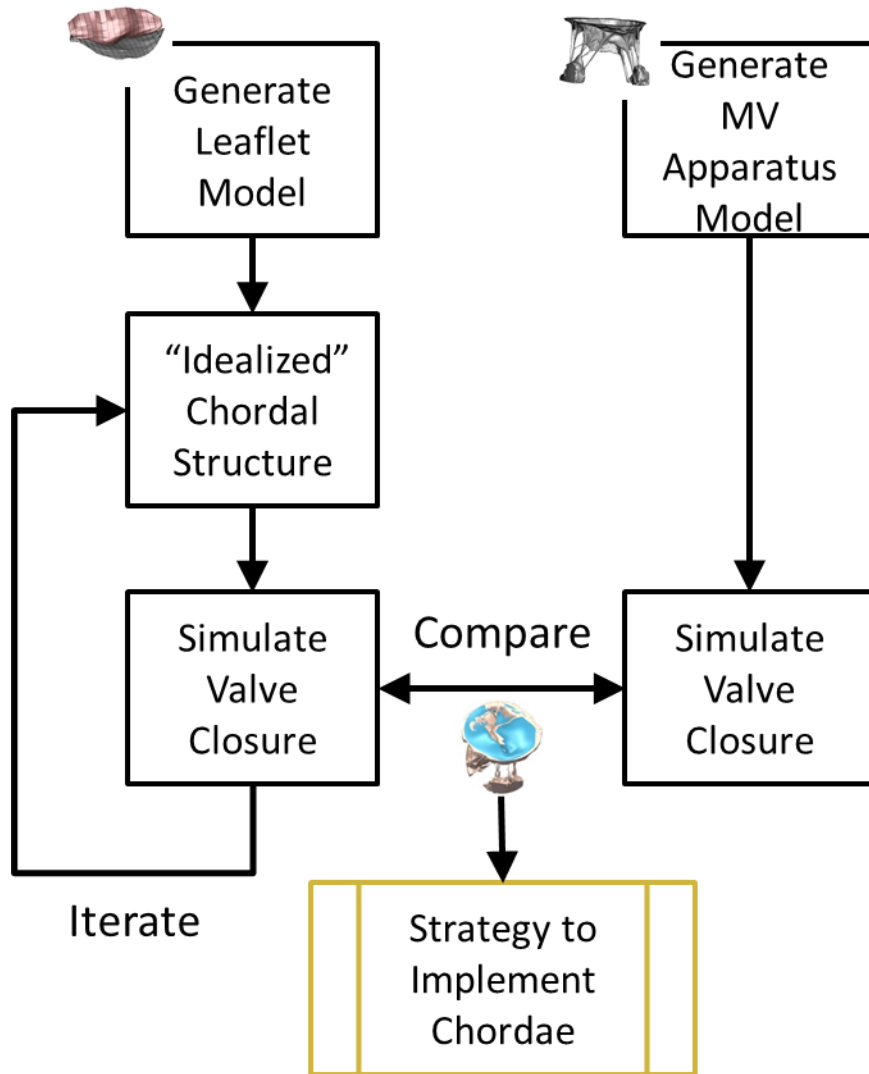


**Figure 8-27 Proposed flow chart to iteratively tune mitral valve anatomy.**

A second example of the unique utilization of these experimental is provided by the Center for Cardiovascular Simulation at the University of Texas. Dr. Sacks et al. are developing a microstructurally accurate mitral valve model to understand the precise interplay between global mechanical stimuli and underlying cellular response [241]. In the short term, Dr. Sacks et al. aims to identify the mechanisms by which global mechanics induce cellular response, which in turn mitigates bulk valvular function. Their

ultimate vision is to utilize these models to understand adaptive mitral valve remodeling following mitral valve repair to understand and predict long-term repair failure.

In the first step in this arduous process, Dr. Sacks et al. have developed a novel method to map the collagenous microstructure of the mitral leaflets through combined micro-computed tomography imaging and Small Angle Light Scattering. This is done by using miniature Ebony glass beads affixed to the atrialis of each mitral leaflet, which then serve as landmarks for both experimental modalities. Microstructural fiber orientation is then mapped to the reconstructed micro-computed tomography valve model (Figure 8-28). To this end, the micro-computed tomography acquisition protocol was amended to include the application of these radio-opaque beads. Scans were performed in the open and closed configuration. Experimental leaflet strain could also be acquired throughout each mitral leaflet using the 3D location of these radio-opaque beads. Static pressure boundary conditions were prescribed for these studies, which can be ultimately applied to the computational simulations. Currently, model development is in place. Preliminary studies replace the complex chordal structure with simple tensile elements, which originate from the papillary muscles and insert into the leaflets as indicated by micro-computed tomography. In the future, stress development in the mitral leaflets will be investigated for pathological and surgical repaired mitral valves. As demonstrated in this thesis, simple annuloplasty and complex adjunctive repairs can be performed with these experimental techniques to provide the necessary data to assess the models predictive accuracy.

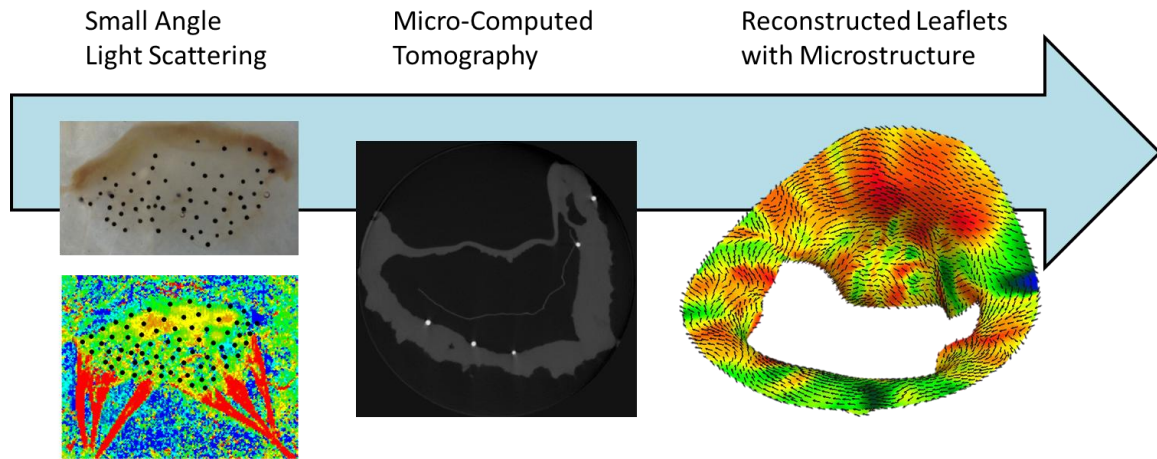


**Figure 8-28 Radio opaque glass beads are used to register microstructure fiber orientation to micro-computed tomography reconstructed mitral leaflet geometry.**

Finally, in collaboration with the University of Maine, Pacific Northwest National Laboratory, and the Cardiovascular Fluid Mechanics Laboratory at Georgia Tech, an anatomically accurate mitral valve fully three-dimensional fluid structure interaction model is being developed. Previous models utilize pressure boundary conditions to drive leaflet dynamics; these models fail to appreciate the intimate relationship between fluid dynamics and mitral valve and ventricular function. Several studies have implicated mitral inflow in deleteriously affecting ventricular vortex dynamics and systolic ventricular function [235-237,242]. Additionally, initial flow reversal and ventricular vortex dynamics have been suggested to impact mitral valve closure [243-245]. Systolic valvular function (Systolic Anterior Motion) has also been shown to be effected by acceleration of left ventricular outflow (Venturi effect) in obstructive hypertrophic cardiomyopathy. Systolic Anterior Motion may also occur following poorly executed surgical repair which displaces the coaptation line anteriorly [246,247]

This model will be the first to fully incorporate the intimate mechanical feedback between mitral valve dynamics and the surrounding fluid flow. The anatomic mitral valve geometry is developed directly from the micro-computed tomography data; no assumptions are made concerning leaflet shape or thickness, and chordal architecture (Figure 8-29). Fluid dynamics through and proximal to the mitral valve will be quantitatively compared to the highly resolved stereoscopic particle image velocimetry data. Because this computational model uses a Smooth Particle Hydrodynamics computational solver, flow boundary conditions were utilized at all inlets and outlets. In this case, pressure conditions experimentally acquired at these locations were used for validation. This model has the potential to accurately simulate mitral regurgitation and predict valve competency following virtual surgical repair procedures.



**Figure 8-29** Highly resolved mesh of the anatomically accurate mitral valve model generated from micro-computed tomography.

The three examples presented above are a short list of possibilities tailored specifically to the individual expertise of each research institution. Through an initiative towards an open access repository, it is believed these and future data will be strategically mined for continued mitral valve model development and validation.

#### **8.4 Conclusions**

Recent advances in computational mitral valve modeling aim to provide an ideal platform for mitral valve surgical planning. These models have ability to mimic complex repair procedures preoperatively and non-invasively [223-230]. However, high-fidelity experimental data are necessary to validate these finite element and fluid-structure interaction models to ensure their clinical accuracy and utility. The current study presents a novel platform to provide these data for direct one-to-one validation of the complex geometry and biomechanical responses of the mitral valve. Multiple state of the art experimental techniques can be combined to create comprehensive benchmark data sets (Table 8-1).

**Table 8-1 Comprehensive experimental benchmark data are generated through multiple complementary experimental techniques.**

<b>Hemodynamic B.C</b>	<b>Geometric B.C</b>	<b>Valvular Dynamics</b>	<b>Fluid Mechanics</b>
Pressure: Atrium, Ventricle, Aorta	CAD of LHS	Leaflet dynamics through 3D echo	Stereoscopic PIV: 3 components of velocity
Flow: Mitral, Ventricular (bladder inlet), Aortic	$\mu$ CT of MV: loaded and unloaded	Force: chordae, papillary muscles	
		Leaflet strain: anterior and posterior	

## CHAPTER 9

### CLINICAL SIGNIFICANCE, LIMITATIONS, AND FUTURE WORK

#### 9.1 Clinical Significance

In this thesis, significant progress was made in developing a new planning paradigm for the surgical treatment of mitral valve disease. This planning paradigm explored three key steps in the surgical management of mitral valve disease, including: (i) clinical diagnosis, (ii) targeted surgical repair efficacy, and (iii) development and validation of novel computational predictive mitral valve models (Figure 9-1).

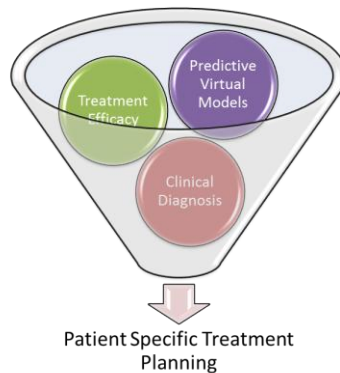


**Figure 9-1 Patient specific treatment planning is a multi-factorial process that combines clinical diagnosis, understanding treatment options and efficacy, and utilizing novel computational methods for predictive virtual modeling.**

The first step in the clinical management of mitral valve disease is to accurately identify patients for surgical referral. Currently, this decision making process relies on an



integrative approach that factors qualitative grading of mitral regurgitation severity, presentation of symptoms, left ventricular function, and likelihood of successful repair [24]. As an example, isolated mitral valve surgery is not indicated for patients with mild or moderate mitral regurgitation, but surgery is beneficial for asymptomatic patients with chronic severe regurgitation and mild to moderate left ventricular dysfunction. These key distinctions underscore the need to accurately quantify mitral regurgitation severity. In particular, clear quantitative delineation between moderate and severe mitral regurgitation would promote timely and beneficial surgical intervention.

Unfortunately, current clinical characterization of mitral regurgitation in of itself can be a complicated, integrative assessment. Qualitative measurements include angiographic grading (invasive), regurgitant jet area and direction, and vena contracta width. Quantitative measurements include regurgitant volume, fraction, and orifice area. These latter measurements, however, are known to underestimate mitral regurgitation and suffer from poor intra- and inter-observer variability. Additionally, these measurements have their largest errors at moderate to severe regurgitation, particularly where mitral regurgitant orifice geometry violates a critical assumption in the methodology.

These issues were recently recognized in an editorial in the Journal of the American Society of Echocardiography where Dr. Stephen H. Little noted, “Ideally what the imaging clinician needs is a single tool to accurately quantify a broad range of MR severity, and to be able to apply that same tool over time to make informed decisions about valve function, and patient prognosis” [18]. In that same editorial, a call for “an irrefutable reference standard – a gold standard – for the quantification of regurgitant

flow volume” was initiated. Clinical studies are limited by this principle lack of a gold standard by which new measurement techniques can be compared.

For this reason, the Georgia Tech Left Heart simulator was used for the development and validation of a novel regurgitant flow quantification tool. The Philips 3D Field Optimization Method presents a great possibility to impact future clinical diagnosis of mitral valve disease. In the studies presented herein, this simple to use technique was demonstrated to have superior accuracy and intra-observer robustness than the current clinical standard, 2D PISA. Through use of these experimental gold standard data, further refinement of the 3D FOM is possible, as is similar development by other researchers.

These quantifiable tools will lead to better delineation of treatment and progression of mitral valve disease and the critical timing of surgical indication. As a result, surgical treatment options may be tailored based on the clinical characterization of the valvular disease. A specific example where targeted treatment is needed is ischemic mitral regurgitation where the current preferred surgical repair option results in unacceptably high rates of recurrent regurgitation within the first 5 years of intervention. Using quantitative metrics of regurgitant flow and functional assessment of the mitral valve and left ventricle, surgical repair may be optimized to ensure long-term repair durability. In particular, patients presenting with ischemic mitral regurgitation that may not benefit from isolated restrictive annuloplasty and require adjunctive surgical treatments may be identified.

Consequently, it is important to understand the efficacy of these targeted adjunctive surgical repairs. Additionally, as these repairs may increase surgical

complexity, it is important to understand the effect of repair variability on resultant valvular function. In this thesis, two such adjunctive surgical repairs were investigated together with ring annuloplasty: (i) anterior leaflet augmentation, and (ii) basal papillary muscle relocation. Both of these repairs were found to restore leaflet coaptation and valve function while reducing tethering through the subvalvular apparatus in the treatment of ischemic mitral regurgitation. Specifically, these results were demonstrated in a setting of extreme papillary muscle displacement often associated with severe left ventricular dilation. Adjunctive surgical repair compared favorably against the surgical preferred treatment, which suggests there may currently be a mismatch between patient valvular dysfunction and applied surgical repair.

The results herein may provide the “average” cardiac surgeon with the confidence to perform such complex adjunctive surgical repairs, which may otherwise be eschewed in favor of simple annuloplasty. Anterior leaflet augmentation was found to be efficacious with two significantly different patch sizes. There were no deleterious effects on valvular function caused by oversizing the pericardial patch. These data show a large range of pericardial augmentation sizes can be performed, or more simply an oversized patch can be targeted to maximize leaflet coaptation.

Similarly, basal papillary muscle relocation did not require a high degree of anatomical precision to restore valvular function and alleviate leaflet-subvalvular tethering. Specifically, two key sources of potential surgical variability were explored. First, the location of the mitral annulus to which the papillary muscles will be suspended from did not affect resultant valvular function. Regardless of the how the repair was performed, apical-basal displacement of the papillary muscle was largely corrected. This

isolated directional improvement was sufficient despite residual displacement in the posterior and lateral directions. Second, a range of apical-basal relocation magnitude was capable of restoring valvular function. As pre- and peri-operatively determining how far the papillary muscles should be relocated is challenging, these findings should be encouraging to the surgical community. Finally, surrogate measurements were identified which could inform the surgical repair by approximating the relationship between systolic leaflet closure and papillary muscle position.

While these studies were able to demonstrate the efficacy and robustness of these adjunctive surgical repairs, they remain limited as patient to patient variability creates an additional aspect of complexity, which may not be reasonably studied in an experimental framework. The pathological conditions created herein were informed from averaged clinical statistical data. As with any statistical measurement, individual nuances are overlooked. For this reason, novel computational tools are being developed for the patient-specific predictive surgical evaluation for mitral valve repair.

These models have evolved from simple and idealist annular, leaflet, and chordal profiles to patient specific models derived from medical imaging. Computational models have the potential to provide unique non-invasive evaluation of mitral valve mechanics and function pre- and post-operatively. These models vary considerably in their execution owing to differences in anatomical construction, material properties, boundary conditions, and preferred numerical solver methods. The mitral valve apparatus has a complex structure, for which any of the components can be modeled through direct image reconstruction or with idealized simplifications. Most notably, the leaflets are often modeled with homogeneous thickness and without commissural scallops [168]. The

chordae are approximated as simple traction only elements without any thickness and minimal anatomical branching, and the papillary muscles are never modeled. Figure 9-2 highlights some of the subtle but important differences that are observed between mitral valve models. Material properties are applied differently between models, despite the well characterized non-linear anisotropic, inhomogeneous tissue response. Boundary conditions may be applied as a dynamic annulus or papillary muscles, the valve may be modeled in isolation or within the anatomy of the left heart, and pressure or flow hemodynamics may be applied. Finally, numerical solvers may utilize finite element analysis, mass-spring modeling, or fluid-structure analysis. These limitations currently affect the clinical accuracy and applicability of such computational simulations.

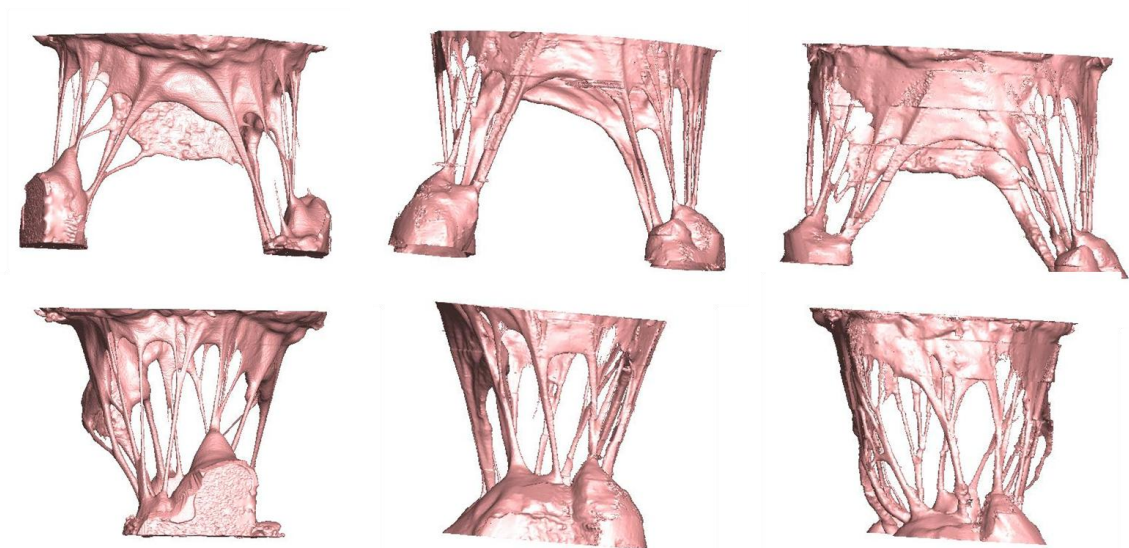


**Figure 9-2 Three separate mitral valves are reconstructed from micro-computed tomography (Top: posterior view; Bottom: anterior commissure view). There are noted differences in leaflet lengths, scallop indentations, chordal branching, and papillary muscle tips.**

Therefore, in this thesis, an experimental framework was developed for the direct one-to-one validation of computational methods against comprehensive, time-resolved experimental data with multiple measured endpoints and well defined boundary conditions (Figure 9-3). Additionally, such systematic data can be used to understand whether increasing model fidelity and complexity provides marked gains in clinically assessing mitral valve function and structural mechanics, particularly as a patient specific surgical planning tool. After these tools have been comprehensively validated, they may be used in pre-operative surgical planning, where surgical options can be assessed virtually on patient specific valvular anatomy. Figure 9-4 shows a simple flow chart, which outlines how a predictive surgical planning tool may be used. Anatomical mitral valve geometry can be created from standard of care echocardiography. The lessons learned from these in-vitro studies will be applied to resolve the differences between observed valvular geometry through clinical imaging with true anatomy. The material properties of the computational model can be initialized based on data from the in vitro studies and subsequently tuned for the patient's native mitral valve by comparing the simulated and observed valve dynamics. Virtual surgical options may then be simulated and assessed for efficacy. Difficult to measure tissue responses such as stress and strain may also be compared to optimize for long-term repair durability. Such a paradigm has been pioneered by the Cardiovascular Fluid Mechanics Laboratory and implemented through a novel virtual interface for countless patient-specific predictive surgical simulations [248].

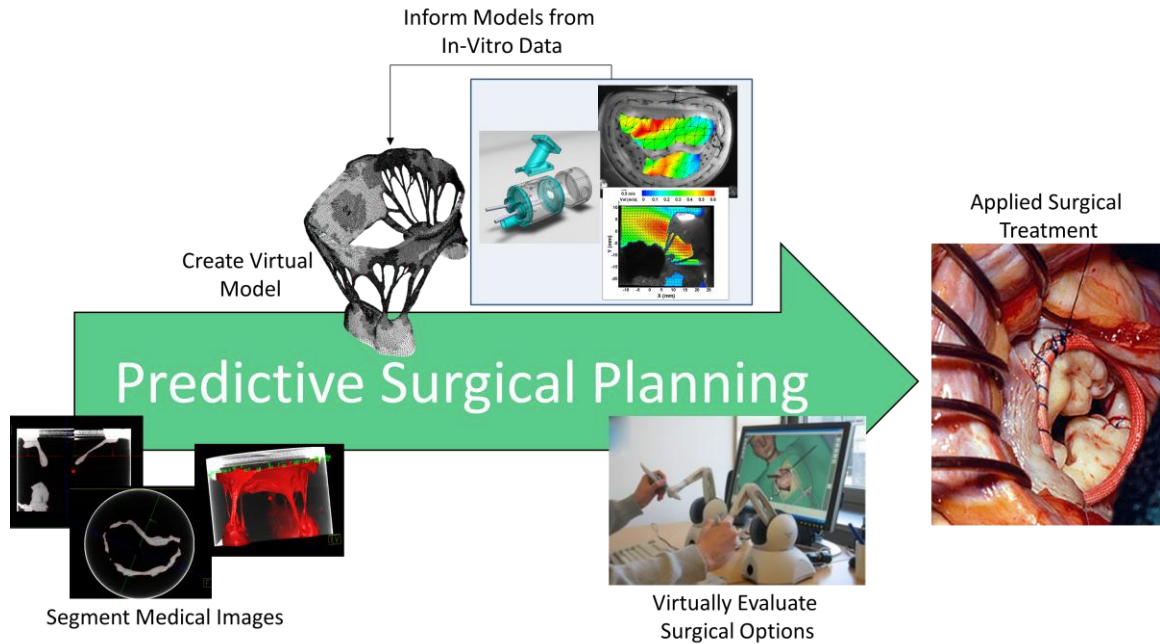


**Figure 9-3 Patient specific treatment planning is a multi-factorial process that combines clinical diagnosis, understanding treatment options and efficacy, and utilizing novel computational methods for predictive virtual modeling.**

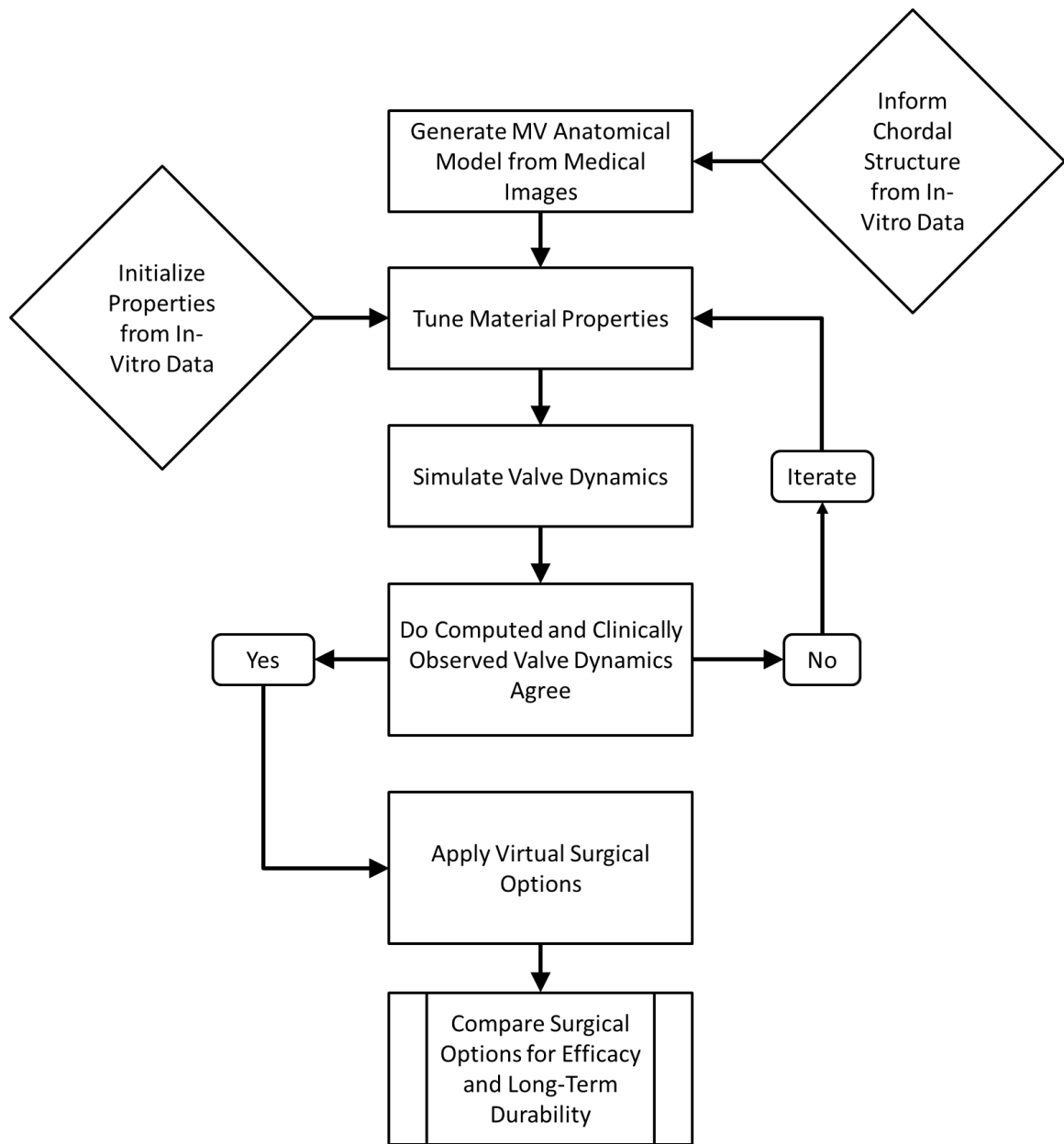


**Figure 9-4 Patient specific predictive surgical planning flow chart.**



## 9.2 Limitations

As with all experimental methods, the studies presented in this thesis are not without limitations. Although the *in vitro* model used in these studies simulate the physiologic function, hemodynamics, and mechanics of the normal and diseased mitral valve, certain limitations remain. An initial limitation of this study is associated with the interspecies variability between ovine and human mitral valves. Ovine mitral valves were used in this study because of the limited availability of human tissue. Fortunately, ovine mitral valves bear close anatomical and functional resemblance to human mitral valves [184,185]. Ovine mitral leaflets have similar dimensions to human valves, which makes creating normal and pathological dysfunction possible. While ovine mitral valves contain less chordae than human valves, both valve types exhibit comparable chordal distribution and structure. For these reasons, large animal studies also employ ovine models to investigate mitral valve dysfunction and surgical repair.

The rigid ventricle used in this thesis did not mimic native dynamic annular and ventricular dynamics: (i) the native mitral annulus changes in size and shape during the cardiac cycle [100,249-251], (ii) the left ventricle undergoes helical apical-basal contraction, and (iii) the papillary muscles contract throughout the cardiac cycle [172,252]. During exercise, these dynamics are known to further exacerbate mitral regurgitation [253], a phenomenon, which cannot be simulated with these methods. Although these dynamics were not simulated, the distance between the papillary muscles and the annular plane have been shown to remain relatively constant throughout the cardiac cycle [252]; the papillary muscle can be considered as shock absorbers to for the mitral apparatus. Furthermore, these dynamics are retarded in functional mitral valve

disease [13,191,209]. All the repairs in this thesis were supported with mitral annuloplasty, which further obliterates native mitral annular dynamics [254].

These recognized limitations can be improved upon by future iterations of the left heart simulator. Preliminary research has been performed to create a dynamic papillary muscle system. In this system, the apical-basal position of the papillary muscles can be controlled through servo motors using custom motion profiles programmed through LabView [255]. A similar approach can be taken to create mitral annular dynamics. The drawstring mechanism which currently allows the mitral annulus to dilate may be motorized to create the sphincteric motion observed in normal physiology. A separate motorized mechanism would be needed to create active non-planarity of the mitral annulus. This out of plane motion may not be critical, however, as the saddle shape of mitral annulus does not affect valvular competency [188]. Despite these limitations, this thesis makes significant contributions to the clinical and academic community through elucidating mitral valve function and mechanics in disease and surgical repair, while improving clinical diagnosis and advancing predictive computational modeling.

While the experimental techniques performed were designed to limit their invasiveness on mitral valve mechanics, the miniature chordal force transducers may effect chordal strain and subsequently valve closure. The brass spring element replaces a small portion of the native chordae. This spring element is designed to limit strain to 3% (the operating range of the strain gage); in comparison, the native strut chordae may strain up to 20% [256]. This more rigid brass element may therefore affect the closure of the valve. Additionally, as the strut chordae vary from valve to valve, the brass element may comprise a larger proportion of the chordae (for smaller strut chordae). This may

affect the total force measured at each chordae, which is a potential source of the large standard deviations observed in the chordal force data.

## 9.3 Future Studies

### 9.3.1 Specific Aim 1

Several future studies have been identified to continually benefit the clinical and scientific communities. Additional data are needed to further assess the efficacy and robustness of the Philips 3D Field Optimization Method with the adaptive z-height algorithm. Specifically, the experimental model needs to be adjusted to simulate apical-basal migration of the regurgitant orifice. This may be challenging to accomplish, but there are 3 possible solutions. First, the echo transducer can be mounted onto a mechanical traverse to artificially create the relative motion between the probe and the dynamic heart as observed clinically. Second, a dynamic mitral annulus plate may be used to create apical-basal translation of the mitral annular plane. This can be done by replacing the rigid acrylic plate with a rubber membrane that can deflect with elevated left ventricular pressure. This was previously done in *in vitro* studies to understand the effect mitral annular non-planarity on subvalvular force distribution [188,217]. A third approach may be possible as described above through a dynamic mitral annulus. Programmable servomotors may be utilized to produce mitral annular contraction and non-planar motion. With the use of one of these options, a range of mitral regurgitation conditions should be performed. As was done in this thesis, mitral annular dilation and papillary muscle displacement could be utilized to create round and slit orifices at mild, moderate, and severe mitral regurgitation grades. These data will help differentiate

between the adaptive radii and adaptive z-height iterations of the 3D Field Optimization Method. They may also be used for the development other similar methods.

Particle image velocimetry may be performed to acquire highly resolved velocities in the flow convergence zone. Because of the difficult viewing angles, stereoscopic-PIV may not be possible, but 2D-PIV should be sufficient. As it may be difficult to identify the location of the regurgitant jet, a traverse system will be needed. Preliminary acquisitions will need to be acquired to assess if the necessary flow fields were captured and the position of the laser plane and imaging window can be optimized. As the regurgitant jet is a three dimensional volume, several planes will need to be acquired. A strategy for acquiring imaging planes and calibration will need to be considered. It is not recommended to acquire data and calibration a single plane at a time, as the dynamics of a regurgitant orifice may be complicated. If full-volume PIV is possible, this is recommended as the entire jet can be captured through a single acquisition.

A final future study is suggested to understand the effect of the hemispherical assumption on the accuracy of the FOM technique. No new data is required for this. A hemi-elliptical approximation to the flow convergence zone is recommended based on the observations by Hopmeyer et al [202,203] (Figure 9-5). This may be calculated using the approximation for the surface area of a hemi-ellipsoid with height A and widths B and C:

$$SA = \pi AB \left( \frac{C^2}{AB} + d \int \sqrt{1 - k^2 \sin^2 \varphi} d\varphi + \frac{1 - \alpha^2}{\alpha} \int_0^{\varphi_0} \frac{d\varphi}{\sqrt{1 - k^2 \sin^2 \varphi}} \right)$$

where:

$$\alpha = \sqrt{1 - \frac{C^2}{A^2}} \quad k = \sqrt{\frac{1 - \frac{C^2}{B^2}}{1 - \frac{C^2}{A^2}}} \quad \varphi_0 = \sin^{-1} \sqrt{1 - \frac{C^2}{A^2}}$$

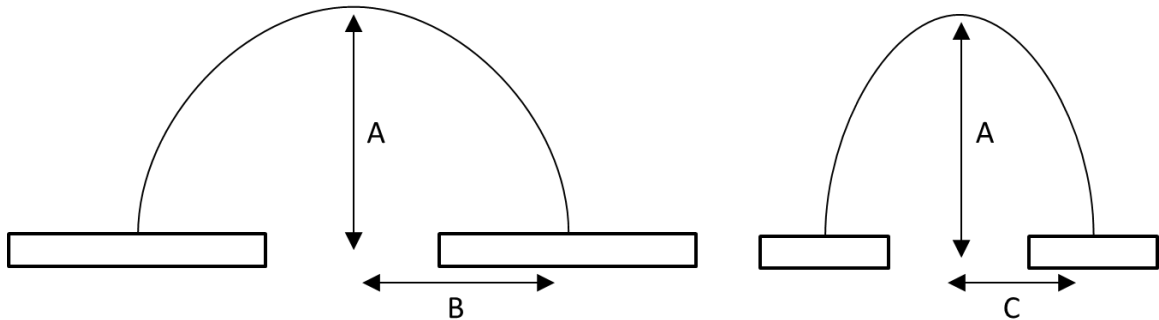


**Figure 9-5 Hemi-ellipsoidal isovelocity contour in two perpendicular planes.**

### 9.3.2 Specific Aim 2

Anterior leaflet augmentation and basal papillary muscle relocation were demonstrated to be efficacious for the repair of ischemic mitral regurgitation in the pulsatile left heart simulator. These repairs should be investigated in randomized clinical trials to best identify which patients should have targeted adjunctive surgical repairs. The clinical

studies should involve a comparison to restrictive mitral annuloplasty. Clinical endpoints of efficacy should include mortality, mitral regurgitation grade, and New York Heart Association (NYHA) functional classification of the stages of heart failure. Preoperative patient characteristics including leaflet coaptation and tethering, papillary muscle position, and ventricular dimensions should be measured.

Animal studies may be performed to investigate the predicative capability of using surrogate leaflet measurements to pre-operatively determine the amount of basal papillary muscle relocation needed to promote leaflet coaptation. These studies should utilize full volume echocardiography to carefully measure leaflet coaptation, annular diameter, and papillary muscle position pre-operatively. The linear relationship between leaflet closure geometry and papillary muscle positioning can be utilized to inform the basal papillary muscle relocation. The expected leaflet coaptation following this applied papillary muscle relocation can then be compared to the postoperative geometry observed. These experiments can be used to refine the previously observed *in vitro* relationships between leaflet geometry and papillary muscle position.

The pinnacle prospective study would involve randomized patient treatment comparing the efficacy of undersized ring annuloplasty to these adjunctive repairs; a ratio of 1:1:1 is suggested. The study should recruit patients with severe mitral regurgitation (carefully graded through a 3D PISA method). End points should include postoperative regurgitation, left ventricular reverse remodeling (end-systolic diameter), mortality, and adverse cardiac events measured acutely and at a 12 month follow up. Patients should also be classified by their degree of preoperative left ventricular diameter. It's expected that the largest benefit of these adjunctive repairs may be found in patients with severe

left ventricular dilation, where isolated ring annuloplasty may not be an appropriate treatment.

### 9.3.3 Specific Aim 3

The development and comprehensive validation of computational mitral valve models will be further aided by additional acquisition of experimental data. If possible, human mitral valves should be procured for these studies. This will limit any errors associated with mapping material properties from the ovine models to human mitral valves. Experimental studies should also aim to produce pathological mitral valve conditions as well as surgical repairs. Functional mitral valve disease can be performed using combinations of mitral annular dilation and papillary muscle displacement. Simulated and experimental mitral valve function and mechanics should be compared. Simulated mitral valve anatomy (specifically leaflet structure and chordal anatomy), and material parameters should not be adapted between conditions. These should be tuned to the physiological conditions, and once established should not be refined. This will allow the predicative capabilities of the simulations to be assessed. Following pathology, a myriad of surgical options can be performed experimentally as well as *in silico*, including those previously mentioned in this thesis. Again, the computed and experimental end points should be compared.

As previously mentioned the *in vitro* model can be improved with the addition of mitral annular and papillary muscle dynamics. This adds another level of complexity for which computational models should be assessed. The motion profiles of the annulus and papillary muscles should be carefully prescribed, such that they can be applied computationally.

Following the development of these computational models through these studies, preliminary clinical evaluation of the computational tools should be assessed. This may be performed through the use of retrospective medical imaging data. Pre- and post-operative echocardiography (or computed tomography) with detailed notes on the implemented surgical strategy will allow a patient specific mitral valve computational model to be created and evaluated. The preoperative data can be used to create and tune the virtual model, while the detailed notes will be used to virtually recreate the implemented surgical strategy. Postoperative computed and actual valve function can be compared to assess the predictive capability of the computational models. A variety of surgical repairs should be targeted, specifically, ring annuloplasty, papillary muscle relocation, and leaflet augmentation.



## CHAPTER 10

### CONCLUSIONS

- A new treatment planning paradigm for mitral valve disease was developed on the strength of recent advances in medical imaging technology, targeted etiology specific repairs, and computational mitral valve repair models. Specifically, an integrative experimental framework was utilized with the intent of improving mitral valve surgical repair outcome through multiple complementary approaches.
- The Philips 3D Field Optimization Method, a clinical tool for the quantitative analysis of mitral regurgitation, was developed and validated against gold-standard experimental data for a range of mitral valve disease conditions (mild to severe mitral regurgitation). This tool was found to be as efficacious and more robust compared to the current clinical standard, 2D PISA. The experimental data may be likewise utilized for development of similar tools in the future.
- Adjunctive repairs for the surgical treatment of ischemic mitral regurgitation were found to be as efficacious as the current surgical preferred treatment, restrictive mitral annuloplasty. These repairs, anterior leaflet augmentation and basal papillary muscle relocation, restored valvular function while reducing the leaflet-subvalvular tethering associated with ischemic left ventricular remodeling. These adjunctive repairs have the potential to withstand late ventricular remodeling, a

common mode of isolated annuloplasty ring failure. Finally, the studies herein discovered the repairs are robust to variability in surgical implementation, which may encourage a more widespread clinical adaptation. Additional studies are needed to best identify which patients will benefit from adjunctive repairs as compared to restrictive mitral annuloplasty.

- An integrative experimental framework was developed for the comprehensive validation and advancement of novel computational surgical planning platforms for mitral valve disease. The experimental framework combines high-resolution state of the art imaging with clinical imaging to provide the most realistic anatomical reconstructions possible, including leaflet heterogeneity and chordal architecture. For the first time, ventricular flow fields through and proximal to the native mitral valve, including its subvalvular structure, were acquired throughout the cardiac cycle using stereoscopic particle imaging velocity. These data are combined with highly resolved geometric and boundary conditions with measurements of leaflet dynamics and subvalvular forces to create the most comprehensive database to date.

## APPENDIX A

### PROTOCOLS

#### A.1 Paraformaldehyde Fixation

Paraformaldehyde fixative (PFA) can be used to pressure fix the mitral valve into the closed or systolic geometry. PFA is preferred to gluteraldehyde fixation if small angle light scattering (SALS) will be performed. 4% Paraformaldehyde fixative can be prepared fresh following the below protocol (the protocol was adapted from Biocare Medical; Concord, CA). To yield 100 mL of 4% PFA fixative:

1. Dissolve 4 g of paraformaldehyde in 90 mL of 1X Phosphate Buffered Saline (PBS)
2. Heat gently to 58 - 60° C under a hood. Do not heat over 60°C (paraformaldehyde disassociates at 60°C)
3. Add 10N NaOH to clear the solution (pH 10 dissolves the paraformaldehyde). Usually 5 – 10 drops
4. Remove from heat and pH
5. Carefully titrate to pH 7.0 – 7.5
6. Bring to volume (100 mL) PBS (for a final concentration of 4 g in 100 mL of 1x PBS)
7. Filter sterilize through a .22 micron filter
8. Use at room temperature

It is best to prepare fixative fresh. However, the fixative can be stored at 4°C for up to 2 weeks. Fixative should be scaled up as needed for proper pressure fixation. Pressure fixation should be performed in a fume hood.

## **A.2 Phosphotungstic Acid**

Phosphotungstic acid (PTA) is a contrast agent which may be used to enhance micro-computed tomography image quality. To prepare 1% (w/v) Phosphotungstic acid in water (protocol was adapted from [195]):

1. Mix 30 mL 1% PTA solution with 70 mL absolute ethanol to make 0.3% PTA in 70% ethanol; this keeps indefinitely
2. Take samples to 70% ethanol
3. Stain overnight or longer
4. Staining is stable for months
5. Samples may be scanned in 70-100% ethanol; samples may also be scanned in saline

## **A.3 Particle Image Velocimetry**

The following operations were performed in Davis 7.2 to process the stereoscopic particle image velocimetry data:

1. Particle Image Velocimetry
  - a. Group: Stereo Vector Field Computation

- b. Operation: Particle Image Velocimetry
- 2. Image Preprocessing
  - a. Sliding background subtraction, scale length: 10 pixels
- 3. Vector Calculation Parameter
  - a. Data range = use masked area: create user defined mask
  - b. Correlation mode: stereo cross-correlation
  - c. Iterations: Multi pass (decreasing window size)
    - i. 64 x 64, square weight (1x1), 50% overlap, 2 passes
    - ii. 32 x 32, square weight (1x1), 50% overlap, 2 passes
  - d. Usage of masked out pixels
    - i. Disable vector if at center of interrogation window there is no valid pixel
    - ii. Allowed ratio of masked out to all pixels before disabling the vector: 0.3 for the first pass, 0.6 for all subsequent passes
    - iii. Allowed ratio of masked out to all pixels before switching to direct correlation: 1 for first pass, 0.1 for all subsequent passes
  - e. Initial reference vector field
    - i. Constant initial interrogation window shift
    - ii. Restrictions implied by (adaptive multipass / initial) reference vector fields
      - 1. Relative vector range restriction = reference +/- all (window size/2) AND absolute vector range restriction = reference +/- 10 pixels

- iii. Symmetrical vector position: in the middle between interrogation windows/images
- f. Correlation function
  - i. Initial Pass(es): standard 11x2 (via FFT, no zero padding)
  - ii. Final Pass(es): standard 11X12 (via FFT, no zero-padding) with high-accuracy mode for final vector result (Whitaker reconstruction)
- g. Correlation peak validation
  - i. 3D vector valid only if error < 5 pixels
  - ii. Quantity stored in peak ratio of vector field: correlation ratio  $\frac{1}{2}$  peak
- h. Multi-pass post processing
  - i. Median filter: strongly remove and iteratively replace
    - 1. Remove if difference to average > 2\*R.M.S of neighbors
    - 2. (re)insert if difference to average < 3\*R.M.S of neighbors
  - ii. Remove groups with < 5 vectors
  - iii. 1x Smooth 3x3

Three components of velocity were averaged over the 50 image pairs and exported as .DAT files for further manipulation. TecPlot was used to visualize the data.

## APPENDIX B

### EXPERIMENTAL DATA

In this section, the raw experimental data from specific Aims 1-3 are presented. These data were used to compile the tables and create the graphs, and compute the statistics seen throughout this thesis.

#### B.1. Specific Aim 1

##### B.1.1 Enface Images of Mitral Regurgitant Orifices

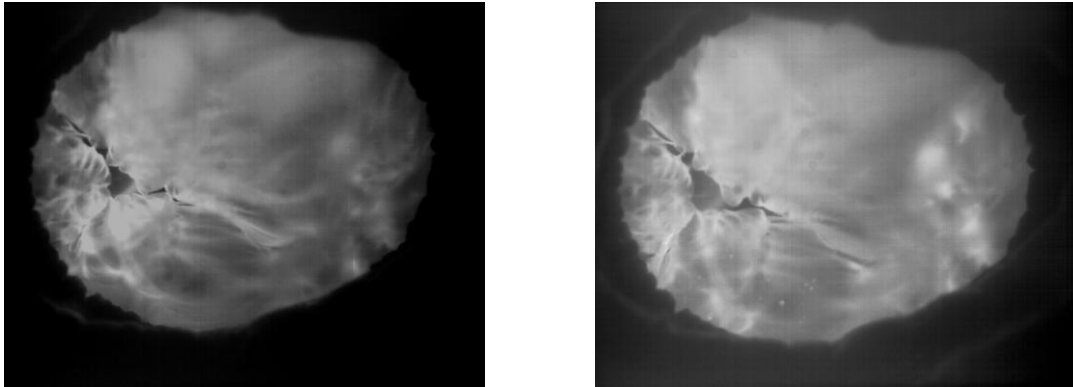
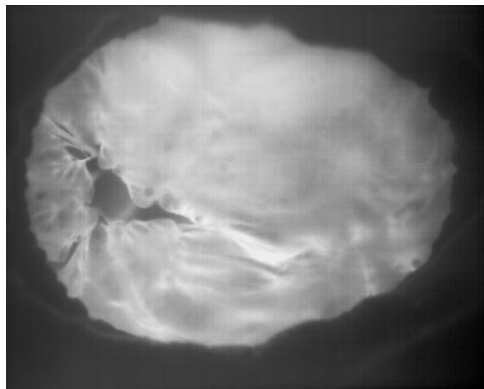
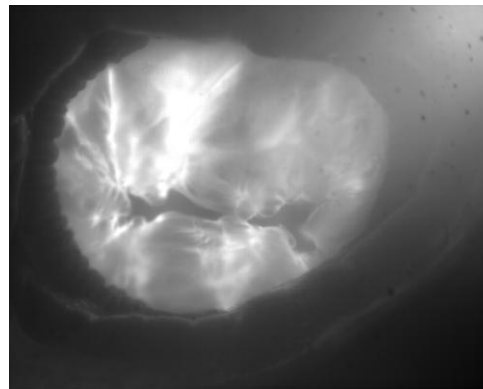
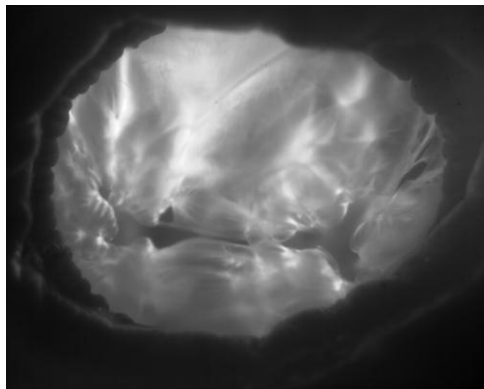


Figure B-1 PISA B, Orifices 1 and 2.



**Figure B-2 PISA B, Orifices 3 and 4.**



**Figure B-3 PISA C, Orifices 1 and 2.**

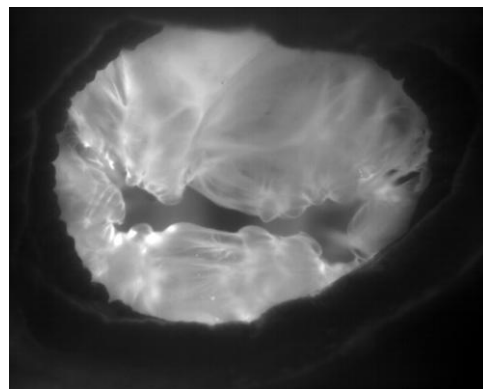
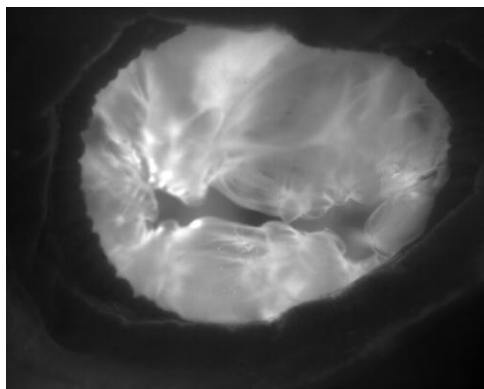


**Figure B-4 PISA C, Orifices 3 and 4.**



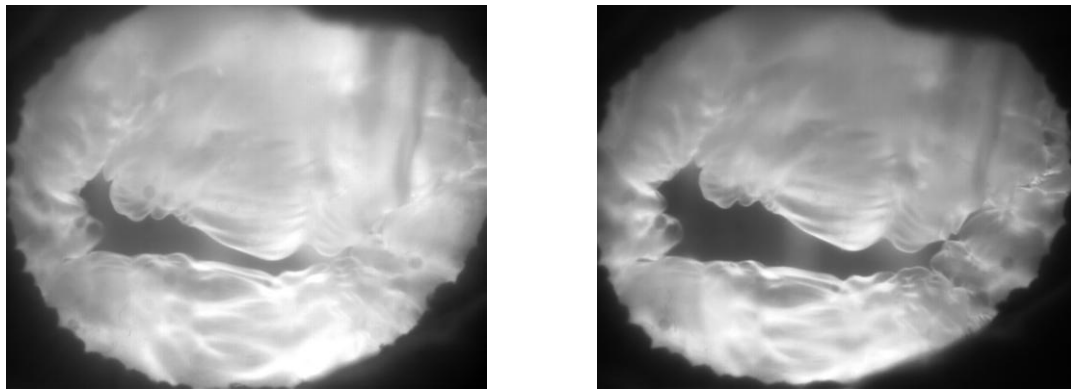


**Figure B-5 PISA E, Orifices 1 and 2.**

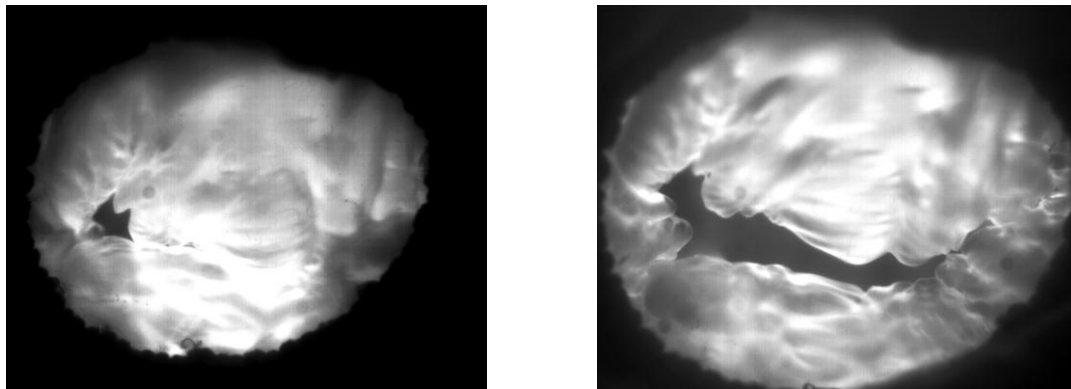


**Figure B-6 PISA E, Orifices 3 and 4.**

### **B.1.2 Enface Reconstruction of Proximal Flow Volume through Manual 3D**

#### **Integrative PISA**

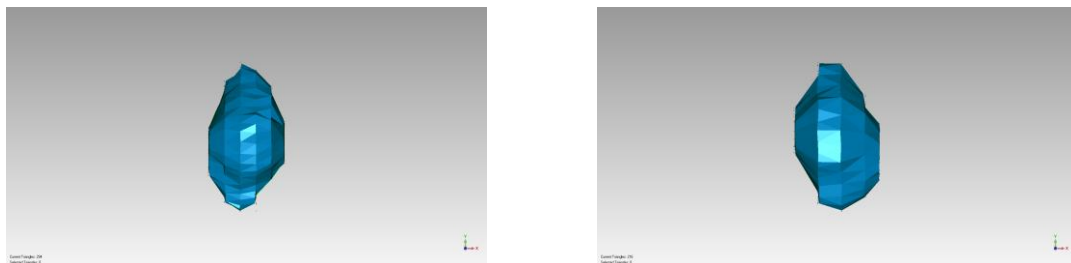


**Figure B-7 PISA A, Orifice 2, Flow 1 and Orifice 3, Flow 2.**

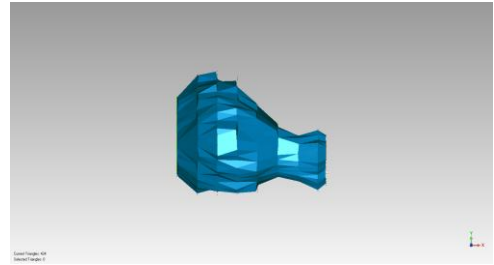
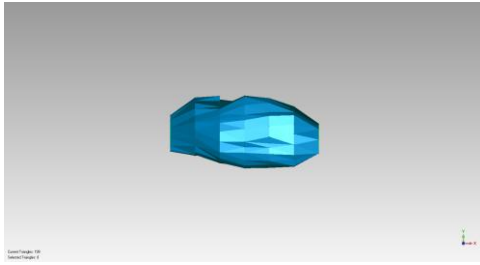


**Figure B-8 PISA A, Orifice 4, Flow 1 and Flow 2.**

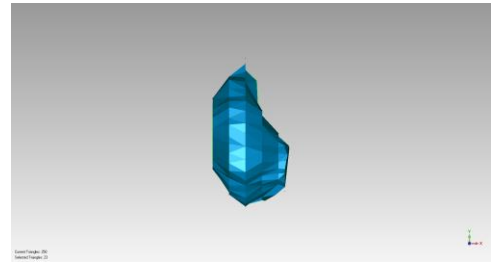
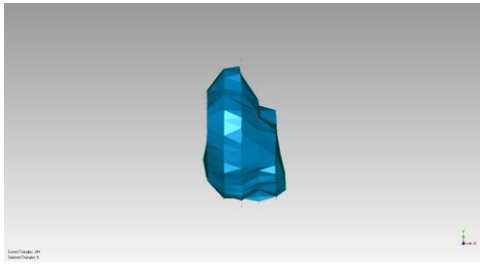


**Figure B-9 PISA B, Orifice 4, Flow 2 and Flow 3.**

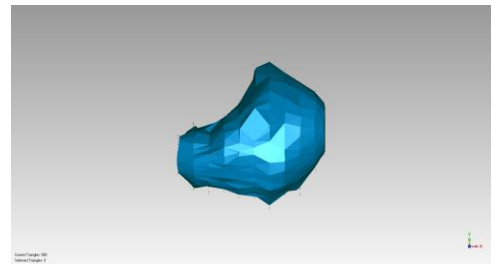
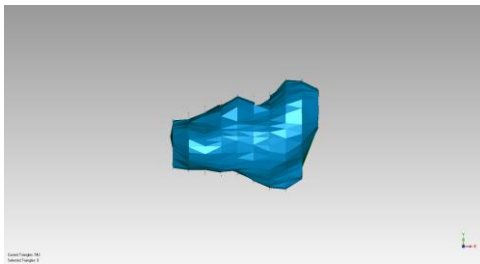


**Figure B-10 PISA C, Orifice 1, Flow 1 and Flow 2.**

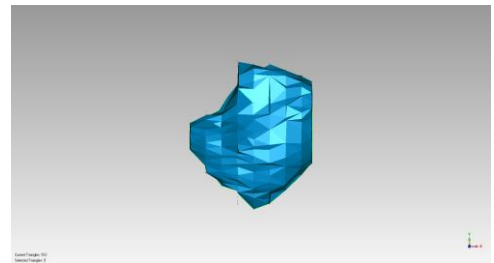
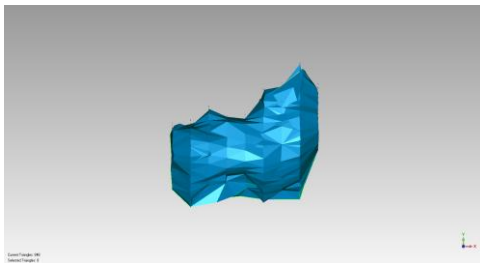


**Figure B-11 PISA C, Orifice 1, Flow 3 and Orifice 2, Flow 1.**

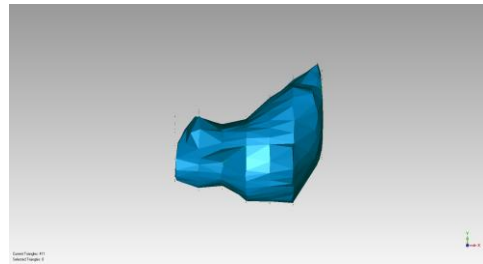
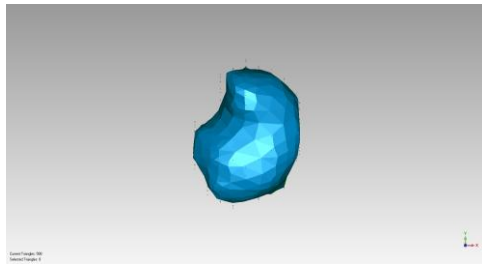


**Figure B-12 PISA C, Orifice 2, Flow 2 and Flow 3.**

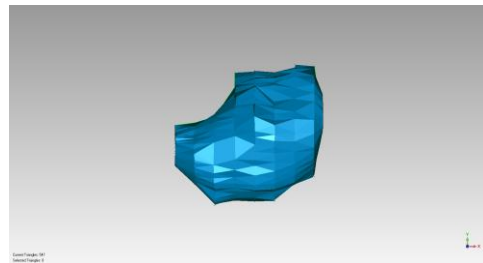
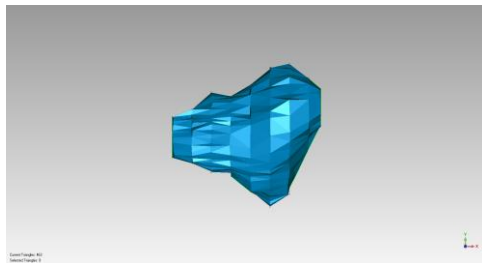


**Figure B-13 PISA C, Orifice 3, Flow 1 and Flow 2.**

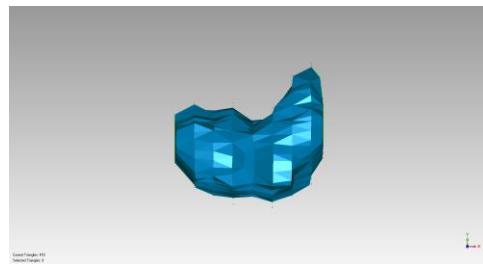
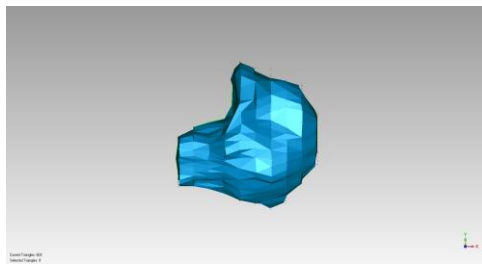


**Figure B-14 PISA C, Orifice 3, Flow 3 and Orifice 4, Flow 1.**

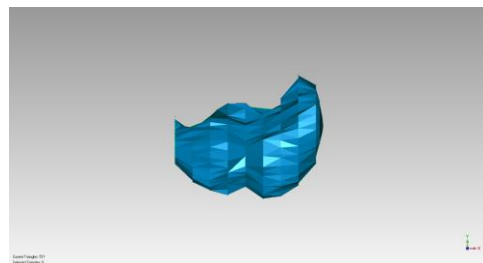
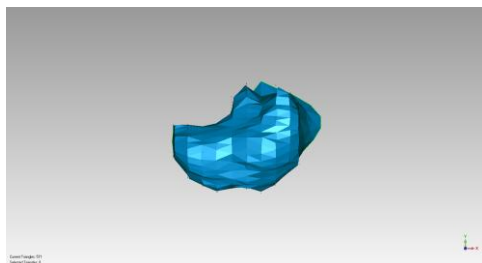


**Figure B-15 PISA C, Orifice 4, Flow 2 and Flow 3.**

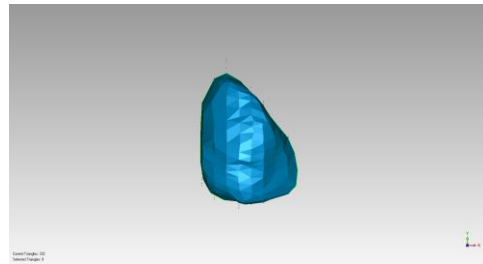
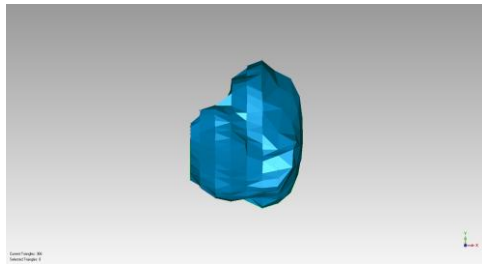


**Figure B-16 PISA E, Orifice 1, Flow 1 and Flow 2.**

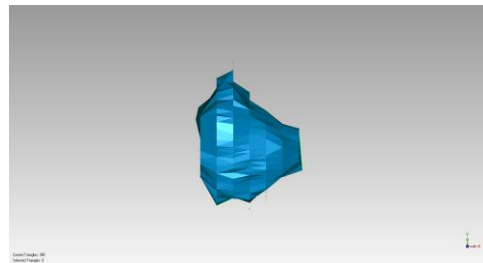
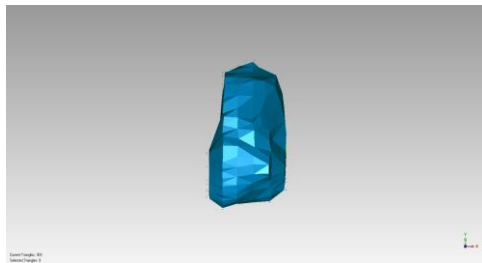


**Figure B-17 PISA E, Orifice 1, Flow 3 and Orifice 2, Flow 2.**

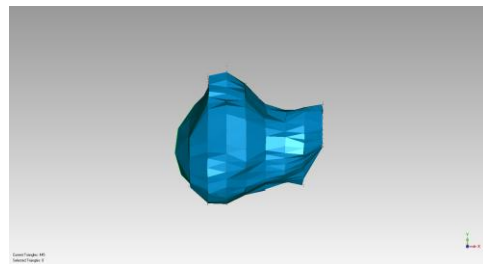
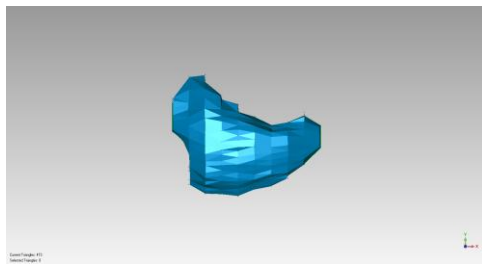


**Figure B-18 PISA E, Orifice 2, Flow 3 and Flow 5.**

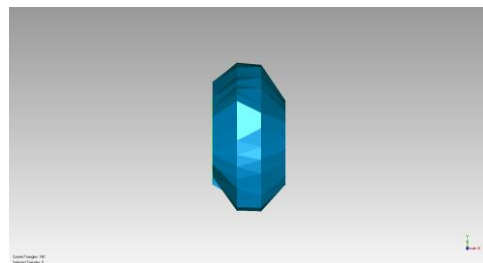
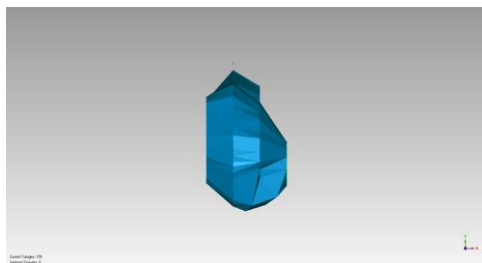


**Figure B-19 PISA E, Orifice 3, Flow 1 and Flow 2.**

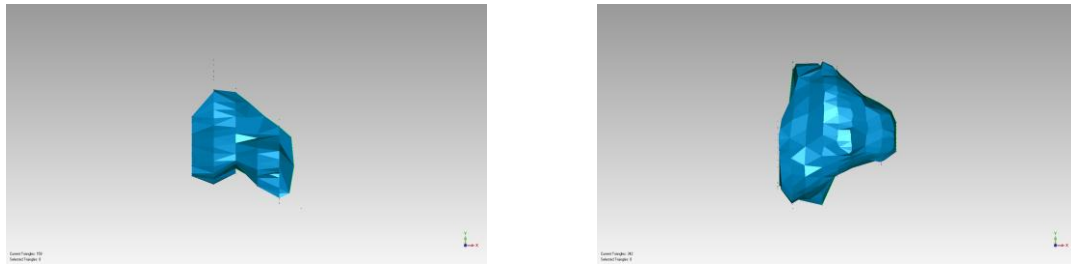


**Figure B-20 PISA E, Orifice 3, Flow 3 and Orifice 4, Flow 1.**

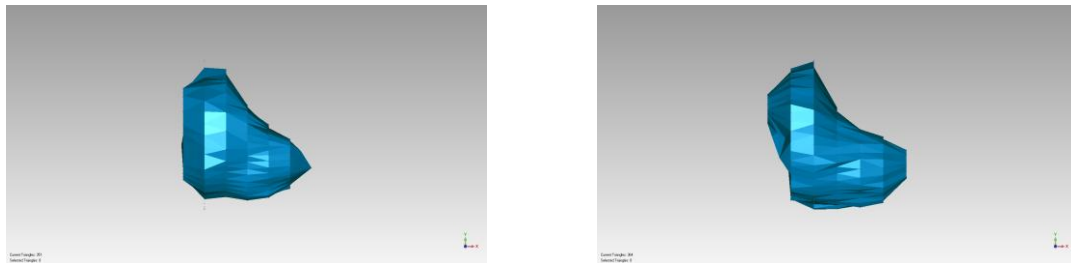


**Figure B-21 PISA E, Orifice 4, Flow 2 and Orifice 4, Flow 3.**

### B.1.3 Summary of Average PISA data for all Analysis Techniques

**Table B-1 Summary of Average PISA data for all analysis techniques.**

#	Expt	Orifice	Flow	Echo Img	Orifice Type	Flow Probe	2D PISA	FOM 1	FOM 2	FOM 3	3D Intg PISA
1	A	2	1	42	round	21.9	--	23.5	--	--	--
2	A	2	2	51	round	28.5	--	31.4	--	--	--
3	A	3	1	68	round	22.7	29.5	23.4	--	--	29.2
4	A	3	2	92	round	31.8	30.0	30.2	--	--	27.9
5	A	4	1	107	slit	21.5	37.1	16.0	17.0	16.5	13.5
6	A	4	2	126	slit	31.2	32.0	36.1	42.4	40.8	33.4
7	A	5	1	176	round	18.2	--	17.1	--	--	--
8	A	5	2	188	round	22.8	--	22.1	--	--	--
9	2	1	1	7	round	13.8	--	10.2	--	--	--
10	2	1	2	14	round	21.2	--	16.9	--	--	--
11	2	2	1	24	round	19.8	--	24.4	--	--	--

12	2	2	2	31	round	19.3	--	20.8	--	--	--
13	2	3	1	38	round	33.8	--	32.7	--	--	--
14	2	3	2	42	round	45.0	--	40.3	--	--	--
15	2	4	1	52	round	52.9	--	17.4	51.2	--	--
16	2	4	2	65	round	36.6	34.2	19.4	52.8	--	36.5
17	2	4	3	74	round	59.4	64.4	12.5	62.8	--	48.2
18	3	1	1	7	slit	59.5	37.6	48.4	56.7	59.9	64.1
19	3	1	2	18	slit	67.8	60.5	46.3	65.7	73.8	61.4
20	3	1	3	25	slit	34.3	21.0	36.7	20.7	25.7	30.1
21	3	2	1	32	slit	37.2	34.6	62.1	42.2	49.1	40.7
22	3	2	2	43	slit	71.2	96.3	37.3	99.5	100.2	74.5
23	3	2	3	59	slit	29.7	30.4	32.8	29.1	31.9	23.9
24	3	3	1	56	slit	52.6	52.7	60.8	58.3	63.2	46.9
25	3	3	2	66	slit	69.5	63.4	55.3	88.0	84.5	64.0
26	3	3	3	76	slit	40.9	37.2	47.1	41.6	44.0	47.1
27	3	4	1	82	slit	48.7	44.3	46.7	43.9	44.0	53.7
28	3	4	2	88	slit	63.1	62.8	61.0	83.2	83.2	69.2
29	3	4	3	97	slit	49.9	55.5	55.9	49.5	51.0	46.2
30	4	1	1	10	slit	30.0	18.4	15.9	23.9	25.6	41.7
31	4	1	2	19	slit	37.9	25.9	26.6	61.6	58.9	47.2
32	4	1	3	28	slit	27.3	20.2	21.8	30.6	37.8	33.9
33	4	2	2	47	slit	61.0	29.2	21.6	53.4	57.9	49.6
34	4	2	3	54	slit	44.1	30.1	20.9	41.6	46.4	47.6
35	4	2	4	63	slit	61.4	--	24.2	65.8	69.0	--
36	4	2	5	69	slit	56.2	34.2	21.4	59.5	51.3	57.0
37	4	3	1	81	round	14.3	12.7	12.5	--	--	11.4
38	4	3	2	90	round	22.5	22.0	20.5	--	--	11.4
39	4	3	3	99	round	20.5	19.3	13.5	--	--	14.4
40	4	4	1	108	slit	39.8	16.0	23.2	48.6	52.2	48.1
41	4	4	2	118	slit	48.1	25.3	22.1	49.3	50.6	50.2
42	4	4	3	127	slit	50.7	27.9	16.1	53.2	49.5	38.4

## B.2 Specific Aim 2

## B.2.1 Anterior Leaflet Augmentation

**Table B-2 Mitral regurgitation for all anterior leaflet augmentation conditions.**

	Mitral Regurgitation [mL]					
	Small Patch		Large Patch		Combined	
	Avg	Stdev	Avg	Stdev	Avg	Stdev
Healthy	23.5	2.0	32.2	3.8	27.6	5.3
IMR	43.4	7.1	51.2	9.0	47.0	8.7
Undersized MA	21.7	3.6	28.6	2.6	27.5	4.6
Anterior Leaflet Patch w. No MA	38.9	8.0	50.5	7.0	24.9	4.7
Anterior Leaflet Patch w. Oversized MA	30.2	5.4	43.6	6.7	44.3	9.4
Anterior Leaflet Patch w. True Sized MA	25.4	4.0	37.2	6.0	36.4	9.0
Anterior Leaflet Patch w. RMA	22.3	2.4	34.2	6.0	30.9	7.8

**Table B-3 Coaptation length for all anterior leaflet augmentation conditions.**

	Coaptation Length [cm]					
	Small Patch		Large Patch		Combined	
	Avg	Stdev	Avg	Stdev	Avg	Stdev
Healthy	0.50	0.05	0.47	0.05	0.48	0.05
IMR	0.34	0.03	0.30	0.07	0.32	0.05
Undersized MA	0.48	0.05	0.47	0.07	0.47	0.06
Anterior Leaflet Patch w. No MA	0.39	0.08	0.40	0.09	0.39	0.08
Anterior Leaflet Patch w. Oversized MA	0.42	0.06	0.48	0.04	0.44	0.05
Anterior Leaflet Patch w. True Sized MA	0.48	0.05	0.58	0.10	0.53	0.09
Anterior Leaflet Patch w. RMA	0.59	0.07	0.63	0.06	0.61	0.06

**Table B-4 Anterior strut chordal force data for all anterior leaflet augmentation conditions from the posteromedial PM.**

	Posteromedial PM - Anterior Strut Force [N]					
	Small Patch		Large Patch		Combined	
	Avg	Stdev	Avg	Stdev	Avg	Stdev
Healthy	0.87	0.24	0.53	0.28	0.71	0.31
IMR	1.50	0.33	0.93	0.36	1.23	0.44
Undersized MA	1.04	0.28	0.71	0.30	0.89	0.33
Anterior Leaflet Patch w. No MA	0.99	0.34	0.84	0.35	0.92	0.34
Anterior Leaflet Patch w. Oversized MA	0.94	0.35	0.78	0.32	0.87	0.33
Anterior Leaflet Patch w. True Sized MA	0.91	0.37	0.74	0.31	0.93	0.34
Anterior Leaflet Patch w. RMA	0.91	0.45	0.68	0.31	0.80	0.39

**Table B-5 Posterior strut chordal force data for all anterior leaflet augmentation conditions from the posteromedial PM.**

	Posteromedial PM - Posterior Strut Force [N]					
	Small Patch		Large Patch		Combined	
	Avg	Stdev	Avg	Stdev	Avg	Stdev
Healthy	0.28	0.08	0.28	0.17	0.28	0.13
IMR	0.45	0.16	0.65	0.37	0.55	0.29
Undersized MA	0.45	0.19	0.56	0.33	0.51	0.26
Anterior Leaflet Patch w. No MA	0.39	0.20	0.52	0.31	0.46	0.26
Anterior Leaflet Patch w. Oversized MA	0.38	0.17	0.52	0.30	0.45	0.25
Anterior Leaflet Patch w. True Sized MA	0.39	0.18	0.45	0.25	0.42	0.21
Anterior Leaflet Patch w. RMA	0.51	0.16	0.45	0.32	0.48	0.24



**Table B-6 Anterior strut chordal force data for all anterior leaflet augmentation conditions from the anterolateral PM.**

	Anterolateral PM - Anterior Strut Force [N]					
	Small Patch		Large Patch		Combined	
	Avg	Stdev	Avg	Stdev	Avg	Stdev
Healthy	0.71	0.54	0.51	0.28	0.62	0.44
IMR	0.79	0.64	0.81	0.40	0.80	0.52
Undersized MA	0.65	0.41	0.66	0.39	0.66	0.39
Anterior Leaflet Patch w. No MA	0.85	0.47	1.13	0.60	0.97	0.53
Anterior Leaflet Patch w. Oversized MA	0.79	0.43	1.09	0.58	0.92	0.50
Anterior Leaflet Patch w. True Sized MA	0.78	0.43	0.94	0.60	0.85	0.50
Anterior Leaflet Patch w. RMA	0.77	0.36	1.01	0.56	0.87	0.45

**Table B-7 Posterior strut chordal force data for all anterior leaflet augmentation conditions from the anterolateral PM.**

	Anterolateral PM - Posterior Strut Force [N]					
	Small Patch		Large Patch		Combined	
	Avg	Stdev	Avg	Stdev	Avg	Stdev
Healthy	0.39	0.28	0.60	0.38	0.49	0.34
IMR	0.51	0.30	0.93	0.62	0.71	0.51
Undersized MA	0.44	0.22	0.65	0.42	0.54	0.33
Anterior Leaflet Patch w. No MA	0.50	0.23	0.81	0.53	0.65	0.41
Anterior Leaflet Patch w. Oversized MA	0.45	0.20	0.76	0.49	0.59	0.39
Anterior Leaflet Patch w. True Sized MA	0.46	0.24	0.63	0.45	0.54	0.35
Anterior Leaflet Patch w. RMA	0.48	0.30	0.53	0.44	0.51	0.36

### B.2.3 Papillary Muscle Relocation

**Table B-8 Leaflet coaptation length and tenting area data for all papillary muscle relocation experimental conditions.**

<b>(Average)</b>	<b>Control</b>	<b>Acute MI</b>	<b>Acute MI with MA</b>	<b>Chronic MI with MA</b>
CL (cm)	0.53	0.37	0.47	0.41
TH (cm)	0.23	0.34	0.32	0.40
TA (cm <sup>2</sup> )	0.17	0.32	0.28	0.40
ATA (cm <sup>2</sup> )	0.09	0.17	0.16	0.23
PTA (cm <sup>2</sup> )	0.07	0.11	0.11	0.13
<b>Commissure Anterolateral PM</b>	<b>2mm</b>	<b>4mm</b>	<b>6mm</b>	<b>8mm</b>
CL (cm)	0.43	0.51	0.60	0.55
TH (cm)	0.38	0.34	0.26	0.23
TA (cm <sup>2</sup> )	0.36	0.30	0.20	0.17
ATA (cm <sup>2</sup> )	0.22	0.19	0.11	0.10
PTA (cm <sup>2</sup> )	0.13	0.09	0.07	0.05
<b>Trigone Anterolateral PM</b>	<b>2mm</b>	<b>4mm</b>	<b>6mm</b>	<b>8mm</b>
CL (cm)	0.47	0.55	0.64	0.64
TH (cm)	0.41	0.36	0.30	0.25
TA (cm <sup>2</sup> )	0.41	0.33	0.28	0.17
ATA (cm <sup>2</sup> )	0.23	0.19	0.16	0.10
PTA (cm <sup>2</sup> )	0.16	0.11	0.08	0.07
<b>Commissure Symmetric</b>	<b>2mm</b>	<b>4mm</b>	<b>6mm</b>	<b>8mm</b>
CL (cm)	0.50	0.58	0.65	0.64
TH (cm)	0.36	0.31	0.23	0.17
TA (cm <sup>2</sup> )	0.36	0.27	0.18	0.11
ATA (cm <sup>2</sup> )	0.19	0.16	0.10	0.07
PTA (cm <sup>2</sup> )	0.13	0.10	0.07	0.04
<b>Trigone Symmetric</b>	<b>2mm</b>	<b>4mm</b>	<b>6mm</b>	<b>8mm</b>
CL (cm)	0.49	0.58	0.63	0.68
TH (cm)	0.36	0.32	0.24	0.22
TA (cm <sup>2</sup> )	0.33	0.29	0.18	0.14
ATA (cm <sup>2</sup> )	0.21	0.18	0.11	0.08
PTA (cm <sup>2</sup> )	0.13	0.09	0.07	0.05

(Standard Deviation)	Control	Acute MI	Acute MI with MA	Chronic MI with MA
CL (cm)	0.15	0.11	0.11	0.07
TH (cm)	0.08	0.04	0.10	0.12
TA (cm <sup>2</sup> )	0.12	0.09	0.11	0.18
ATA (cm <sup>2</sup> )	0.06	0.05	0.07	0.10
PTA (cm <sup>2</sup> )	0.05	0.02	0.04	0.06
<b>Commissure Anterolateral PM</b>	<b>2mm</b>	<b>4mm</b>	<b>6mm</b>	<b>8mm</b>
CL (cm)	0.12	0.12	0.15	0.14
TH (cm)	0.11	0.15	0.11	0.07
TA (cm <sup>2</sup> )	0.18	0.20	0.12	0.10
ATA (cm <sup>2</sup> )	0.11	0.11	0.08	0.07
PTA (cm <sup>2</sup> )	0.07	0.07	0.04	0.02
<b>Trigone Anterolateral PM</b>	<b>2mm</b>	<b>4mm</b>	<b>6mm</b>	<b>8mm</b>
CL (cm)	0.16	0.13	0.17	0.21
TH (cm)	0.14	0.16	0.14	0.08
TA (cm <sup>2</sup> )	0.22	0.20	0.19	0.13
ATA (cm <sup>2</sup> )	0.13	0.11	0.12	0.08
PTA (cm <sup>2</sup> )	0.09	0.07	0.05	0.06
<b>Commissure Symmetric</b>	<b>2mm</b>	<b>4mm</b>	<b>6mm</b>	<b>8mm</b>
CL (cm)	0.15	0.14	0.16	0.20
TH (cm)	0.12	0.11	0.09	0.07
TA (cm <sup>2</sup> )	0.18	0.14	0.12	0.06
ATA (cm <sup>2</sup> )	0.11	0.08	0.08	0.04
PTA (cm <sup>2</sup> )	0.07	0.04	0.04	0.01
<b>Trigone Symmetric</b>	<b>2mm</b>	<b>4mm</b>	<b>6mm</b>	<b>8mm</b>
CL (cm)	0.15	0.17	0.16	0.21
TH (cm)	0.12	0.15	0.09	0.08
TA (cm <sup>2</sup> )	0.17	0.19	0.10	0.08
ATA (cm <sup>2</sup> )	0.12	0.13	0.07	0.04
PTA (cm <sup>2</sup> )	0.07	0.05	0.04	0.03

### B.3 Specific Aim 3

#### B.3.1 Particle Image Velocimetry

Presented below are representative images of the left ventricular filling through a mitral valve with normal and altered papillary muscle positioning at low and high flows.

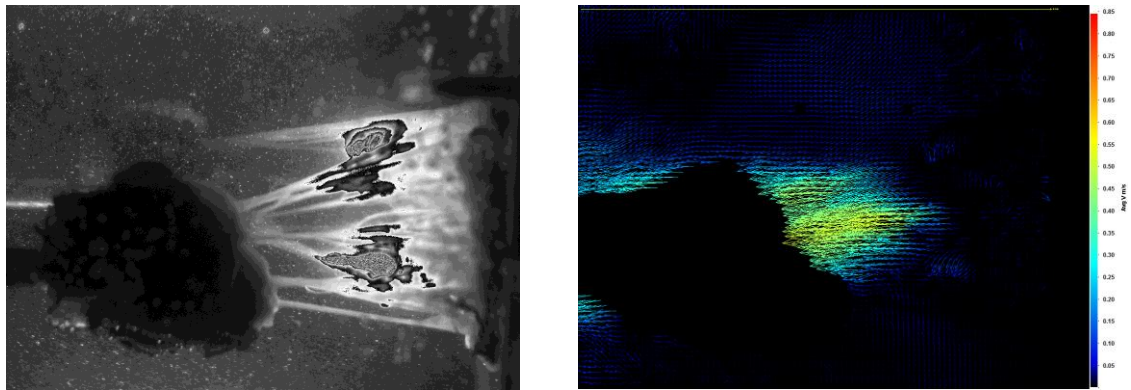


Figure B-22 Normal Papillary Muscle Position: Low Flow.

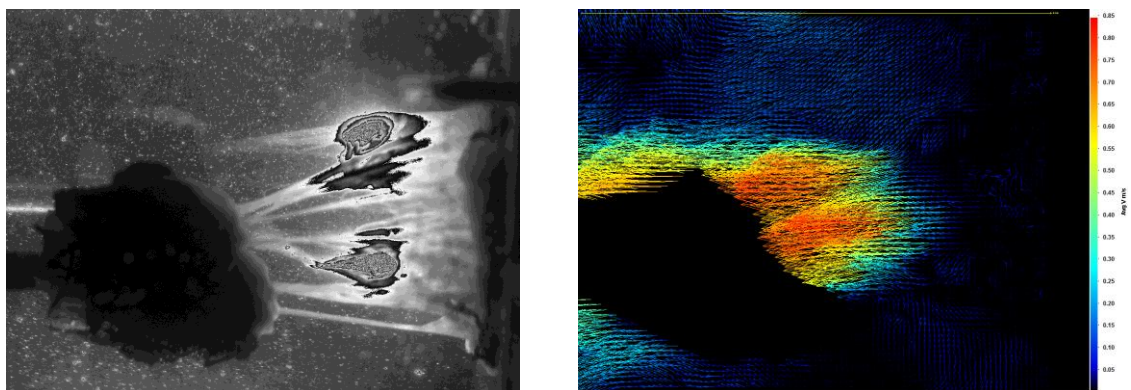
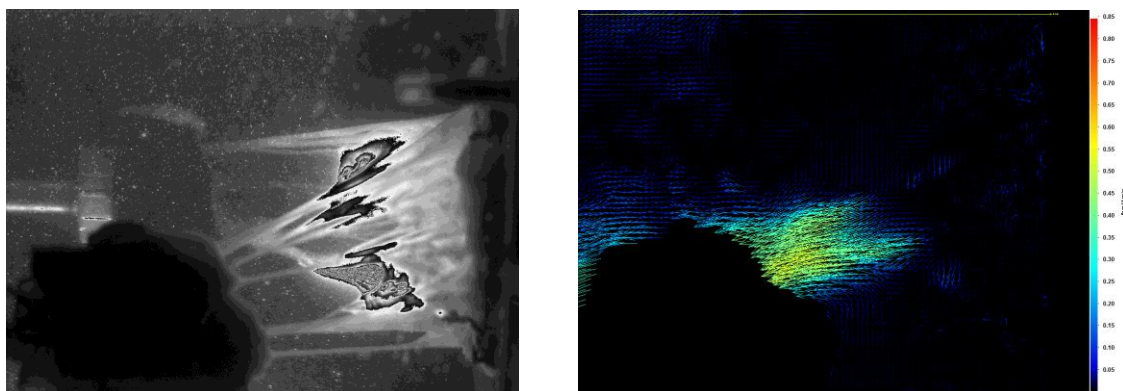
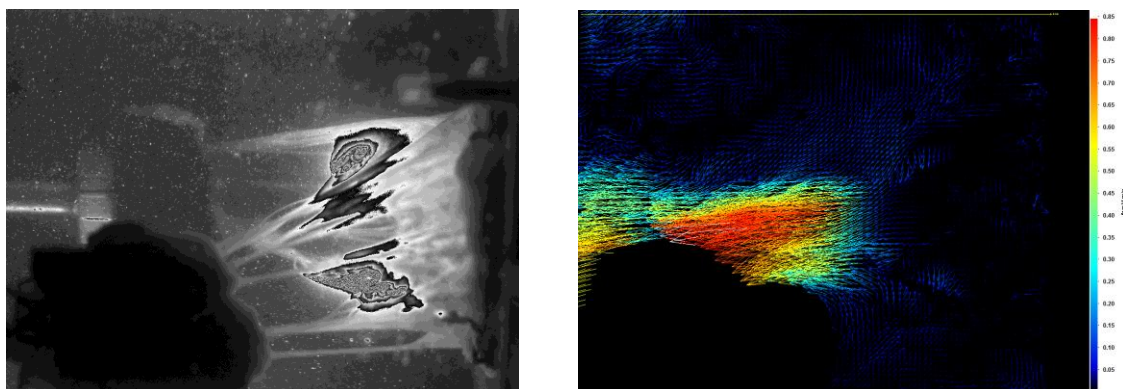


Figure B-23 Normal Papillary Muscle Position: High Flow.



**Figure B-24 Anterolateral Papillary Muscle Displaced Anteriorly, Posteriorly, Apically: Low Flow.**



**Figure B-25 Anterolateral Papillary Muscle Displaced Anteriorly, Posterior, Apically: High Flow.**

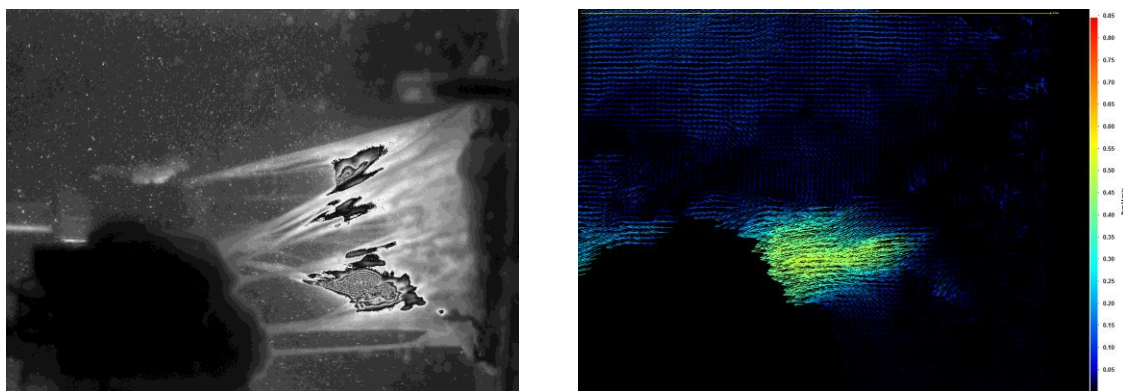


**Figure B-26 Symmetric Anterior, Posterior, and Apical PM Displacement: Low Flow.**

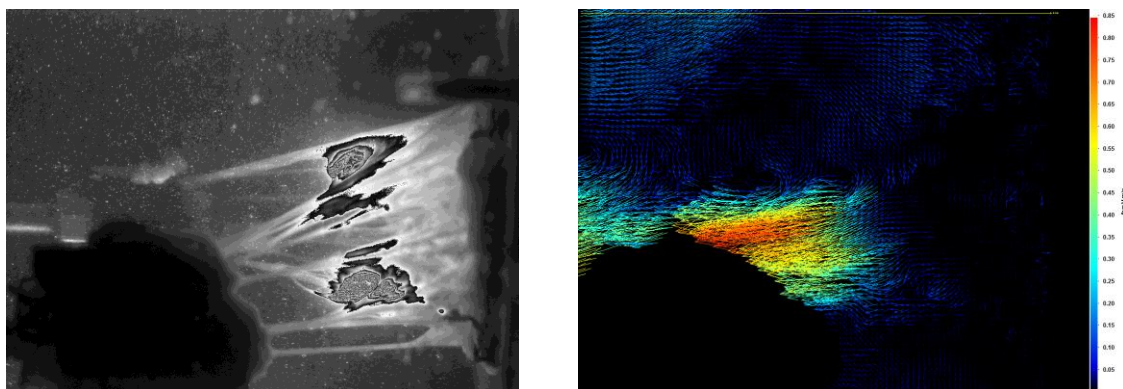


**Figure B-27 Symmetric Anterior, Posterior, and Apical PM Displacement: High Flow.**

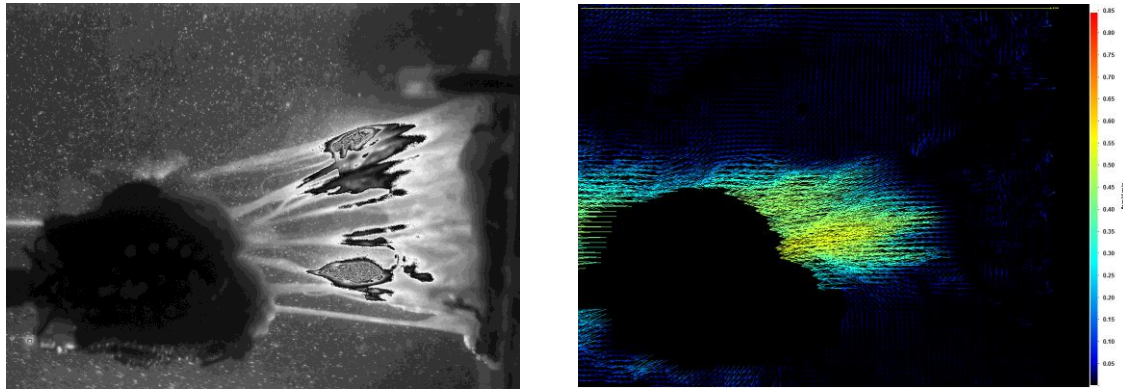


**Figure B-28 Posteromedial Papillary Muscle Displaced Anteriorly, Posteriorly, Apically: Low Flow.**

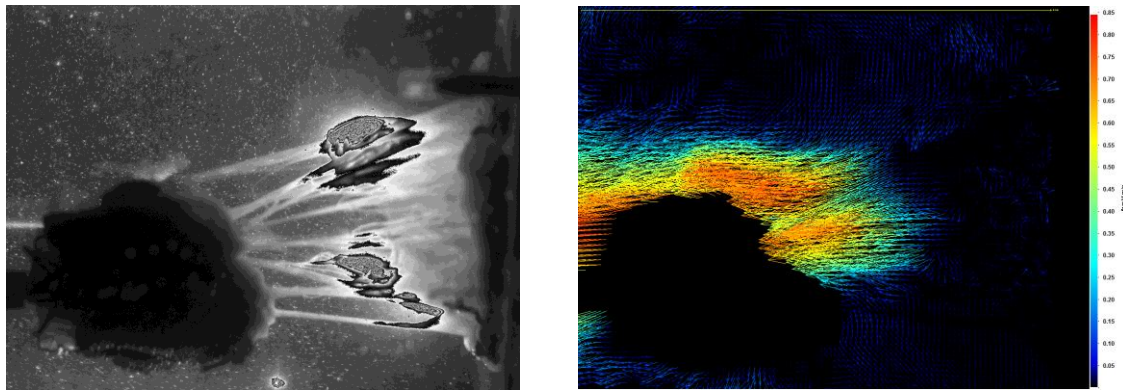


**Figure B-29 Posteromedial Papillary Muscle Displaced Anteriorly, Posterior, Apically: High Flow.**

## APPENDIX C

### MATLAB CODES

The following Matlab codes are included:

1. MicroCT.M: Micro-computed tomography point cloud generation from black and white (post-threshold) images
2. EnsembleAVG.M: ensemble average hemodynamic data
3. MAA.M: calculates mitral annular area from en-face images (echo or high-speed)

#### C.1 MicroCT.M

```
%This program reads in an image stack of black and white
%micro-CT geometries (already passed through band-pass thresholding.
%The program will write out a .txt file of geometry point cloud.

%% change value of numims to reflect total number of images to be
processed
numims = 631;

%% change filepath to reflect directory where black and white images
are stored
filepath = ('C:\Users\Jean-Pierre\Desktop\2010 09 09\microCT_');
temp = imread(sprintf('%s0000.TIF',filepath));
[m,n]= size(temp);
clear temp

%% change output_filename to reflect desired of point cloud
output_filename = ('valve_8.txt');

dlmwrite(output_filename, []);

%% loop through all images
for i = 1:numims;
```



```

    %% print i on screen to see which image the code is currently
segmenting
    i
    im = imread(sprintf('%s%4.4d.tif',filepath,i));
    im = double(im);
    %% use canny edge detection
    BW = edge(im, 'canny');

    [x,y]=find(BW~=0);
    output=[x y ones(length(x),1)*i];
    dlmwrite(output_filename,output,'delimiter',' ','newline','pc','-
append');
end

```

## C.2 EnsembleAVG.M

```

%% This program reads in raw hemodynamic data over 10 cycles acquired
%% through lab view. The program ensemble averages the data and .
%% creates an excel spreadsheet. The excel spreadsheet will contain a
%% column for each acquired parameter, typically flow, left atrial
pressure,
%% ventricular pressure.

```

```

function Flow
clear
clc

```

```

%% Change input_file and output_file to reflect labview text file for
%% ensemble averaging and desired excel file output.
input_file = string('C:\Users\Jean-
Pierre\Desktop\4_19_2013_pisa3v2_3.txt')
output_file = string('C:\Users\Jean-
Pierre\Desktop\4_19_2013_pisa3_8.xlsx')

```

```

num=dlmread(input_file);
CT=856;
HB=70;
max = 7;
time=num(1:CT,1);
int1=num(1:CT,2:max);
int2=num(CT+1:CT*2,2:max);
int3=num(CT*2+1:CT*3,2:max);
int4=num(CT*3+1:CT*4,2:max);
int5=num(CT*4+1:CT*5,2:max);
int6=num(CT*5+1:CT*6,2:max);
int7=num(CT*6+1:CT*7,2:max);
int8=num(CT*7+1:CT*8,2:max);
int9=num(CT*8+1:CT*9,2:max);
int10=num(CT*9+1:CT*10,2:max);

```

```

Averageint=(int1+int2+int3+int4+int5+int6+int7+int8+int9+int10)/10;
data = time;
data(:,2:max) = Averageint;

xlswrite(output_file, data);

```

### C.3 MAA.M

```

% Mitral Annular Area Calculator
% Description: Digital photographs are read in. According to a scale
mitral
% annulus area (MAA) is manually segmented and calculated.

% picture of annulus is read in and displayed
M = imread('photo (2).jpg');
imshow(M);
warning off

% distance between two points (distance 10mm) on a scale is calculated
ref = ginput(2);
dist = sqrt( (ref(2,1)-ref(1,1))^2 + (ref(2,2)-ref(1,2))^2 );

% calculating orifice area
N = ginput(); % inner perimeter of annulus is manually picked
pixelArea = polyarea(N(:,1),N(:,2)); % area in pixels^2
mmAreaSept = pixelArea/dist/dist*100 % area in mm^2

% display selected points
hold on
plot(N(:,1),N(:,2));
hold off

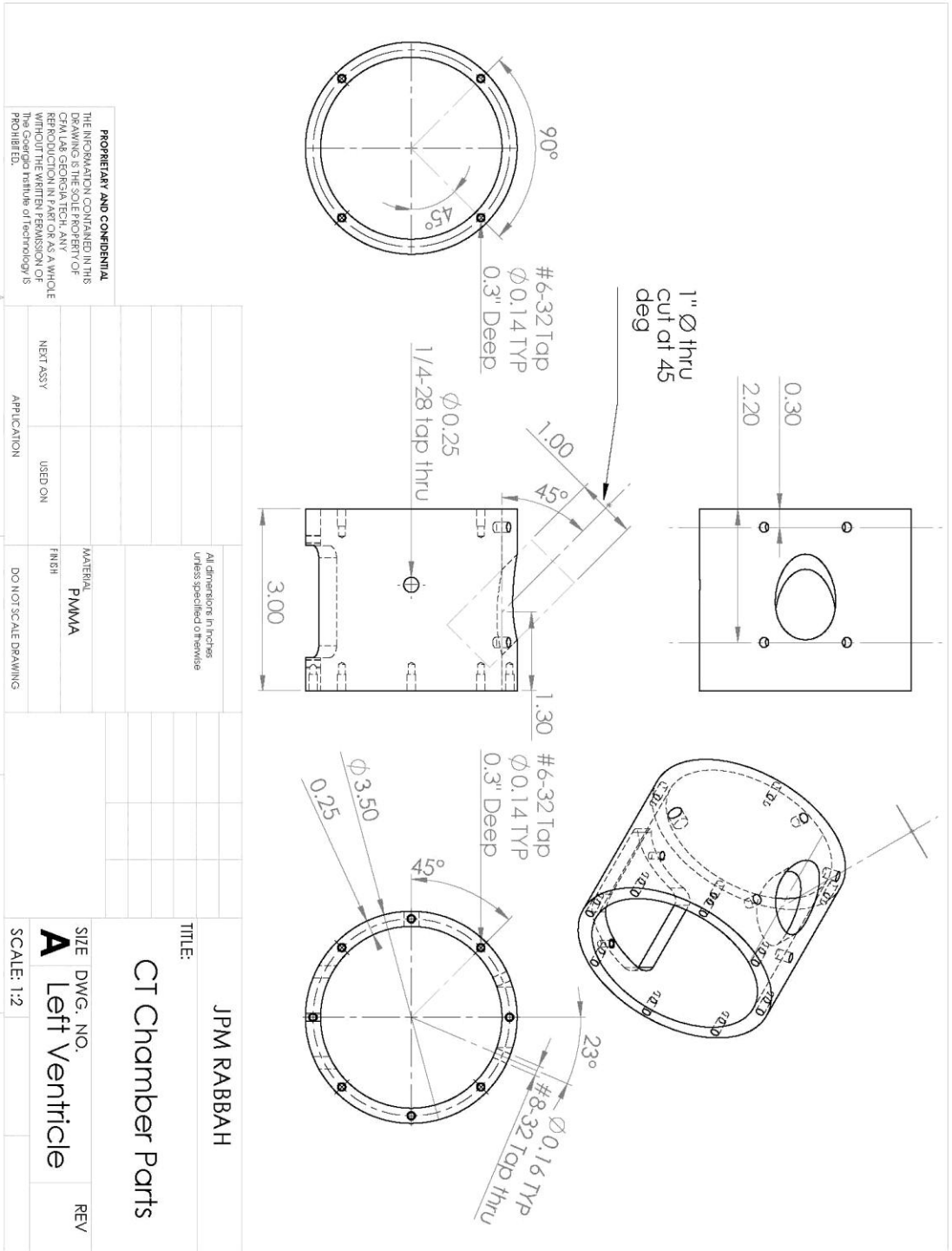
```

## APPENDIX D

### COMPUTER AIDED DESIGN

In this appendix, the CAD files of the modified left heart simulator are presented. These include:

1. Left ventricular chamber
2. Left ventricular apical plate with papillary muscle through wall fitting
3. Papillary muscle ball (ball and socket joint)
4. Papillary muscle socket
5. Left atrial chamber
6. Left atrial basal plate
7. Annulus plate – size 30 mitral annulus.



**PROPRIETARY AND CONFIDENTIAL**  
 THE INFORMATION CONTAINED IN THIS DRAWING IS THE SOLE PROPERTY OF CFM LAB. GEORGIA TECH. ANY REPRODUCTION IN PART OR AS A WHOLE WITHOUT THE WRITTEN PERMISSION OF THE ORIGINAL AUTHOR IS PROHIBITED.

5

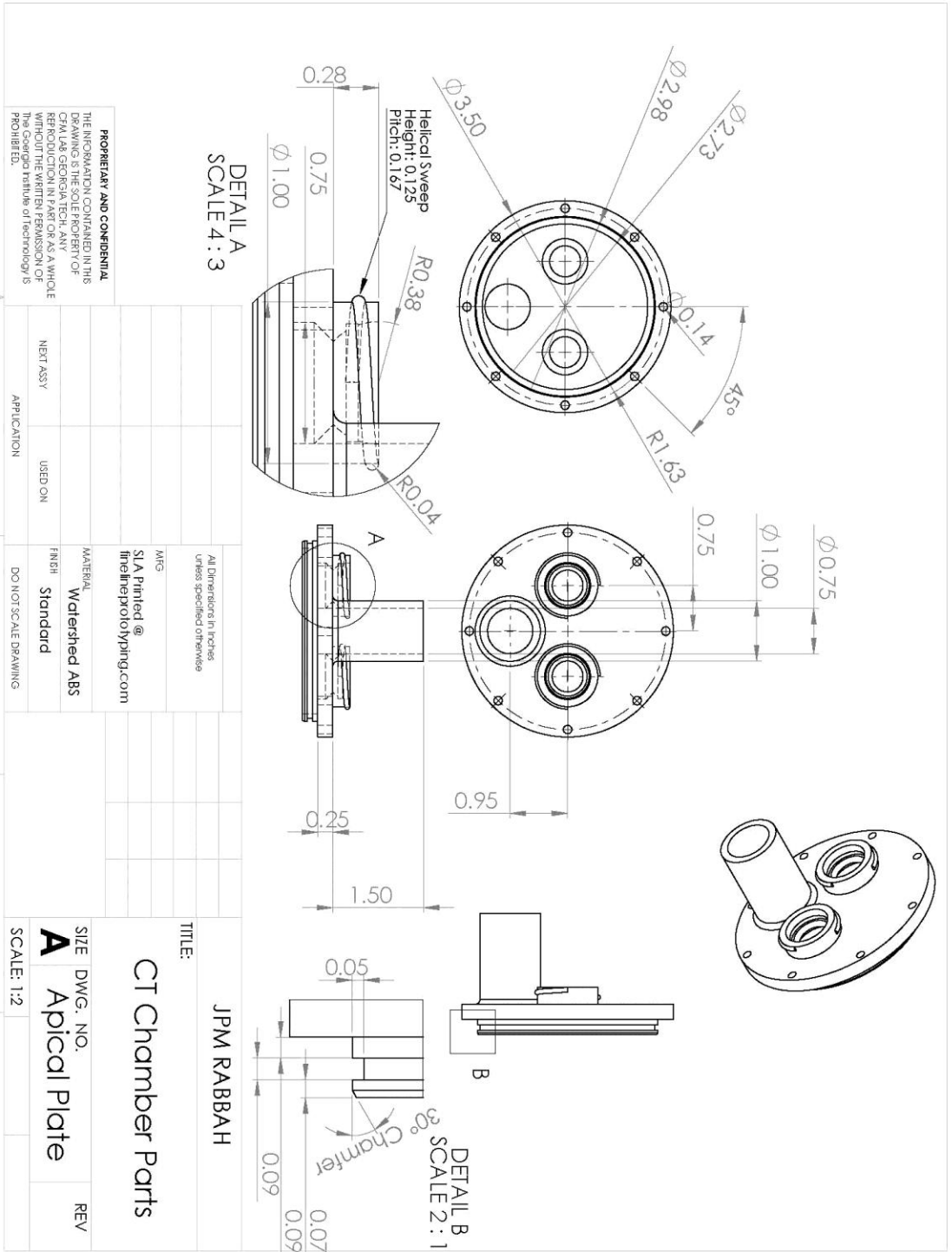
4

3

2

1

TITLE: JPM RABBAN		All dimensions in inches unless specified otherwise	
SIZE DWG. NO. A Left Ventricle		MATERIAL PMMA	
SCALE: 1:2		FINISH	
REV		DO NOT SCALE DRAWING	
NEXT ASSY		USED ON	
APPLICATION			



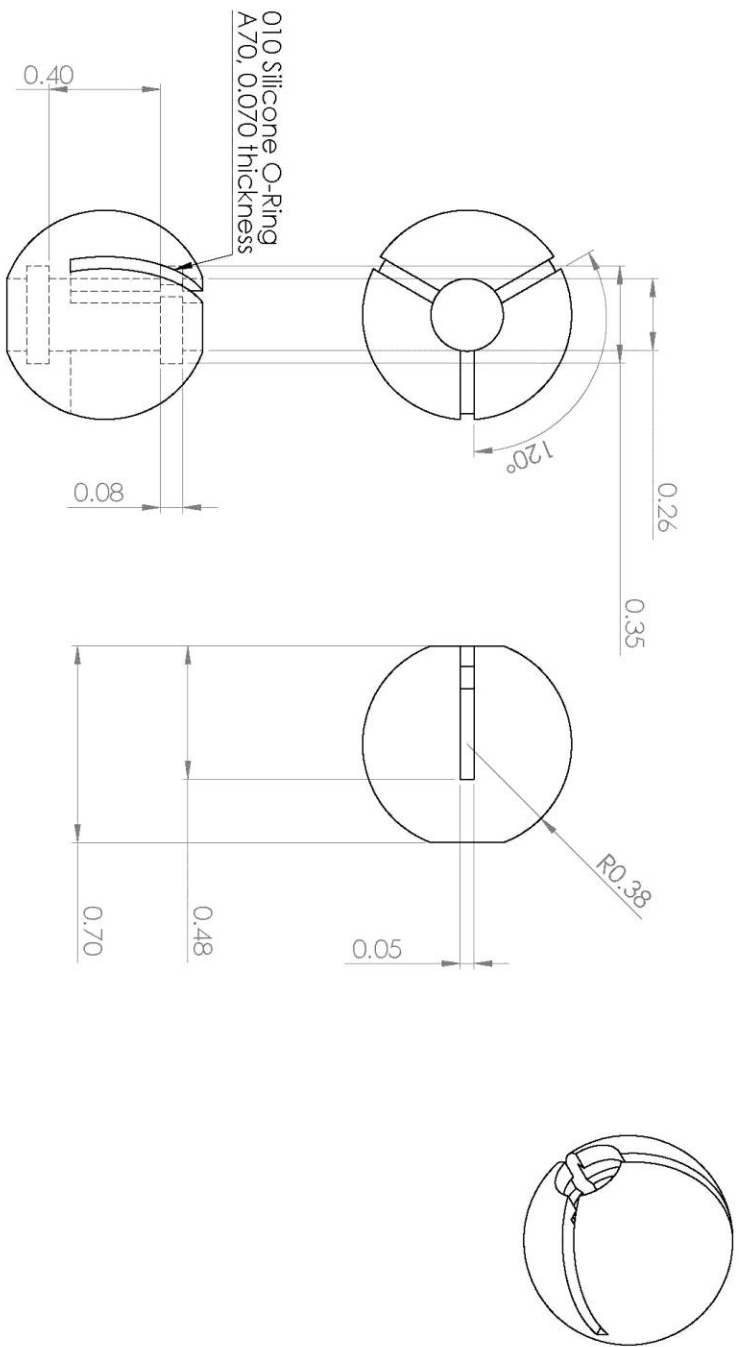
5

4

3

2

1



**PROPRIETARY AND CONFIDENTIAL**  
 THE INFORMATION CONTAINED IN THIS DRAWING IS THE SOLE PROPERTY OF CFM LAB, GEORGIA TECH. ANY REPRODUCTION IN PART OR AS A WHOLE WITHOUT THE WRITTEN PERMISSION OF THE AUTHOR IS STRICTLY PROHIBITED.

5

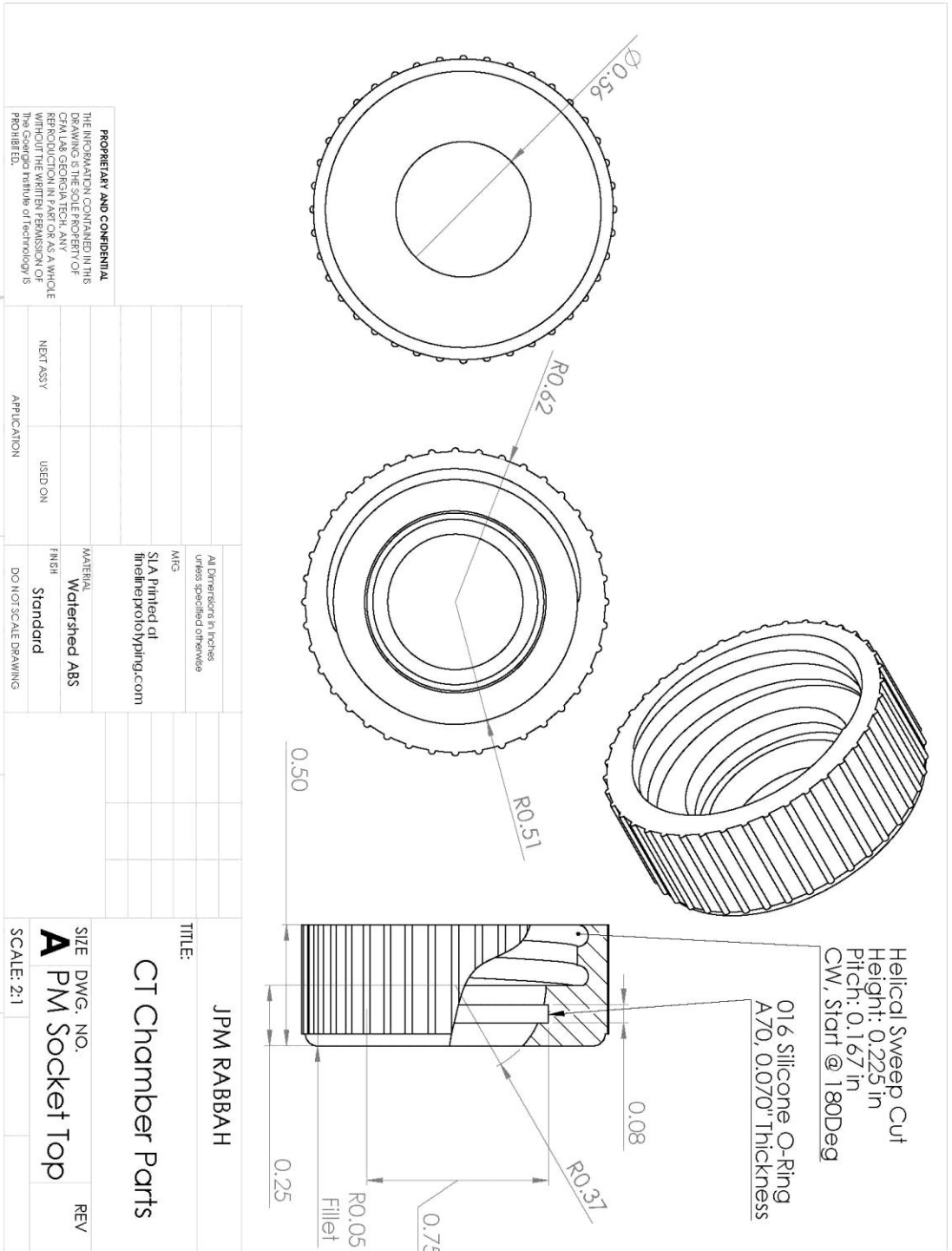
4

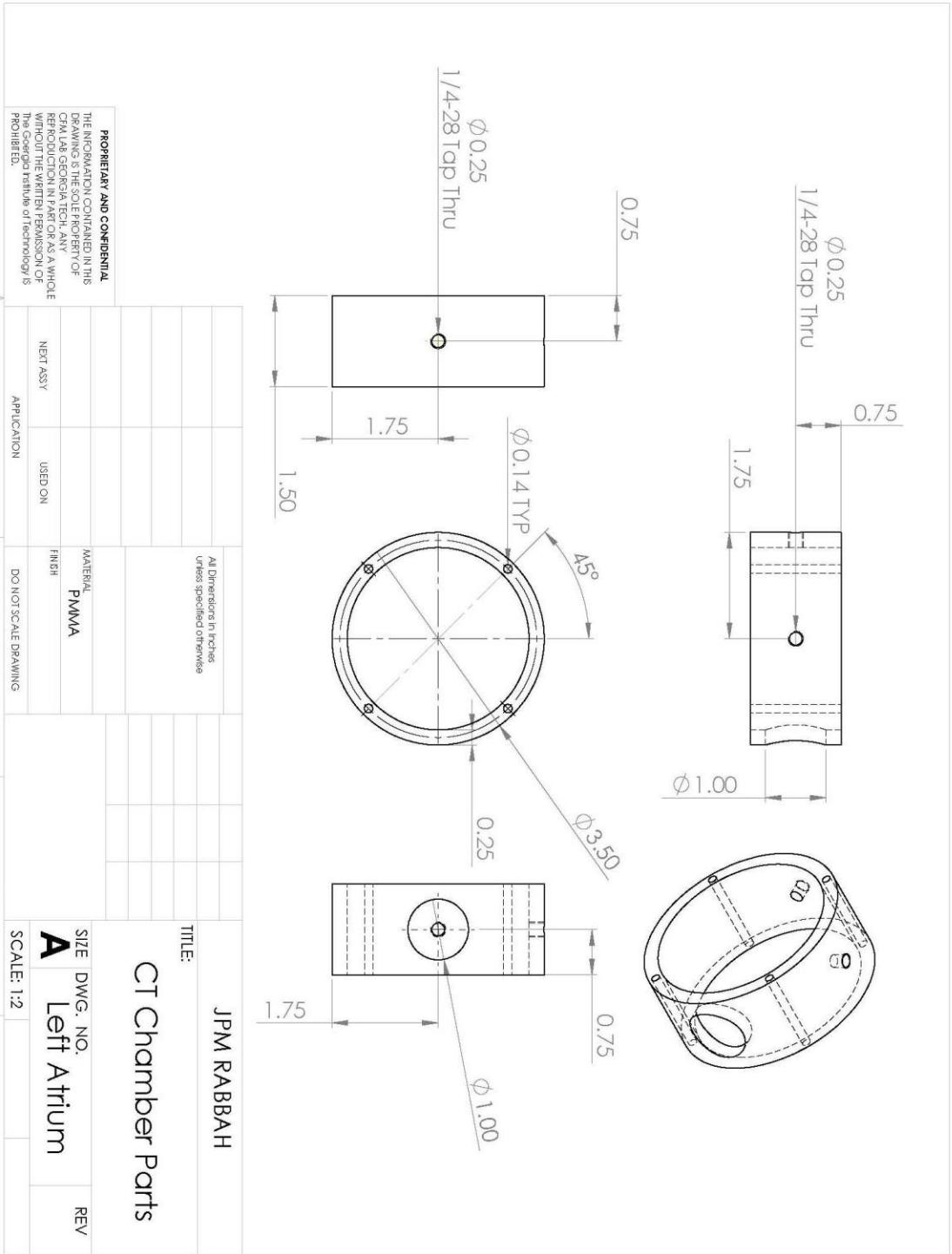
3

2

1

All Dimensions in inches unless specified otherwise		TITLE:	
MFG:		JPM RABBAN	
SI A Printed at <a href="http://fineinertprototyping.com">fineinertprototyping.com</a>		CT Chamber Parts	
MATERIAL:		SIZE DWG. NO.	
Watershed ABS		A PM Socket Ball	
FINISH:		SCALE: 2:1	
Standard		REV	
DO NOT SCALE DRAWING			
APPLICATION	USED ON		
NEXT ASSY			





**PROPRIETARY AND CONFIDENTIAL**  
 THE INFORMATION CONTAINED IN THIS DRAWING IS THE SOLE PROPERTY OF CFM LAB GEORGIA TECH. ANY REPRODUCTION IN PART OR AS A WHOLE WITHOUT THE WRITTEN PERMISSION OF THE COMPANY IS STRICTLY PROHIBITED.

5

4

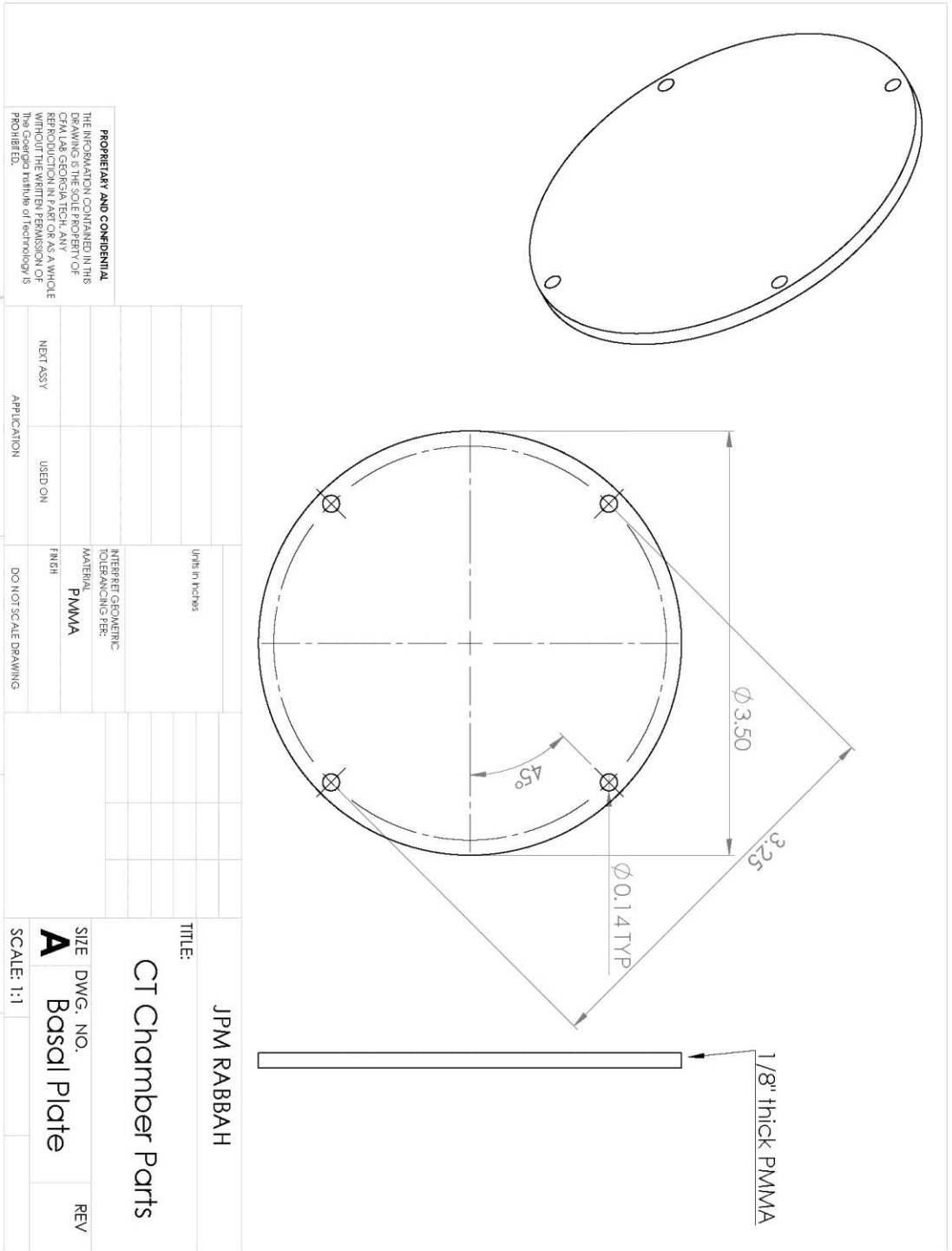
3

2

1

TITLE: <b>JPM RABBAN</b>		All Dimensions in inches Unless specified otherwise	
CT Chamber Parts		MATERIAL: <b>PMMA</b>	
SIZE DWG. NO. <b>A</b>		FINISH:	
Left Atrium		DO NOT SCALE DRAWING	
REV	SCALE: 1:2	APPLICATION	USED ON
		NEXT ASSY	





**PROPRIETARY AND CONFIDENTIAL**  
 THE INFORMATION CONTAINED IN THIS DRAWING IS THE SOLE PROPERTY OF CFM LAB. GEORGIA TECH. ANY REPRODUCTION IN PART OR AS A WHOLE WITHOUT THE WRITTEN PERMISSION OF THE ORIGINAL CONTRIBUTOR OR TECHNOLOGY IS PROHIBITED.

TITLE:		JPM RABBAN	
CT Chamber Parts			
SIZE	DWG. NO.	REV	
<b>A</b>	Basal Plate		
NEXT ASSY		USED ON	
APPLICATION		DO NOT SCALE DRAWING	
5		4	
3		2	
1			



## REFERENCES

- [1] Liao, J., I. Vesely. A structural basis for the size-related mechanical properties of mitral valve chordae tendineae. *Journal of Biomechanics* 2003.
- [2] Jensen, M.Ø.J., A.A. Fontaine, A.P. Yoganathan. Improved In Vitro Quantification of the Force Exerted by the Papillary Muscle on the Left Ventricular Wall: Three-Dimensional Force Vector Measurement System. *Annals of Biomedical Engineering* 2001;29:406-413.
- [3] Ahmad, R.M., A.M. Gillinov, P.M. McCarthy et al. Annular Geometry and Motion in Human Ischemic Mitral Regurgitation: Novel Assessment With Three-Dimensional Echocardiography and Computer Reconstruction. *The Annals of Thoracic Surgery* 2004;78:2063-2068.
- [4] Grashow, J., A. Yoganathan, M. Sacks. Biaxial Stress–Stretch Behavior of the Mitral Valve Anterior Leaflet at Physiologic Strain Rates. *Annals of Biomedical Engineering* 2006;34:315-325.
- [5] Rausch, M.K., F.A. Tibayan, D. Craig Miller et al. Evidence of adaptive mitral leaflet growth. *Journal of the Mechanical Behavior of Biomedical Materials* 2012;15:208-217.
- [6] Sacks, M.S., Y. Enomoto, J.R. Graybill et al. In-vivo dynamic deformation of the mitral valve anterior leaflet. *Annals of Thoracic Surgery* 2006;82:1369-77.
- [7] Rausch, M., W. Bothe, J.-P. Escobar-Kvitting et al. In-Vivo Dynamic Strains of the Ovine Anterior Mitral Valve Leaflet. *Journal of Biomechanics* 2011;44:1149-1157.
- [8] Nielsen, S.L., D.D. Soerensen, P. Libergren et al. Miniature C-shaped transducers for chordae tendineae force measurements. *Annals of Biomedical Engineering* 2004;32:1050-1057.

- [9] Askov, J.B., J.L. Hønge, M.O. Jensen et al. Significance of force transfer in mitral valve-left ventricular interaction: In vivo assessment. *The Journal of Thoracic and Cardiovascular Surgery* 2012.
- [10] Grigioni, F., M. Enriquez-Sarano, K.J. Zehr et al. Ischemic Mitral Regurgitation : Long-Term Outcome and Prognostic Implications With Quantitative Doppler Assessment. *Circulation* 2001;103:1759-1764.
- [11] Watanabe, N., Y. Ogasawara, Y. Yamaura et al. Mitral Annulus Flattens in Ischemic Mitral Regurgitation: Geometric Differences Between Inferior and Anterior Myocardial Infarction: A Real-Time 3-Dimensional Echocardiographic Study. *Circulation* 2005;112:I-458-462.
- [12] Magne, J., M. Sénéchal, J.G. Dumesnil et al. Ischemic Mitral Regurgitation: A Complex Multifaceted Disease. *Cardiology* 2009;112:244-259.
- [13] Tibayan, F.A., F. Rodriguez, M.K. Zasio et al. Geometric Distortions of the Mitral Valvular-Ventricular Complex in Chronic Ischemic Mitral Regurgitation. *Circulation* 2003;108:II-116-121.
- [14] He, S., J. Jack D. Lemmon, M.W. Weston et al. Mitral Valve Compensation for Annular Dilation: In Vitro Study into the Mechanisms of Functional Mitral Regurgitation with an Adjustable Annulus Model. *The Journal of Heart Valve Disease* 1999;8:294-302.
- [15] Tahta, S.A., J.H. Oury, J.M. Maxwell et al. Outcome after mitral valve repair for functional ischemic mitral regurgitation. *The Journal of Heart Valve Disease* 2002;11:11-8.
- [16] Romano, M.A., H.J. Patel, F.D. Pagani et al. Anterior Leaflet Repair With Patch Augmentation for Mitral Regurgitation. *The Annals of Thoracic Surgery* 2005;79:1500-1504.
- [17] Peeler, B.B., I.L. Kron. Suture Relocation of the Posterior Papillary Muscle in Ischemic Mitral Regurgitation. *Operative Techniques in Thoracic and Cardiovascular Surgery* 2005;10:113-122.

- [18] Little, S.H. Is it really getting easier to assess mitral regurgitation using proximal isovelocity surface area? *Journal of American Society of Echocardiography* 2012;25:824-826.
- [19] Wang, Q., W. Sun. Finite Element Modeling of Mitral Valve Dynamic Deformation Using Patient-Specific Multi-Slices Computed Tomography Scans. *Annals of Biomedical Engineering* 2012:1-12.
- [20] Mansi, T., I. Voigt, B. Georgescu et al. An integrated framework for finite-element modeling of mitral valve biomechanics from medical images: Application to MitralClip intervention planning. *Medical image analysis* 2012.
- [21] Neumann, D., S. Grbic, T. Mansi et al. Multi-modal pipeline for comprehensive validation of mitral valve geometry and functional computational models. 2013.
- [22] Lamas, G.A., G.F. Mitchell, G.C. Flaker et al. Clinical Significance of Mitral Regurgitation After Acute Myocardial Infarction. *Circulation* 1997;96:827-833.
- [23] Koelling, T.M., K.D. Aaronson, R.J. Cody et al. Prognostic significance of mitral regurgitation and tricuspid regurgitation in patients with left ventricular systolic dysfunction. *American Heart Journal* 2002;144:524-529.
- [24] Bonow, R.O., B.A. Carabello, K. Chatterjee et al. ACC/AHA 2006 Guidelines for the Management of Patients With Valvular Heart Disease. *Circulation* 2006;114:e84-231.
- [25] Bolling, S.F., S. Li, S.M. O'Brien et al. Predictors of Mitral Valve Repair: Clinical and Surgeon Factors. *The Annals of Thoracic Surgery* 2010;90:1904-1912.
- [26] Gillinov, A., D. Cosgrove, E. Blackstone et al. Durability of mitral valve repair for degenerative disease. *J Thorac Cardiovasc Surg* 1998;116:734-743.
- [27] Gillinov, A.M., P.N. Wierup, E.H. Blackstone et al. Is repair preferable to replacement for ischemic mitral regurgitation? *The Journal of thoracic and cardiovascular surgery* 2001;122:1125-1141.

- [28] Shuhaiber, J., R.J. Anderson. Meta-analysis of clinical outcomes following surgical mitral valve repair or replacement. *European Journal of Cardio-Thoracic Surgery* 2007;31:267-275.
- [29] Vassileva, C.M., T. Boley, S. Markwell et al. Meta-analysis of short-term and long-term survival following repair versus replacement for ischemic mitral regurgitation. *Eur J Cardiothorac Surg* 2011;39:295-303.
- [30] Adams, D.H., A.C. Anyanwu. The Cardiologist's Role in Increasing the Rate of Mitral Valve Repair in Degenerative Disease. *Current Opinion in Cardiology* 2008;23:105-110.
- [31] Adams, D.H., A. Anyanwu. Seeking a higher standard for degenerative mitral valve repair: begin with etiology. *the Journal of thoracic and cardiovascular surgery* 2008;136:551-556.
- [32] He, S., A.A. Fontaine, E. Schwammenthal et al. Integrated Mechanism for Functional Mitral Regurgitation : Leaflet Restriction Versus Coapting Force: In Vitro Studies. *Circulation* 1997;96:1826-1834.
- [33] He, S., M.W. Weston, J. Lemmon et al. Geometric distribution of chordae tendineae: an important anatomic feature in mitral valve function. *J Heart Valve Dis* 2000;9:495-501; discussion 502-3.
- [34] He, S., J.H. Jimenez, Z. He et al. Mitral Leaflet Geometry Perturbations with Papillary Muscle Displacement and Annular Dilation: an In-Vitro Study of Ischemic Mitral Regurgitation. *The Journal of Heart Valve Disease* 2003;12:300-7.
- [35] Jimenez, J.H., D.D. Soerensen, Z. He et al. Effects of Papillary Muscle Position on Chordal Force Distribution: An In-Vitro Study. *The Journal of Heart Valve Disease* 2005;14:295-302.
- [36] Padala, M., R.A. Hutchison, L.R. Croft et al. Saddle Shape of the Mitral Annulus Reduces Systolic Strains on the P2 Segment of the Posterior Mitral Leaflet. *The Annals of Thoracic Surgery* 2009;88:1499-1504.

- [37] Rabbah, J.-P., N. Saikrishnan, A. Yoganathan. A Novel Left Heart Simulator for the Multi-modality Characterization of Native Mitral Valve Geometry and Fluid Mechanics. *Annals of Biomedical Engineering* 2012;[Epub ahead of print]:1-11.
- [38] Rabbah, J.-P., B. Chism, A. Siefert et al. Effects of Targeted Papillary Muscle Relocation on Mitral Leaflet Tenting and Coaptation. *The Annals of Thoracic Surgery* 2013;95:621-628.
- [39] Siefert, A.W., J.P.M. Rabbah, K.J. Koomalsingh et al. In Vitro Mitral Valve Simulator Mimics Systolic Valvular Function of Chronic Ischemic Mitral Regurgitation Ovine Model. *The Annals of Thoracic Surgery* 2013;95:825-830.
- [40] Gorman, J.H., R.C. Gorman, B.M. Jackson et al. Annuloplasty ring selection for chronic ischemic mitral regurgitation: lessons from the ovine model. *Annals of Thoracic Surgery* 2003;76:1556-1563.
- [41] Zhu, F., Y. Otsuji, G. Yotsumoto et al. Mechanism of Persistent Ischemic Mitral Regurgitation After Annuloplasty: Importance of Augmented Posterior Mitral Leaflet Tethering. *Circulation* 2005;112:I-396-I-401.
- [42] Alfieri, O., M. De Bonis. Mitral Valve Repair for Functional Mitral Regurgitation: Is Annuloplasty Alone Enough? *Current Opinion in Cardiology* 2010;25:114-118.
- [43] Grossi, E.A., C.S. Bizakis, A. LaPietra et al. Late Results of Isolated Mitral Annuloplasty for “Functional” Ischemic Mitral Insufficiency. *Journal of Cardiac Surgery* 2001;16:328-332.
- [44] Hung, J., L. Papakostas, S.A. Tahta et al. Mechanism of Recurrent Ischemic Mitral Regurgitation After Annuloplasty. *Circulation* 2004;110:II-85-II-90.
- [45] Matsunaga, A., S.A. Tahta, C.M.G. Duran. Failure of Reduction Annuloplasty for Functional Ischemic Mitral Regurgitation. *The Journal of Heart Valve Disease* 2004;13:390-7.

- [46] McGee, J.E.C., A.M. Gillinov, E.H. Blackstone et al. Recurrent mitral regurgitation after annuloplasty for functional ischemic mitral regurgitation. *Journal of Thoracic and Cardiovascular Surgery* 2004;128:916-924.
- [47] Kuwahara, E., Y. Otsuji, Y. Iguro et al. Mechanism of Recurrent/Persistent Ischemic/Functional Mitral Regurgitation in the Chronic Phase After Surgical Annuloplasty: Importance of Augmented Posterior Leaflet Tethering. *Circulation* 2006;114:I-529-534.
- [48] Braun, J., N.R. van de Veire, R.J.M. Klautz et al. Restrictive Mitral Annuloplasty Cures Ischemic Mitral Regurgitation and Heart Failure. *The Annals of Thoracic Surgery* 2008;85:430-437.
- [49] Kongsarepong, V., M. Shiota, A.M. Gillinov et al. Echocardiographic Predictors of Successful Versus Unsuccessful Mitral Valve Repair in Ischemic Mitral Regurgitation. *The American Journal of Cardiology* 2006;98:504-508.
- [50] Gelsomino, S., R. Lorusso, G. De Cicco et al. Five-year echocardiographic results of combined undersized mitral ring annuloplasty and coronary artery bypass grafting for chronic ischaemic mitral regurgitation. *European Heart Journal* 2008;29:231-240.
- [51] Magne, J., P. Pibarot, F. Dagenais et al. Preoperative Posterior Leaflet Angle Accurately Predicts Outcome After Restrictive Mitral Valve Annuloplasty for Ischemic Mitral Regurgitation. *Circulation* 2007;115:782-791.
- [52] Calafiore, A.M., S. Gallina, M. Di Mauro et al. Mitral valve procedure in dilated cardiomyopathy: repair or replacement? *The Annals of Thoracic Surgery* 2001;71:1146-1152.
- [53] Roshanali, F., M.H. Mandegar, M.A. Yousefnia et al. A Prospective Study of Predicting Factors in Ischemic Mitral Regurgitation Recurrence After Ring Annuloplasty. *The Annals of Thoracic Surgery* 2007;84:745-749.
- [54] Fattouch, K., P. Lancellotti, S. Castrovinci et al. Papillary muscle relocation in conjunction with valve annuloplasty improve repair results in severe ischemic mitral regurgitation. *The Journal of thoracic and cardiovascular surgery* 2012;143:1352-1355.



- [55] Hvass, U., T. Joudinaud. The papillary muscle sling for ischemic mitral regurgitation. *The Journal of thoracic and cardiovascular surgery* 2010;139:418-423.
- [56] Kron, I.L., G.R. Green, J.T. Cope. Surgical relocation of the posterior papillary muscle in chronic ischemic mitral regurgitation. *The Annals of Thoracic Surgery* 2002;74:600-601.
- [57] Kincaid, E.H., R.D. Riley, M.H. Hines et al. Anterior leaflet augmentation for ischemic mitral regurgitation. *The Annals of Thoracic Surgery* 2004;78:564-568.
- [58] Hines, M.H., E.H. Kincaid, A.L. Cook et al. Anterior leaflet augmentation for ischemic mitral regurgitation in patients with anomalous left coronary artery from the pulmonary artery and preserved left ventricular function. *The Journal of thoracic and cardiovascular surgery* 2011;In Press, Corrected Proof.
- [59] Wong, V.M., J.F. Wenk, Z. Zhang et al. The Effect of Mitral Annuloplasty Shape in Ischemic Mitral Regurgitation: A Finite Element Simulation. *Annals of Thoracic Surgery* 2012;93:776-782.
- [60] Prot, V., R. Haaverstad, B. Skallerud. Finite element analysis of the mitral apparatus: annulus shape effect and chordal force distribution. *Biomechanics and Modeling in Mechanobiology* 2009;8:43-55.
- [61] Votta, E., F. Maisano, S.F. Bolling et al. The Geoform Disease-Specific Annuloplasty System: A Finite Element Study. *Annals of Thoracic Surgery* 2007;84:92-101.
- [62] Kunzelman, K.S., D.W. Quick, R.P. Cochran. Altered collagen concentration in mitral valve leaflets: biochemical and finite element analysis. *Annals of Thoracic Surgery* 1998;66:S198-S205.
- [63] Avanzini, A. A Computational Procedure for Prediction of Structural Effects of Edge-to-Edge Repair on Mitral Valve. *Journal of Biomechanical Engineering* 2008;130:031015-10.

- [64] Reimink, M.S., K.S. Kunzelman, R.P. Cochran. The effect of chordal replacement suture length on function and stresses in repaired mitral valves: a finite element study. *J Heart Valve Dis* 1996;5:365-75.
- [65] Kunzelman, K., M.S. Reimink, E.D. Verrier et al. Replacement of Mitral Valve Posterior Chordae Tendineae with Expanded Polytetrafluoroethylene Suture: A Finite Element Study. *Journal of Cardiac Surgery* 1996;11:136-145.
- [66] Salgo, I.S. Effect of Annular Shape on Leaflet Curvature in Reducing Mitral Leaflet Stress. *Circulation* 2002;106:711-717.
- [67] Xu, C., C.J. Brinster, A.S. Jassar et al. A novel approach to in vivo mitral valve stress analysis. *American Journal of Physiology - Heart and Circulatory Physiology* 2010;299:H1790-H1794.
- [68] Carpentier, A., D.H. Adams, F. Filsoofi. *Carpentier's reconstructive valve surgery*. Maryland Heights, Missouri: Saunders, 2010.
- [69] He, S., J. Jimenez, Z. He et al. Mitral leaflet geometry perturbations with papillary muscle displacement and annular dilatation: an in-vitro study of ischemic mitral regurgitation. *J Heart Valve Dis* 2003;12:300-7.
- [70] Fenoglio, J.J., Tuan-Duc-Pham, A.L. Wit et al. Canine mitral complex. Ultrastructure and electromechanical properties. *Circulation research* 1972;31:417-430.
- [71] Kunzelman, K.S., R.P. Cochran, C. Chuong et al. Finite element analysis of the mitral valve. *J Heart Valve Dis* 1993;2:326-240.
- [72] Grande-Allen, K.J., A. Calabro, V. Gupta et al. Glycosaminoglycans and proteoglycans in normal mitral valve leaflets and chordae: association with regions of tensile and compressive loading. *Glycobiology* 2004;14:621-633.
- [73] Kunzelman, K.S., R.P. Cochran, S. Murphree et al. Differential Collagen Distribution in the Mitral Valve and Its Influence on Biomechanical Behaviour. *Journal of Heart Valve Disease* 1993;2:236-44.

- [74] Lam, J.H., N. Ranganathan, E.D. Wigle et al. Morphology of the human mitral valve. I. Chordae tendineae: a new classification. *Circulation* 1970;41:449-458.
- [75] Ranganathan, N., J.H. Lam, E.D. Wigle et al. Morphology of the human mitral valve. II. The valve leaflets. *Circulation* 1970;41:459-467.
- [76] Sedransk, K.L., K.J. Grande-Allen, I. Vesely. Failure mechanics of mitral valve chordae tendineae. *J Heart Valve Dis* 2002;11:644-650.
- [77] Ritchie, J., J. Jimenez, Z. He et al. The material properties of the native porcine mitral valve chordae tendineae: an in vitro investigation. *Journal of Biomechanics* 2006;39:1129-1135.
- [78] Lim, K.O., D.R. Boughner. Morphology and relationship to extensibility curves of human mitral valve chordae tendineae. *Circulation research* 1976;39:580-585.
- [79] Millington-Sanders, C., A. Meir, L. Lawrence et al. Structure of chordae tendineae in the left ventricle of the human heart. *Journal of Anatomy* 1998;192:573-581.
- [80] Quill, J.L., A.J. Hill, T.G. Laske et al. Mitral leaflet anatomy revisited. *J Thorac Cardiovasc Surg* 2009;137:1077-1081.
- [81] Degandt, A.A., P.A. Weber, H.A. Saber et al. Mitral Valve Basal Chordae: Comparative Anatomy and Terminology. *Annals of Thoracic Surgery* 2007;84:1250-1255.
- [82] Anderson, R.H., M. Kanani. Mitral valve repair: critical analysis of the anatomy discussed. *Multimedia Manual of Cardiothoracic Surgery* 2007;0219:2147:1-9.
- [83] Joudinaud, T.M., C.L. Kegel, E.M. Flecher et al. The papillary muscles as shock absorbers of the mitral valve complex. An experimental study. *European journal of cardiothoracic surgery* 2007;32:96-101.

- [84] Gorman, J.H., R.C. Gorman, B.M. Jackson et al. Distortions of the mitral valve in acute ischemic mitral regurgitation. *Annals of Thoracic Surgery* 1997;64:1026-1031.
- [85] Madu, E.C., D.S. Baugh, I.A. D'Amico;Cruz et al. Left ventricular papillary muscle morphology and function in left ventricular hypertrophy and left ventricular dysfunction. *Medical science monitor : international medical journal of experimental and clinical research* 2001;7:1212-1218.
- [86] Ormiston, J.A., P.M. Shah, C. Tei et al. Size and motion of the mitral valve annulus in man. I. A two-dimensional echocardiographic method and findings in normal subjects. *Circulation* 1981;64:113-120.
- [87] Chan, J.K.M., R. Merrifield, R.R. Wage et al. Two-dimensional M-Mode display of the mitral valve from CMR cine acquisitions: insights into normal leaflet and annular motion. *J Cardiovasc Magn Reson* 2008;10:A351.
- [88] Boltwood, C.M., C. Tei, M. Wong et al. Quantitative echocardiography of the mitral complex in dilated cardiomyopathy: the mechanism of functional mitral regurgitation. *Circulation* 1983;68:498-508.
- [89] Levine, R.A., M.O. Triulzi, P. Harrigan et al. The relationship of mitral annular shape to the diagnosis of mitral valve prolapse. *Circulation* 1987;75:756-767.
- [90] Ahmad, R.M., A.M. Gillinov, P.M. McCarthy et al. Annular Geometry and Motion in Human Ischemic Mitral Regurgitation: Novel Assessment With Three-Dimensional Echocardiography and Computer Reconstruction. *Annals of Thoracic Surgery* 2004;78:2063-2068.
- [91] Rausch, M.K., W. Bothe, J.P. Kvitting et al. Characterization of mitral valve annular dynamics in the beating heart. *Annals of Biomedical Engineering* 2011;39:1690-702.
- [92] Gorman III JH, J.B., Moainie SL, Enomoto Y, Gorman RC. Influence of Inotropy and Chronotropy on the Mitral Valve Sphincter Mechanism. *Annals of Thoracic Surgery* 2004;77:852-858.

- [93] Yiu, S.F., M. Enriquez-Sarano, C. Tribouilloy et al. Determinants of the Degree of Functional Mitral Regurgitation in Patients With Systolic Left Ventricular Dysfunction : A Quantitative Clinical Study. *Circulation* 2000;102:1400-1406.
- [94] Veronesi F, C.C., Sugeng L Quantification of Mitral Apparatus Dynamics in Functional and Ischemic Mitral Regurgitation Using Real-time 3-Dimensional Echocardiography. *Journal of the American Society of Echocardiography* 2008;21:347-354.
- [95] Timek, T.A., G.R. Green, F.A. Tibayan et al. Aorto-mitral annular dynamics. *Annals of Thoracic Surgery* 2003;76:1944-1950.
- [96] Levine, R.A., M.D. Handschumacher, A.J. Sanfilippo et al. Three-dimensional echocardiographic reconstruction of the mitral valve, with implications for the diagnosis of mitral valve prolapse. *Circulation* 1989;80:589-598.
- [97] Gorman, J.H., B.M. Jackson, Y. Enomoto et al. The effect of regional ischemia on mitral valve annular saddle shape. *Annals of Thoracic Surgery* 2004;77:544-548.
- [98] Tibayan, F.A., F. Rodriguez, F. Langer et al. Annular Remodeling in Chronic Ischemic Mitral Regurgitation: Ring Selection Implications. *Annals of Thoracic Surgery* 2003;76:1549-1555.
- [99] Ryan, L.P., B.M. Jackson, H. Hamamoto et al. The influence of annuloplasty ring geometry on mitral leaflet curvature. *Annals of Thoracic Surgery* 2008;86:749-60; discussion 749-60.
- [100] Komoda T, H.R., Oellnger J. Mitral annular flexibility. *Journal of cardiothoracic surgery* 1997;1997:102-109.
- [101] Itoh, A., D.B. Ennis, W. Bothe et al. Mitral annular hinge motion contribution to changes in mitral septal-lateral dimension and annular area. *The Journal of Thoracic and Cardiovascular Surgery* 2009;138:1090-9.
- [102] Kaplan SR, B.G., Gaddipatti A. . Three-dimensional echocardiographic assessment of annular shape changes in the normal and regurgitant valve. *American Heart Journal* 2000;139:378-387.

- [103] Jimenez, J.H., S.W. Liou, M. Padala et al. A saddle-shaped annulus reduces systolic strain on the central region of the mitral valve anterior leaflet. *The Journal of Thoracic and Cardiovascular Surgery* 2007;134:1562-8.
- [104] Padala, M., R.A. Hutchison, L.R. Croft et al. Saddle Shape of the Mitral Annulus Reduces Systolic Strains on the P2 Segment of the Posterior Mitral Leaflet. *Annals of Thoracic Surgery* 2009;88:1499-1504.
- [105] Jimenez, J.H., D.D. Soerensen, Z. He et al. Effects of a saddle shaped annulus on mitral valve function and chordal force distribution: an in vitro study. *Annals of Biomedical Engineering* 2003;31:1171-1181.
- [106] Kunzelman, K.S., R.P. Cochran. Stress/Strain Characteristics of Porcine Mitral Valve Tissue: Parallel versus perpendicular collagen orientation. *Journal of Cardiac Surgery* 1992;7:71-8.
- [107] May-Newman, K., F.C. Yin. Biaxial mechanical behavior of excised porcine mitral valve leaflets. *American Journal of Physiology - Heart and Circulatory Physiology* 1995;269:H1319-H1327.
- [108] Chen, L., F.C.P. Yin, M.D et al. The Structure and Mechanical Properties of the Mitral Valve Leaflet-Strut Chordae Transition Zone. *Journal of Biomechanical Engineering* 2004;126:244-251.
- [109] Imanaka, K., S. Takamoto, T. Ohtsuka et al. The Stiffness of Normal and Abnormal Mitral Valves. *Annals of Thoracic and Cardiovascular Surgery* 2007;13:178-184.
- [110] Liao, J., L. Yang, J. Grashow et al. The Relation Between Collagen Fibril Kinematics and Mechanical Properties in the Mitral Valve Anterior Leaflet. *Journal of Biomechanical Engineering* 2007;129:78-87.
- [111] Krishnamurthy, G., D.B. Ennis, A. Itoh et al. Material properties of the ovine mitral valve anterior leaflet in vivo from inverse finite element analysis. *American Journal of Physiology - Heart and Circulatory Physiology* 2008;295:H1141-H1149.

- [112] Itoh, A., G. Krishnamurthy, J.C. Swanson et al. Active stiffening of mitral valve leaflets in the beating heart. *American Journal of Physiology - Heart and Circulatory Physiology* 2009;296:H1766-H1773.
- [113] Krishnamurthy, G., A. Itoh, W. Bothe et al. Stress–strain behavior of mitral valve leaflets in the beating ovine heart. *Journal of Biomechanics* 2009;42:1909-1916.
- [114] Stephens, E.H., N.d. Jonge, M.P. McNeill et al. Age-Related Changes in Material Behaviour of Porcine Mitral and Aortic Valves and Correlation to Matrix Composition. *Tissue Engineering Part A* 2010;16:867-878.
- [115] Grashow, J., M. Sacks, J. Liao et al. Planar Biaxial Creep and Stress Relaxation of the Mitral Valve Anterior Leaflet. *Annals of Biomedical Engineering* 2006;34:1509-1518.
- [116] Skallerud, B., V. Prot, I. Nordrum. Modeling active muscle contraction in mitral valve leaflets during systole: a first approach. *Biomechanics and Modeling in Mechanobiology* 2011;10:11-26.
- [117] Grande-Allen, K.J., J.E. Barber, K.M. Klatka et al. Mitral valve stiffening in end-stage heart failure: Evidence of an organic contribution to functional mitral regurgitation. *The Journal of thoracic and cardiovascular surgery* 2005;130:783-790.
- [118] Sacks, M.S., Z. He, L. Baijens et al. Surface Strains in the Anterior Leaflet of the Functioning Mitral Valve. *Annals of Biomedical Engineering* 2002;30:1281-1290.
- [119] He, Z., M. Sacks, L. Baijens et al. Effects of Papillary Muscle Position on In-Vitro Dynamic Strain on the Porcine MV. *Journal of Heart Valve Disease* 2003;12:488-94.
- [120] He, Z., J. Ritchie, J.S. Grashow et al. In Vitro Dynamic Strain Behavior of the Mitral Valve Posterior Leaflet. *Journal of Biomechanical Engineering* 2005;127:504-511.

- [121] Bothe, W., J.C. Swanson, N.B. Ingels et al. How much septal-lateral mitral annular reduction do you get with new ischemic/functional mitral regurgitation annuloplasty rings? *The Journal of Thoracic and Cardiovascular Surgery* 2010;140:117-21, 121 e1-3.
- [122] Amini, R., C.E. Eckert, K. Koomalsingh et al. On the in vivo deformation of the mitral valve anterior leaflet: effects of annular geometry and referential configuration. *Annals of Biomedical Engineering* 2012;40:1455-67.
- [123] Salgo, I.S., J.H. Gorman, III, R.C. Gorman et al. Effect of Annular Shape on Leaflet Curvature in Reducing Mitral Leaflet Stress. *Circulation* 2002;106:711-717.
- [124] Maurer, G. Mitral Leaflet in Functional Regurgitation. *Circulation* 2009;120:275-277.
- [125] Chaput, M., M.D. Handschumacher, J.L. Guerrero et al. Mitral Leaflet Adaptation to Ventricular Remodeling. *Circulation* 2009;120:S99-S103.
- [126] Chaput, M., M.D. Handschumacher, F. Tournoux et al. Mitral Leaflet Adaptation to Ventricular Remodeling. *Circulation* 2008;118:845-852.
- [127] Timek, T.A., D.T. Lai, P. Dagum et al. Mitral Leaflet Remodeling in Dilated Cardiomyopathy. *Circulation* 2006;114:I-518-I-523.
- [128] Stephens, E.H., T.A. Timek, G.T. Daughters et al. Significant Changes in Mitral Valve Leaflet Matrix Composition and Turnover With Tachycardia-Induced Cardiomyopathy. *Circulation* 2009;120:S112-S119.
- [129] Stephens, E.H., T.C. Nguyen, A. Itoh et al. The Effects of Mitral Regurgitation Alone Are Sufficient for Leaflet Remodeling. *Circulation* 2008;118:S243-S249.
- [130] Dal-Bianco, J.P., E. Aikawa, J. Bischoff et al. Active Adaptation of the Tethered Mitral Valve. *Circulation* 2009;120:334-342.



- [131] Obadia, J.F., C. Casali, J.F. Chassignolle et al. Mitral subvalvular apparatus: different functions of primary and secondary chordae. *Circulation* 1997;96:3124-3128.
- [132] Goetz, W.A., H.-S. Lim, E. Lansac et al. The aortomitral angle is suspended by the anterior mitral basal stay chords. *The Thoracic and cardiovascular surgeon* 2003;51:190-195.
- [133] Clark, R.E. Stress-strain characteristics of fresh and frozen human aortic and mitral leaflets and chordae tendineae. Implications for clinical use. *The Journal of Thoracic and Cardiovascular Surgery* 1973;66:202-208.
- [134] Lim, K.O., D.R. Boughner. Mechanical properties of human mitral valve chordae tendineae: variation with size and strain rate. *Canadian journal of physiology and pharmacology* 1975;53:330-339.
- [135] Lim, K.O., D.R. Boughner, C.A. Smith. Dynamic elasticity of human mitral valve chordae tendineae. *Canadian journal of physiology and pharmacology* 1977;55:413-418.
- [136] Kunzelman, K.S., R.P. Cochran. Mechanical properties of basal and marginal mitral valve chordae tendineae. *ASAIO transactions / American Society for Artificial Internal Organs* 1990;36:M405-8.
- [137] Salisbury, P.F., C.E. Cross, P.A. Rieben. Chorda tendinea tension. *American journal of physiology* 1963;205:385-392.
- [138] Lomholt, M., S.L. Nielsen, S.B. Hansen et al. Differential tension between secondary and primary mitral chordae in an acute in-vivo porcine model. *J Heart Valve Dis* 2002;11:337-345.
- [139] Nielsen, S.L., S.B. Hansen, K.O. Nielsen et al. Imbalanced chordal force distribution causes acute ischemic mitral regurgitation: mechanistic insights from chordae tendineae force measurements in pigs. *The Journal of Thoracic and Cardiovascular Surgery* 2005;129:525-531.

- [140] Nielsen, S.L., H. Nygaard, A.A. Fontaine et al. Chordal force distribution determines systolic mitral leaflet configuration and severity of functional mitral regurgitation. *Journal of the American College of Cardiology* 1999;33:843-853.
- [141] Nielsen, S.L., H. Nygaard, L. Mandrup et al. Mechanism of incomplete mitral leaflet coaptation--interaction of chordal restraint and changes in mitral leaflet coaptation geometry. Insight from in vitro validation of the premise of force equilibrium. *Journal of Biomechanical Engineering* 2002;124:596-608.
- [142] Nielsen, S.L., T.A. Timek, G.R. Green et al. Influence of anterior mitral leaflet second-order chordae tendineae on left ventricular systolic function. *Circulation* 2003;108:486-491.
- [143] Jimenez, J.H., D.D. Soerensen, Z. He et al. Mitral valve function and chordal force distribution using a flexible annulus model: an in vitro study. *Annals of Biomedical Engineering* 2005;33:557-566.
- [144] Jimenez, J.H., D.D. Soerensen, Z. He et al. Effects of papillary muscle position on chordal force distribution: an in-vitro study. *Journal of Heart Valve Disease* 2005;14:295-302.
- [145] Jimenez-Mejia, J.H. The effects of mitral annular dynamics and papillary muscle position of chordal force distribution and valve function: an in vitro study. 2003.
- [146] Granier, M., M.O. Jensen, J.L. Hongo et al. Consequences of mitral valve prolapse on chordal tension: ex vivo and in vivo studies in large animal models. *The Journal of Thoracic and Cardiovascular Surgery* 2011;142:1585-1587.
- [147] He, Z., C. Jowers. A novel method to measure mitral valve chordal tension. *Journal of Biomechanical Engineering* 2009;131:014501.
- [148] He, S., A.A. Fontaine, E. Schwammenthal et al. Integrated mechanism for functional mitral regurgitation: leaflet restriction versus coapting force: in vitro studies. *Circulation* 1997;96:1826-34.

- [149] Padala, M., L. Gyoneva, A.P. Yoganathan. Effect of anterior strut chordal transection on the force distribution on the marginal chordae of the mitral valve. *The Journal of Thoracic and Cardiovascular Surgery* 2012;144:624-633.e2.
- [150] Nielsen, S.L., M. Lomholt, P. Johansen et al. Mitral ring annuloplasty relieves tension of the secondary but not primary chordae tendineae in the anterior mitral leaflet. *The Journal of Thoracic and Cardiovascular Surgery* 2011;141:732-737.
- [151] Ostli, B., J. Vester-Petersen, J.B. Askov et al. In Vitro System for Measuring Chordal Force Changes Following Mitral Valve Patch Repair. *Cardiovascular Engineering and Technology* 2012;3:263-268.
- [152] Messas, E., J.L. Guerrero, M.D. Handschumacher et al. Chordal cutting: a new therapeutic approach for ischemic mitral regurgitation. *Circulation* 2001;104:1958-1963.
- [153] He, Z., C.W. Jowers. Effect of mitral valve strut chord cutting on marginal chord tension. *J Heart Valve Dis* 2008;17:628-634.
- [154] Hashim, S.R., A. Fontaine, S. He et al. A three-component force vector cell for in vitro quantification of the force exerted by the papillary muscle on the left ventricular wall. *Journal of Biomechanics* 1997;30:1071-1075.
- [155] Bursi, F., M. Enriquez-Sarano, S.J. Jacobsen et al. Mitral Regurgitation After Myocardial Infarction: A Review. *The American journal of medicine* 2006;119:103-112.
- [156] Grigioni, F., D. Detaint, J.-F. Avierinos et al. Contribution of ischemic mitral regurgitation to congestive heart failure after myocardial infarction. *Journal of the American College of Cardiology* 2005;45:260-267.
- [157] Watanabe, N., Y. Ogasawara, Y. Yamaura et al. Geometric Differences of the Mitral Valve Tenting Between Anterior and Inferior Myocardial Infarction with Significant Ischemic Mitral Regurgitation: Quantitation by Novel Software System with Transthoracic Real-time Three-dimensional Echocardiography. *Journal of the American Society of Echocardiography : official publication of the American Society of Echocardiography* 2006;19:71-75.

- [158] Vergnat, M., A.S. Jassar, B.M. Jackson et al. Ischemic Mitral Regurgitation: A Quantitative Three-Dimensional Echocardiographic Analysis. *The Annals of Thoracic Surgery* 2011;91:157-164.
- [159] Kumanohoso, T., Y. Otsuji, S. Yoshifuku et al. Mechanism of higher incidence of ischemic mitral regurgitation in patients with inferior myocardial infarction: Quantitative analysis of left ventricular and mitral valve geometry in 103 patients with prior myocardial infarction. *The Journal of thoracic and cardiovascular surgery* 2003;125:135-143.
- [160] Bax, J.J., J. Braun, S.T. Somer et al. Restrictive Annuloplasty and Coronary Revascularization in Ischemic Mitral Regurgitation Results in Reverse Left Ventricular Remodeling. *Circulation* 2004;110:II-103-II-108.
- [161] Filsoufi, F., S.P. Salzberg, D.H. Adams. Current Management of Ischemic Mitral Regurgitation. *Mount Sinai Journal of Medicine* 2005;72:105-115.
- [162] Braun, J., J.J. Bax, M.I.M. Versteegh et al. Preoperative left ventricular dimensions predict reverse remodeling following restrictive mitral annuloplasty in ischemic mitral regurgitation. *European Journal of Cardio-Thoracic Surgery* 2005;27:847-853.
- [163] Magne, J., P. Pibarot, J.G. Dumesnil et al. Continued Global Left Ventricular Remodeling Is Not the Sole Mechanism Responsible for the Late Recurrence of Ischemic Mitral Regurgitation after Restrictive Annuloplasty. *Journal of the American Society of Echocardiography* 2009;22:1256-1264.
- [164] Little, S.H., S.R. Igo, B. Pirat et al. In Vitro Validation of Real-Time Three-Dimensional Color Doppler Echocardiography for Direct Measurement of Proximal Isovelocity Surface Area in Mitral Regurgitation. *The American Journal of Cardiology* 2007;99:1440-1447.
- [165] de Agustín, J.A., P. Marcos-Alberca, C. Fernandez-Golfin et al. Direct Measurement of Proximal Isovelocity Surface Area by Single-Beat Three-Dimensional Color Doppler Echocardiography in Mitral Regurgitation: A Validation Study. *Journal of the American Society of Echocardiography* 2012;25:815-823.

- [166] Thavendiranathan, P., S. Liu, S. Datta et al. Quantification of Chronic Functional Mitral Regurgitation by Automated 3-Dimensional Peak and Integrated Proximal Isovelocity Surface Area and Stroke Volume Techniques Using Real-Time 3-Dimensional Volume Color Doppler Echocardiography: In Vitro and Clinical Validation. *Circulation: Cardiovascular Imaging* 2013;6:125-133.
- [167] Choon-Hwai, Y., K. Thiele, W. Qifeng et al. Novel method of measuring valvular regurgitation using three-dimensional nonlinear curve fitting of doppler signals within the flow convergence zone. *Ultrasonics, Ferroelectrics and Frequency Control, IEEE Transactions on* 2013;60:1295-1311.
- [168] Votta, E., E. Caiani, F. Veronesi et al. Mitral valve finite-element modelling from ultrasound data: a pilot study for a new approach to understand mitral function and clinical scenarios. *Philosophical Transactions of the Royal Society A: Mathematical, Physical and Engineering Sciences* 2008;366:3411-3434.
- [169] Lim, K., J. Yeo, C.M. Duran. Three-dimensional asymmetrical modeling of the mitral valve: a finite element study with dynamic boundaries. *J Heart Valve Dis* 2005;14:386-92.
- [170] Stevanella, M., E. Votta, A. Redaelli. Mitral Valve Finite Element Modeling: Implications of Tissues' Nonlinear Response and Annular Motion. *Journal of Biomechanical Engineering* 2009;131:121010.
- [171] Padala, M., M.S. Sacks, S.W. Liou et al. Mechanics of the mitral valve strut chordae insertion region. *Journal of Biomechanical Engineering* 2010;132:081004.
- [172] Cochran, R.P., K.S. Kunzelman. Effect of papillary muscle position on mitral valve function: relationship to homografts. *Annals of Thoracic Surgery* 1998;66:S155-S161.
- [173] Prot, V., B. Skallerud, G.A. Holzapfel. Transversely isotropic membrane shells with application to mitral valve mechanics. Constitutive modelling and finite element implementation. *International Journal for Numerical Methods in Engineering* 2007;71:987-1008.

- [174] Einstein, D.R., K.S. Kunzelman, P. Reinhall et al. Non-linear fluid-coupled model of the mitral valve. *J Heart Valve Dis* 2005;14:376-85.
- [175] Dal Pan, F., G. Donzella, C. Fucci et al. Structural effects of an innovative surgical technique to repair heart valve defects. *Journal of Biomechanics* 2005;38:2460-2471.
- [176] Wenk, J.F., Z. Zhang, G. Cheng et al. First Finite Element Model of the Left Ventricle With Mitral Valve: Insights Into Ischemic Mitral Regurgitation. *Annals of Thoracic Surgery* 2010;89:1546-1553.
- [177] Lau, K.D., V. Díaz-Zuccarini, P. Scambler et al. Fluid–structure interaction study of the edge-to-edge repair technique on the mitral valve. *Journal of Biomechanics* 2011;44:2409-2417.
- [178] Bouma, W., I.C.C. van der Horst, I.J. Wijdh-den Hamer et al. Chronic ischaemic mitral regurgitation. Current treatment results and new mechanism-based surgical approaches. *European Journal of Cardio-Thoracic Surgery* 2010;37:170-185.
- [179] Kaji, S., M. Nasu, A. Yamamuro et al. Annular Geometry in Patients With Chronic Ischemic Mitral Regurgitation: Three-Dimensional Magnetic Resonance Imaging Study. *Circulation* 2005;112:I-409-I-414.
- [180] Jensen, H., M. Jensen, S. Ringgaard et al. Geometric determinants of chronic functional ischemic mitral regurgitation: insights from three-dimensional cardiac magnetic resonance imaging. *The Journal of Heart Valve Disease* 2008;17:16-22.
- [181] Watanabe, N., Y. Ogasawara, Y. Yamaura et al. Geometric deformity of the mitral annulus in patients with ischemic mitral regurgitation: a real-time three-dimensional echocardiographic study. *The Journal of Heart Valve Disease* 2005;14:447-52.
- [182] Yamaura, Y., N. Watanabe, Y. Ogasawara et al. Geometric change of mitral valve leaflets and annulus after reconstructive surgery for ischemic mitral regurgitation: Real-time 3-dimensional echocardiographic study. *The Journal of thoracic and cardiovascular surgery* 2005;130:1459-1461.

- [183] McCarthy, P.M. Does the intertrigonal distance dilate? Never say never. *The Journal of Thoracic and Cardiovascular Surgery* 2002;124:1078-1079.
- [184] Walmsley, R. Anatomy of human mitral valve in adult cadaver and comparative anatomy of the valve. *British Heart Journal* 1978;40:351-366.
- [185] Hill, A.J., P.A. Iaizzo. *Comparative Cardiac Anatomy. Handbook of Cardiac Anatomy, Physiology, and Devices* 2009:87-108.
- [186] Veronesi, F., C. Corsi, L. Sugeng et al. A Study of Functional Anatomy of Aortic-Mitral Valve Coupling Using 3D Matrix Transesophageal Echocardiography / CLINICAL PERSPECTIVE. *Circulation: Cardiovascular Imaging* 2009;2:24-31.
- [187] Nielsen, S.L., H. Nygaard, A.A. Fontaine et al. Chordal force distribution determines systolic mitral leaflet configuration and severity of functional mitral regurgitation. *Journal of the American College of Cardiology* 1999;33:843-853.
- [188] Jimenez, J., D. Soerensen, Z. He et al. Effects of a Saddle Shaped Annulus on Mitral Valve Function and Chordal Force Distribution: An In Vitro Study. *Annals of Biomedical Engineering* 2003;31:1171-1181.
- [189] Nielsen, S.L., D.D. Soerensen, P. Libergren et al. Miniature C-Shaped Transducers for Chordae Tendineae Force Measurements. *Annals of Biomedical Engineering* 2004;32:1050-1057.
- [190] Gorman, J.H., III, R.C. Gorman, T. Plappert et al. Infarct Size And Location Determine Development Of Mitral Regurgitation In The Sheep Model. *J Thorac Cardiovasc Surg* 1998;115:615-622.
- [191] Jensen, H., M.O. Jensen, M.H. Smerup et al. Three-dimensional assessment of papillary muscle displacement in a porcine model of ischemic mitral regurgitation. *J Thorac Cardiovasc Surg* 2010;140:1312-1318.
- [192] Hashim, S.R., A. Fontaine, S. He et al. A three-component force vector cell for in vitro quantification of the force exerted by the papillary muscle on the left ventricular wall. *Journal of Biomechanics* 1997;30:1071-1075.

- [193] Jimenez, J.H., S.W. Liou, M. Padala et al. A saddle-shaped annulus reduces systolic strain on the central region of the mitral valve anterior leaflet. *The Journal of thoracic and cardiovascular surgery* 2007;134:1562-1568.
- [194] Rausch, M.K., W. Bothe, J.-P.E. Kvitting et al. In vivo dynamic strains of the ovine anterior mitral valve leaflet. *Journal of Biomechanics* 2011;44:1149-1157.
- [195] Metscher, B.D. MicroCT for comparative morphology: simple staining methods allow high-contrast 3D imaging of diverse non-mineralized animal tissues. *BMC Physiology* 2009.
- [196] Bouxsein, M.L., S.K. Boyd, B.A. Christiansen et al. Guidelines for assessment of bone microstructure in rodents using micro-computed tomography. *Journal of Bone and Mineral Research* 2010;25:1468-1486.
- [197] Siefert, A., D. Icenogle, J.-P. Rabbah et al. Accuracy of a Mitral Valve Segmentation Method Using J-Splines for Real-Time 3D Echocardiography Data. *Annals of Biomedical Engineering* 2013;41:1258-1268.
- [198] Dyn, N., D. Levine, J.A. Gregory. A butterfly subdivision scheme for surface interpolation with tension control. *ACM Trans Graph* 1990;9:160-169.
- [199] Hui, H. Stereo Particle Image Velocimetry Techniques: Technical Basis, System Setup, and Application.
- [200] Pu, M., P.M. Vandervoort, N.L. Greenberg et al. Impact of wall constraint on velocity distribution in proximal flow convergence zone Implications for color Doppler quantification of mitral regurgitation. *Journal of the American College of Cardiology* 1996;27:706-713.
- [201] Pu, M., P. Vandervoort, J. Rivera et al. Proximal flow constraint by the ventricular wall causes overestimation of regurgitant flow in mitral regurgitation: in-vitro assessment. *Circulation*, 1993:110-110.
- [202] Hopmeyer, J., E. Whitney, D.A. Papp et al. Computational simulations of mitral regurgitation quantification using the flow convergence method: Comparison of



hemispheric and hemielliptic formulae. *Annals of biomedical engineering* 1996;24:561-572.

- [203] Hopmeyer, J., S. He, K.M. Thorvig et al. Estimation of Mitral Regurgitation with a Hemielliptic Curve-Fitting Algorithm: In Vitro Experiments with Native Mitral Valves. *Journal of the American Society of Echocardiography* 1998;11:322-331.
- [204] Levine, R.A., L. Rodriguez, E.G. Cape et al. The proximal flow convergence method for calculating orifice flow rate requires correction for surrounding leaflet geometry. *Journal of the American College of Cardiology* 1991;17:A359-A359.
- [205] Yamachika, S., E. Cape, D. Savani et al. Role of three-dimensional valve angle on calculation of regurgitant volume by the proximal isovelocity surface area method in clinical valvular regurgitation. *J Am Coll Cardiol* 1993;21:3A.
- [206] Cape, E.G., J.D. Thomas, A.E. Weyman et al. Three-dimensional surface geometry correction is required for calculating flow by the proximal isovelocity surface area technique. *Journal of the American Society of Echocardiography* 1995;8:585-594.
- [207] Utsunomiya, T., T. Ogawa, H. Tang et al. Doppler color flow mapping of the proximal isovelocity surface area: a new method for measuring volume flow rate across a narrowed orifice. *Journal of the American Society of Echocardiography: official publication of the American Society of Echocardiography* 1991;4:338.
- [208] Lawden, D.F. *Elliptic functions and applications*: Springer New York, 1989.
- [209] Gorman, R.C., J.S. McCaughan, M.B. Ratcliffe et al. Pathogenesis of acute ischemic mitral regurgitation in three dimensions. *The Journal of thoracic and cardiovascular surgery* 1995;109:684-693.
- [210] Messas, E., J.L. Guerrero, M.D. Handschumacher et al. Chordal Cutting: A New Therapeutic Approach for Ischemic Mitral Regurgitation. *Circulation* 2001;104:1958-1963.

- [211] Ueno, T., R. Sakata, Y. Iguro et al. New Surgical Approach to Reduce Tethering in Ischemic Mitral Regurgitation by Relocation of Separate Heads of the Posterior Papillary Muscle. *The Annals of Thoracic Surgery* 2006;81:2324-2325.
- [212] Robb, J.D., M. Minakawa, K.J. Koomalsingh et al. Posterior leaflet augmentation improves leaflet tethering in repair of ischemic mitral regurgitation. *European Journal of Cardio-Thoracic Surgery* 2011;40:1501-1507.
- [213] Yosefy, C., R. Beerli, J.L. Guerrero et al. Mitral Regurgitation After Anteroapical Myocardial Infarction: New Mechanistic Insights. *Circulation* 2011;123:1529-1536.
- [214] Gorman, J.H., R.C. Gorman, B.M. Jackson et al. Distortions of the Mitral Valve in Acute Ischemic Mitral Regurgitation. *The Annals of Thoracic Surgery* 1997;64:1026-1031.
- [215] Jimenez, J., D.D. Soerensen, Z. He et al. Effects of papillary muscle position on chordal force distribution: an in-vitro study. *the Journal of Heart Valve Disease* 2005;14:295-302.
- [216] Rahmani, A., A.Q. Rasmussen, J.L. Honge et al. Mitral valve mechanics following posterior leaflet patch augmentation. *The Journal of heart valve disease* 2013;22:28.
- [217] Jimenez, J.H., D.D. Soerensen, Z. He et al. Mitral Valve Function and Chordal Force Distribution Using a Flexible Annulus Model: An In Vitro Study. *Annals of Biomedical Engineering* 2005;33:557-566.
- [218] Smerup, M., J. Funder, C. Nyboe et al. Strut chordal-sparing mitral valve replacement preserves long-term left ventricular shape and function in pigs. *The Journal of thoracic and cardiovascular surgery* 2005;130:1675-1682.
- [219] Jensen, H., M.O. Jensen, M.H. Smerup et al. Impact of Papillary Muscle Relocation as Adjunct Procedure to Mitral Ring Annuloplasty in Functional Ischemic Mitral Regurgitation. *Circulation* 2009;120:S92-98.

- [220] Nielsen, S.L., H. Nygaard, A.A. Fontaine et al. Papillary Muscle Misalignment Causes Mitral Regurgitant Jets: an Ambiguous Mechanisms for Functional Mitral Regurgitation. *The Journal of Heart Valve Disease* 1999;8:551-64.
- [221] Kunzelman, K.S., D.R. Einstein, R.P. Cochran. Fluid–structure interaction models of the mitral valve: function in normal and pathological states. *Philosophical Transactions of the Royal Society B: Biological Sciences* 2007;362:1393-1406.
- [222] Kunzelman, K.S., M.S. Reimink, R.P. Cochran. Annular dilatation increases stress in the mitral valve and delays coaptation: a finite element computer model. *Cardiovascular Surgery* 1997;5:427-434.
- [223] Pouch, A.M., C. Xu, P.A. Yushkevich et al. Semi-automated mitral valve morphometry and computational stress analysis using 3D ultrasound. *Journal of Biomechanics* 2012;45:903-907.
- [224] Stevanella, M., F. Maffessanti, C. Conti et al. Mitral Valve Patient-Specific Finite Element Modeling from Cardiac MRI: Application to an Annuloplasty Procedure. *Cardiovascular Engineering and Technology* 2011;2:66-76.
- [225] Ionasec, R.I., I. Voigt, B. Georgescu et al. Patient-Specific Modeling and Quantification of the Aortic and Mitral Valves From 4-D Cardiac CT and TEE. *Medical Imaging, IEEE Transactions on* 2010;29:1636-1651.
- [226] Arnoldi, A., A. Invernizzi, R. Ponzini et al. Mitral Valve Models Reconstructor: a Python based GUI software in a HPC environment for patient-specific FEM structural analysis *Innovations and Advances in Computer Sciences and Engineering*. In: Sobh T, editor: Springer Netherlands, 2010:215-219.
- [227] Hammer, P., P. del Nido, R. Howe. Anisotropic Mass-Spring Method Accurately Simulates Mitral Valve Closure from Image-Based Models *Functional Imaging and Modeling of the Heart*. In: Metaxas D, Axel L, editors.: Springer Berlin / Heidelberg, 2011:233-240.
- [228] Wong, V.M., J.F. Wenk, Z. Zhang et al. The Effect of Mitral Annuloplasty Shape in Ischemic Mitral Regurgitation: A Finite Element Simulation. *The Annals of Thoracic Surgery* 2012;93:776-782.

- [229] Mansi, T., I. Voigt, E. Mengue et al. Towards Patient-Specific Finite-Element Simulation of MitralClip Procedure Medical Image Computing and Computer-Assisted Intervention. In: Fichtinger G, Martel A, Peters T, editors.: Springer Berlin / Heidelberg, 2011:452-459.
- [230] Tenenholtz, N.A., P.E. Hammer, R.J. Schneider et al. On the Design of an Interactive, Patient-Specific Surgical Simulator for Mitral Valve Repair. IEEE/RSJ International Conference on Intelligent Robots and Systems. San Francisco, California, USA, 2011.
- [231] Stewart, S., E. Paterson, G. Burgreen et al. Assessment of CFD Performance in Simulations of an Idealized Medical Device: Results of FDA's First Computational Interlaboratory Study. Cardiovascular Engineering and Technology:1-22.
- [232] Einstein, D.R., F. Del Pin, X. Jiao et al. Fluid–structure interactions of the mitral valve and left heart: Comprehensive strategies, past, present and future. International Journal for Numerical Methods in Biomedical Engineering 2010;26:348-380.
- [233] Bargiggia, G., C. Bertucci, F. Recusani et al. A new method for estimating left ventricular dP/dt by continuous wave Doppler-echocardiography. Validation studies at cardiac catheterization. Circulation 1989;80:1287-1292.
- [234] Kunzelman, K.S., R.P. Cochran, C. Chuong et al. Finite Element Analysis of the Mitral Valve. The Journal of Heart Valve Disease 1993;2:326-40.
- [235] Kim, W.Y., P.G. Walker, E.M. Pedersen et al. Left ventricular blood flow patterns in normal subjects: A quantitative analysis by three-dimensional magnetic resonance velocity mapping. Journal of the American College of Cardiology 1995;26:224-238.
- [236] Reul, H., N. Talukder, E.W. Müller. Fluid mechanics of the natural mitral valve. Journal of Biomechanics 1981;14:361-372.
- [237] Domenichini, F., G. Pedrizzetti, B. Baccani. Three-dimensional filling flow into a model left ventricle. Journal of Fluid Mechanics 2005;539:179-198.

- [238] Kilner, P.J., G.-Z. Yang, A.J. Wilkes et al. Asymmetric redirection of flow through the heart. *Nature* 2000;404:759-761.
- [239] Kheradvar, A., H. Houle, G. Pedrizzetti et al. Echocardiographic Particle Image Velocimetry: A Novel Technique for Quantification of Left Ventricular Blood Vorticity Pattern. *Journal of the American Society of Echocardiography* 2010;23:86-94.
- [240] Hong, G.-R., G. Pedrizzetti, G. Tonti et al. Characterization and Quantification of Vortex Flow in the Human Left Ventricle by Contrast Echocardiography Using Vector Particle Image Velocimetry. *JACC: Cardiovascular Imaging* 2008;1:705-717.
- [241] Lee, C.-H., P.J. Oomen, J.P. Rabbah et al. A high-fidelity and micro-anatomically accurate 3d finite element model for simulations of functional mitral valve. *Functional Imaging and Modeling of the Heart: Springer Berlin Heidelberg*, 2013:416-424.
- [242] McQueen, D.M., C.S. Peskin, E.L. Yellin. Fluid dynamics of the mitral valve: physiological aspects of a mathematical model. *American Journal of Physiology - Heart and Circulatory Physiology* 1982;242:H1095-H1110.
- [243] BELLHOUSE, B.J. Fluid mechanics of a model mitral valve and left ventricle. *Cardiovascular Research* 1972;6:199-210.
- [244] Meisner, J.S., D.M. McQueen, Y. Ishida et al. Effects of timing of atrial systole on LV filling and mitral valve closure: computer and dog studies. *American Journal of Physiology - Heart and Circulatory Physiology* 1985;249:H604-H619.
- [245] Little, R.C. The mechanism of closure of the mitral valve: a continuing controversy. *Circulation* 1979;59:615-8.
- [246] Lee, K., W.J. Stewart, H. Lever et al. Mechanism of outflow tract obstruction causing failed mitral valve repair. Anterior displacement of leaflet coaptation. *Circulation* 1993;88:1124-9.

- [247] Levine, R.A., G.J. Vlahakes, X. Lefebvre et al. Papillary Muscle Displacement Causes Systolic Anterior Motion of the Mitral Valve: Experimental Validation and Insights Into the Mechanism of Subaortic Obstruction. *Circulation* 1995;91:1189-1195.
- [248] Pekkan, K., B. Whited, K. Kanter et al. Patient-specific surgical planning and hemodynamic computational fluid dynamics optimization through free-form haptic anatomy editing tool (SURGEM). *Medical & biological engineering & computing* 2008;46:1139-1152.
- [249] Flachskampf, F.A., S. Chandra, A. Gaddipatti et al. Analysis of Shape and Motion of the Mitral Annulus in Subjects With and Without Cardiomyopathy by Echocardiographic 3-Dimensional Reconstruction. *Journal of the American Society of Echocardiography* 2000;13:277-287.
- [250] Kaplan, S.R., G. Bashein, F.H. Sheehan et al. Three-dimensional echocardiographic assessment of annular shape changes in the normal and regurgitant mitral valve. *American Heart Journal* 2000;139:378-387.
- [251] Rausch, M., W. Bothe, J.-P. Kvitting et al. Characterization of Mitral Valve Annular Dynamics in the Beating Heart. *Annals of Biomedical Engineering* 2011:1-13.
- [252] Joudinaud, T.M., C.L. Kegel, E.M. Flecher et al. The papillary muscles as shock absorbers of the mitral valve complex. An experimental study. *European Journal of Cardio-Thoracic Surgery* 2007;32:96-101.
- [253] Lebrun, F., P. Lancellotti, L.A. Piérard. Quantitation of functional mitral regurgitation during bicycle exercise in patients with heart failure. *Journal of the American College of Cardiology* 2001;38:1685-1692.
- [254] Rausch, M., W. Bothe, J.-P. Kvitting et al. Mitral Valve Annuloplasty. *Annals of Biomedical Engineering* 2012;40:750-761.
- [255] Pedersen, B., T. Bechsgaard. *In Vitro Model of Left Side of the Heart: Instrumentation and Programming*. Springer 2010.

- [256] Ritchie, J., J. Jimenez, Z. He et al. The material properties of the native porcine mitral valve chordae tendineae: An in vitro investigation. *Journal of Biomechanics* 2006;39:1129-1135.